DISS. ETH NO. 19931

NUMERICAL SIMULATION OF ROCKFALL PROTECTION GALLERIES

A dissertation submitted to

ETH ZURICH

for the degree of

Doctor of Sciences

presented by

SARA GHADIMI KHASRAGHY

Master of Engineering, Asian Institute of Technology

born 07.04.1978

citizen of Iran

accepted on the recommendation of

Prof. Thomas Vogel, examiner

Prof. Dr. Norimitsu Kishi, co-examiner

Prof. Dr. Sarah M. Springman, co-examiner

2011

Summary

Rockfall is one of the major natural hazards that occur regularly in mountainous areas, the risk associated with which, tends to increase due to climate change. The consequences of rockfall hazards can be severe, which makes them important to consider, even though the overall risk may be low. Rockfall protection galleries are one of the adequate structural measures that provide protection against rockfalls.

In the past, the galleries were designed to sustain impact energies of up to 3 MJ, and recent developments allow energies up to 6 MJ by improving the performance through the use of alternative cushion layers as well as high strength materials and shear stirrups for the slab. The question is, whether if these structures are actually capable of sustaining the impacts they are designed for. Many of the existing galleries are designed based on oversimplification by engineers and may not be able to uphold the mentioned energy limit, and they are not designed following the Swiss design guideline, which was established only in 1998. However, it is important to be able to rationally design new protection galleries, besides being able to accurately determine the capacity of the existing ones. The Swiss design guideline considers application of a static equivalent force, which is formulated by conservatively extrapolating experimental results using elastic numerical analyses, and the dynamic behavior of the structure is not well incorporated.

This dissertation contributes to the improvement of the predictive accuracy of the impact capacity of rockfall protection galleries and to the establishment of a performance-based design procedure for these structures. Furthermore, it facilitates the understanding of the dynamic response of cushion layers and slabs subjected to impact loading. A numerical method using explicit finite element analyses is proposed in this study in order to investigate the dynamic response of reinforced concrete rockfall protection galleries. The applicability of the method to predict the response of slabs covered by soil is verified by comparison with suitable experimental data.

The main challenges tackled in this respect are appropriate modeling of the soil cushion, failure of the slab, as well as incorporating stress histories for consecutive rockfall impacts. A material model is adapted, which considers shear yielding of the soil as well as its hardening properties. A failure criterion is established in this study to account for failure of reinforced concrete slabs using elastic-plastic finite element analysis, which is based on the ratio between the maximum and residual deflection of the slab. In addition, a new numerical analysis procedure is developed to model consecutive impact loading on reinforced slabs.

Using the failure criterion and the numerical analysis procedure proposed, finite element analyses are applied for extension of the available physical tests that covered input energy levels of up to 0.3 MJ (Schellenberg 2008), and the influence of the boulder shape, shear reinforcement, and consecutive impact loading on the response of slabs is investigated. The finite element method is utilized as a tool to improve the assumptions made for an existing analytical model based on a system of multiple degrees of freedom proposed by Schellenberg (2008). In addition, a simplified new method using a two degrees of freedom system is

proposed. A case study is performed, which enabled comparison of different numerical methods, and finite element methods are used to simulate the gallery subjected to high impact energies of up to 2.7 MJ. The response of the gallery subjected to energies higher than 2.7 MJ is studied using analytical models.

A performance-based design procedure, called elastic recovery-based design (ERBD) is established, which incorporates the failure criterion suggested in this research to define the performance of galleries based on numerical modeling.

Zusammenfassung

Steinschlag ist eine der Naturgefahren in Bergregionen, deren Eintrittswahrscheinlichkeit sich durch klimatische Veränderungen erhöht. Die Folgen von Steinschlag können schwerwiegend sein, weshalb es wichtig ist, diese Gefahr nicht zu vernachlässigen, auch wenn die Eintrittswahrscheinlichkeit eines schwerwiegenden Falles verhältnismässig niedrig ist. Steinschlagschutzgalerien sind eine der wirksamen Strukturen, die Schutz vor Steinschlag bieten.

In der Vergangenheit wurden Galerien so gebaut, dass sie Einschlagenergien bis zu 3 MJ aushalten konnten. Durch neue Erkenntnisse im Bereich alternative Eindeckungsmaterialen, sowie hochfester Materialen, und Verbügelung der Platten kann das Verhalten auf bis zu 6 MJ erhöht werden. Die Frage ist, ob die Bauwerke tatsächlich die Einschläge aushalten, für die sie konzipiert wurden. Viele der bestehenden Galerien wurden von Ingenieuren auf Basis stark vereinfachter Annahmen bemessen und könnten die genannten Anforderungen unter Umständen nicht erfüllen. Die meisten wurden auch nicht gemäss der aktuellen Schweizer Richtlinie, die erst seit 1998 besteht, berechnet. Das Ermöglichen rationaler Entscheidungen beim Neubau und genauerer Ergebnisse bei der Überprüfung bestehender Galerien ist unbestritten von höchster Wichtigkeit. Die Richtline berücksichtigt die Belastung als eine statische Ersatzkraft, die durch konservative Extrapolation der experimentellen Ergebnisse mit Hilfe von elastischen numerischen Analysen bestimmt wird. Das dynamische Verhalten des Tragwerks wird dabei nicht genügend berücksichtigt.

Diese Dissertation trägt zur Verbesserung der Vorhersagegenauigkeit der Tragfähigkeit von Steinschlagschutzgalerien bei und schlägt die Etablierung eines verhaltensbasierten Bemessungsverfahrens für den Bau dieser Tragwerke vor. Desweiteren wird zu einem besseren Verständnis des dynamischen Tragverhaltens der Eindeckung und der Platten beigetragen. In dieser Arbeit wird eine numerische Analysemethode, welche explizite Finite Elemente Methoden nutzt, verwendet, um die dynamische Tragfähigkeit von Steinschlagschutzgalerien zu untersuchen. Die Einsetzbarkeit dieser Methode zur Einschätzung des Verhaltens von mit Lockergestein bedeckten Betonplatten wird durch den Vergleich mit experimentellen Bemessungen verifiziert.

Die grössten Herausforderungen, die in dieser Hinsicht gemeistert werden mussten, sind die Modellierung der Eindeckung, der Bruch der Platte sowie die Berücksichtigung der Spannungsgeschichte bei wiederholten Einschlägen. Dabei wird ein Materialmodell so angepasst, dass Scheren des Lockergesteins sowie seine Verfestigungseigenschaften einfliessen. Ein Kriterium zur Untersuchung des Versagens der Platte mit elastisch-plastischer Finite Elemente Analyse wird vorgeschlagen, welches auf einem Quotienten von maximaler zu residualer Verschiebung der Platte basiert. Zusätzlich wird ein numerischer Ansatz für die Modellierung bewehrter Stahlbetonplatten, die wiederholten Einschlägen ausgesetzt sind, vorgeschlagen.

Unter Anwendung des Ausfallkriteriums und der vorgeschlagenen numerischen Analyse werden Finite Elemente Analysen zur Erweiterung der von Schellenberg (2008)

durchgeführten Fallversuche, mit simulierten Energien bis zu 0.3 MJ, benutzt. Dabei wird der Einfluss der Form des Felsblocks, der Bügel und wiederholter Einschläge auf das Verhalten der Betonplatte untersucht. Der Einsatz der Finiten Elemente Methode dient der Untersuchung der Einflüsse verschiedener Eingabeparameter, wobei das von Schellenberg (2008) vorgeschlagene analytische Modell, welches auf einem nichtlinearen Dreimassenschwinger basiert, verbessert wird. Zusätzlich wird ein simplifiziertes Modell mit einem nichtlinearen Zweimassenschwinger vorgeschlagen. Eine Fallstudie, welche den Vergleich verschiedener numerischer Methoden ermöglicht, wurde durchgeführt. Um das Verhalten der Galerie bei hohen Aufprallenergien bis zu 2.7 MJ zu simulieren, wurden Finite-Element-Methoden eingesetzt. Die Bauwerksantwort der Galerie bei Energien grösser als 2.7 MJ wurde mittels analytischer Modelle untersucht.

Abschliessend wird ein verhaltensbasiertes Bemessungsverfahren genannt „Elastic Recovery-Based Design" (ERBD) als Kriterium zur Definierung der Leistung von Galerien in numerischen Modellen vorgeschlagen.

Table of contents

x

1 Introduction

Mountainous areas have a complicated topography, and exhibit geological and environmental conditions, which combined with climate changes, cause a variety of natural hazards. Rockfall is one of the hazards, the risk associated with which, tends to increase in Alpine areas of Switzerland. In addition to the large uncertainties involved in the prediction of their occurrence, rockfalls involve high energies and not enough time for taking an action once they occur, and they may lead to severe consequences. Therefore, it is important to consider rockfall hazards, even though the ones that are very significant do not occur frequently.

Rockfall protection research requires an interaction among different disciplines including natural sciences, engineering, and risk assessment. These disciplines contribute to the following:

- identification of the problem, i.e. identification of potential detachment zones and unstable slopes;
- estimation of occurrence frequencies of rockfalls of different magnitude;
- determination of potential of special propagation of falling rocks;
- risk assessment and definition of protection levels;
- risk mitigation and management.

Once these risks are identified and assessed for a given location, they can be managed by different means. For instance, if there are no existing infrastructure and transportation networks, such locations can probably be avoided by land use planning. If infrastructure and transportation networks exist and the risk due to rockfall is exceeding certain acceptance criteria, protection measures need to be taken.

The most appropriate protection measure can be chosen for the rockfall initiation zone as well as the transit path and the deposit zone based on the geology and topography of the location, and the frequency and intensity of rockfall. At the initiation zone, the measures can be taken by stabilizing the slope and removal of unstable volumes of rock. Along the transit path, planting can be used as a protection measure as well to form hybrid barriers. Figure 1-1 shows some of the common protection measures at disposal for the deposit zone to manage the risk associated with rockfall with respect to their absorption of kinetic energy.

Smaller rockfalls are more frequent than the large rockfall events or landslides. Usually magnitude-cumulative frequency relationships are used for bed-rock derived movements, which can be obtained from the observed data for a specific location. The shape of such curves on a log-log plot (see Hungr et al. 1999) is developed in a way that the cumulative frequency becomes lower with increase in the landslide volume. Rockfall protection galleries are one of the few adequate types of structures that provide protection against rare events of relatively high level of impact energies and at the same time, they require low maintenance after more frequent events of low energy.

The kinetic energy is commonly used to indicate the impact load carrying capacity, or in other terms, the absorption capacity of these structures. The energies for which protection galleries are considered to be adequate vary from 0.2 to 3.0 MJ, according to Swiss Federal Road Office classifications (ASTRA 2003). Flexible barriers are also capable of absorbing high energies up to 5 MJ, and they are well suited for less frequent events. There has been a significant improvement of capacity of newly designed structures, such as flexible barriers and galleries in recent years by augmenting their capacity for energy absorption. An extension of the capacity in terms of kinetic energy dissipated based on the latest developments is shown in dotted lines in Figure 1-1 (proposed by Vogel et al. 2009).
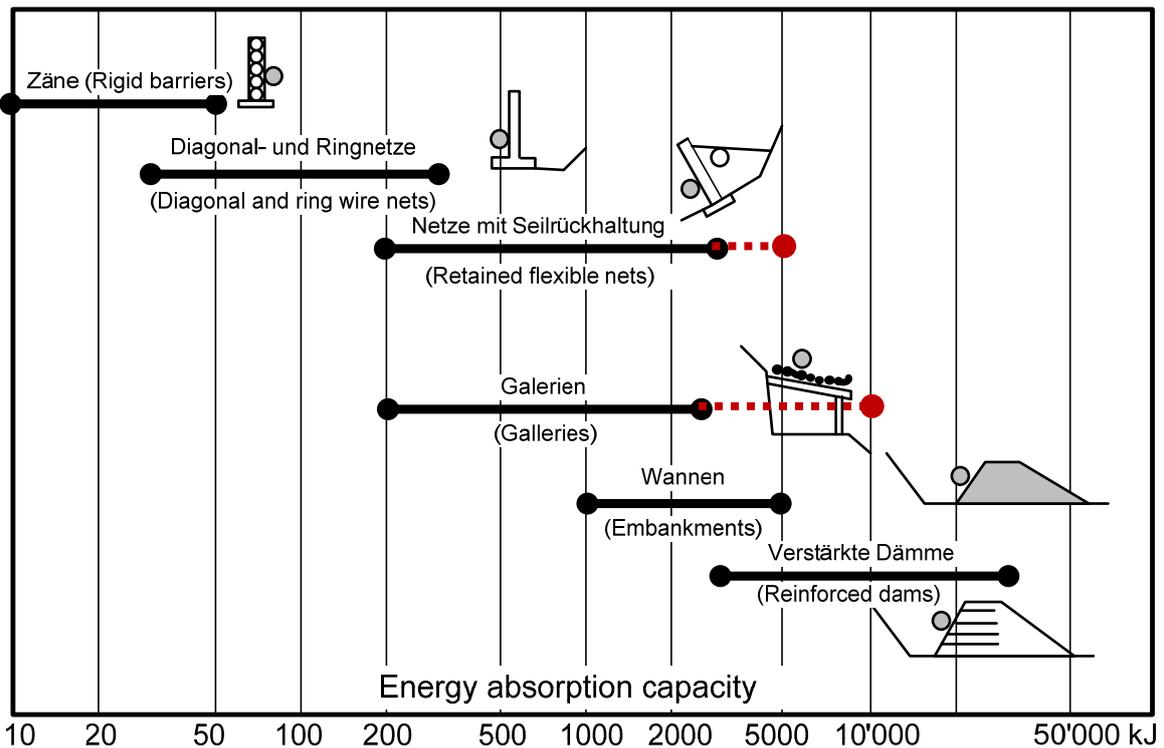
Figure 1-1: Rockfall protection measures (ASTRA 2003) and latest development in dotted lines (Vogel et al. 2009)

1.1 Background and motivation

A survey of about 350 existing rockfall protection galleries in Switzerland has shown that most of them are covered by a soil cushion layer (Schellenberg 2008). The most common type of the galleries has a cast in situ reinforced concrete flat roof slab without prestressing with a typical span of 9 m and a slab thickness of approximately 0.70 m. Figure 1-2 shows a typical rockfall protection gallery. The back side of such galleries is continuously supported on a retaining wall, and the valley side is supported on columns, with a typical spacing of 7 m.

Many rockfall events have occurred in Switzerland with kinetic impact energies ranging from 1 up to 450 MJ over the last two decades (Chikatamarla 2006), and some of the events lead to the failure of the galleries. The rockfall protection galleries are supposed to withstand rockfalls with energies up to 3 MJ, which is the limit in Switzerland according to Swiss Federal Road Office (ASTRA 2003) classifications. However, many galleries are designed based on oversimplifications by engineers and may not be able to sustain the mentioned

energy limit. Some of the rockfall incidents, as outlined by Chikatamarla (2006) and Schellenberg (2008), have led to fatalities. These incidents have shown that rockfall protection needs to be improved in order to reduce fatalities and damage to infrastructure. The prediction of impact load carrying capacity of existing structures should be improved to enhance the protection against rockfalls. Rockfall events may also happen in areas that were not classified as rockfall hazard zones so far, so it is necessary to improve the basis for the design of new structures in order to sustain rockfall impacts without severe damage.
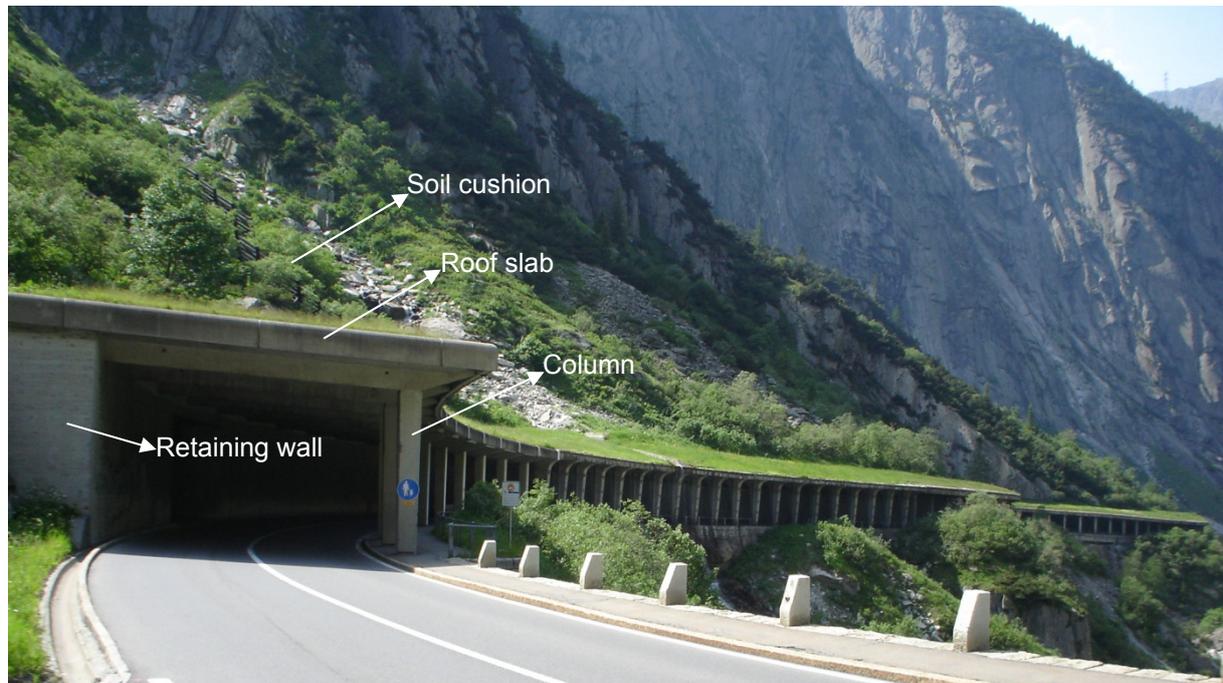
Figure 1-2: A typical rockfall protection gallery in Switzerland (Tanzenbein Gallery, Gotthard pass)

The impact capacity of rockfall protection galleries has already been a topic of interest among civil engineers in Switzerland. The Swiss design guideline for rockfall galleries (Section 2.3) is based on falling-weight impact experiments carried out at the laboratory of the Swiss Federal Institute of Technology, Lausanne (EPFL) (Section 2.1.4), which examined the impact on a concrete slab covered by a cushion layer with variation of impact velocity, boulder size, etc. (Montani 1998). The maximum impact energy achieved was 0.1 MJ due to size restrictions and it can only present the real situation partially. Higher energies were conservatively extrapolated by means of elastic numerical simulations (Bucher 1997) and an empirical equation was proposed for the evaluation of an equivalent static force for design. The design assumptions are outlined in Section 2.3 and the application of the guideline is limited to a penetration depth of a maximum of half of the cushion thickness.

Further studies related to the cushion layer were done at ETH Zurich. Experimental, numerical, and analytical studies (Section 2.1.4) were carried out to investigate damping properties of cushion layers (Chikatamarla 2006). Laboratory physical modeling of the impact in the centrifuge was carried out to determine physical, dynamic and geotechnical parameters of different cushion material and full-scale events, during which impact energies of up to 20 MJ were replicated. The study contributes largely to the understanding of behavior and stress distribution of different types of cushion materials. However, the structural model was

very simple and the influence of the stress distribution on the behavior of the gallery roof needs further investigations.

In order to improve the predictive accuracy of the impact load capacity of rockfall protection galleries and to calibrate an analytical model (Section 2.4), large-scale falling-weight tests on reinforced concrete slabs covered by a cushion layer (Section 2.1.2) were carried out at a scale of 1:2 in April 2007 (Schellenberg 2008). Impact energies of up to 0.3 MJ were achieved during these experiments, which can be used to calibrate numerical models within limits. These are used here to extend the analysis for higher energies (up to 2.7 MJ) and to simulate a full scale gallery, as well as to validate the assumptions made for different parameters of the analytical model.

1.2 Objective and scope of work

The current work focuses on the dynamic capacity of rockfall protection galleries covered by a soil cushion (Figure 1-2). The kinetic energies and velocities of impacts (design levels) are assumed to be known. The focus of the study is on the capacity of the reinforced concrete slab. Therefore, only the vertical component of the impact forces, which is critical for slabs, is considered here. It is assumed that the horizontal components can be treated separately. The impact location is defined to be at mid-span and a plane loading surface is considered.

This work is a direct continuation of the research carried out in the Institute of Structural Engineering at ETH Zurich (Schellenberg 2008), where experimental studies were carried out in order to develop and calibrate an analytical model. The current work aims at improving the design method proposed, and investigating the dynamic behavior of reinforced concrete slabs using numerical studies. Numerical analyses are carried out using the finite element method with the following objectives:

- to investigate the potential of finite element analysis techniques to predict the behavior of slabs covered by soil, by comparing the results to the experiments;
- to establish a failure criterion to account for failure using elastic-plastic dynamic finite element analysis;
- to establish a numerical analysis procedure to model consecutive impacts on reinforced concrete structures;
- to use finite element analyses for a parametric study of impact on reinforced concrete slabs and galleries for different material models, support conditions, mesh sizes, spacing of shear reinforcement, and for consecutive impact loading;
- to apply the finite element method as a tool to investigate the influence of the input parameters and to improve the assumptions made for the existing analytical model;
- to establish a new simple analytical approach that can be applied for design of new galleries and evaluation of existing ones;
- to further provide recommendations for a performance-based design of rockfall protection galleries and recommendation to study the influence of the different assumptions on the design of galleries.

1.3 Methodology

The structure of this dissertation follows the methodology used in establishing the entire research project. The state of the art of the research on dynamic analysis of reinforced concrete members and the relevant topics for the design of protection galleries are discussed in Chapter 2.

This work demonstrates the use of finite element methods to model rockfall impact on reinforced concrete protection galleries, and interprets the numerical results. The general aspects of the simulation, the method and the software used, as well as the material models adapted for the finite element simulations, are described (Chapter 3).

The results obtained from finite element analyses are compared with available experimental data in Chapter 4. The applicability of finite element methods for simulating impact on concrete members is reviewed in Section 2.2.1. This work further investigates the efficiency of the method in modeling reinforced concrete slabs covered by a layer of soil, which is achieved by simulating the experiments. A numerical analysis procedure for modeling consecutive impacts on reinforced concrete slabs is proposed and its applicability is investigated. Moreover, the potential of the finite element methods to model the global and punching behavior of the slab is investigated. A criterion can be established based on this comparison to account for failure of reinforced concrete members using elastic-plastic finite element analysis.

Once the applicability of the finite element method is investigated and a failure criterion is established, the analyses can be extended beyond the range of the experiments conducted (Chapter 5). Various finite element models developed to study the behavior of slabs are described in this chapter. Sensitivity analyses are carried out in order to decide on various input parameters for finite element models, such as material models and mesh sizes. Results of these extensions are employed for calibration of parameters of the system of multiple degrees of freedom proposed by Schellenberg (2008) in Chapter 6. In addition, an analytical model using a system with two degrees of freedom is proposed. This chapter provides a summary of the results obtained using the improved and the proposed analytical models and gives an overview on the most important findings.

A case study combining the analyses of the finite element method and the analytical method is explained in Chapter 7. Finally, the last chapter outlines the conclusions and suggestions for future research, as well as recommendations for a performance-based design procedure.

2 State of the art

This chapter provides an insight into the past findings and research into the dynamic capacity of reinforced concrete members, as well as rockfall protection galleries. Moreover, it highlights the research gaps and shortcomings, as well as the need for further work. The following aspects are presented here:

- experimental impact studies carried out on reinforced concrete beams, slabs and galleries, as well as selected impact experiments on soil layers (2.1);
- numerical analyses of the performance of structures under impact (2.2);
- a short reference to existing design guidelines and recommendations (2.3);
- analytical models for analyzing the dynamic response of rockfall protection galleries (2.4).

A more general state of the art review of rockfall protection measures can be found in the literature (e.g. Montani 1998, Chikatamarla 2006, Schellenberg 2008, Vogel et al. 2009).

2.1 Experimental studies

This section outlines various impact tests conducted on reinforced concrete beams, slabs, and galleries. In addition, impact experiments on soil and gravel layers or cushions, as well as on reinforced concrete slabs and galleries covered by soil, are described. Figure 2-1 shows the range impact energies for impact tests outlined in the following sub-sections.
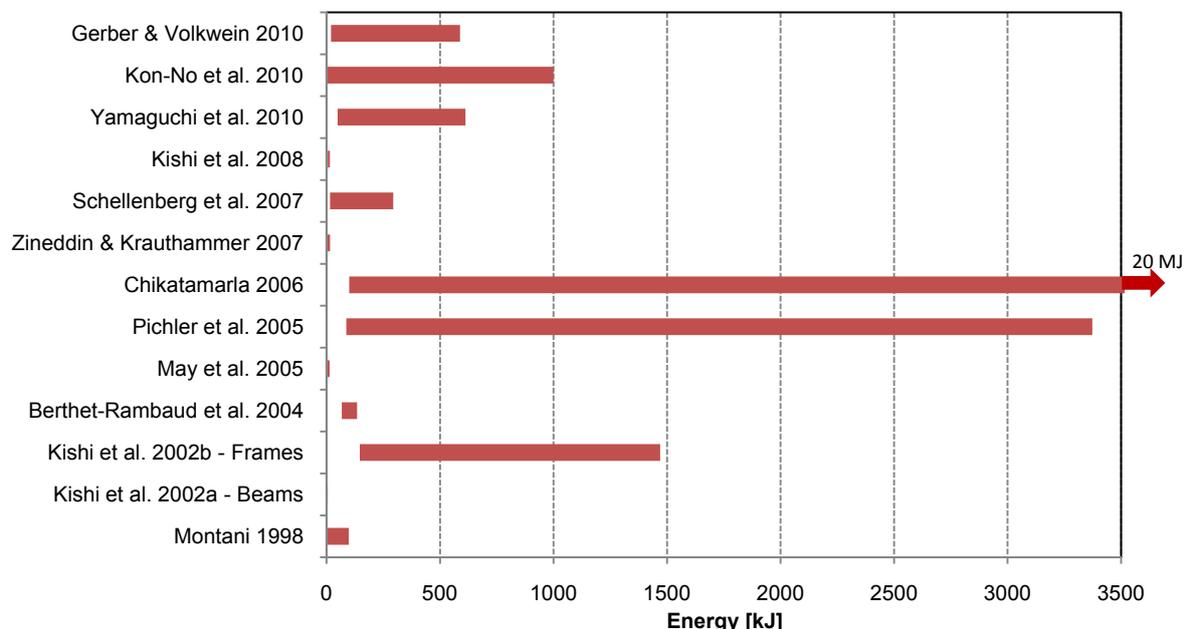

Figure 2-1: Overview of impact experiments

2.1.1 Impact tests on reinforced concrete members

Various impact tests have been carried out on reinforced concrete beams. A series of impact tests was performed on reinforced concrete beams to investigate their response (Yamamoto et al. 2001) and suggestions were made on suitable measurement methods for impact tests.

Furthermore, crack patterns, response of the beam, and absorbed energies were discussed. Additionally, reinforced concrete beams were subjected to falling-weight impact tests by Kishi et al. (2002a). Twenty-seven simply supported reinforced concrete beams, of 150 mm width and 250 mm depth without shear reinforcement, were subjected to the impact of a 300 kg spherical steel weight (Figure 2-2 a). Impact velocities between 1 to 6 m/s were used. The impact forces, reaction forces, mid-span displacements and crack patterns were observed during the experiment. The ratio of absorbed energy and input kinetic energy was studied for these experiments, and a mean value of 0.6 was observed.

These tests provide a good understanding of the behavior of reinforced concrete beams subjected to impact loading. However, it is of great importance to study the performance of slabs subjected to impact loading, when designing for the impact behavior of reinforced concrete slab-type rockfall protection galleries. The experiments on reinforced concrete slabs can further highlight the three dimensional behavior of these structures.

Additional experiments are reported on reinforced concrete beams and slabs subjected to an impact of a cylindrical drop mass, in order to study the impact behavior of reinforced concrete members (May et al. 2005). Beams with a maximum span of 3 m and slabs of 2.3 m^2 were subjected to the impact of weights up to 200 kg being dropped from heights up to 4 m (Figure 2-2 b). The load-time-histories, impactor accelerations, strain in reinforcement and concrete, crack formations and propagations were obtained. The global behavior, the order of crack formation, and the local behavior in the vicinity of the impact were studied for the reinforced concrete beams. For the slab tests, the modes of failure including scabbing were investigated as well. The beam tests confirmed that the beam span has a higher influence on the impact forces than the supports.

a)   b)

Figure 2-2: View of impact test on reinforced concrete beams in a) Japan (Kishi et al. 2002a), and b) United Kingdom (May et al. 2005)

Experimental investigation on reinforced concrete slabs subjected to impact loading was reported by Uchida et al. (1985). About 30 square shaped slabs, supported on four points, with a 1.5 m span length, including specimens for static loading, were tested. An impact loading method was developed, which enabled the control of peak values and duration of contact force. A rubber pad was installed on the specimen at the contact point of the falling-weight to limit the peak value of the impact force for the given impact velocity, and the impact duration by the thickness of the rubber pad. The impact duration was mainly affected by the thickness of the rubber pad and was kept constant regardless of the input impact velocity. The maximum impact force varied almost linearly with increase in the impact velocity for the same thickness of the rubber. Maximum impact force of up to 84 tonnes and maximum impact duration up to 8.5 ms were achieved during experiments. The energies absorbed under static and impact loadings were compared. It was observed that the energies absorbed in the slabs subjected to impact increase in proportion to the loading rate, up to almost twice the static values.

Seven 1:7.5 scale models of different types of reinforced concrete slabs used in industrial facilities were loaded vertically with a 15 cm^2 steel loading plate (Saito et al. 1995). Static, low speed and high speed loadings with vertical loading rates of $3 \cdot 10^{-5}$, $3 \cdot 10^{-2}$, and 3 ms^{-1}, respectively, were used for this experiment. The relationships between the load and the displacement at the loading point, as well as the slab failure modes, were studied. When the slab was subjected to static loading, punching shear failure occurred. During the experiment with high speed loading, bending compression failure occurred and the specimen cracked at the center. It was observed that the strength of the slab increased with the increase in the loading rate.

Three different sets of impact tests, using the same test setup, were performed on reinforced concrete slabs (Zineddin & Krauthammer, 2007). The slabs were 90 x 1524 x 3353 mm in size. The impact tests were performed with a cylindrical drop hammer device of approximately 2608 kg dropped from heights of up to 610 mm at the center of the slab. Changes in mechanism from a fracture mode from a ductile mode (bending failure) at lower drop heights (152 mm), to a brittle mode (shear failure) under higher drops (610 mm) was observed using a high-speed video camera. The tendency for local shear failure or brittle failure increases with increase of the loading rate, thus when a local failure is not desirable (since it leads to a sudden failure) the, favorable increase in the strength due to the loading rate can be offset. For rockfall protection galleries, however, local punching should be the governing mode of failure since a bending failure and the collapse of the whole gallery is not favorable. The impact load histories, deflections, reinforcement strains, and accelerations measured during experiments were presented as well in this study.

The above mentioned experiments describe the behavior of reinforced concrete slabs subjected to impact loadings. In most cases a local damage can be expected due to the direct impact of the loading device, which can be minimized for rockfall protection galleries by the use of appropriate damping materials such as soil. This also can enhance the energy absorption of the slabs. Therefore, it is important to perform experimental studies on slabs covered by a soil cushion. The experiments mentioned herein were carried out at small scale.

It is important to carry out large-scale testing to fully explore the dynamic response of structures.

It is also possible to reduce the damage to rockfall protection galleries, which are not covered by a soil cushion. A new concept was proposed for rockfall protection (Berthet-Rambaud et al. 2004, Mougin et al. 2005) by providing reinforced concrete slabs with special supports to absorb rockfall energy. An experimental approach using this system to analyze the response of this type of slab to impact loading was presented, in which the damage due to an impact of a rock would mainly be concentrated at dissipating supports, which can be replaced when it is required. However, the slab will still sustain some local damage, which may need to be assessed and repaired. The system has already been used for several galleries in France. There may still be a more economic solution combining this system with a thin layer of soil on top of the slab to reduce local damage and spalling.

2.1.2 Impact tests on slabs covered by a soil cushion

As many existing galleries are covered by soil, establishing experimental studies for slabs covered by a soil layer is desirable, especially for large-scale and full-scale tests at equivalent energy levels given for galleries (Figure 1-1). This facilitates the prediction of the protection level of existing structures.

Large-scale falling-weight impact tests were carried out at a scale of 1:2 compared to an average Swiss rockfall protection gallery. During these experiments, six reinforced concrete slabs, with lateral dimensions of 3.5 x 4.5 m and a thickness of 0.25 or 0.35 m, covered by a gravel cushion were subjected to falling-weight impacts with increasing impact energy until the slabs failed. The slabs had one line and two single supports. Two steel beams welded to an elbow were cast-in over the single supports to avoid a shear failure. Concrete boulders of 800 kg and 4000 kg were dropped from heights of up to 15 m and 7.5 m, respectively (Schellenberg et al. 2007, Schellenberg 2008). The test setup is shown in Figure 2-3. The slab thickness was varied to explore its influence on the behavior. Shear reinforcement was placed in two of the slabs. Acceleration of the boulders, reaction forces at the load cells, crack patterns at the soffit of the slabs, as well as acceleration and strains within the slabs were measured during the experiment. A combined bending shear failure mode that developed close to simply supported corners was observed.

Figure 2-3: Experimental setup for large-scale impact tests carried out in Switzerland (Schellenberg et al. 2007)

A series of falling-weight impact tests with predefined impact velocities was carried out to study the punching failure due to impact load (Kishi et al. 2008). Four reinforced concrete slabs having 2 m side length and a thickness of 0.18 m were subjected to impact by a 300 kg mass (Figure 2-4 a). Reinforcing bars of 16 mm diameter were placed at 150 mm spacing in both directions. Two impacting cylinders of diameters 60 and 150 mm were used. A 100 mm thick sand cushion was placed on top of two of the slabs. Two slabs impacted by the 60 mm diameter cylinder, were subjected to an impact velocity of 6 m/s. The other two slabs were impacted by the 150 mm diameter cylinder. Impact velocities of up to 10 m/s were applied. The impact forces and the reaction forces were measured using load cells placed within the falling-weight and below the line supports, respectively. The strains in the reinforcement, and the deflections at the slab center were measured as well. Punching failure was reached in all slabs.

a)
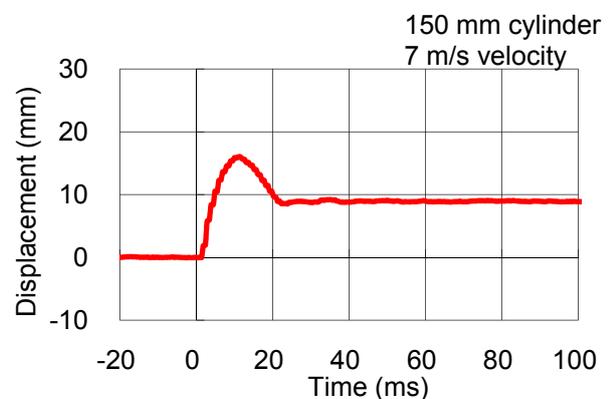
b)
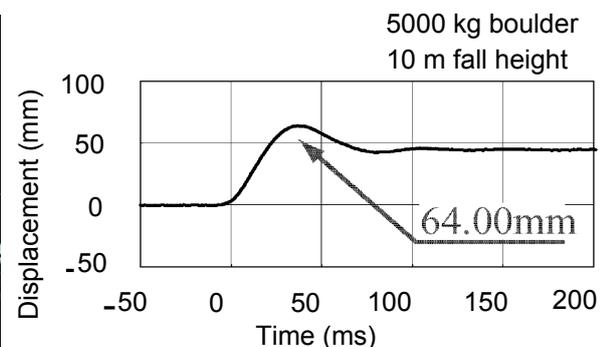
Figure 2-4: Experimental setup of a) 2 m x 2 m slab under falling-weight impact (Kishi et al. 2008), and b) large-scale falling-weight tests on a slab with a 4 m span (Yamaguchi et al. 2010)

Large-scale falling-weight impact tests on reinforced concrete slabs covered with sand and gravel cushions have been performed recently at a scale of 2:5 to typical rockfall protection galleries in Japan (Yamaguchi et al. 2010). Reinforced concrete slabs having a lateral clear span of 4 m and a thickness of 0.4 m, were subjected to impact of a 5000 kg boulder dropped from heights up to 12.5 m, as shown in Figure 2-4 b. The slabs were placed on steel supports equipped by load cells for measuring support reactions. The impact forces, reaction forces, and displacements at the slab centers were compared for different drop heights, for the slabs covered with two different cushion materials. A relationship was established between the slab response and input energy. Therefore, values of maximum impact forces, maximum slab

deflection, and residual displacements were compared to the input impact energies. It was found from these results that the impact forces for slabs covered by sand can be evaluated approximately using Hertz's contact theory with a Lamé constant $\lambda = 1000 \text{ kN/m}^2$. It was observed from experimental results that the penetration of the boulder into the cushion layer increased linearly with increase in the impact energy within the range investigated.

The large-scale falling-weight impact tests outlined in this section covered impact energies of up to 613 kJ. Impact energies of up to 5 MJ, however, are relevant for the real structures, and the behavior of galleries under higher impact energies needs to be investigated. These experiments provide a benchmark for numerical analyses of rockfall protection galleries, which can be used for extrapolation of the physical tests. Therefore, some of these experimental data are used to calibrate the finite element analyses in the current study, which will be explained in following chapters. The finite element analysis can further be used to simulate the slabs subjected to higher impact energies as well as the real-scale galleries, which is difficult and expensive to simulate physically.

2.1.3 Impact tests on rockfall protection galleries

The support conditions of large-scale tests are designed to resemble the boundaries of galleries as closely as possible. However, the load distribution may differ from that of the real case. Therefore, some experiments have been carried out on large-scale models of galleries, in order to study the impact behavior of rockfall protection galleries (Kon-No et al. 2010). Two gallery models were tested with, and without, a sand cushion. They represented an average Japanese gallery at a scale of 2:5 (Figure 2-5). A cylindrical impacting mass of 2 tonnes with a spherical bottom, was dropped from heights of up to 1.25 m on the gallery that was not covered by a sand cushion. The impacting mass was increased to 10 tonnes, dropped from heights of up to 10 m for the gallery covered by a 500 mm thick layer of sand.

The reaction forces, displacements, and cracks were obtained from experiments. The experiments explored the impacts at various locations on the slab (some closer to supports) and the forces as well as the cracking at the supporting columns were studied. The roof of the gallery without cushion collapsed in a punching shear failure mode. It was found that the impact forces for the gallery covered by a sand cushion can be estimated using a design formula derived on the basis of Hertz's contact theory with a Lamé constant $\lambda = 1000 \text{ kN/m}^2$. The roof of the gallery with the sand cushion reached its ultimate limit state subjected to an impact energy of 1000 kJ with punching shear failure.

$$P = 2.108\,(m\,g)^{2/3}\lambda^{2/5}H^{3/5}a$$

a is the ratio between thickness of sand and diameter of the boulder
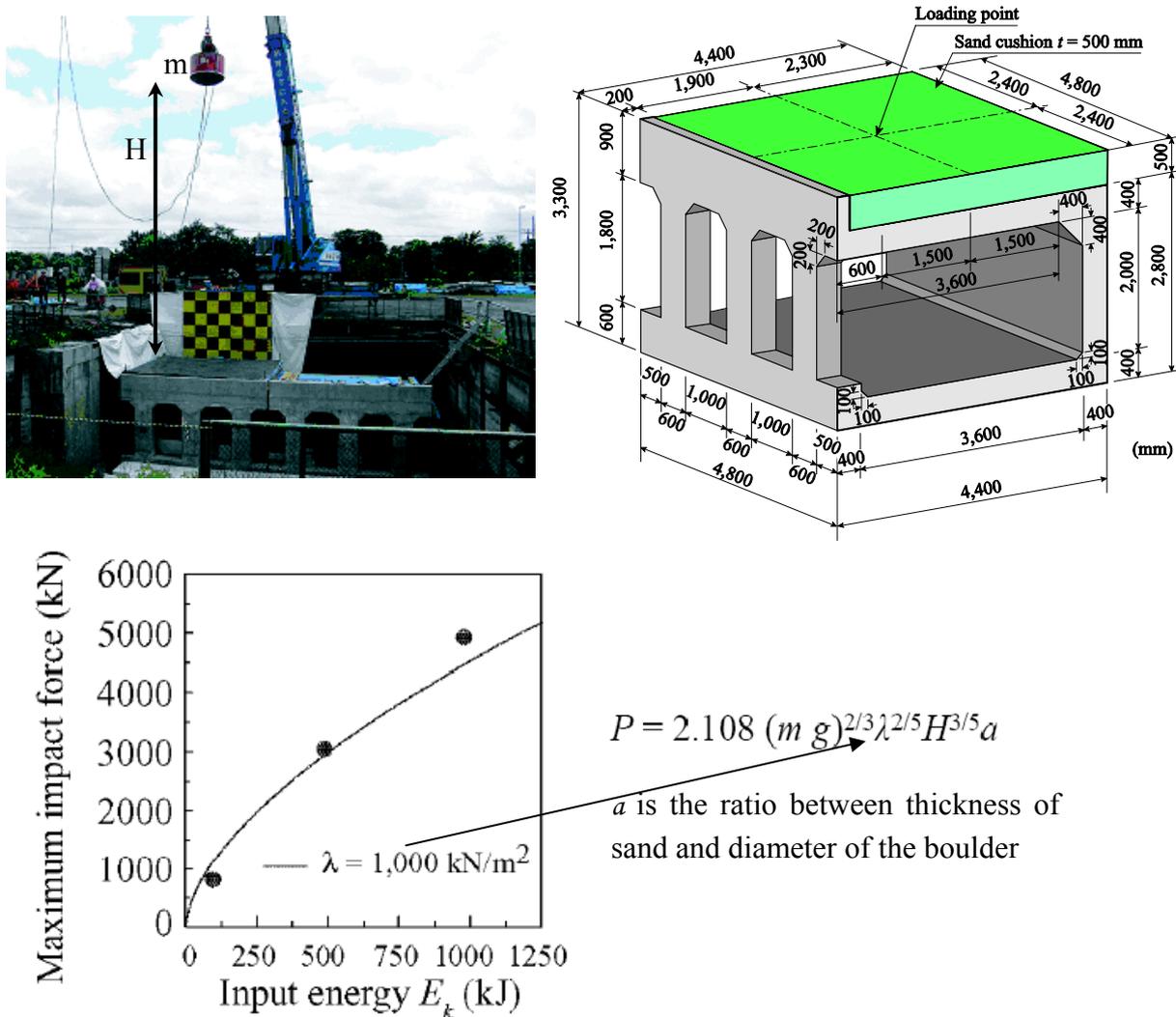
Figure 2-5: Experimental setup for falling-weight impact tests on 2:5 scale galleries (Kon-No et al. 2010)

It would be desirable to carry out full-scale tests on real rockfall protection galleries. There have been limited possibilities for performing such experiments. Full-scale impact tests on a reinforced concrete gallery were reported by Kishi et al. (1994). The experiments were conducted so that the concrete roof of the gallery remained in its elastic range and the gallery was not cracked.

Prototype impact tests were conducted on two types of prestressed concrete frames, namely an inverted L frame and a rigid frame having similar dimensions (Kishi et al. 2002b). Cylindrical steel boulders having a spherical bottom and weights of 3000 and 5000 kg were dropped from heights of up to 30 m onto the center of a 90 cm thick sand cushion (Figure 2-6). The ultimate impact resistance capacities of both frames were compared. It was seen that the fully rigid frame has more than 1.7 times impact resistance capacity than the inverted L frame subjected to the same impact energy. The fully rigid frame and inverted L frame, designed based on a allowable stress design procedure, had more than five and three times the margin against collapse referring to the design input energy, respectively, since they were initially designed to withstand the impact of a 1000 kg boulder falling from 30 m height (0.3

MJ). The collapse energy was 1.5 MJ and 0.9 MJ for fully rigid frame and inverted L frame, respectively.

Similar full-scale experiments on slab type rockfall protection galleries subjected to high impact energies, can make a significant contribution to understanding the response of these structures.
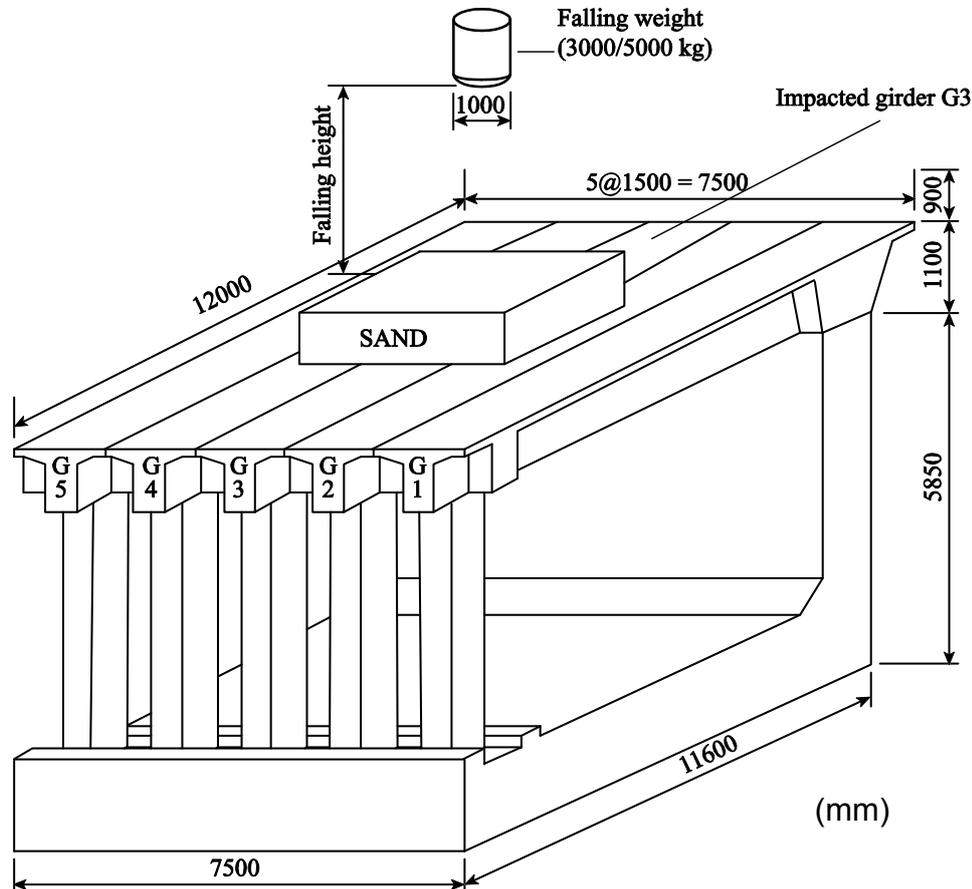
Figure 2-6: Full-scale experimental setup for prestressed concrete rock-sheds (Kishi et al. 2002b)

2.1.4 Impact tests on cushion layers

As the dynamic load distribution onto the galleries depends on the energy dissipation in the cushion layer covering the gallery, a review of the relevant experiments on such soil layers is given here. The impact energy is dissipated by shearing and compaction of the soil, as well as crushing of soil grains, if the soil is subjected to impact of a falling boulder. Discussion on soil behavior under impact and the modeling aspects are provided in Section 3.3.3 and Section 6.1.1.

An experimental study was carried out by dropping blocks from various heights on a reinforced concrete slab covered with three different cushion materials in order to study the damping achieved through soil cushions (Labiouse et al. 1996, Montani 1998). These laboratory tests (Figure 2-7 a) were restricted to a maximum drop height of 10 meters and an input impact energy of 100 kJ. Falling blocks of 100, 500, and 1000 kg were dropped on a 3.4 x 3.4 x 0.2 m slab covered by 0.35, 0.5, and 1 m thick cushion layers. The slab was restrained from lifting during these impact tests. The acceleration of the boulder was measured by the accelerometer installed on the falling boulder, and the velocities and the end

state penetration of the boulder were determined based on the measured accelerations. The penetrations were checked against the measurements of the final distance the boulder traveled compared to the surface of the cushion. The soil pressures were measured on the top surface of the slab using five soil pressure gages fixed unto the slab, and the resultant forces acting on the slab were evaluated by integrating the soil pressure. In addition, the reaction forces were measured in the slab by summing up the recorded values at four load cells and the deflections were obtained by means of four displacement transducers. A formula was proposed to calculate the maximum impulsive force based on the experimental observations. The experiments were numerically extended (Bucher 1997), which is explained in Section 2.3, and the formula for calculation of equivalent static impact forces acting on galleries was suggested and modified based on the extrapolations. The formula based on the extrapolations mentioned was later adapted as the Swiss guideline (see Section 2.3, Equation 2-1), and is only applicable for impact velocities, which do not lead to low penetration depth (less than half of the thickness of the cushion layer). It is obtained based on a rather conservative extrapolation of the slab behavior by means of numerical simulations based on elastic material models and simplified boundary conditions.

A study on the energy absorption of cushion materials has been carried out in a geotechnical centrifuge using small-scale models at enhanced gravity (Chikatamarla 2006). Experimental, analytical, and numerical modeling of rockfall was carried out. The laboratory tests were performed to determine physical, dynamic, and geotechnical parameters of different cushion materials. Physical modeling of the impact in the centrifuge (Figure 2-7 b) was carried out to replicate full-scale events with impact energies of up to 20 MJ. The knowledge gained from these experiments is useful in understanding the response of various cushion materials (Figure 2-7 c) in order to improve the stress distribution and to reduce the impact forces on top of galleries. Carefully instrumented small-scale model tests can be conducted as part of a parametric study on the effect of key damping variables. Most important in any estimation of soil response is the effect of stress level. Numerical modeling was performed to calculate the stresses and forces induced in the gallery. Rigid base simulations were carried out in order to validate the centrifuge tests and the tests performed by Montani. The numerical study carried out was a preliminary investigation using a simplified material model for soil and can be developed further. An analytical model was proposed using lumped mass parameters and considers the elastic, plastic, and visco-elastic behavior, which can be applied for modeling impact on soil.
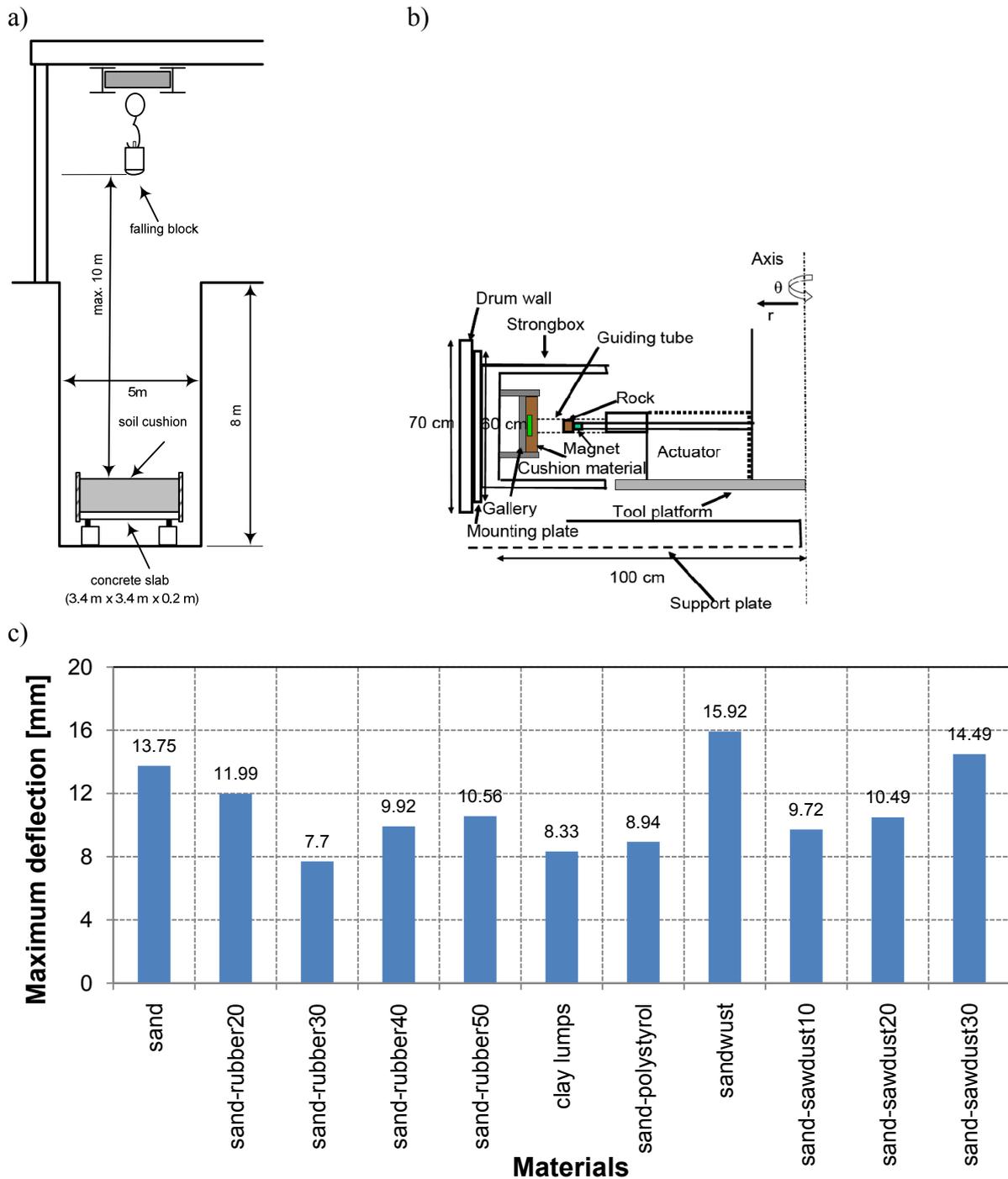
Figure 2-7: a) Falling-weight impact test on concrete slab covered by soil (Montani 1998) b) Centrifuge test (Chikatamarla 2006), and c) Maximum deflection of the slab for different cushion materials for 1.25 MJ impact (Chikatamarla 2006)

Experiments to study the impact of boulders onto gravel have also been carried out by Pichler et al. (2005), where cubic boulders of up to 18'260 kg were dropped from heights of up to 18.85 m such that they hit the ground with a face, an edge, or a tip. The impact characteristic of soil was studied incorporating and extrapolating the knowledge about projectiles impacting concrete (Li & Chen 2003). In order to calculate the penetration depth into a layer of soil, the dimensionless formulae for penetration depth of the concrete target impacted by a non-deformable projectile were calibrated using the impact experiments on soil. The formulae proposed by Li & Chen (2003) consider slip line fields for a flat nose projectile as shown in

Figure 2-8 a. An arbitrary shaped projectile head is assumed to penetrate into concrete (Figure 2-8 b). The slip lines can resemble the shear planes in soil, but soil crushing and compaction can't be considered by this assumption. On the other hand, the depth of the shear zone in soil is different from the depth of the plastic zone for concrete.
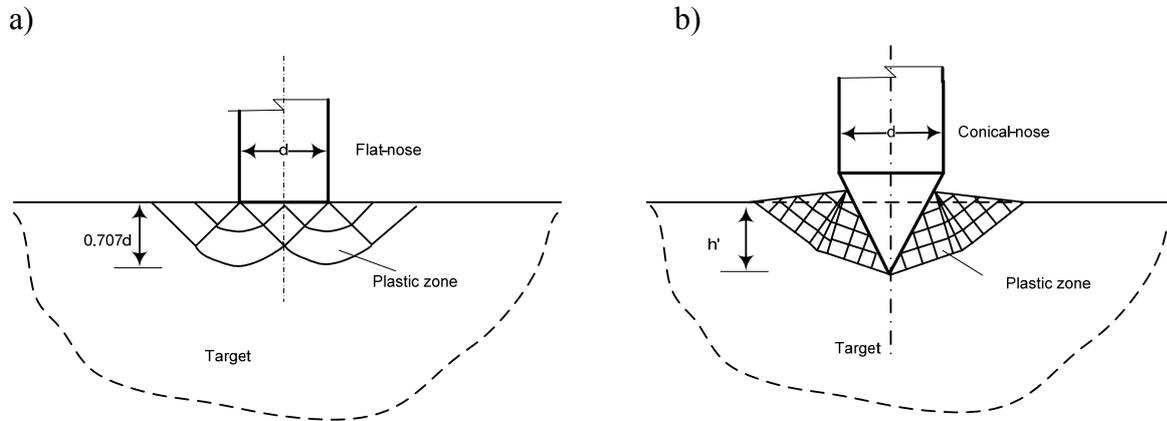
Figure 2-8: Slip line field for a) flat-nose, and b) conical projectiles impacting concrete (Li & Chen 2003)

The penetration depth of an impacting mass has been studied by falling-weight impact tests on granular material (Gerber & Volkwein 2010). Fifty-four impact tests were carried out, using two blunt boulders with masses of 800 and 4000 kg, dropped from heights up to 15 m on two different ground layers. These layers were prepared with thicknesses of 0.5 and 1.3 m above the bedrock (Figure 2-9). Three samples of ground layer material were sieved and prepared according to Swiss code SN 670 008a. The analysis indicated material of well graded gravel with silt and sand (GW-GM). The maximum penetration depth and acceleration were measured during the experiments. The dependency of the penetration depth and the maximum deceleration on the drop height was studied and a formula was proposed according to the work-energy principle for maximum deceleration, as a function of impact velocity and penetration depth.
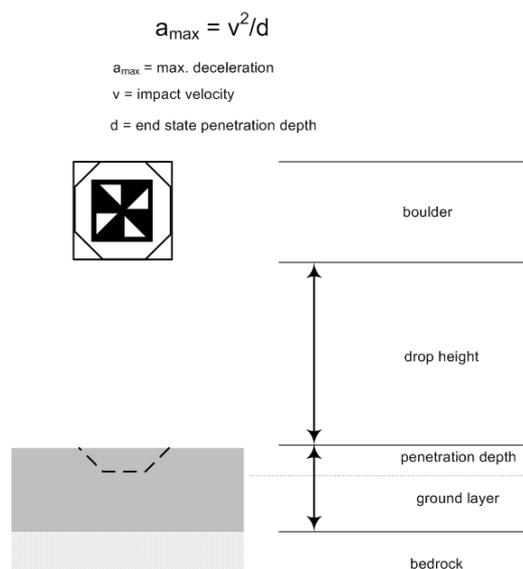
Figure 2-9: Falling-weight impact test on soil layer with hard underlying bedrock (Gerber et al. 2010)

2.2 Numerical studies

Numerical methods help in analyzing and visualizing the effects of static and dynamic loads on structures. They can provide an approximate but accurate solution of a system of differential equations. If the numerical model of the structure is adequately developed based on appropriate assumptions and sound validation (e.g. calibration with the experimental data), it can help minimizing the experimental costs. There has been a tremendous improvement in numerical analysis techniques in recent years, which corresponds to the development of computer systems. Various numerical analysis methods can be applied for the simulation of impact loading on structures. A number of these methods, especially finite element simulations of reinforced concrete members subjected to impact loading, are outlined here.

2.2.1 Finite element method

Pioneering work in the still evolving field of finite element analysis of reinforced concrete structures was initiated by Ngo and Scordelis (1967) and Nilson (1968). Nilson introduced an incremental load method for nonlinear analysis of reinforced concrete. Nonlinear material properties for concrete and steel and nonlinear bond-slip relationship were also introduced by Nilson (1972). There has been considerable progress ever since regarding finite element procedures for reinforced concrete members, which include consideration of cracking, damage, and strain rate for the concrete material models, layered two-dimensional and full three-dimensional analysis, etc. A detailed description of the early development of finite element analysis of reinforced concrete structures can be found in an ASCE report (1982). The application of the finite element method to study the impact on reinforced concrete members is outlined in this section.

2.2.1.1 Layered finite element analyses

The structural analysis of slab-type structural members is usually done by applying plate or shell elements. Shell elements need to be divided into layers in order to model the behavior realistically. This allows the application of different material properties for different layers. Each layer can represent concrete and reinforcement, respectively.

A nonlinear dynamic layered finite element analysis was used for reinforced concrete guardrails and slabs (King et al. 1990, and Miyamoto et al. 1991). Reinforced concrete slabs with doubly reinforced sections were analyzed using this method. The types of slabs simulated in this study were normal strength concrete slabs and high strength concrete slabs (King et al. 1990). Doubly reinforced concrete slabs were modeled, applying the external impulsive load at slab mid-span (Miyamoto et al. 1991). The layered finite element mesh is shown in Figure 2-10 a. Concrete was modeled using a four parameter triaxial failure model, and was treated as an orthotropic material after cracking. The slab was divided into eight layers, six of concrete and two of reinforcement. Four-node Mindlin type rectangular elements were used. Impulse load versus mid-span deflection curves for different ranges of loading rates, and the failure modes were produced (King et al. 1990). The shapes of curves (Figure 2-10 b) were used to classify the failure mode. The shear failure curves had a larger gradient, small deflection, and a high impulse load at failure. The curves for flexural failure had a smaller gradient, large deflection, and a higher impulse load.
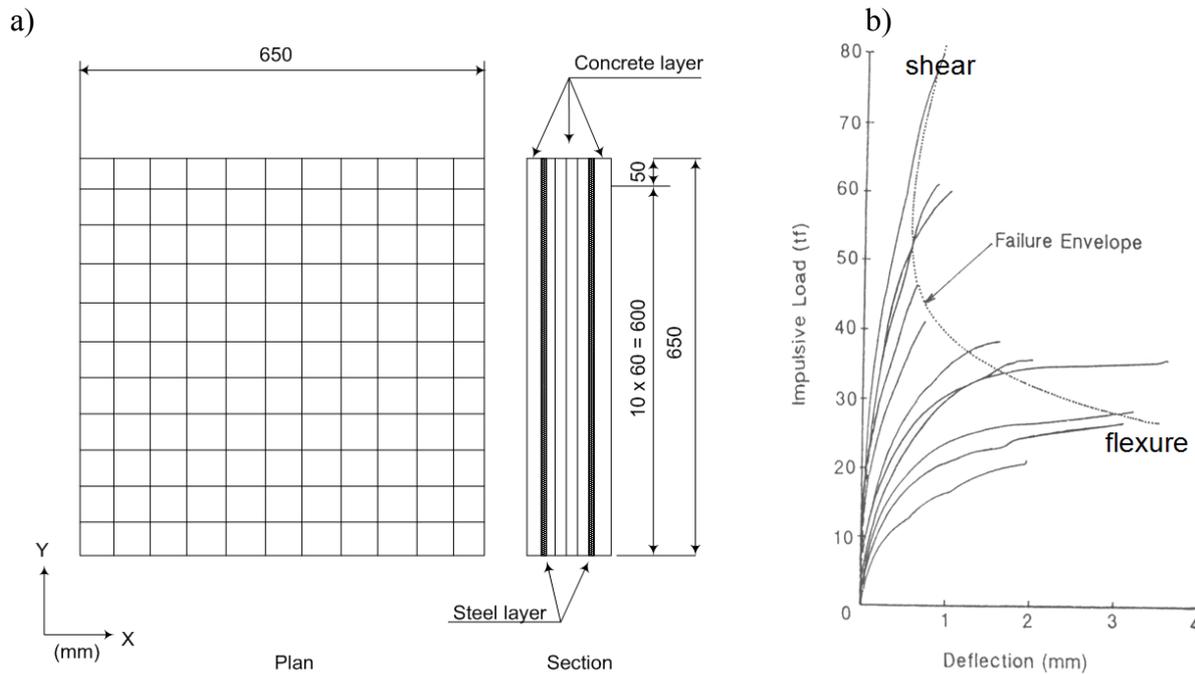
Figure 2-10: Layered finite element analysis a) mesh of a slab, and b) impulsive load-deflection curves up to failure for various loading rates (King et al. 1990)

Using shell elements is a suitable approach for global analysis of structures, but they ignore the contribution of local shear deformations. There are some formulations using layered shell elements, which account for transverse shear effects (Polak 1998). It is possible to model reinforced concrete slabs subjected to high concentrated loads with such a concept.

2.2.1.2 Three-dimensional finite element analyses

Three dimensional solid elements are appropriate for modeling details of structures because they consider punching at the impact location and are able to model transverse shear. A three-dimensional simulation of reinforced concrete members subjected to impact loading was performed using a triaxial failure criterion (Thabet & Haldane 2000). An elastic-plastic fracture model was used to simulate concrete nonlinearity, loading and unloading. A smeared crack model with tension-softening was used for concrete in tension. Reinforced concrete beams and portal frames were analyzed. A microconcrete beam with a span of 442 mm subjected to impact of a steel projectile was modeled. The width and depth of the beam were 44 mm and 65 mm, respectively. Solid elements were used to model the concrete. The impact forces and crack patterns were predicted. The simulations produced results that were in reasonable agreement with the experimental ones.

A reinforced concrete slab with dimensions of 12 x 4.4 x 0.25 m was analyzed using finite element methods (Berthet-Rambaud et al. 2003). Structural response was studied using three dimensional elements for the slab and its supporting elements; the reinforcement was represented using bar elements. A model based on damage mechanics represented concrete response. The vertical displacements of the slab were calculated and compared to the experimental measurements. Deformed shapes of the supports provided a similar shape to those obtained during the experiment.

Nonlinear analysis of large-scale and prototype reinforced concrete girders subjected to falling-weight impact loading has also been a recent topic of research (Kishi et al. 2006, Kishi & Bhatti 2010). A three-dimensional elastic-plastic explicit finite element analysis was applied to analyze a reinforced concrete girder (Kishi et al. 2010). The finite element mesh including the girder dimensions is shown in Figure 2-11 where a quarter of the beam is modeled based on symmetrical arrangement and symmetrical boundary conditions have been applied. Stress-strain response of concrete is assumed to be a bilinear model in compression, and a cut-off model in tension. An equivalent fracture energy concept was proposed in order to reduce the mesh size dependency of the analysis. When the strain energy accumulated in the concrete element reaches the value of the tensile fracture energy, smeared cracking occurs in the whole element and the tensile stress cannot be transferred. Assuming that the tensile fracture energy is the same for all elements irrespective of their sizes, fictitious tensile strengths are defined for the elements. It was observed that similar results can be obtained irrespective of element sizes when applying this method.
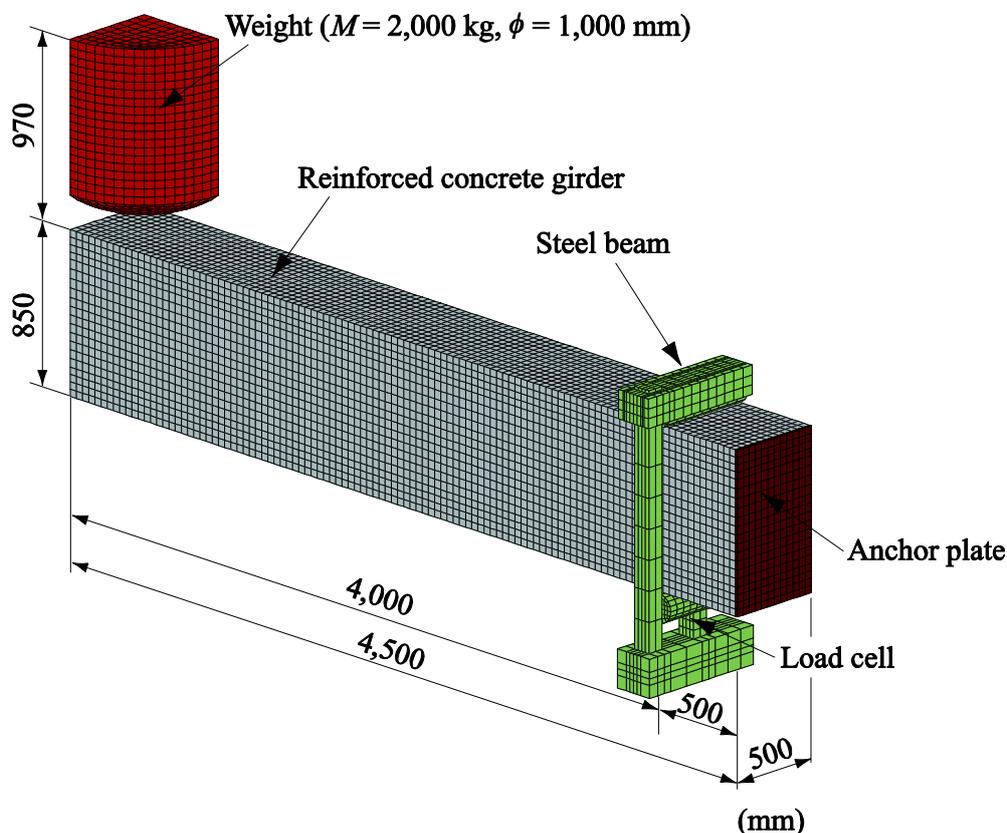
Figure 2-11: Finite element mesh of a reinforced concrete girder (Kishi et al. 2010)

Three-dimensional, quasi-static, elastic-plastic finite element analysis has been used to model steel pipes buried in gravel and subjected to rockfall (Pichler et al. 2006) as shown in Figure 2-12 a (the figure is reprinted with the permission from The American Society of Civil Engineers). The pipeline was covered by a well graded gravel layer, and was subjected to impact of single boulders of up to 18'260 kg. The cubic shape rock boulders were dropped so that they impacted the gravel with a corner. The diameter of the pipe was 1016 mm, and it was buried by gravel with overburden to diameter ratio of up to 3.

20

An elastic-plastic cap model (DiMaggio and Sandler 1971) is used to represent the gravel layer in finite element analysis (see Section 3.3.3). The relevance of the model was discussed by comparing the numerical predictions to the experimental measurements, where the stresses in the pipeline obtained from finite element analysis were compared with stresses determined in a real-scale structural test. The relative errors based on this comparison are illustrated in Figure 2-12 b.

Five impact events with the same impact energies as in the real-scale test ($E = 3'880$ kJ), were investigated. In regions with highest loading of the steel pipes, good agreement was observed between the numerical predictions and experiments. It was concluded that, in the case of rockfalls with potential energies up to 3'500 kJ, gravel was an effective energy absorbing system for pipelines due to the high stiffness of trench embedment and the large cover to diameter ratio of the pipe. However, for higher energies it was less effective as a protection system. In the modeling the dead weight of the gravel backfill over the pipe was neglected and only stresses due to the impact are considered. This assumption is not valid for large heights of backfill. Dynamic simulations are more favorable than quasi-static ones when the duration of impact is short.

a)   b)
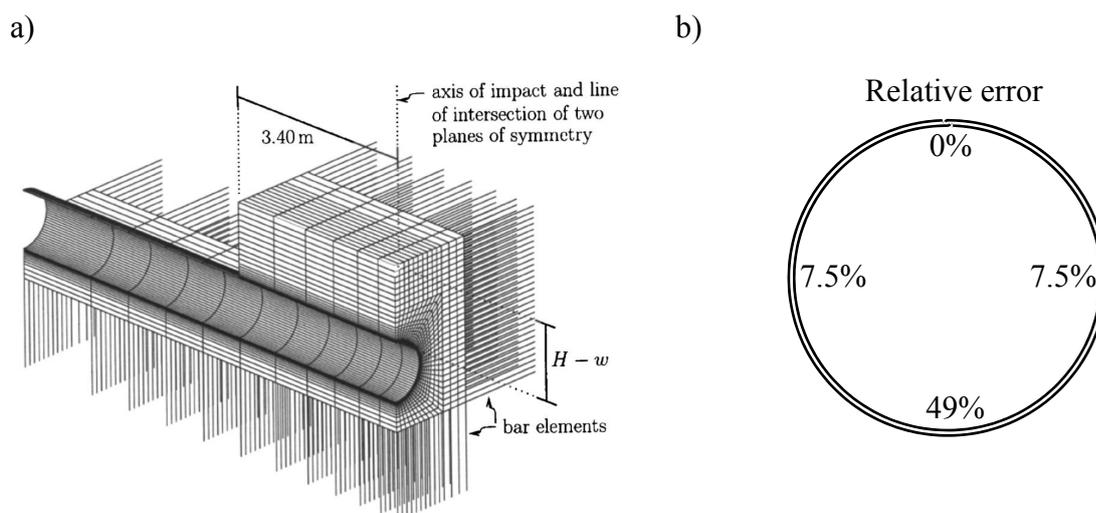
Figure 2-12: Simulation of pipes buried in gravel: a) finite element model (Pichler et al. 2006), and b) relative error of stresses in pipe by comparing the numerical simulations and experiments

Reinforced concrete structures were analyzed under severe high speed impact loads using different finite element programs, and the results were compared with each other and with those from large-scale impact tests (Zinn et al. 2007). The mass of the projectile was 1000 kg, and the impact velocities were in the range of 200-250 m/s. The displacement results obtained from two different finite element programs SOFiSTiK and ADINA showed good agreement with the experimental data. However, ADINA showed a better representation of the post peak displacements. The concrete elements were modeled using shell elements and volume elements, respectively. A limitation of the shell element is that shear deformations are only partially included, the experiments simulated in this study, however, showed bending deformations and the shear and punching effects were not significant.

A nonlinear finite element analysis procedure employing Disturbed Stress Field Model-DSFM (Vecchio 2000), as an advanced method of modeling shear behavior under impact conditions, was presented (Saatci & Vecchio 2009). The DSFM method is a formulation for describing the cracked behavior of reinforced concrete elements, which considers modeling of shear slip along cracks. Simply supported reinforced concrete beams, subjected to impact of drop-weights with masses of 600 and 211 kg, falling from a height of 3.26 m, were modeled (Figure 2-13 a). Mid-span displacements (Figure 2-13 b), crack profiles, and longitudinal reinforcement strains at mid-span were well predicted using finite element analysis. The methodology based on the DSFM could predict the shear-dominant behavior of the specimens under impact loads and performed well in predicting displacements, damage levels, and reinforcement strains. Local damage such as penetration, perforation, or scabbing under high velocity impacts could not be predicted using this methodology, which is the disadvantage of finite element modeling.
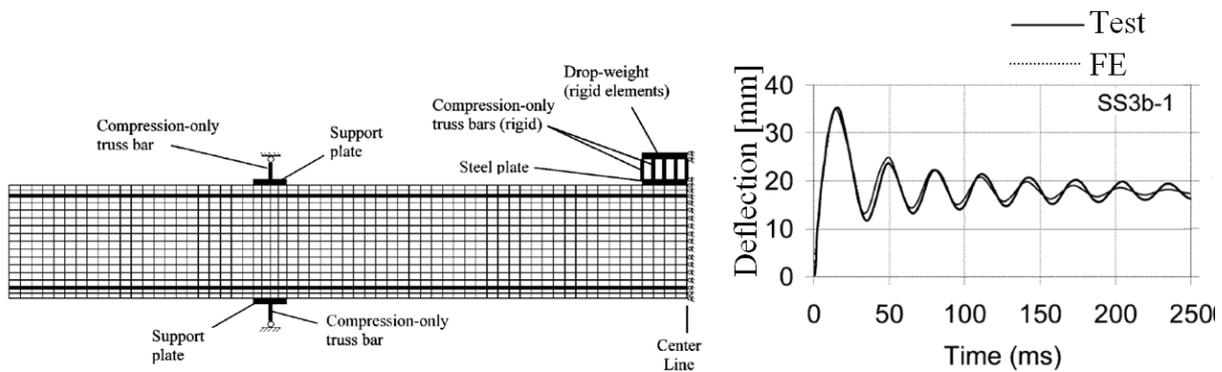
Figure 2-13: Reinforced concrete beam subjected to impact: a) Finite element model, and b) mid-span deflection of a beam with 0.3 % transverse reinforcement ratio (Saatci & Vecchio 2009)

Further finite element analyses investigating drop weight impact test on reinforced concrete slabs were carried out by Sangi & May (2009). Four 0.76 m square slabs, subjected to impact of masses of up to 380 kg and velocities of up to 8.7 m/s, were analyzed in this study (Figure 2-14 a). Three dimensional solid elements were used to model the concrete and the impacting body. Two different material models were used for concrete: the concrete damage model and the Winfrith concrete model (Broadhouse & Neilson 1987), respectively. The crack patterns using Winfrith model showed a better agreement with test results, impact force histories using both material models showed good agreement with the tests. However, the maximum impact forces were overestimated using finite element analysis (Figure 2-14 b). The slabs simulated in this study were rather small and were subjected to small impact energies (14.5 kJ).

The simulations carried out in various research projects discussed previously, represent behavior of reinforced concrete members, and of pipes buried in gravel that have been subjected to impact loading. However, in order to investigate the behavior of rockfall protection galleries, it is important to simulate the impact on slabs, which are covered by soil, and not only the direct impact on slabs.
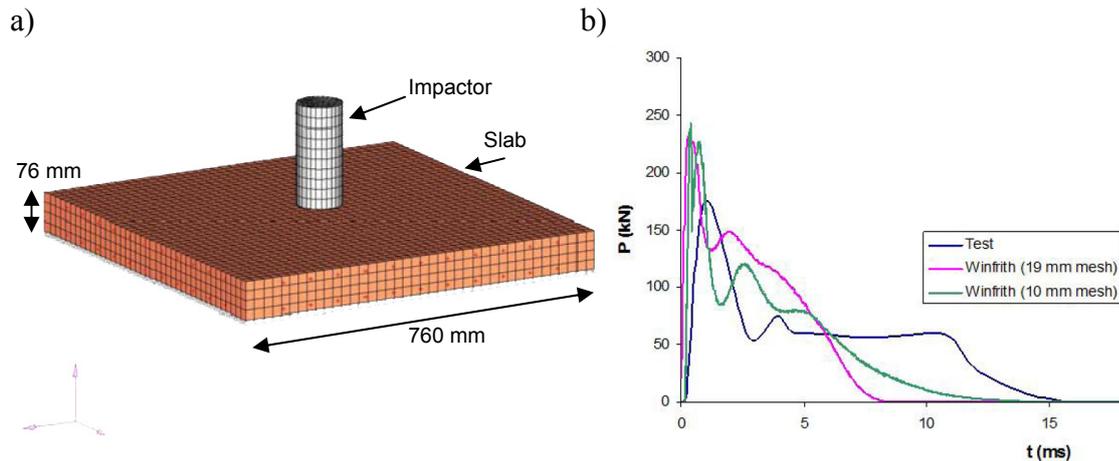
Figure 2-14: Impact on a slab: a) finite element mesh, and b) comparison of impact force-time histories (Sangi & May 2009)

Numerical simulation using three-dimensional finite element analysis of a prototype rockfall protection gallery covered with a sand cushion, subjected to falling-weight impact load, has also been discussed by Kishi et al. (2009). The concrete was modeled using a bilinear elastic-plastic model based on the Drucker-Prager yield criterion. The influence of the reinforcement was defined through a bilinear isotropic hardening model. Figure 2-15 shows the finite element mesh of the gallery. Penetration depth of the boulder, impact forces, support reaction forces, displacements, and the crack patterns obtained from analysis were discussed. The study confirmed that, in terms of impact energy, the galleries that have been designed, based on Japanese guidelines, have very high safety margins. The safety margin is about 35 times for the serviceability limit state and up to 60 times for the ultimate limit state. A similar simulation using gravel as cushion material is carried out in the current study, to resemble typical rockfall protection galleries in Switzerland.
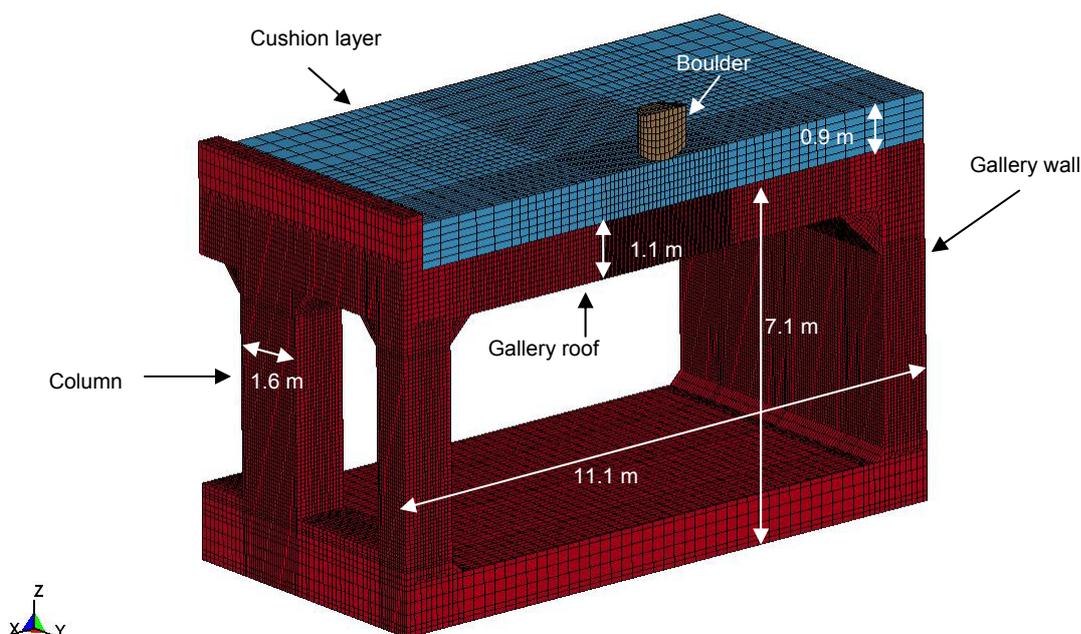

Figure 2-15: Finite element model of a prototype rockfall protection gallery (Kishi et al. 2009)

2.2.2 Discrete element method

The discrete element method (Cundall & Strack 1979) is one of the numerical approaches, which is based on the use of an explicit numerical scheme. The method is used for calculating motion of a large number of particles. While widely used for modeling granular material, the method has been applied to rock, soil, and concrete mechanics subsequently. The application of a discrete model to analyze the behavior of reinforced concrete structures under impact is outlined here.

A reinforced concrete slab with dimensions of 12 x 4.4 x 0.25 m, subjected to impact of a 450 kg cubic block, released from a height of 30 m, analyzed using finite element methods by Berthet-Rambaud et al. (2003, see Section 2.2.1.2) was also modeled using the discrete element method (Hentz et al. 2003). The discrete element model of the slab is shown in Figure 2-16 a. The modeling of the impact test did not give satisfying agreement between maximum displacement values for this study. Further numerical investigation of these slabs was carried out (Daudeville et al. 2005), and three impacts with 15 and 30 m drop heights were simulated (Figure 2-16 b). The mismatch of the maximum displacement of the slab computed by Hentz et al. (2003) with the experimental measurements, is due to the high stiffness of the slab in the simulations. The displacement results were also compared by Daudeville et al. (2005) and the relative errors concerning the displacements ranged between 5 to 8% (Figure 2-16 c).

This approach provides an insight into concrete fracture, but makes the real structure modeling impossible as the computation cost becomes "gigantic" (Dauville et al. 2005). It still remains time consuming to analyze a whole rockfall gallery using this method, with the computer capacities in 2011, but it may be possible in future. On the other hand, if developed accurately, a combined discrete element method and finite element method analysis can combine both local and global modeling of structures. Such a combined distinct element (explicit discrete element method) and finite element approach has been proposed for the analysis of rock-sheds by Nakata et al. (1997). A reinforced concrete slab, with dimensions of 3.4 x 3.4 x 0.2 m, covered by a 0.5 m layer of sand, was analyzed using this method. The sand cushion was represented by discrete elements, and the slab was modeled using finite beam elements. The action forces between the cushion elements and the distinct-finite-combination elements were calculated at each time step. The rock-shed was analyzed on the basis of these action forces, using the finite element method. The energy transmission to the gallery can be studied as well using such a simulation. Considering the behavior of slab and plates, the forces are distributed in the transverse direction as well, and simulating a slab using beam elements is not the best approximation to analyze the behavior of the slab. The method can be extended to three dimensional modeling of rockfall protection galleries in future.

a)

b)

c)
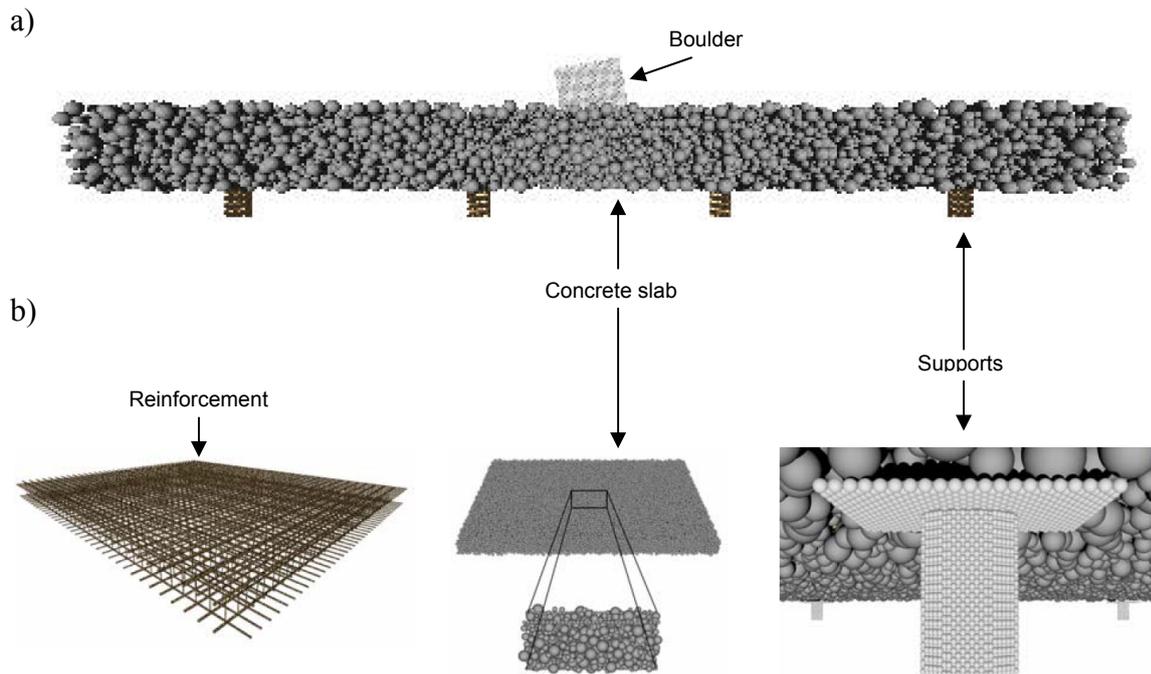
Test	Experiment	Simulation
Centered 30 m high	Max. displ.: *22,5 mm* No fuse buckling Yielding of vertical frames	Max. displ.: *21.4 mm* No fuse buckling Yielding of reinforcement
Centered 15 m high	Max. displ.: *14,5 mm* No fuse buckling No horizontal reinforcement yielding	Max. displ.: *13,9 mm* No fuse buckling No reinforcement yielding
30 m high on the edge	Max. displ.: *21,5 mm* Buckling of three fuses No horizontal reinforcement yielding, no information on vertical frames	Max. displ.: *19,9 mm* Buckling of four fuses Reinforcement yielding

Figure 2-16: Discrete element modeling of a) slab and its supports (Hentz et al. 2003), b) reinforcement, slab, and supports (Daudeville et al. 2005), and c) comparison of results (Daudeville et al. 2005)

A combined method has also been applied to model block impacts on rockfall protection embankments (Breugnot et al. 2010). A part of the embankment in the vicinity of the impact zone was modeled in this study using the discrete element method and a continuum approach was used to model the rest of the embankment.

2.2.3 Mesh-free method

The mesh free approach (Belytschko et al. 1994) is another method that has been applied to study the dynamic failure of concrete structures under blast and impact loading (Rabczuk & Eibl 2006). Reinforced concrete slabs with dimension of 0.61 x 0.61 x 0.178 m were subjected to impact of a steel projectile and were analyzed using this method (Figure 2-17).
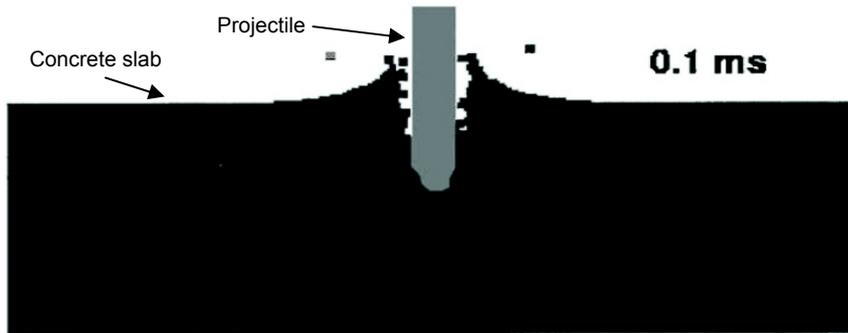
Figure 2-17: Deformed configuration of the slab subjected to projectile impact at 0.1 ms, using the mesh-free method (Rabczuk et al. 2006)

Mesh-free methods offer a promising solution for computation of many problems, especially for crack propagation and fracture mechanics. They have an advantage over finite element analysis for dynamic problems concerning the spalling of concrete, as large deformations can be easily handled. This method uses moving least square approximation (Lancaster & Salkauskas 1981), which makes it computationally expensive and it is better applied to problems where its unique advantages can be used. From the viewpoint of computational time, it is more convenient to make use of an element-free method only on the part of the domain where a better approximation of the solution is required, and to make use of the finite element method for the remaining part of the domain (Hegen 1996). The procedure to combine element-free methods with finite element approaches was already developed in the 1990s (Belytschko et al. 1995 and Hegen 1996). However, the application of a combined method to analyze reinforced concrete members subjected to impact loading can be studied further.

2.2.4 Material point method

The Material Point Method (MPM) is a finite element-based method (Sulsky et al. 1993), with capability to detect the contact without inter-penetration, and thus can be applied to dynamic problems with large deformations. Even though the MPM method is less complex than other methods, it has a computational cost factor of two compared to the finite elements, since it is a particle based method (Chen & Brannon 2002). Therefore, it is more appropriate for solving problems with small domains.

2.3 Codes, guidelines, and recommendations

The Swiss and Japanese guidelines have been developed to quantify the measures required to dimension a gallery and any other energy reducing components such as a soil cushion. These documents are briefly discussed in this section.

The Federal Road Office of Switzerland (FEDRO) provides a guideline for the design of rockfall protection galleries. The FEDRO guideline is based on falling-weight impact tests carried out in 1996 (Montani 1998), which are explained in Section 2.1. The laboratory tests, which were conducted only for impact energies up to 100 kJ, were extrapolated numerically for higher impact energies (Bucher 1997). Concrete and soil were modeled as a linear elastic material. The results were used as a basis to derive empirical equations for an equivalent static

impact force on galleries, as well as the calculation of the penetration depth of the boulder into the soil. These simulations involved various simplifications. The slabs were assumed to be circular with supports along the circumference; this assumption does not represent the support conditions of rockfall protection galleries. Moreover, the contact forces between the cushion and the slab as well as the effect of slab deflection on the impact forces have been neglected.

The guideline was first published in 1998 (ASTRA 1998) and was later adapted to a new generation of SIA codes (Swiss structural codes) in 2008 (ASTRA 2008). However, the technical content does not differ from the 1998 guideline.

The impact force F_k, which is the maximum value of impulse action of the boulder on the gallery, is calculated according to equation (2-1). Please note that characteristic angle of internal friction of the cushion layer is represented by φ_κ in ASTRA 2008.

$$F_k = 2.8 \cdot e^{-0.5} \cdot R_0^{0.7} \cdot M_{E,k}^{0.4} \cdot \tan \varphi_k \left(\frac{m_k \cdot v_k^2}{2} \right)^{0.6} \tag{2-1}$$

Where:

- e Thickness of cushion layer [m]
- R_0 Radius of an equivalent sphere [m]
- $M_{E,k}$ Soil modulus of the cover layer [kN/m^2]
- φ_κ Internal friction angle of the cover layer [°]
- m_k Characteristic block mass [t]
- v_k Characteristic impact velocity [m/s]

An equivalent static force A_d is calculated using a coefficient C, based on ductile ($C = 0.4$) or brittle ($C = 1.2$) failure of the structure, according to equation (2-2):

$$A_d = C \cdot F_k \tag{2-2}$$

As explained earlier, this formulation was based on experiments with limitation of the input impact energy to 100 kJ where the soil remains in elastic range, and the numerical extrapolations were oversimplified. Surcharging the galleries with a static equivalent force provides a simple approach for use in practice. However, it is important to adequately consider the dynamic behavior of the galleries and the nonlinear response of all its components. This provision limits the application of the Equation 2-1 to cushion layers with a thickness of at least the double of the calculated penetration depth, which limits its applicability.

The Japanese Road Association provides a handbook including recommendations for all types of protective measures, which was published in 1983. This handbook provides recommendations for different types of protection measures. Hokkaido Development Bureau, Ministry of Land, Infrastructure and Transportation also published some recommendations in 2001, which are used by local engineers.

Dynamic design for impact is highlighted in European Standards (EN 1991-1-7 Annex C). Recommendations are provided for the approximate dynamic design of structures, subject to accidental impact by road vehicles, rail vehicles and ships, on the basis of simplified or empirical models. In addition, hard and soft impacts on structures are discussed. For soft impacts, where the structure is designed to absorb the impact energy by plastic deformations, it suggests that the ductility should be sufficient to absorb the total kinetic energy of the colliding object. In the limit case of rigid-plastic response of the structure, this requirement is satisfied by the following expression:

$$\frac{1}{2}mv_r^2 \leq F_0 y_0 \tag{2-3}$$

Where:

- F_0 Plastic strength of structure, i.e. the limit value of the static force F

- y_0 Deformation capacity, i.e. the displacement of the point of impact that the structure can undergo

Detailed description of Swiss and Japanese guidelines, as well as other formulations for calculation of impact forces, can be found in Schellenberg (2008). A brief introduction to the design basis, and various empirical formulae for assessment of the impact performance of concrete structures, are outlined in CEB bulletin N° 187 (1988), which contains a general introduction to impact problems. It should be noted that CEB bulletin defines the soft impact as the case where the energy is absorbed mainly by deformation of the impacting body, which is in contradiction to the definition soft impact by EN 1991-1-7 mentioned earlier.

2.4 Analytical models

There are various ways of analyzing the dynamic response of structures, which are subjected to rockfall loading. Some of the analytical approaches are addressed here. In general, one degree simple elastic systems, simple degrees of freedom analysis, multiple degrees of freedom analysis, continuous systems without transformation to equivalent lumped mass, intermediate and advanced computational methods are some of the approaches used. Some details of the above mentioned approaches can be found in Biggs (1964) and Krauthammer (2008). The application of advanced computational methods, for impact analysis is explained separately in Section 2.2. This includes finite element, discrete element, and mesh-free methods. The application of single and multiple degrees of freedom systems to model rockfall protection galleries, with and without a cushion layer, as well as the rockfall impact on a pure soil layer, are discussed in this section.

Roesset et al. (1994) applied a simple mass-spring-dashpot model to evaluate the forces transmitted by impact of a weight falling onto the ground (soil layer). It uses soil stiffness and damping properties as proposed by Lysmer (1965). It was concluded that a simple mass-spring-dashpot model is not satisfactory if inelastic effects are neglected, as the falling-weight always rebounds. According to this study, the drop height does not affect the duration of contact, but an increase in the drop weight leads to an increase in contact time. The larger drop mass affects the stiffness and damping constant of soil since it's generally associated

with a larger contact area with the soil. This leads to increase in the natural period. Increases in the drop weight increase the coefficient of restitution (ratio of rebound velocity and impact velocity) and the energy actually transferred to the ground grows at a rate slower than the mass.

In order to investigate the response of reinforced concrete slabs subjected to impact, a variety of analytical methods are compared to experiments (Abdel-Rohman & Sawan 1985). The methods used in this study are the impact factor method, the equivalent mass method, and the continuous mass method. A moving object collides with a stationary slab in the impact factor method, in which the impact is considered to be completely plastic. An upper bound on results was obtained, which is very conservative. Impact happens at the center of the panel represented as one degree of freedom system for the equivalent mass method. The results using this method were in good agreement with experimental ones, but the response of the slab was assumed to be elastic. The continuous mass method considers the slab as a continuous elastic system of infinite degrees of freedom, which also provided results that were in agreement with experiments. Comparison of dynamic deflection of the slab using all three models with the experimental data is shown in Figure 2-18 b.

A one-dimensional simple degree of freedom was proposed for modeling the motion of a gallery under a vertical rockfall impact, as shown in Figure 2-18 a (Sonoda 1999). In order to provide a simple equation for practical application, the dynamic energy of the rockfall impact is set to be equal to the static energy dissipated by deformation of the slab. This energy (E_s) is expressed using the following equation:

$$E_s = \alpha_b W_B H + (M_s g + W_B)\delta_u \tag{2-4}$$

Where:

- W_B Weight of falling rock mass
- H Height of fall
- α_b Energy transfer rate to the gallery
- M_s Effective mass of the gallery for motion
- g Acceleration due to gravity
- δ_u Ultimate static vertical deflection of rock-shed

An elastic-plastic response is assumed for a slab, in which F_y is the first yielding load and F_u is the ultimate load. δ_y is the static vertical deflection of the gallery at first yielding.

a)   b)
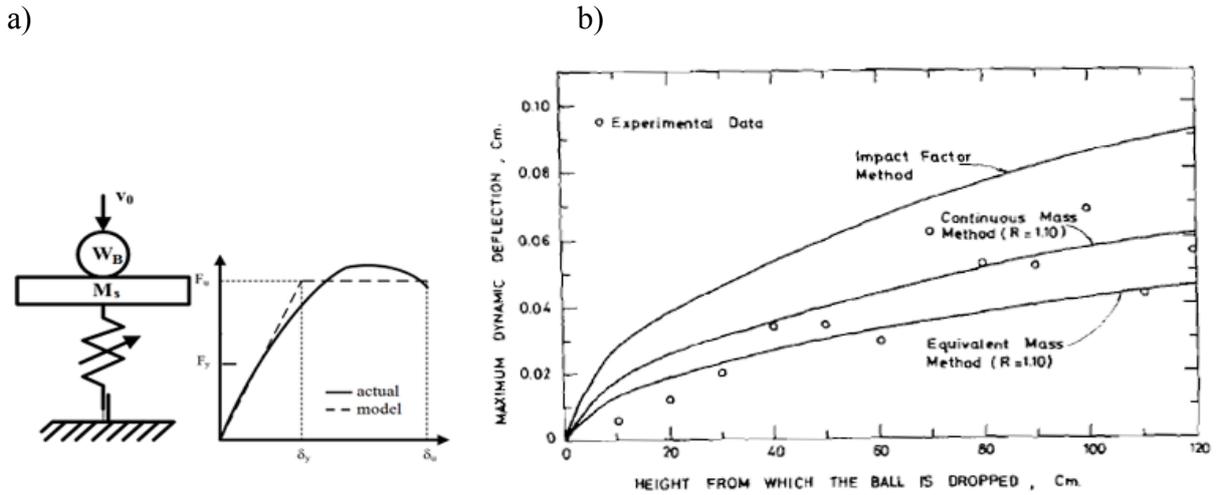
Figure 2-18: Analytical models: a) one degree of freedom system and its static load deflection curve (Sonoda 1999), and b) deflections of a slab using various models (Abdel-Rohman & Sawan 1985)

An analytical model was proposed for the evaluation of the response of reinforced concrete beams subjected to vertical impact loading (Fujikake 2007). The model was based on a two degree of freedom mass-spring-damper system (Figure 2-19 a). In this model, k_1 represents the load-deflection relationship of the beam, and k_2 is the contact spring based on Hertz's contact theory. m_1 and m_2 refer to the equivalent mass of the beam and of the drop hammer.

a)

b)
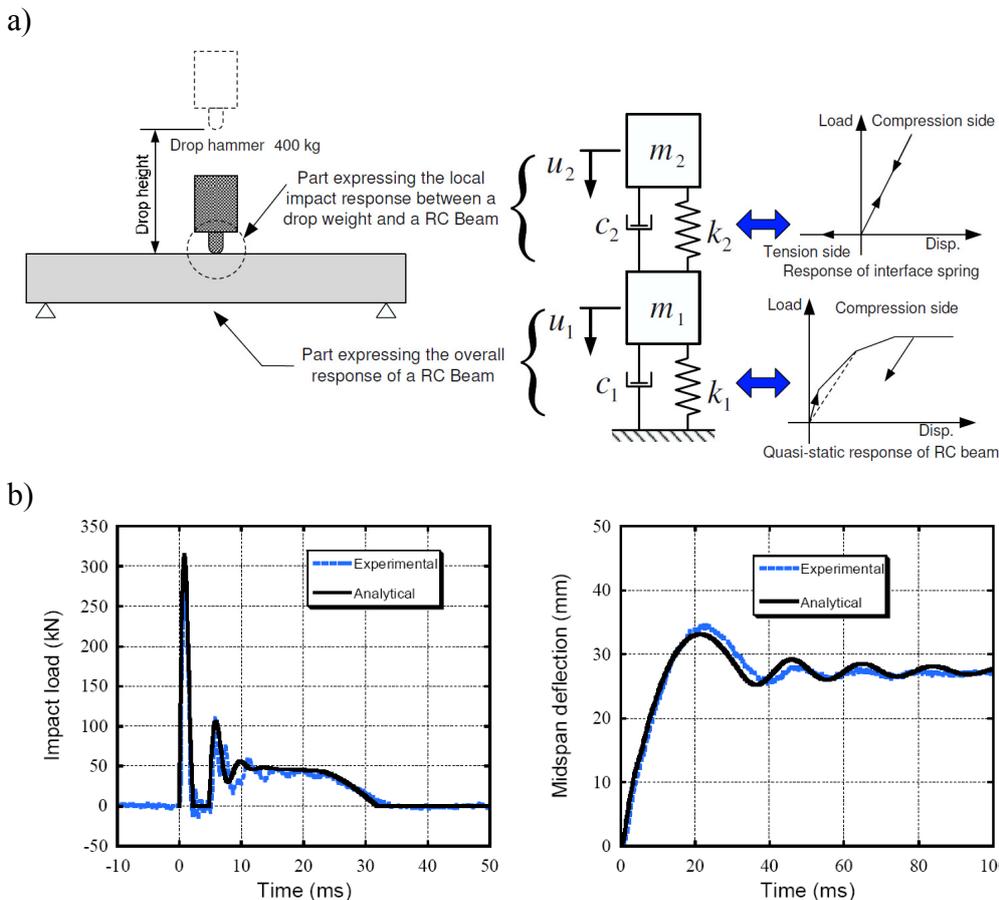
Figure 2-19: Two-degree-of-freedom mass-spring-damper system: a) model representation, and b) comparison of results (Fujikake 2007)

The validity of the method was investigated by analyzing experiments carried out on a reinforced concrete beam with dimensions of 2.4 x 0.15 x 0.25 m subjected to impact of a drop hammer with a mass of 300 kg and a velocity of 4 m/s. The results obtained using the analytical model, were in good agreement with the experiments (see Figure 2-19 b) when a high damping ratio (20%) was assumed for the local response at the contact point.

A simplified mass-spring model was proposed by French researchers for the simulation of the impact of a block falling onto a reinforced concrete slab (Delhomme et al. 2007). The slab displacement and contact forces obtained from this model can be used for the design of slabs (Figure 2-20).
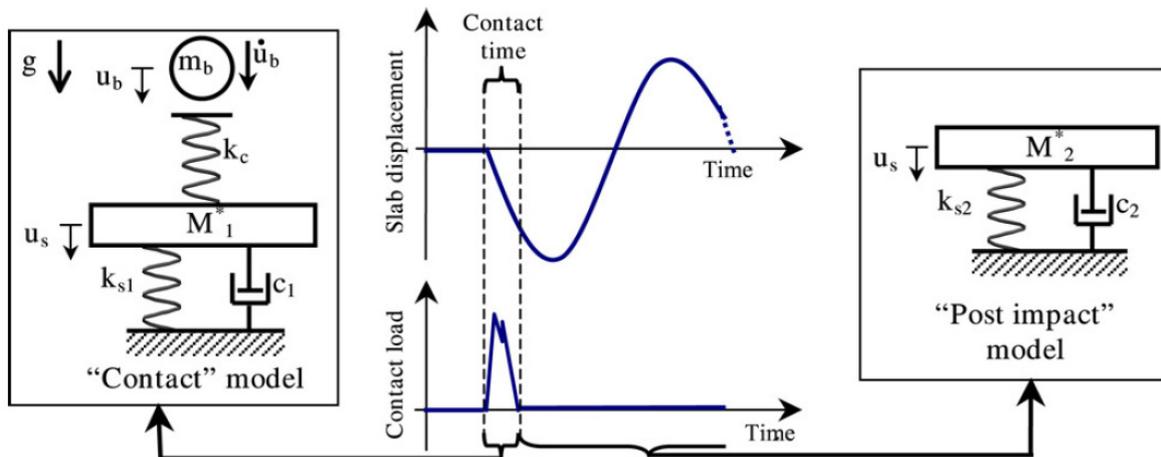
Figure 2-20: Analytical method with two "mass-spring" models: "contact" model and "post impact" model (Delhomme et al. 2007)

These analytical methods can be developed further to incorporate the energy dissipation in the soil, in order to apply them to the design of rockfall protection galleries. A Spring-Mass-Slider-Dashpot system (SMSD) was proposed for modeling impact on soil (Chikatamarla 2006) as shown in Figure 2-21, which represents elasto-plastic as well as visco-elastic behavior of the soil. The system was extended for 2-D by adding a horizontal slider. However, the thickness of the cushion material covering a gallery is limited and development of a full shear slip surface in such a case may not be expected. An analytical model which incorporates different thicknesses of cushion material should be used for modeling the behavior of the cushion material covering a gallery.
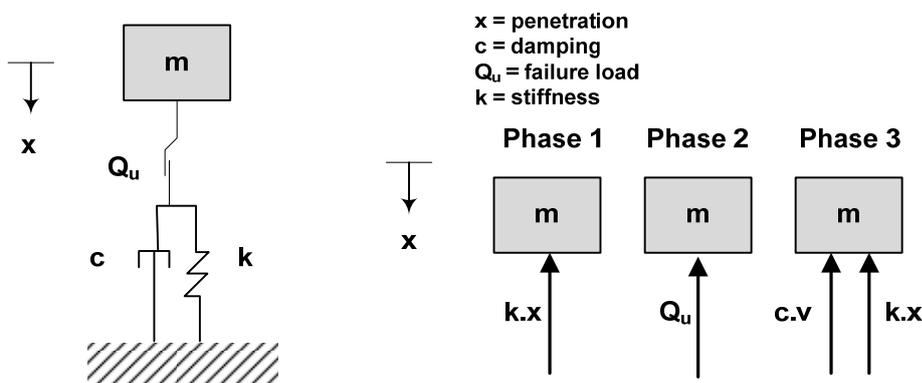
Figure 2-21: SMSD model after Chikatamarla (2006)

The application of a System of Multiple Degrees of Freedom (SMDF) was proposed by Schellenberg (2008) for modeling the dynamic behavior of rockfall protection galleries covered by a cushion layer. The SMDF consists of three masses and three nonlinear springs, similar to the model proposed for analysis of aircraft collisions with reactor containments (Eibl et al. 1988). The model is explained in Chapter 6. In this model an additional spring is added for the simulation of punching failure of the reinforced concrete slab.

3 Numerical models

Application of different numerical methods for modeling large reinforced concrete rockfall protection galleries involves various complexities (Section 2.2). Finite element methods have been used in the current research due to the advantages in handling complex geometry, loading, and restraints with a reasonable computation time.

A preliminary study was carried out to investigate the applicability of finite element methods to model the behavior of concrete slabs covered by soil, subjected to impact (Ghadimi Khasraghy 2008). A simplified model using multilayered shell elements with nine integration points representing concrete and smeared reinforcement was used to represent the reinforced concrete slab. Two impacts of low energies (40 & 60 kJ) on a reinforced concrete slab were modeled. Comparing the reaction forces and the strains at specific locations in the concrete slab to the experimental data, it was observed that shell elements performed well to simulate the overall behavior of the slab. Full three dimensional modeling using solid elements for the concrete slabs is required to obtain a detailed insight to the local behavior of slabs, to study the effect of shear reinforcement on the increase of load carrying capacity of slabs, and to study the behavior of slabs subjected to higher impact energies. Therefore, only the three dimensional analyses of slabs will be outlined here.

3.1 Method and software

There is a variety of finite element analysis software available for analysis of the structures subjected to dynamic loading including LS-DYNA, AUTODYN, ABAQUS, etc. LS-DYNA and ABAQUS are widely used for analysis of impact on reinforced concrete members since they are powerful in nonlinear dynamic analysis using explicit time integration and include a range of constitutive models, which can be applied for modeling reinforced concrete structures. The explicit finite element program LS-DYNA is used here for three-dimensional structural analyses of rockfall impacts on reinforced concrete slabs. The program was developed in 1976 and it is widely used for by automotive industry, sheet-metal forming, aerospace industry, as well as civil and earthquake engineering. The explicit time integration algorithms used in LS-DYNA are in general much less sensitive to machine precision than other finite element solution methods (LS-DYNA 2007). LS-DYNA is a finite element code for analyzing the large deformation dynamic response of structures. More information about LS-DYNA can be found in the LS-DYNA Keyword User's Manual (LS-DYNA 2007) and the LS-DYNA Theory Manual (LS-DYNA 2006).

JVISION and LS-PrePost are used as pre- and post-processers for use with LS-DYNA. JVISION is a multipurpose pre- and post-processor produced by JSOL Corporation, Japan. LS-PrePost is an advanced pre- and post-processor that is available from LS-DYNA.

3.2 Element types

Different elements can be used for discretization of a continuum media. Reinforced concrete slabs are represented by solid elements for concrete, beam elements for reinforcement as well as stirrups for shear. The impacting bodies, cushion layers, and supporting systems are also modeled by solid elements.

Eight-noded hexahedron constant stress solid elements, and two-noded beam elements with Hughes-Liu beam formulation are used for modeling. The beam element formulation is based on the shell element formulation introduced by Hughes & Liu (1981a, 1981b). The Hughes-Liu beam element is based on a degeneration of an isoparametric eight-noded solid element.

3.3 Material models

3.3.1 Concrete

A bilinear model is assumed for concrete in compression; the concrete is assumed to yield after having reached its compressive strength. The model adapted is similar to the one used for modeling reinforced concrete members (Kishi et al. 2006, Kishi et al. 2009, Kishi & Bhatti 2010). In general, the values for the compressive strength and the elastic modulus of concrete are taken from experiments on concrete cylinders or cubes. The values adapted for different models are explained in the respective sections in Chapter 4.

Concrete in tension is assumed to behave linearly until a tension cutoff value of 10% of its compressive strength is reached (Figure 3-1 a). If the stresses drop below the mentioned cutoff value, they are reset to the tension cutoff value and the deviatoric stress tensor is zeroed. This facilitates tracing the crack patterns of concrete members, by plotting the contours of stresses small enough to be considered zero.
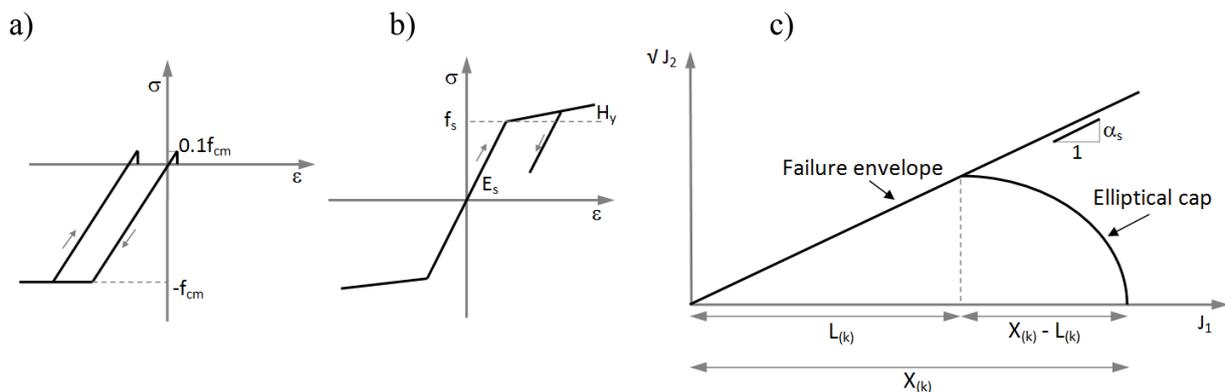
Figure 3-1: Material model for a) concrete, b) reinforcement, and c) gravel layer.

The von-Mises yield criterion (von Mises 1913) is used for its simplicity and efficiency in modeling a bilinear response of concrete. The Drucker-Prager yield criterion (Drucker & Prager 1952) has been considered as well, and the results obtained did not differ much from the original von-Mises formulations. Dynamic material property has been integrated in terms of strain rate effects on concrete, which were found to have had virtually a small influence

(see Section 5.1). Therefore, strain rate effects are not considered for further analysis. A parametric study of the concrete material properties is given in Chapter 5.

### 3.3.2 Reinforcement

The constitutive model for the longitudinal bars and stirrups is bilinear, with strain hardening (Figure 3-1 b). The concrete and reinforcement elements are assumed to have a perfect bond, and the concrete solid elements are connected to the reinforcement beam elements at nodal points. The same nodes are defined for reinforcement and concrete where they are in contact with each other. The assumption of the perfect bond can be justified for members critical in bending since using a bond link element may not have a great influence on results (see Ghadimi Khasraghy 2005). However, for members critical in shear the results can differ, and the load-deflection response of the structure is stiffer when a perfect bond is assumed. It is worthwhile to consider the bond for modeling shear critical structure (e.g. deep beams) if a detailed investigation at disturbed regions is desired.

3.3.3 Soil cushion

When soil is subjected to impact of a falling boulder, the impacting energy is dissipated by shearing and compaction of the soil as well as crushing of soil grains. The three modes of shear failure identified in soil, namely, general shear, local shear, and punching shear mechanisms are shown in Figure 3-2 (Vesic 1963). General shear failure can be expected in dense soils that exhibit low compressibility. The local shear failure refers to significant compression of loose soil and partial development of slip surfaces, which is associated with soils of high compressibility and results in relatively large settlements. The punching shear failure occurs when soil is under high compression loading, and shearing forms in the vertical direction around the edges of a footing (impacting boulder in this case). It occurs in soils of very high compressibility like clays. The ultimate bearing capacity of soil in shear can be defined as the pressure which can cause shear failure immediately below the impacting boulder (Craig 1997).

If the depth of the shear failure mechanism is larger than the thickness of the soil layer, a shear slip surface cannot be fully developed in the same form and the mechanism will change. In that case, the behavior is governed by a combination of compression beneath the boulder and a subsequent partial shearing in the soil. When the thickness of the soil layer is small (e.g. less than half of the size of the boulder) the behavior of soil is mainly governed by compression below the boulder, crushing of the grains, and the shear at the sides of the boulder. The grain crushing contributes to the phenomenon of plastic compression of brittle, granular media (McDowell et al. 1996). When there is a high compression load below the impacting body, particle crushing contributes to the reduction of volume. Particle crushing is the main contributor to energy dissipation for brittle materials with low strength. The mechanism of the failure in soil also changes if it is composed of different layers with different properties, so in the case of a layered soil cushion a mechanism of failure should be investigated based on the individual case (see Nater 2005). Therefore, it is important to incorporate the real mechanism of soil failure for different thicknesses and properties of the soil cushion.
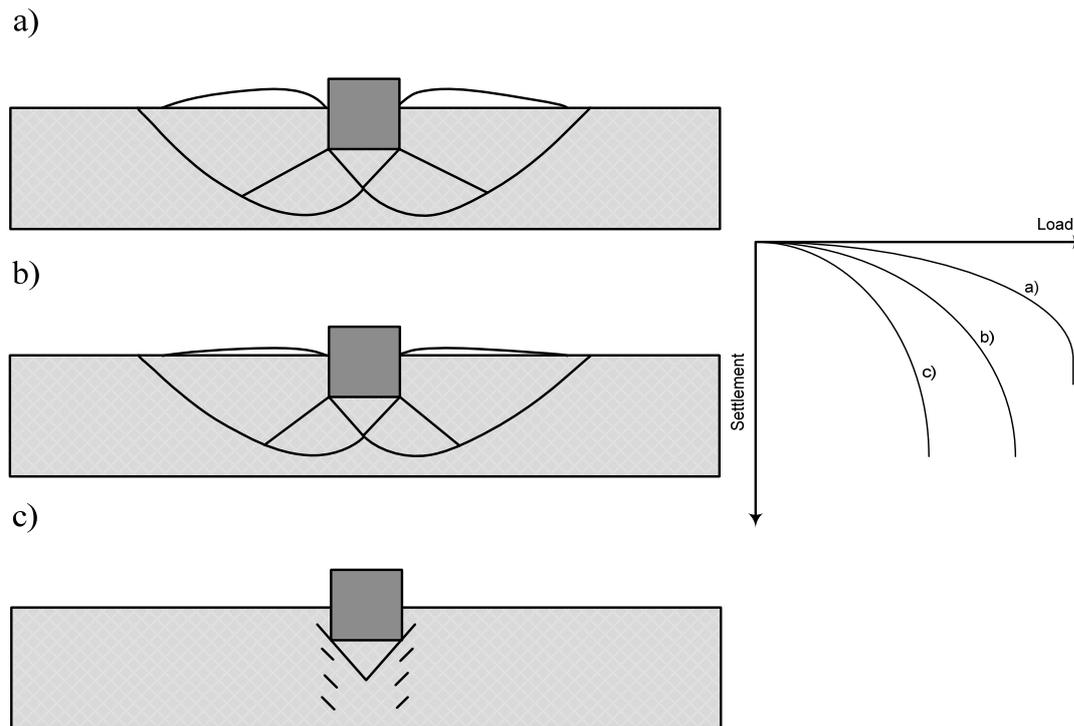
Figure 3-2: Modes of soil failure: a) general shear b) local shear, and c) punching shear according to Vesic (1963)

It must be noted that the dilatancy of soil and its strength parameters are affected by the effective stress and soil density. Therefore, the angle of internal friction of soil which forms the slip surface as shown in Figure 3-2 a, is not constant as the stresses in different locations below the impacting boulder are not the same. The value of angle of internal friction of soil that is derived from a single triaxial test can provide a conservative value for design and a full range of soil strength should be expressed in terms of variation of the angle (see Bolton 1986). The angle of internal friction of soil, if set as a constant value for numerical modeling should be chosen carefully. Figure 3-3 a (Lau 1988) shows the variation of the angle of internal friction under circular footings with diameters of 0.4, 1.42, and 5 m, respectively. It can be seen that the angle varies between 39 to 57 degrees for these cases. An average value of 45 degrees is thus assumed for the current study, since the sizes of the boulders modeled vary within the range of footing sizes shown in this figure. The Poisson's ratios of sand and gravelly sand, range from 0.3 to 0.4 (Bowles 1996). A value of 0.33 is assumed in this study.

It is challenging to carry out triaxial tests on materials used as a cushion layer for rockfall protection galleries, due to the size effect relating the maximum particle size to the diameter of the platen. The triaxial device should be large enough that the largest particle size does not highly influence the outcome of the test. Prior work by Guldenfels (1995) on aging of the grains used for construction of railway ballast and a study on soil properties of moraines by Teysseire (2007), have been carried out by testing soil samples in a large triaxial apparatus of 25 cm diameter. The results of the tests by Teysseire (2007) were studied in order to assess the selection of the parameters in the zones for which there is dilatancy occurring at low values of porosity as shown in Figure 3-3 b. It can be seen that the angle of internal friction of about 45 degrees was obtained for triaxial tests on the soil with a maximum grain size of 30 mm, when the porosity was about 20%.
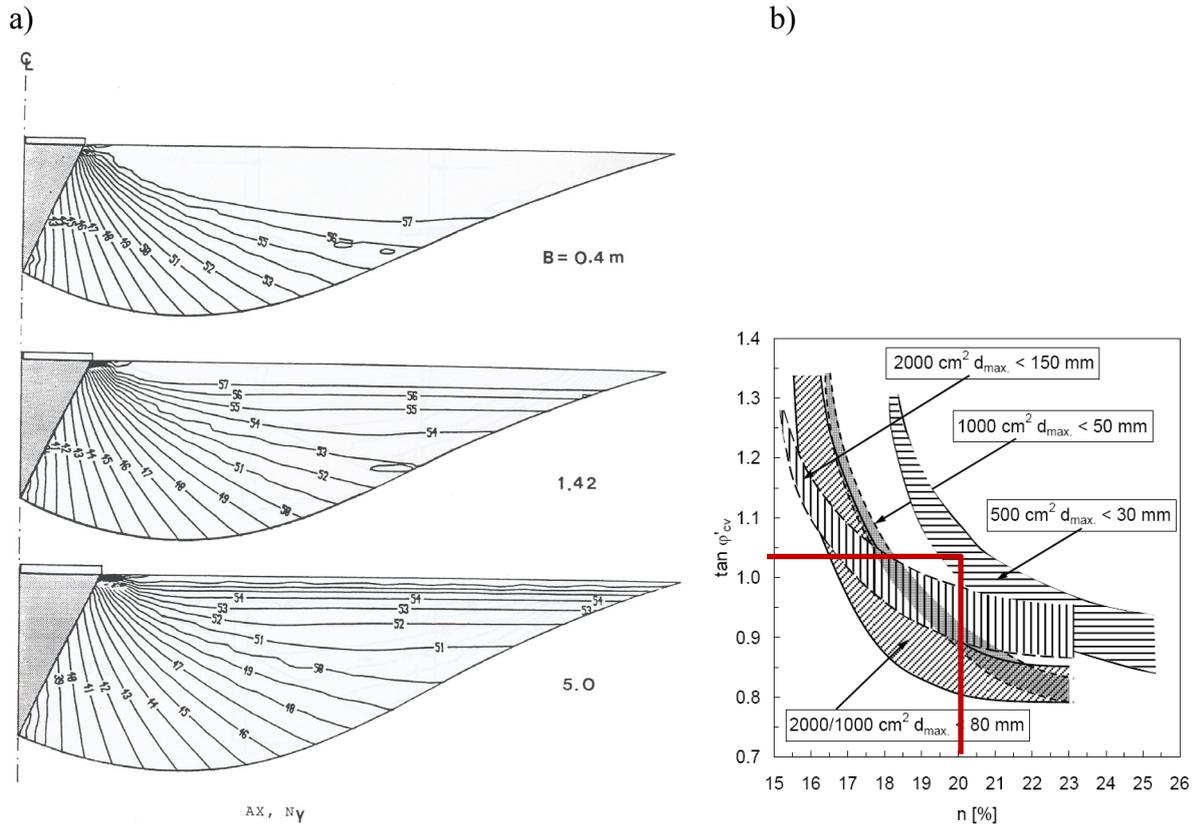
Figure 3-3: The angle of internal friction: a) variation under rough circular footings with different sizes (Lau 1988), and b) relation with porosity and maximum grain size (Teysseire 2007)

The material model adapted for soil cushion considers shearing and compression (hardening) of the material, using a cap-hardening model. The grain crushing is not considered in this model. The model is similar to the one used for the simulation of gravel material behavior for pipes buried in gravel (Pichler et al. 2006). The material model for granular materials based on the classical plasticity theory is proposed by DiMaggio and Sandler (1971). This combines an ideally plastic Drucker-Prager yield condition with a strain hardening cap. The parameters of the model are determined by curve fitting through experimental data for the respective soil. Details of the model as well as the definition of the parameters can be found in DiMaggio and Sandler (1971), and Chen and Baladi (1985). The model is shown in Figure 3-1 c; where J_1 is the first invariant of the stress tensor, and J_2 is the second invariant of the deviatoric stress.

Depending on the stresses acting in the soil element, either plastic yielding behavior or hardening can be expected using this model. The behavior of the assumed cap hardening model under isotropic compression as well as the shear behavior is shown in Figure 3-4, in which ε_{kk} is the volumetric strain. Isotropic compression behavior is shown in Figure 3-4 a for the stress following the path 1-2-3-1. Shear behavior (Figure 3-4 b) can be illustrated for the path 1-2-3, which is the state of developing bearing capacity failure. An ideal isotropic hardening behavior cannot be expected for cushion material subjected to impact loading in reality. The elastic-plastic idealization provides an estimate for the shear failure of the soil, after plastic yielding the strains keep increasing while subjected to the same or higher loading. The limitation to the modeling is the element size, once the plastic yielding is reached, the strains increase, and thus the volume of the elements keep decreasing. The calculation

becomes unstable and is terminated when the element volumes become small or equal to zero. Therefore, using this model it is not possible to model the post-failure behavior of soil.
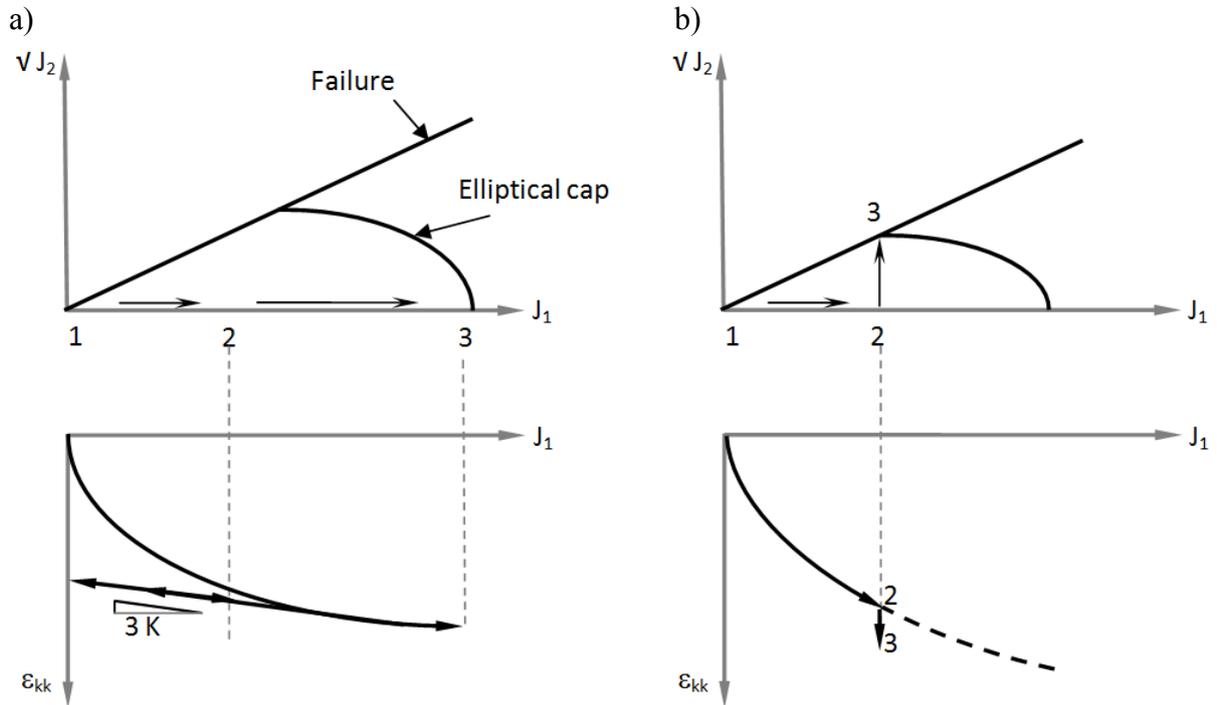
Figure 3-4: Behavior of assumed cap hardening model under a) isotropic compression following path 1-2-3-2-1, and b) shear behavior for a constant mean normal stress following path 1-2-3 (following a representation by Chen & Baladi 1985).

The stress invariants J_1 and J_2 are defined as:

$$J_1 = 3p \qquad \text{and} \qquad \sqrt{J_2} = \frac{q}{3} \qquad\qquad (3\text{-}1)$$

where, p is the mean stress and q is the deviatoric stress and can be calculated as:

$$p = \frac{\sigma_1 + 2\sigma_3}{3} \qquad \text{and} \qquad q = \sigma_1 - \sigma_3 \qquad\qquad (3\text{-}2)$$

where σ_1 and σ_3 are axial and lateral stresses.

Table 3-1 lists the parameters used for the elastic-plastic cap-hardening model of gravel. The failure coefficient α_s is a material constant related to the friction angle (Equation 5-2). W defines the maximum plastic volumetric compaction that material can experience under hydrostatic loading. R is a curved shape function for an elliptical cap, and D_s is a material constant. The parameters of the compaction (hardening cap) surface can be calibrated using the strain data from uniaxial compression, and triaxial compression tests. A fitting procedure is obtained by trial and error procedure in which some initial parameters are assumed and are varied until a best fit is obtained.

Table 3-1: Parameters selected for the cap hardening model

Parameter	Bulk modulus	Shear modulus	Failure envelope coefficient	Cap surface axis ratio	Hardening law exponent	Max. plastic strain
Symbol	K	G	α_s	R	D_s	W
Unit	MPa	MPa	-	-	MPa^{-1}	-
Value	192	88.5	0.356	4.15	0.04	0.2

The parameters used in Table 3-1 are calibrated based on the oedometric test carried out on a gravel sample with a diameter of 0.25 m and a height of 0.188 m. The test set-up is shown in Figure 3-5. The sample was prepared based on the grain size distribution of the gravel used for the falling-weight experiments (Schellenberg 2008). The experimental results as well as the calibration of the parameters shown in Table 3-1 are outlined in Appendix A.

Figure 3-5: Oedometric test on a gravel mix

3.4 Loading

Impact loads defined here occur due to acceleration of the mass under gravity, and forces measured using finite element analyses result from the contact forces between the members.

3.4.1 Single impact

To save computational time, the initial position of all impacting bodies is defined at the surface of the cushion layer, or in case of slabs without a cushion layer, on the surface of the slab. The impacting body is subjected to a pre-defined initial velocity. At the same time the rest of the model is subjected to acceleration due to gravity, in order to account for self-weight of the structure.

3.4.2 Consecutive impacts

As slab softening and plastic deformation affect the reaction forces of the slab during consecutive impacts, a method is established to model a slab subjected to repeated loading. The modeling aims at following the load history and related deterioration in the slab due to the consecutive loading. The procedure developed is explained in Section 4.1.2.2 (see Figure 4-3).

3.5 Support conditions and contacts

The impacting bodies, and the supporting systems are modeled using linear elastic material models, since there were no plastic deformations observed in the supporting systems during the experiments (Schellenberg 2008). The supporting systems for various slabs and galleries are modeled accurately according to the real shapes of the supports.

Symmetrical arrangements have been taken into consideration for slabs and galleries analyzed in this study. Half or a quarter of the structures are modeled based on symmetrical arrangements. Symmetrical boundary conditions have been applied accordingly.

The contact forces between relevant members are calculated by applying the penalty method, which was developed by Fiacco & McCormick (1968) for solving a constrained optimization problem. The method is also used for colliding surfaces, and it consists of placing normal interface springs between all penetrating nodes and the contact surface. Inner pairs of forces are applied at the locations where penetrations are observed. These forces are calculated based on penetration depth and contact stiffness. In theory, the procedure is neutral in energy.

4 Finite element results and validation with experimental studies

This chapter presents results obtained from finite element modeling of some of the experiments, in order to validate and calibrate the numerical approach. While considering the impact load carrying capacity of reinforced concrete slabs, two failure mechanisms are of importance, namely bending failure (global response) of the slabs, and punching shear under impact (local response). Both modes of behavior are outlined here. Discretization of some of the finite element models has been carried out in collaboration with Muroran Institute of Technology, Japan. Parts of the work presented in this chapter have already been published in Ghadimi Khasraghy et al. (2009a and 2009b).

4.1 Prediction of bending failure

Bending (the global response) is studied for slabs with and without shear reinforcement in this section. Shear reinforcement increases the capacity of the slab in the zones where the shear forces are critical. Punching shear was not the governing failure mode for the experiments mentioned here. There were zones above the supports, however, where shear forces were governing the response.

As the capacity of the slab is increased by adding shear reinforcement, these slabs are also mentioned here. Shear reinforcements increase the punching capacity of the slab as well; this needs to be further investigated by conducting direct impact experiments on shear reinforced slabs (which are not covered by soil).

4.1.1 Test description

The large-scale falling-weight impact tests carried out in Switzerland (Schellenberg 2008) are used as benchmark for finite element analyses (see Section 2.1.2 and Figure 2-3). The experimental series A, B and E refer to two slabs without, and one with, shear reinforcement, respectively, and are discussed in the sub-sections hereinafter. The slab A had a thickness of 0.25 m, slabs B and E were both 0.35 mm thick. Table 4-1 gives an overview of these experiments. The slabs had lateral dimensions of 3.5 x 4.5 m and were covered by a 0.4 m thick layer of gravel.

Tensile reinforcement of 18 mm in diameter with a spacing of 150 mm was used for Slab A. The B and E slabs had tensile reinforcement of 22 mm in diameter placed at 150 mm spacing. The compressive reinforcement of all slabs was of 10 mm in diameter with a spacing of 300 mm. The shear reinforcement used for slab E had a diameter of 10 mm and a spacing of 150 mm.

Table 4-1: Experiment details

Series A, impact No:	A1	A2	A3	A4	A5	A6	A7	A8
Falling weight [kg]	800	800	800	800	800	800	800	800
Falling height [m]	2	5	5	5	7.5	10	12.5	15
Impact energy [kJ]	16	39	39	39	59	78	98	118
Series B, impact No:	**B1**	**B2**	**B3**	**B4**	**B5**	**B6**	**B7**	
Falling weight [kg]	800	800	800	800	800	4000	4000	
Falling height [m]	5	7.5	10	12.5	15	2	5	
Impact energy [kJ]	39	59	78	98	118	78	196	
Series E, impact No:	**E1**	**E2**	**E3**					
Falling weight [kg]	800	4000	4000					
Falling height [m]	15	5	7.5					
Impact energy [kJ]	118	196	295					

4.1.2 Discretization and finite element model

4.1.2.1 Single impact loading

The impact due to a single impact loading implies that it is assumed to act on a virgin slab, and the effect of consecutive loading and pre-damage on the slab is not considered. The finite element models of B1 and E2 are shown in Figure 4-1 and Figure 4-2, respectively. A concrete compressive strength of 35 MPa, and a tensile strength of 3.5 MPa are used for these models. The yield strength of steel is 550 MPa. A global damping ratio of 1.5% is assumed for the structure, which is the coefficient for the fundamental natural vibration in vertical direction. The free oscillation of the slab without cushion layer, subjected to a short impulse at the slab's center is used for obtaining the damping ratio (Schellenberg 2008). The impactor is modeled as elastic material with a Young's modulus of 30 GPa.
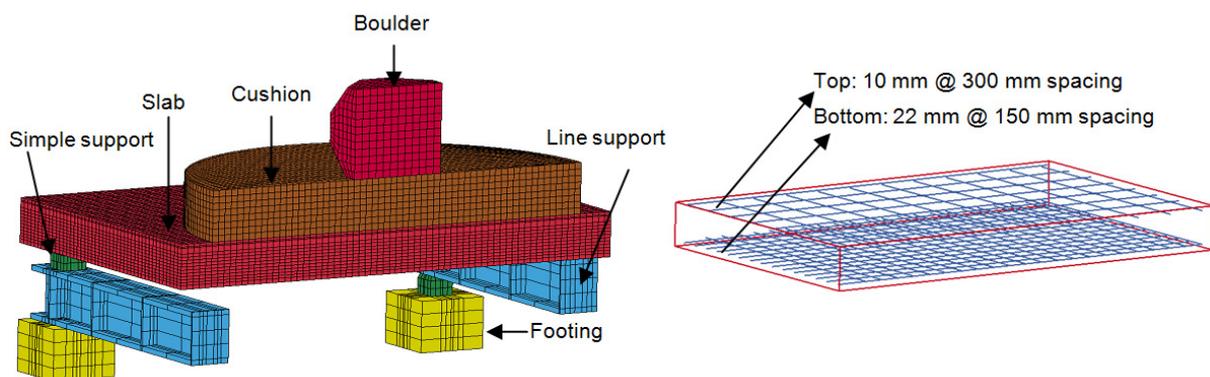
Figure 4-1: Impact B1: a) finite element model, and b) reinforcement layout

The reaction forces during the experiment were measured with load cells. The load cells and supporting beams were further supported by four reinforced concrete footings (Figure 4-1 a). No visible damage and deformation was noticed in these footings, so they are assumed to be rigid and their stiffness is assumed to have no significant influence on the results. Therefore, they are not modeled for the impact E2 (Figure 4-2 a) and the supports are simplified. The load cells are set to have fixed support conditions. A 50 mm mesh is used for the slab. The reinforcement and their spacing is similar to the impact B1 (Figure 4-1). U-shaped shear reinforcement of diameter 10 mm with spacing of 150 mm are placed additionally (Figure 4-2 b).
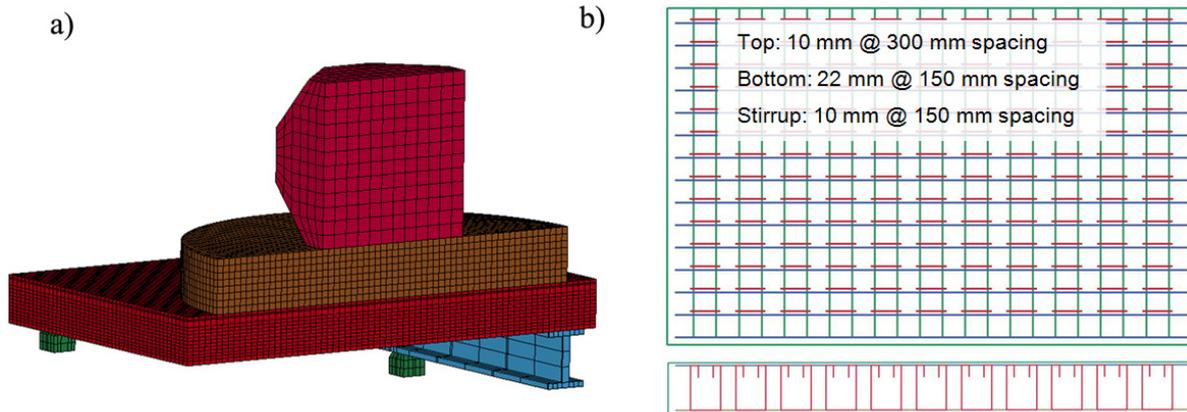
Figure 4-2: Impact E2: a) finite element model, and b) bending and shear reinforcement layout

4.1.2.2 Consecutive impact loading

All seven impacts of series B are modeled. The slab was subjected to impacts of an 800 kg boulder, with increasing falling height to a maximum of 15 m, then to impacts of a 4000 kg boulder, with increasing falling height until the slab failed (Table 4-1).

The gravel layer was loosened and compacted after every impact during the experiment. Furthermore, the falling height (input impact velocity) was increased for every impact and after reaching the maximum operational falling height, the size and mass of the boulder was increased to 4000 kg. This loading history should be incorporated into the finite element model for the slab; the loading history can't be developed for the soil, since the properties of cushion was changed after the impact. All the impacting boulders and the soil cushion layers need to be defined at the same location from the beginning, each set representing the boulder and soil cushion during a specific impact. However, only the boulder and the cushion layer relevant for the individual impact are activated at each step.

To eliminate the effect of the self-weight of these members on the slab at the initial stage and to allow only the relevant members to be active during each impact, fictitious members called "stoppers" are defined for every boulder and cushion layer. The stoppers are defined to be elastic with a high stiffness and have fixed support conditions. The stoppers provide a way of controlling the motion of the members. The method can be described in the following steps:

1. Initially the model is run solely for gravity loading, so the slab is subjected to its self-weight only. During this step, all the boulders and the cushion layers are inactive as their motion is controlled by the stoppers;

2. The stoppers of the first boulder and the first cushion layer, as well the contact between the respective members and their stoppers are removed, and the first boulder is subjected to its initial velocity;

3. Using a "restart" option, the model continues to run and the calculation restarts from the previous termination point. The calculation time is reset to the next termination time during this step. The "restart" allows the analysis to be portioned into several steps. The results of calculation can be checked after every step. The global damping ratio is set to be 1.5% during calculation;

4. After the analysis under the first impact is completed, the first boulder is removed. During this step, the slab is subjected to the critical damping until it stops vibrating, then the first cushion layer is removed and the next loading step can be applied;

5. The fifth step is similar to the second one concerning the boulders, the corresponding cushion layers, and their stoppers. The calculation is made as the second boulder is subjected to its initial velocity. The global damping ratio is again set to be 1.5% during this step;

6. When the slab is subjected to more than two impacts, steps 2 to 4 are repeated for further impacts, and the same procedure is applied until the slab is loaded to its final impact loading. The slab is subjected to the critical damping after every impact.
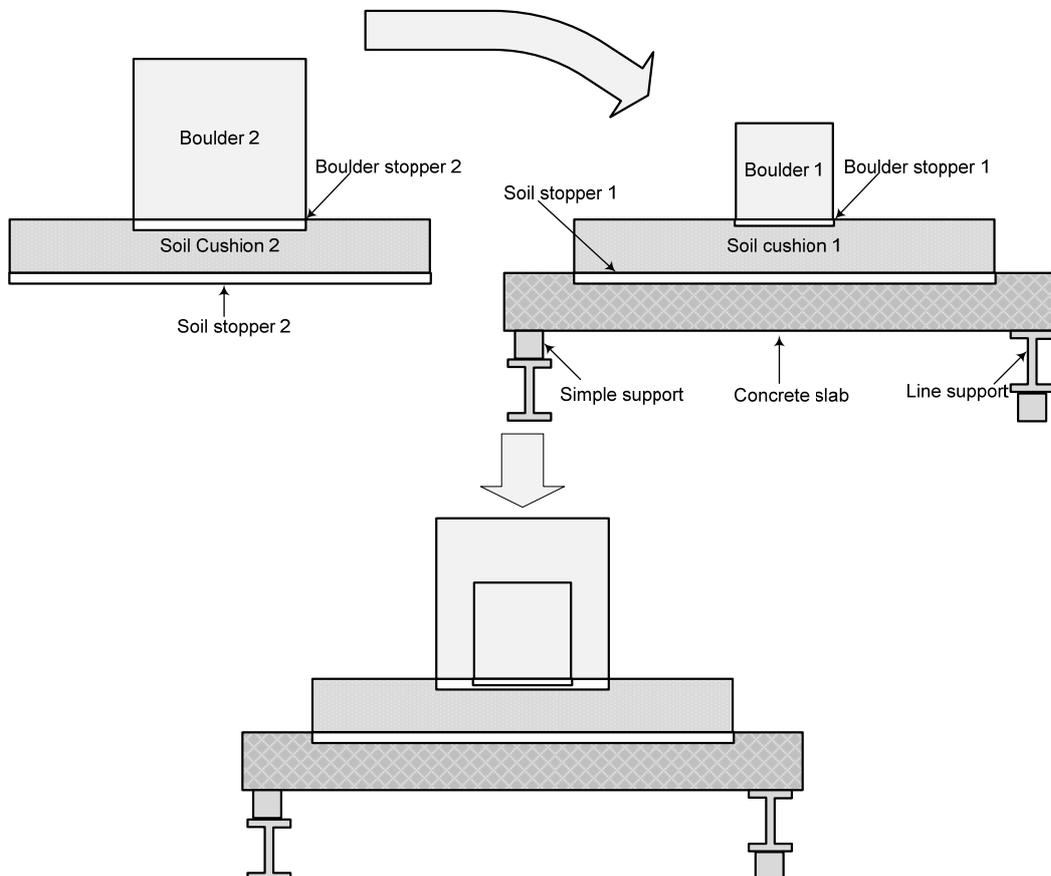
Figure 4-3: Modeling two consecutive impacts on a slab

Figure 4-3 shows the application of the consecutive impact simulation method developed to model two consecutive impacts on a slab. As shown in the figure, there are two boulders, two boulder stoppers, two layers of soil cushion, and two soil stoppers set at the same location.

4.1.3 Results

4.1.3.1 Single impact loading

A comparison between the reaction force time histories for the finite element and test results for impact B1 are shown in Figure 4-4 a. The results obtained from finite element simulation match the shape of the measured total reaction forces at the load cells and the time duration of the impact is similar to the experiments. The experimental data was filtered by a Bessel low-pass filter with a cut off frequency of 150 Hz, and therefore is strongly smoothed. The curve obtained from finite element analysis is also smoothened using the Bessel low-pass filter (Appendix C1) for a better comparison as represented in the figure. The maximum slab deflection under impact B1 at the longer span of the slab, between the two simple supports (Figure 4-4 b) shows that the finite element results match the shape of the impact time history measured by video camera, but the maximum value of the deflection obtained from analysis is higher than the one measured. This may imply that the stiffness of the slab modeled is lower than the experiment. On the other hand, the experimental measures of deflection are at 5 ms time intervals and may underestimate the actual deflection of the slab.

a)
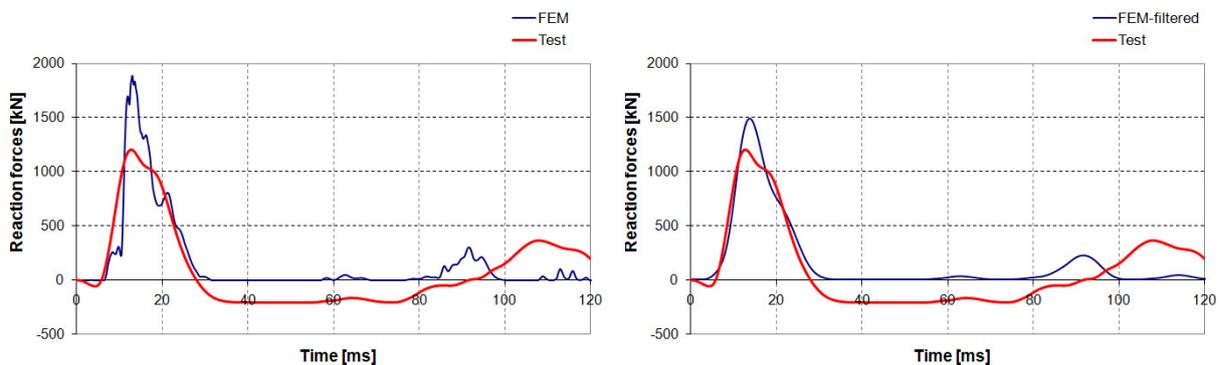
b)

Figure 4-4: Comparison between results for impact B1 (E = 39 kJ): a) reaction force time histories, and b) slab deflection time histories at the longer span

The reaction force time histories obtained from finite element analysis are displayed in Figure 4-5 for each of the three impacts on the shear reinforced sla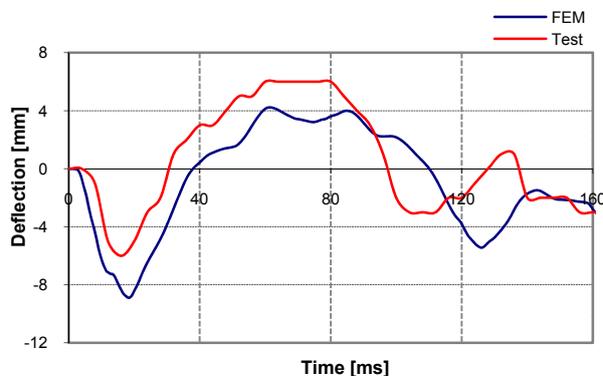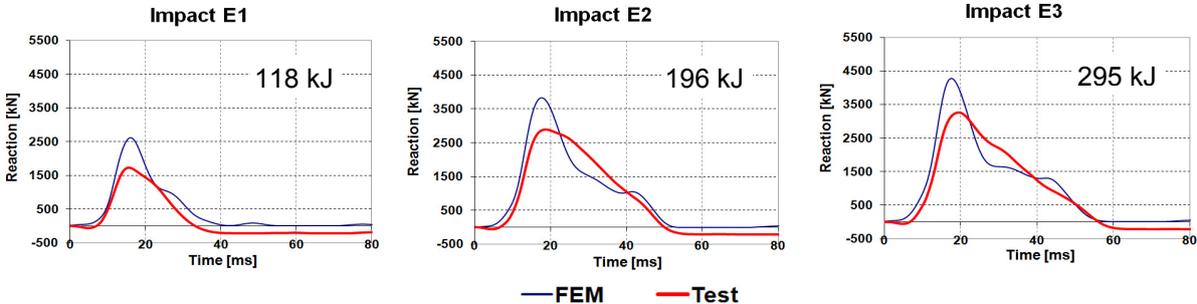bs. The reaction force time histories follow the shape measured during the tests. The impact duration is well predicted, but the peak values of the reaction forces obtained from analysis are higher than the experimental values.

Figure 4-5: Comparison between the reaction force time histories for a slab with shear reinforcement (E series)

To study the influence of shear reinforcement on increasing the capacity of the slabs (series E), finite element results of the impacts on slabs with and without shear reinforcement are compared. These consist of a 0.35 m thick slab with shear reinforcement, and slabs having 0.35 and 0.25 m thickness without shear reinforcement.

Figure 4-6 a shows a comparison of maximum deflection load histories obtained from finite element analyses for the slabs with and without shear reinforcement at the longer span of the slab between the two simple supports. For the slab with shear reinforcement (E series), the maximum deflections due to bending under the same impact energy are reduced and the slab could eventually dissipate greater impact energy leading to more ductile behavior. The slab without shear reinforcement (B series) shows a high residual deflection and lower elastic recovery under the impact energy of 196 kJ, which lead to the slab failure. During the experiment both slabs had failed due to bending as well as excessive shear over the supports. The slab with shear reinforcement subjected to the same impact energy could sustain the impact with a higher elastic recovery; this slab failed when exposed to higher impact energy of 294 kJ. The numerical results match the shape of the deflection time histories observed during experiments (Figure 4-6 b). However, the maximum values cannot be directly compared here as the numerical simulations are carried out considering the single impact on the slab and does not consider the damage history of the slab due to the previous loading.

a)

b)
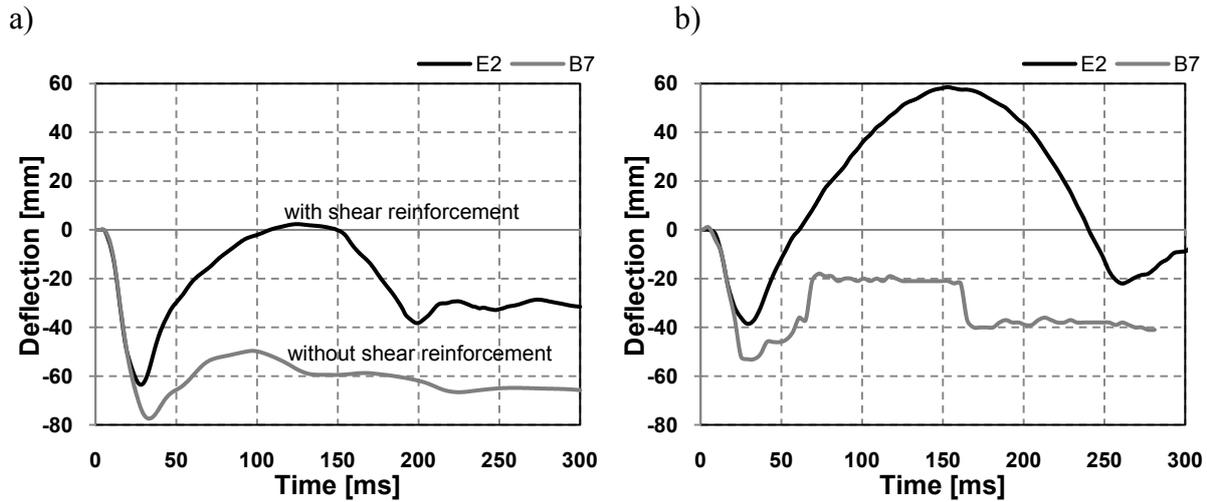
Figure 4-6: Maximum deflections in two different slabs under similar impact (E =196 kJ) a) numerical simulation of single impact, and b) experimental results (consecutive loading)

4.1.3.2 Consecutive impact loading

The applicability of the proposed method to model consecutive impact loading is discussed here by comparison between the numerical results and the experimental ones. Figure 4-7 represents the comparison of the reaction force-time histories, which are in a good agreement regarding the form of the curves, time duration of the reaction forces, and the peak values. The peak values show a larger difference for impacts B3, which gives about 45% relative error. The average relative error of the peak value for other six tests amounts to 23%.
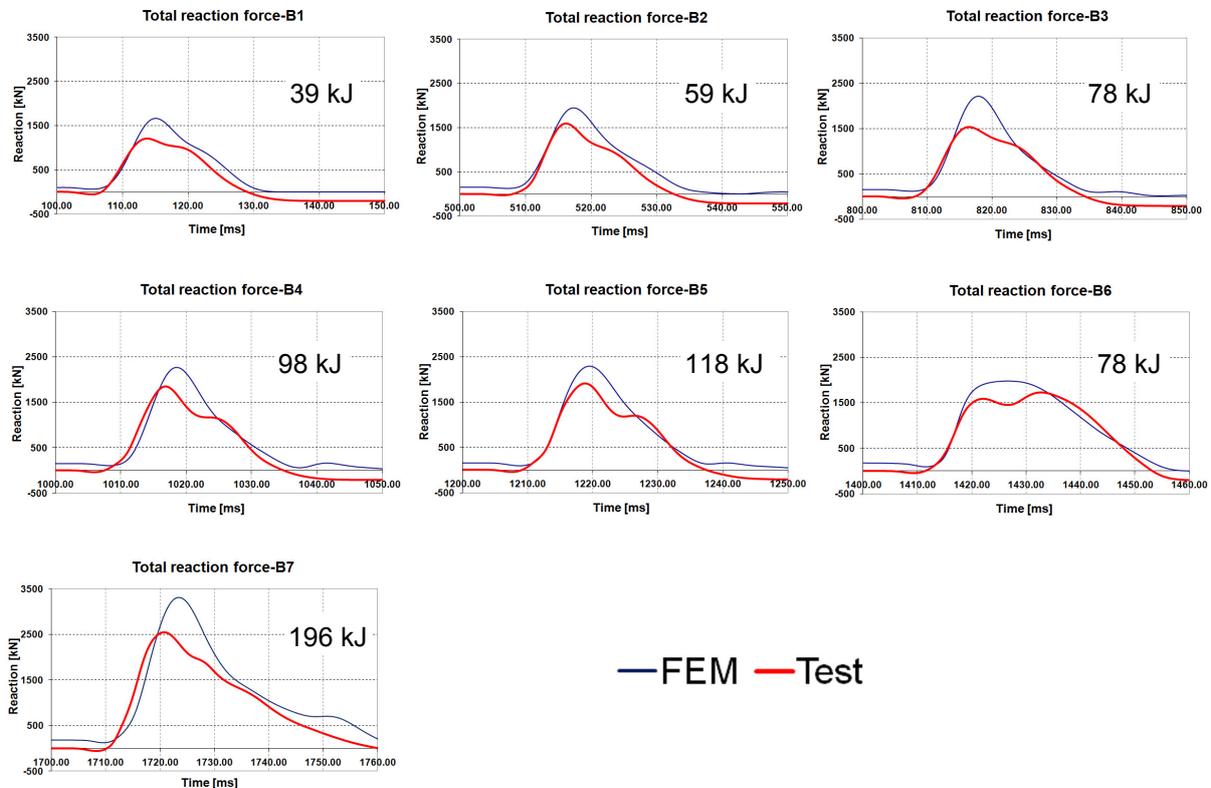
Figure 4-7: Comparison between reaction force time histories for all tests in the B series

Figure 4-8 shows the comparison between the final crack pattern after impacts B1-B6 (the slab failed subjected to impact B7 during the experiment) obtained from finite element

47

analysis with those observed during the experiment (Schellenberg et al. 2008). The line supported sides are depicted at the top edge in the figures.

The crack patterns observed at the bottom surface of the slab during the experiments are compared to the distribution of the 1st principal tensile stresses obtained from the simulations. The contours in light color show the stresses small are enough to be considered as zero. These may refer to elements that are fully cracked or are subjected to no significant stresses (Kishi et al. 2009). The cracks are formed under the impact zone during impact B1. Finite element results for this impact show more cracking than the experiments. During impact B2, the cracks propagate towards the edges between two single supports and the span between the line and single supports. A few shear cracks are formed above the supports. For impacts B3 to B6, the number of bending cracks and shear cracks above the supports increases at each impact. The slab is cracked extensively during impact B7. The finite element results show relatively good agreement with the experimental ones except for impact B1.
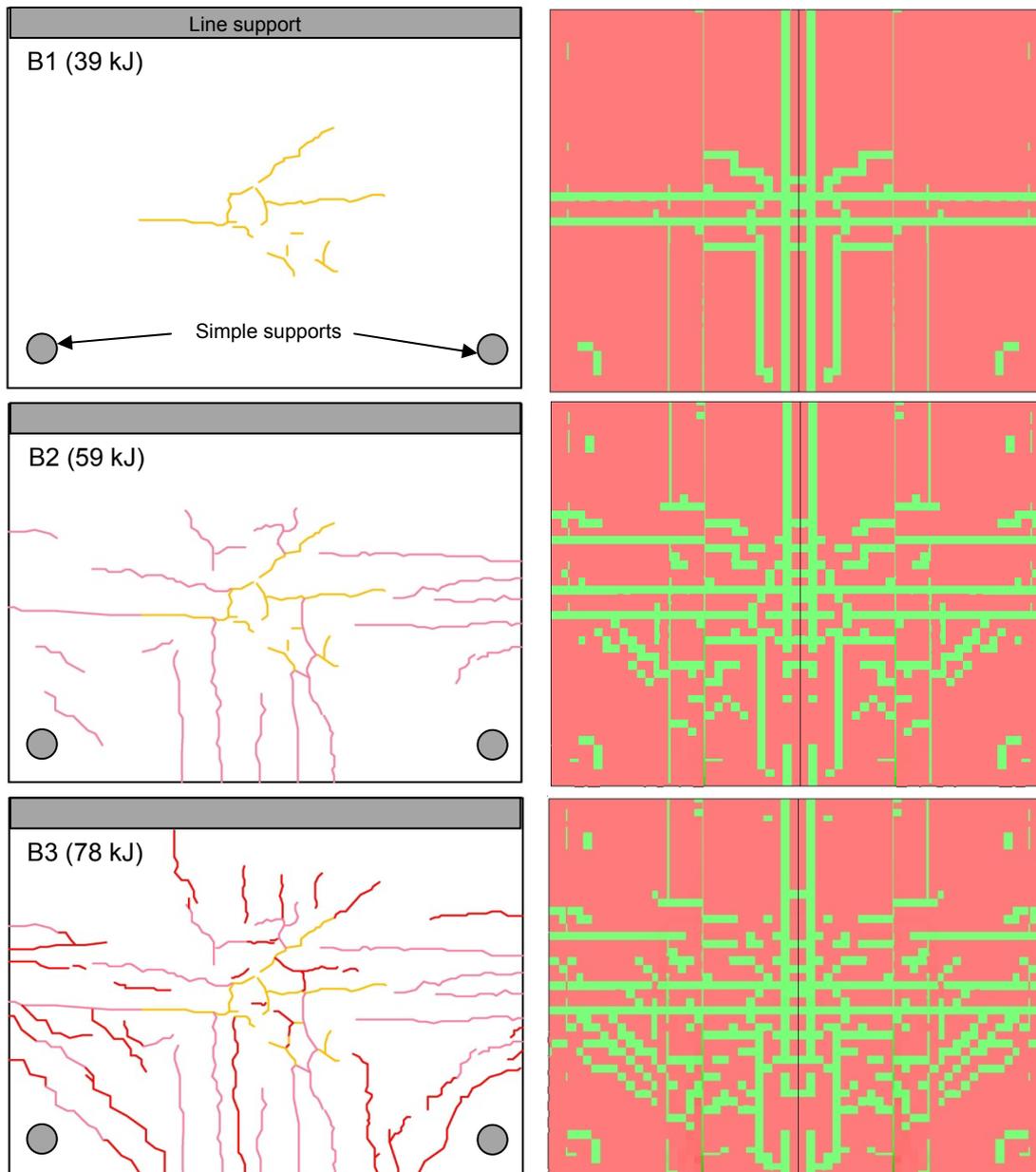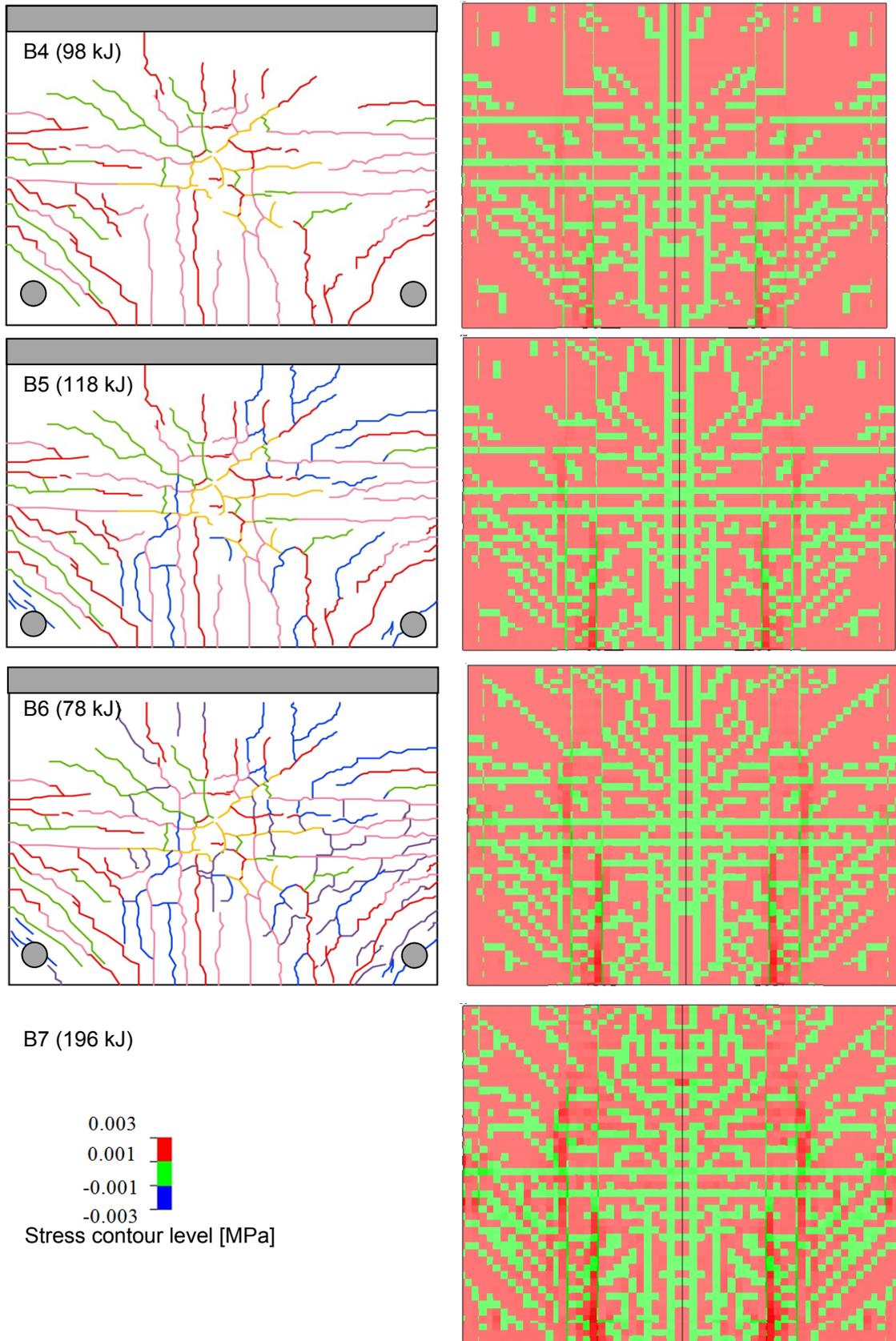
Figure 4-8: Comparison of crack patterns in the bottom surface of the slab for series B

Figure 4-9 is a graphical representation of the reinforcement strains at the center of the slab in the direction of both the larger and the shorter span, and maximum slab deflections at the center of the free edge of the slab between two simple supports, obtained from analysis and

measured during the experiment. The numerical results for reinforcement strains vary on average about 23% from the experimental ones. However, the experimental measures using strain gauges may not be very accurate due to the cracking of the concrete. The maximum slab deflections obtained from analysis are in a very close agreement with the experimental measurements.
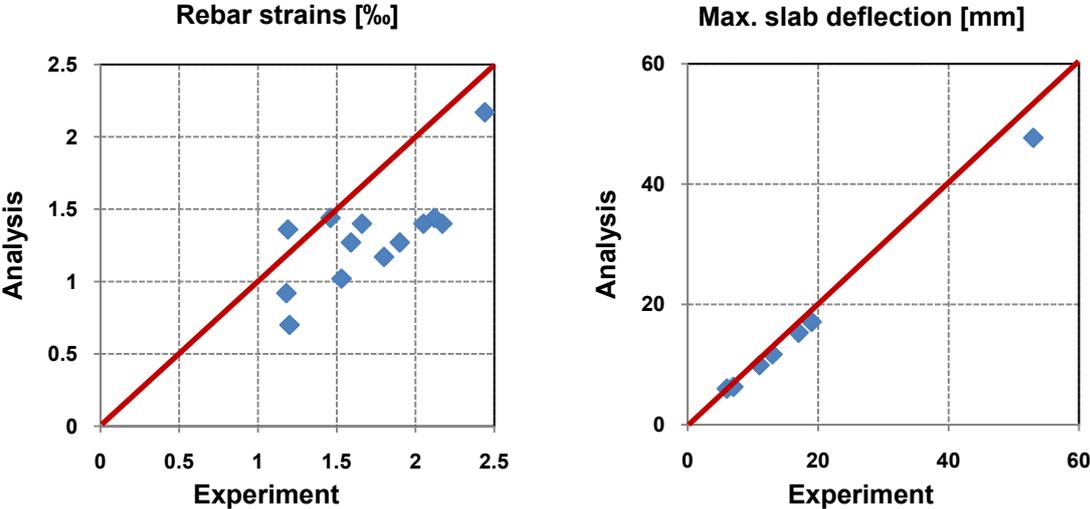
Figure 4-9: Comparison of slab response values for series B

The comparison of the penetration depth of the boulder into the soil for all seven impacts as shown in Table 5-5 provides a good agreement to experiments.

Nodal displacement vectors of soil after impact B1 and B7 as shown in Figure 4-10 are used to understand the response of the cushion material to the boulder impact. The sizes of the boulder used for B1 and B7 are 700 and 1200 mm, respectively, and the soil layer has a thickness of 400 mm. The slab and the rest of the structure beneath the soil cushion are not shown in this figure.

The displacement vectors for B1 show a combined uniaxial compression and shear behavior, where compression is observed below the boulder and the soil has moved to the side developing a shear surface. For impact B7, the behavior is governed mainly by compression below the boulder. Since the boundary conditions at two opposed edges of the slab are different, the soil is displaced less on the side where the slab is supported continuously on the girder.
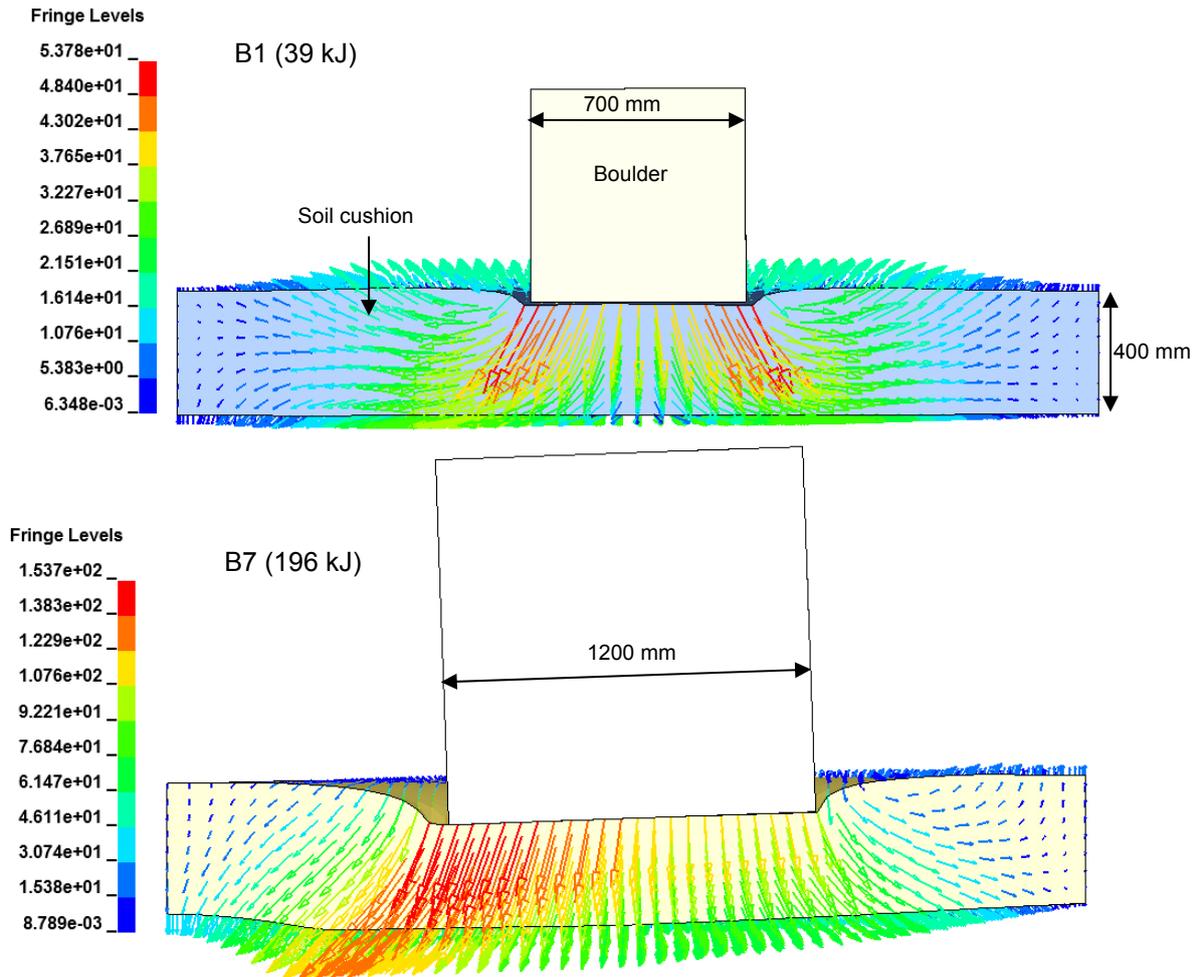
Figure 4-10: Maximum displacements [mm] in soil during impacts B1 and B7

4.2 Prediction of punching failure

4.2.1 Test description

One of the punching impact tests carried out in Japan, which is explained in Section 2.1.2, is modeled using finite elements. The experimental setup is shown in Figure 2-4 a. The impacting body had a diameter of 0.15 m and was subjected to a velocity of 6 m/s.

Initially, the impact on a slab without a cushion layer is being considered in order to explore the applicability of the finite element method in modeling punching behavior. Since, the cushion layer usually distributes the impact on a larger area, the local capacity for punching failure increases.

4.2.2 Discretization and finite element model

Symmetrical conditions of loading cell, specimen, and support conditions allow only a quarter of the slab to be modeled. Figure 4-11 shows the finite element model of the experiment. The loading setup and the support conditions are modeled to represent the experimental setup.

A 25 mm mesh size is used for the slab. Impact loads are modeled as single impacts. A concrete compressive strength of 26.2 MPa, and a tensile strength of 2.6 MPa are used for this

model. The yield strength of steel is 423 MPa. The cylindrical impactor with a tapered base is modeled as an elastic material with a Young modulus of 206 GPa.
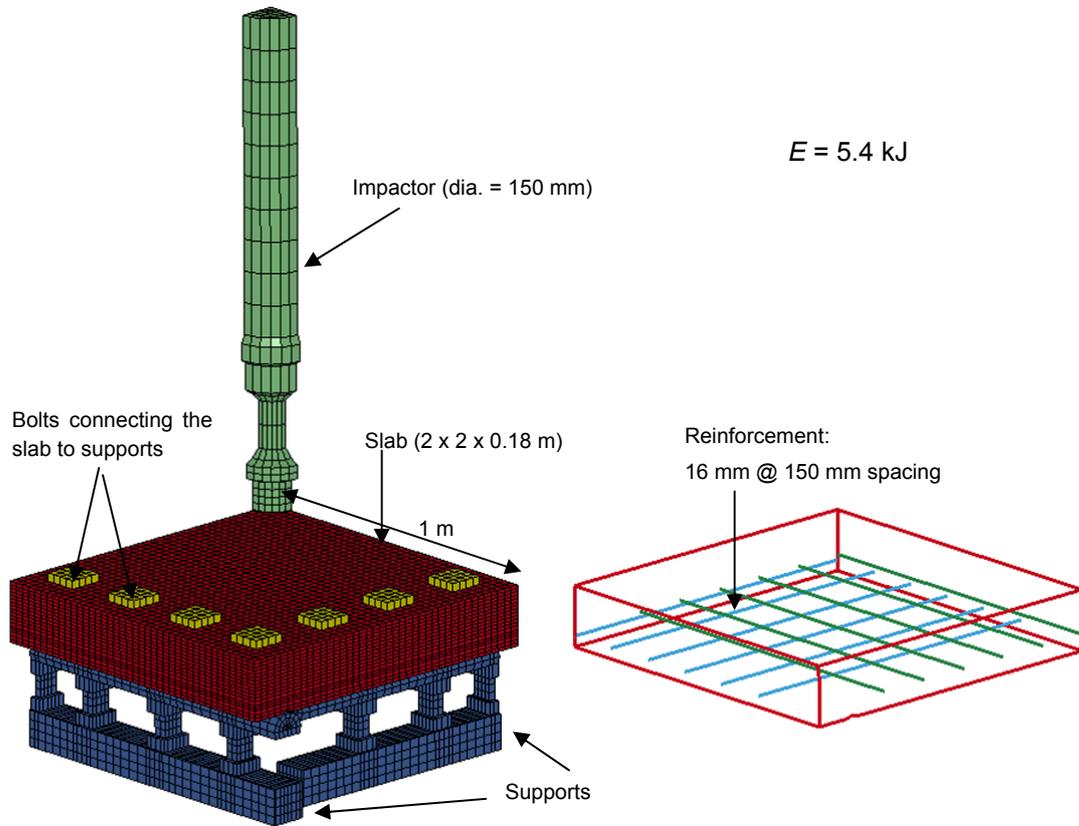
Figure 4-11: Punching impact test by Kishi et al. (2008): a) Finite element mesh of the slab, and b) reinforcement layout

4.2.3 Results

The impact force time histories, reaction force time histories, and displacement time histories obtained from the experiment as well as the finite element simulations are compared (Figure 4-12). The reaction forces were measured at the load cells placed below the line supports during the experiment. As observed from the diagrams, the impact force histories, the reaction force histories, and the displacement time histories below the impact zone show good agreement with the experimental data. The impact force was measured by using a load cell within the impacting boulder.
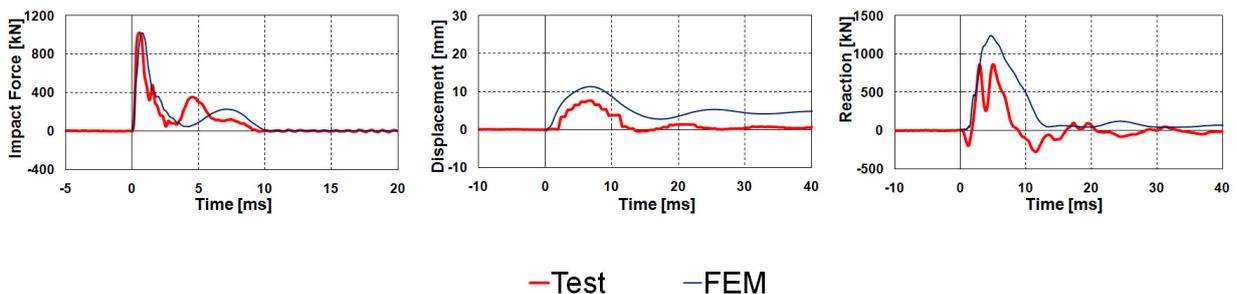
Figure 4-12: Impact force history, reaction force history, and displacement history for a slab without a cushion (E = 5.4 kJ)

The crack patterns observed in the slab cross section and its bottom surface during the experiment are compared to those obtained from simulations (Figure 4-13). The cracks are shown using the contour in light color, which are the stresses small enough to be considered as zero. The punching cracks at the soffit of the slab match well with the patterns during the experiments. The cross sectional cracks cannot be observed using finite element analysis, since the section at this location is fully cracked. The shape of the diagonal crack, however, follows the formation of cracks during the experiment.

Cross section

Lower surface
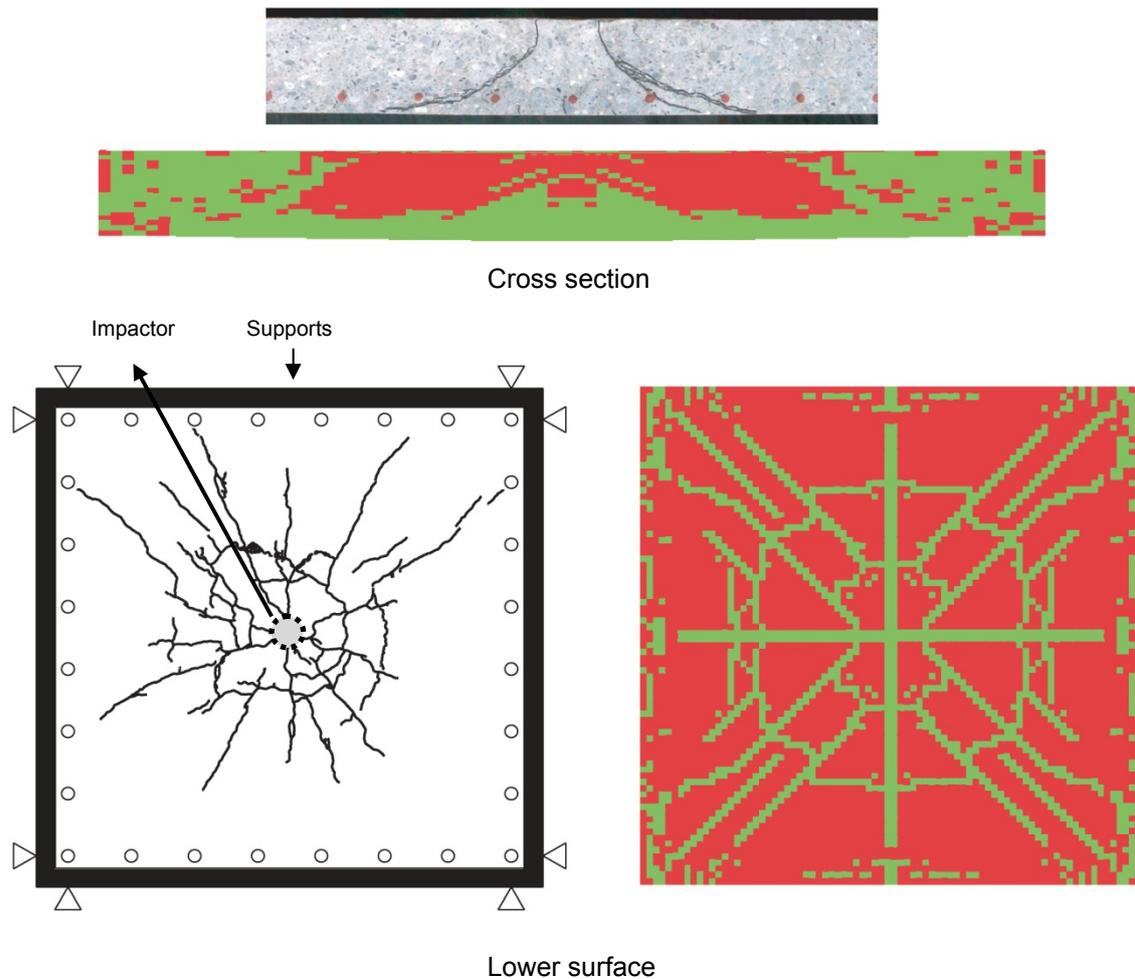
Figure 4-13: Cracks in cross section, and bottom surface of the slab

It was observed for concrete slabs, when different mesh sizes were analyzed, that elements of about 25-50 mm in size give a reasonable agreement to the experiments (see Section 5.2).

4.3 Failure criterion for finite element analysis

Validation of the finite element results with the experimental data provided a benchmark for the analyses, which are extended beyond the range of experiments in the following chapters. In order to set a criterion to attribute failure using elastic-plastic finite element analysis, the residual deflections in the slabs obtained from finite element analysis of the slab experiments have been studied further. The maximum deflections for three different types of slabs used in the experimental series conducted by Schellenberg (2007), as shown in Figure 4-14 are

obtained from finite element analyses of the impacts, which led to failure of slabs during the tests.
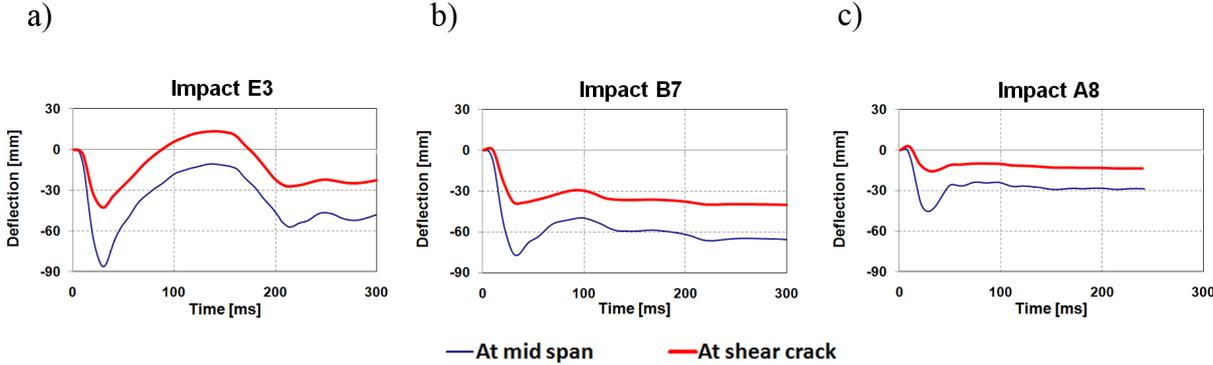
Figure 4-14. Maximum deflections at ultimate load at mid span and in the shear zone for a) slab E b) slab B and c) slab A

Based on the results obtained, the slab that has not been reinforced for shear can be considered to have failed when the residual deflection is larger than 80% of the peak deflection of the slab under the impact, at any location within the slab. The limit that is used to define failure in a shear reinforced slab is considered to be 60% of the peak deflection. In other terms, the failure is considered to be associated with an elastic rebound of less than 20% for the slabs without shear reinforcement. Low elastic rebound can refer to a state in which the slab is cracked and the reinforcement has yielded. The results, summarized in terms of percentage elastic recovery of the slabs, are shown in Table 4-2.

Table 4-2: Percentage of elastic recovery of the slab deflections at failure

Impact	At mid-span [%]	At "shear crack" [%]
E3	40	41
B7	17	0
A8	36	18

This can also be used to account for the failure mode of the slabs. As cracks occurred close to the single supports during the experiment due to shear, the residual deflections of the slab at the location where these "shear cracks" developed have also been plotted and studied. The ratio of residual deflection to the initial peak value at failure for the slab with shear reinforcement is almost the same at mid-span as in the shear zone. This can indicate that the slab has reached failure at both of the bending and shear zones. This ratio is higher for shear zones compared to mid-span for the slabs without shear reinforcement, so there is a small or no elastic recovery in the shear zone. Therefore, it can be concluded that shear was the governing failure mode for these slabs. However, slab B has also reached failure in the bending zone (mid-span), showing an elastic recovery of less than 20%.

The concept of elastic recovery of the slab is illustrated in Figure 4-15 using a typical deflection time history at any location of a slab, where *RD*, *MD*, and *ER* refer to residual deflection, maximum deflection, and elastic rebound, respectively.

Elastic recovery

$$ER = 1 - \frac{RD}{MD} \geq 0$$

Failure criterion:

ER <= 20% for slab without shear reinforcement
ER <= 40% for slab with shear reinforcement
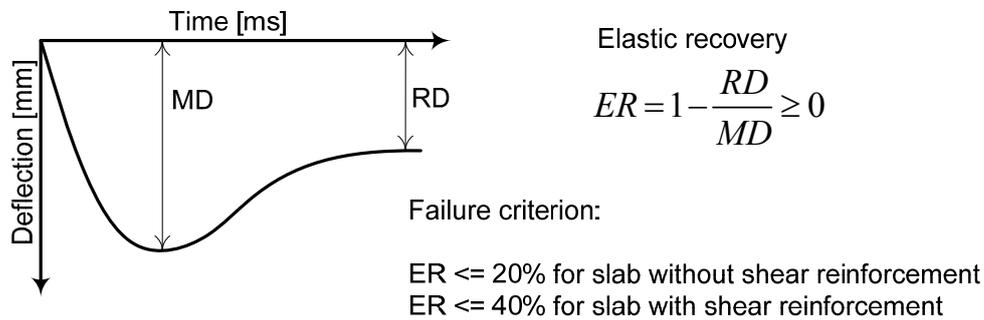
Figure 4-15: Failure criterion used in finite element analysis

The elastic recovery vs. the maximum impact force transmitted through the soil to the slab for experimental series B, as demonstrated in Figure 4-16, shows that the elastic recovery reduces with increase in the impact force until it drops below the *ER* failure criterion. Therefore, such a curve can be used to demonstrate the performance of a slab or gallery subjected to different impact forces. The curve is the plot of finite element results for impacts B1 through B7 with the exception of impact B6. Impact B6 is shown as a single point in this plot, since the impact energy and thus the impact force was lower than for impact B5. The elastic recovery is also shown vs. the input impact energy. The failure criterion is shown as a dotted line in these diagrams.
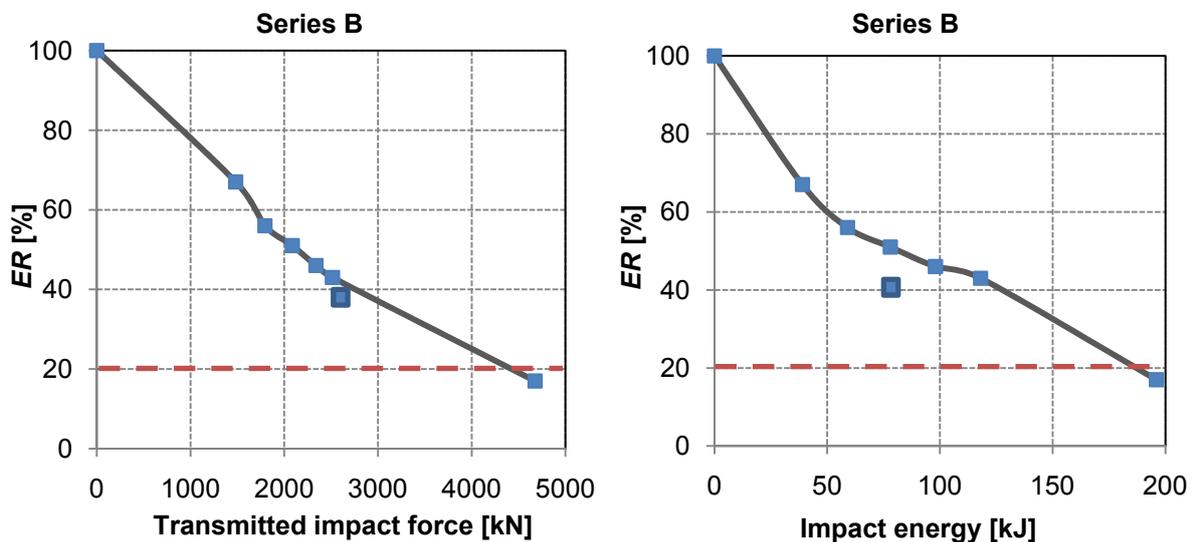
Figure 4-16: Slab performance diagram for series B

Failure is initiated at any point in the slab where the elastic rebound falls below the chosen criterion. The values of *ER* along the simply supported edge of slab B is shown in Figure 4-17. Comparison is made for the 800 kg boulder falling from 5 m and 25 m, respectively. It is seen from the figure that the mid-span is the critical for the section here. This means that bending behavior governs these impacts. The sudden change in the slope of the curve may indicate that the shear forces at the given location lead to the failure. During the experiments the slab was only in contact with the supports and was not restrained from bouncing up. The

ER values are set to zero at the supports and they are only measured from the points next to the supports where deflections occurred in the direction of loading.
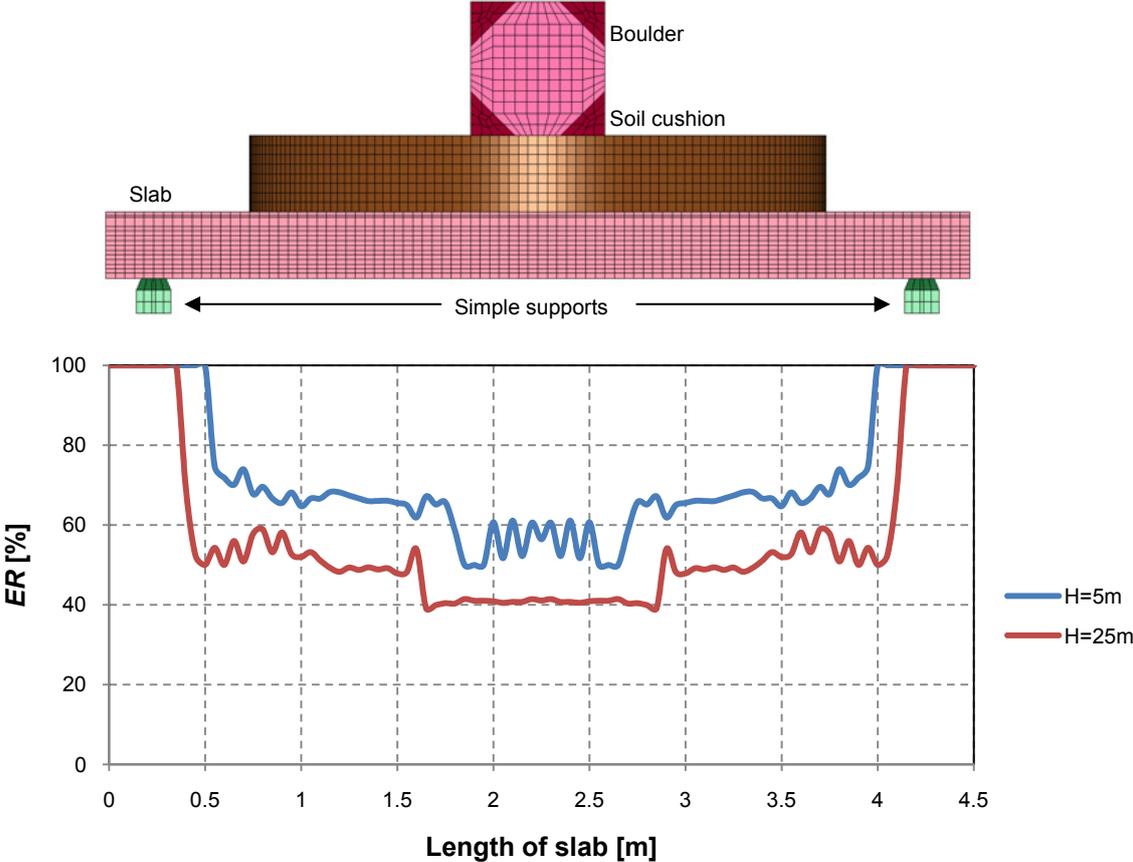
Figure 4-17: Plot of elastic recovery along the length between the two simple supports of the slab for series B

A similar approach can be implemented, when using finite element analysis, to identify the punching failure mode in slabs. The ratio of residual deflection to peak deflection or the elastic rebound of the slabs can be compared at different locations in a slab to identify the governing failure mode using finite element analysis. However, if the critical section for punching and bending is at the same location, it is possible to identify the failure but not the governing failure mode. This criterion will be used in the following chapters to account for failure in the slab, while extending the simulations beyond the range of the experiments carried out. Looking at the deflection histories obtained from some other experiments (Yamaguchi et al. 2010), the criterion seems reasonable, and can be investigated further by conducting more experiments.

5 Sensitivity analyses and extrapolations

Sensitivity studies using finite element analysis and extrapolation of numerical analysis beyond the range of the physical experiments performed are presented to study the variation of results with respect to the input data. Finite element analyses can provide an extension of the tests performed as well as a basis for acquiring proper assumptions for the model, but their applicability needs to be validated in comparison with experimental data. Sensitivity analyses are carried out in order to provide a basis to decide on the appropriate input parameters for finite element models, such as material models and mesh sizes. In addition, the influence of the boulder shape, reinforcement behavior, and consecutive impact loading on the response of slabs and different influences on the response of soil layers is investigated. The selection of the test used as reference for each case of sensitivity analysis and extrapolations is based on the influence of the parameter studied.

5.1 Material model for concrete

A von Mises material model is adapted for concrete (Section 3.3.1) and is compared to the Drucker-Prager yield criterion. Moreover, the influence of considering strain rate effects on the capacity of the structure is investigated. The aim here was to adapt a simple but still effective material model for concrete that can provide good results in comparison with the experimental data. Sophisticated material models, which may produce more accurate results, have not been a focus of this study and are not considered.

5.1.1 Drucker-Prager yield criterion

Drucker and Prager extended the von Mises criterion to incorporate the effect of hydrostatic pressure on the shear resistance of the material (Drucker & Prager 1952). The criterion was originally introduced to deal with the plastic deformation of soils.

The yield criterion f takes the following form:

$$f = \sqrt{J_2} - \alpha_M J_1 = k_M \tag{5-1}$$

where J_1 and J_2 are stress invariants; α_M and k_M are material constants. In a three dimensional principal-stress space, the constants are obtained as:

$$\alpha_M = \frac{2\sin\varphi}{\sqrt{3}(3-\sin\varphi)} \qquad k_M = \frac{6c\cos\varphi}{\sqrt{3}(3-\sin\varphi)} \tag{5-2}$$

φ and c are the angle of internal friction and the cohesion, respectively. A detailed explanation of the model can be found in Drucker & Prager (1952), and Chen (1982).

5.1.2 Strain rate effect

The strain rate during a falling-weight impact is observed to be between 10^{-3} and 10^{-2} s^{-1} for concrete, and from 10^{-2} to 10^{-1} s^{-1} for reinforcement, based on the experimental results of

Schellenberg (2008). The values are shown in comparison to the different strain rates for a range of impact loadings (Schmidt-Hurtienne, 2001) in Figure 5-1.
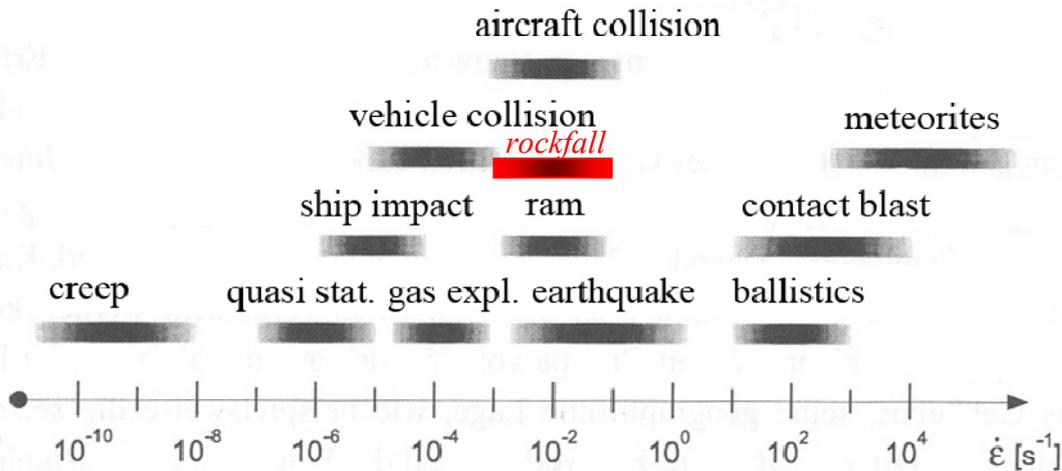
Figure 5-1: Comparison of rockfall strain rates (in italic) with typical strain rates for different impacts, as classified by Schmidt-Hurtienne (2001)

The influence of strain rate is studied by applying the provisions of the FIB model code (FIB 2010) to investigate the necessity of considering the effect for modeling the impact.

Impact B1 is used for the parametric study of the concrete material model, since cracking of concrete occurred during this impact. The input strain rate is calculated based on preliminary finite element results observed for concrete during impact for B1. The maximum strain rate in the concrete obtained from a first impact simulation was $0.023 \ s^{-1}$. This value is then used as the input strain rate to modify the material properties of concrete for impact B1 using von-Mises yield criterion, meaning that the entire slab is modified using concrete properties, for this particular strain rate.

According to the code, the compressive strength of concrete under high rates of loading may be estimated as:

$$\frac{f_{c,imp,k}}{f_{cm}} = \left[\frac{\dot{\varepsilon}_c}{\dot{\varepsilon}_{c0}} \right]^{0.014} \qquad \text{for} \qquad \dot{\varepsilon}_c \leq 30 s^{-1} \qquad (5\text{-}3)$$

The tensile strength may be estimated from:

$$\frac{f_{ct,imp,k}}{f_{ctm}} = \left[\frac{\dot{\varepsilon}_{ct}}{\dot{\varepsilon}_{ct0}} \right]^{0.018} \qquad \text{for} \qquad \dot{\varepsilon}_{ct} \leq 10 s^{-1} \qquad (5\text{-}4)$$

and the effect of strain rate on the modulus of elasticity may be estimated from:

$$\frac{E_{c,imp}}{E_c} = \left[\frac{\dot{\varepsilon}_c}{\dot{\varepsilon}_{c0}} \right]^{0.026} \qquad (5\text{-}5)$$

with $\quad \dot{\varepsilon}_{c0} \leq 30 \cdot 10^{-6} s^{-1} \qquad$ for compression

and $\quad \dot{\varepsilon}_{ct0} \leq 1 \cdot 10^{-6} s^{-1}$ for tension

5.1.3 Results and comparison

The comparison of deflections for impact B1 obtained by applying the von Mises and the Drucker-Prager yield criteria, as well as those obtained considering strain rate effects for concrete, are shown in Table 5-1. The deflections and residual deflections are compared in the bending zone between the two single supports, since the deflections of the concrete slab have been the highest at this location.

The maximum deflections and maximum residual deflections in the slabs for the three models are close to each other and differ slightly from the experimental data obtained by a highspeed camera. The experimental data was measured at 5 ms time interval and may underestimate the maximum deflection. The values for the elastic recovery (*ER*) of the slab is compared in order to investigate its response. The behavior of the slab using all three material models has been softer compared to the value seen during the experiment. The simulation results not considering the strain rate effets are conservative and on a safer side, since they predict the failure earlier. Therefore, the resistances considering the strain rate effects are higher and the effect of strain rate is not taken into consideration. This approach is simplified and a strain rate dependent material model would be required for a deeper investigation of strain rate effects on modeling.

Table 5-1: Comparison of results between the experimental and numerical prediction with von Mises, Drucker-Prager yield criteria, and the strain rate effect

	Experiment	von Mises	Drucker-Prager	Strain rate effect
Max. deflection [mm]	6	9.3	9.3	7.6
Residual deflection [mm]	1	3.1	4.0	2.2
Elastic recovery [%]	83	67	57	71

Crack patterns obtained from finite element analyses (contours of zero stresses) using the von Mises criterion, the Drucker-Prager criterion, and the strain rate effects are compared to those observed during the experiment (Figure 5-2). The crack patterns obtained from the von Mises and Drucker-Prager criteria are similar to each other. Fewer cracks are obtained by modifying the strength based on strain rate effects, as expected. All three cases show more cracking than observed during the experiments, thus the slab exhibits less strength during the numerical simulations. The slab modeled using von Mises' criterion shows more cracking than when the slab was modeled using the consecutive impact method (Figure 4-8). The slab was first subjected to its self-weight during the consecutive impact load and then subjected to an impact load. The slab modeled here by single impact loading was subjected simultaneously to the impact loading and gravity due to the self weight, which is the reason for the greater number of cracks seen in this case. However, the damage to the slab is overestimated by assuming the slab to crack earlier than in the real situation, which means the analysis results are conservative.

a)

b)

c)

d)
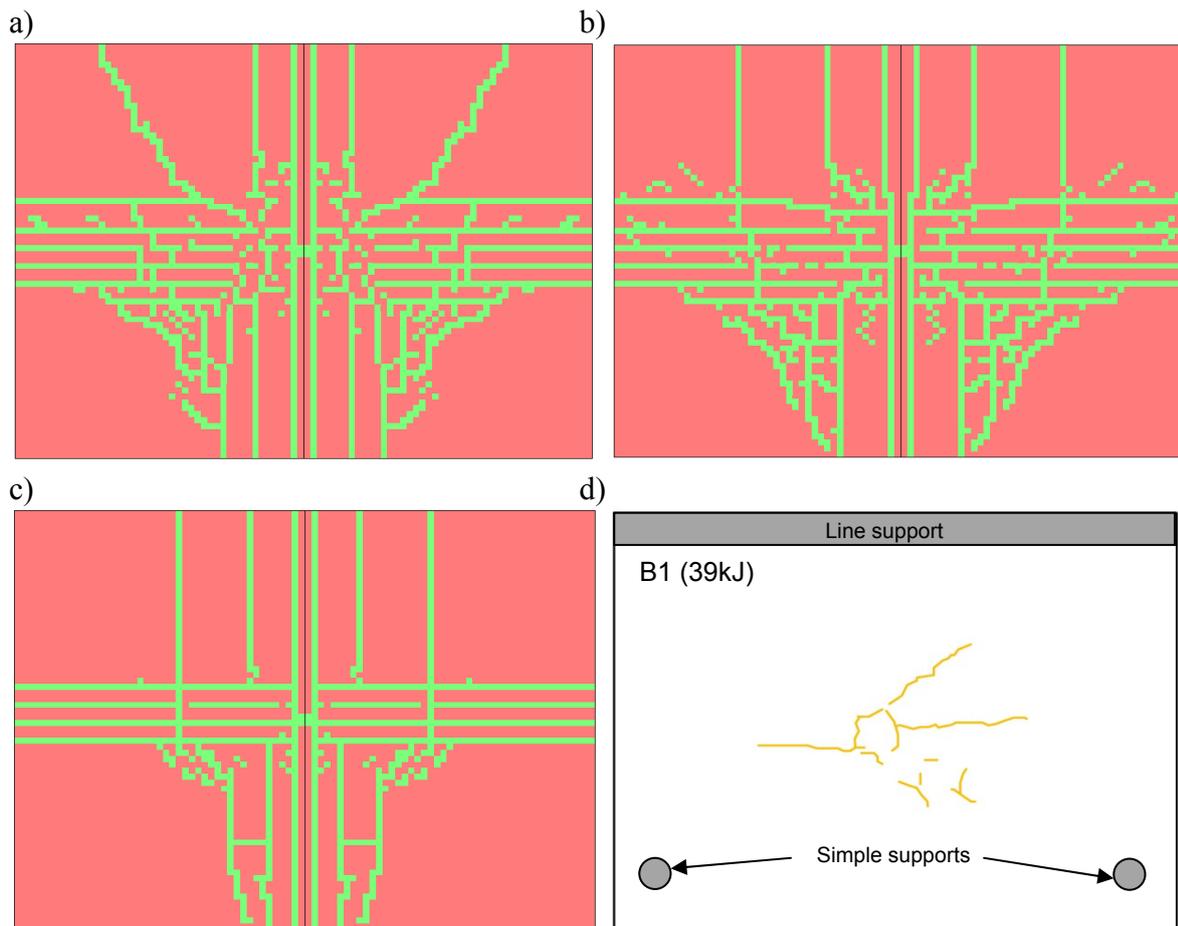
Figure 5-2: Crack patterns a) von Mises criterion b) Drucker-Prager criterion c) strain rate effect d) experiment (Schellenberg 2008)

In addition to the investigation of different material models for concrete on the finite element results, the influences of the concrete properties using von Mises criterion on the results are investigated here. This includes the tensile strength f_{ctm} and the Young's modulus of concrete E_c. The comparison of deflections for impact B1 is shown in Table 5-2. The initial values of f_{ctm} and E_c are 3.5 MPa, and 42'000 MPa, respectively. The values are modified for $\pm$ 10% and the new results using the modified values are shown.

The maximum deflection remained the same for E_c (-10%). However, it is important to look at residual deflections with reference to the dynamic behavior of the slab. The residual deflections become higher in this case, since the slab is softer and the elastic recovery of the slab is reduced. The *ER* becomes higher for E_c (+10%) since the slab behaves more stiffly.

Table 5-2: Sensitivity analysis for the concrete material model

	Max. deflection		Residual deflection		ER [%]	
	[mm]	Δ [%]	[mm]	Δ [%]	[%]	Δ [%]
Reference value	9.3	--	3.1	--	67	--
f_{ctm} (+10%)	8.87	-5	2.8	-10	68	1
f_{ctm} (-10%)	10.4	12	3.9	23	63	-4
E_c (+10%)	9.9	6	3.1	0	69	3
E_c (-10%)	9.3	0	4	29	57	-15

5.2 Mesh size for concrete

The mesh size sensitivity of the model is studied with cubic solid elements with a side length of 25, 50, and 150 mm for the in-plane (along the surface) mesh. The model of impact B1 is analyzed using these three different mesh sizes. In addition, two mesh sizes are studied with respect to the thickness. Impact B1 is modeled using 25 and 50 mm thick elements for the out-of-plane mesh (along the cross section).

Comparisons of deflections obtained using the different mesh sizes to the experimental measurements are shown in Table 5-3. All residual deflections obtained from finite element analysis are higher than the experimental values indicating that the slab cracks earlier than in the experiments. Comparing the elastic recovery of the slab obtained from the analysis to the experiments, it is seen that the closest agreement is achieved for the slab using an in-plane mesh of 25 and 50 mm. The out-of-plane mesh size of 25 mm is used, while considering in-plane mesh sizes. Both, maximum and residual deflections decrease with the increase in the mesh size, since the larger sizes of elements lead to a stiffer behavior.

Table 5-3: Comparison between deflections obtained using different mesh sizes for impact B1

In-plane mesh size:	Experiment	25 mm	50 mm	150 mm
Max deflection [mm]	6	10.9	9.8	6.9
Residual deflection [mm]	1	4	3.4	3.5
Elastic recovery [%]	83	63	65	49
Out-of plane mesh size:	**Experiment**	**25 mm**	**50 mm**	
Max deflection [mm]	6	9.8	9.3	
Residual deflection [mm]	1	3.4	3.1	
Elastic recovery [%]	83	65	66	

While considering the out-of-plane mesh sizes, an in-plane mesh size of 50 mm is used. The deflections and elastic recoveries using an out-of-plane mesh of 25 and 50 mm have been rather similar. However, using a larger out-of-plane mesh size, it is difficult to get a good distribution of shear forces and cracks. The results obtained emphasize the fact that modeling of reinforced concrete slabs is sensitive to the mesh size selection and the results of the displacements obtained may vary considerably. This underlines the need of a mesh size independent method for the analyses. An equivalent fracture energy concept as proposed by Kishi & Bhatti (2010) or similar approaches can be used to eliminate the mesh size sensitivity. The approach uses equivalent tensile fracture energy for elements, regardless of their size. A reference element size of between 25 and 50 mm can be used for applying such a concept.

The in-plane mesh size effects the location and the distribution of the cracks along the surface of the slab, while the out-of-plane mesh size influences the development of the crack in the cross section. A better distribution of the crack pattern can be obtained in the cross section of the slab if finer out-of-plane mesh is used, especially for smaller slab thickness. The slab investigated here had a thickness of 350 mm and the selection of out-of-plane mesh did not have a big influence on the results. A cross sectional mesh size of smaller than 25 mm may be chosen when the thickness of the slab is small (e.g. less than 200 mm).

5.3 Material model for reinforcement

The sensitivity analysis is performed, varying the yield strength f_s and the hardening modulus H_y, with initial values of 550 MPa, and 1% of the elastic modulus of steel, respectively (see Figure 3-1 b). The influences of these parameters on finite element results are shown in Table 5-4. Slab B is subjected to the impact of an 800 kg boulder falling from a height of 25 m for this study. Based on finite element results, it is concluded that the reinforcement reached yielding during impact B5 for the first time, where the 800 kg boulder fell onto the slab from a height of 15 m (118 kJ). To study the influence of the reinforcement material model on the slab behavior, it is important to model the post yielding behavior of the slab. Therefore, a falling height of 25 m is chosen here. The initial maximum rebar stress is 560 MPa, which exceeds the yield stress by 10 MPa. Increasing the yield stress by 10% (to 605 MPa), it is seen that the maximum stress in a rebar exceeds the increased yield stress by 5 MPa. If the yield stress is reduced by 10% (to 495 MPa), the maximum stress in a rebar exceeds the decreased yield stress by 15 MPa. The maximum deflections in the slab are not affected much by small changes in yield stress and hardening.

Table 5-4: Sensitivity analysis for the reinforcement material model (E = 200 kJ)

	Max. rebar stress		Max. reaction force		Max. deflection	
	[MPa]	Δ [%]	[kN]	Δ [%]	[mm]	Δ [%]
Reference value	560	--	3660	--	30.5	--
f_s (+10%)	610	9	3530	-4	30.4	-0.5
f_s (-10%)	510	-9	3530	-4	30.7	1
H_y = 5%	600	7	3630	-1	30.3	-1
H_y = 10%	625	12	3660	0	30.2	-1

5.4 Material model for soil

5.4.1 Elastic-plastic model

A bilinear elastic-plastic material model proposed by Muroran Institute of Technology, Japan, is used to represent the behavior of soil. The model was calibrated using one of the falling-weight impact tests carried out at Swiss Federal Institute of Technology, Lausanne (Montani 1998). Based on these calibrations, a yield strength of 1.23 MPa, an elastic modulus of 200 MPa, and a hardening modulus of 15 MPa have been obtained (Figure 5-3). However, the model is developed based on simple curve fitting and does not exhibit the physical behavior of the soil cushion.
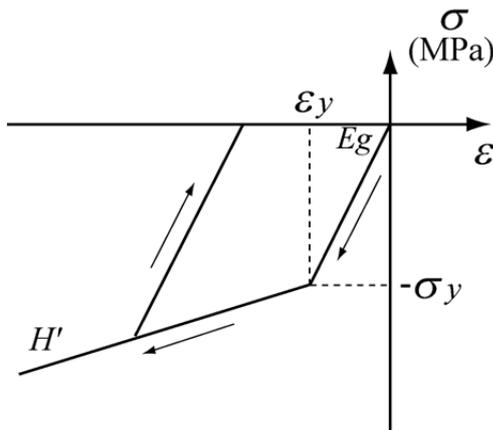
Figure 5-3: Elastic-plastic model for soil, as proposed at Muroran Institute of Technology, Japan

5.4.2 Cap hardening model

The cap hardening model as explained in Section 3.3.3 is also used to study the behavior of soil. The shape of the cap hardening model in stress strain space depends on the stress path of the elements (see Figure 3-4). A perfect plastic or a hardening curve can be expected depending on the stress path, which is the difference in comparison to the elastic-plastic curve shown in Figure 5-3. The yield strength using the cap hardening model is not a constant value.

5.4.3 Results and discussions

Results of the maximum penetration depth of the boulder into the soil obtained from both models are shown in Table 5-5 in comparison with the experimental measurements. This is the only comparison that can be made related to the soil behavior, since there were no other measurements made within the soil layer during the experiments.

Table 5-5: Maximum boulder penetration depth

Penetration depth	B1	B2	B3	B4	B5	B6	B7
Experiment [m]	0.046	0.067	0.089	0.084	0.09	0.092	0.104
Elastic-plastic model [m]	0.128	0.191	0.231	0.245	0.265	0.128	0.196
Cap hardening model [m]	0.047	0.066	0.077	0.084	0.094	0.075	0.116

The penetration depths obtained using the cap hardening model, demonstrate a reasonable agreement with the experiments with respect to the final penetration of the boulder into the soil. Therefore, this material model was adapted for modeling soil in the finite element analysis. The model represents a better agreement to the physical behavior of soil, as it considers plastic yielding as well as hardening of the material below the shear failure line in the cap region. The bilinear model on the other hand, provides a mathematical solution through curve fitting and it does not represent the physical behavior of the material in all respects.

The sensitivity analysis for the soil cap hardening model is performed varying the bulk modulus K, the failure envelope coefficient α_s, the cap surface axis ratio R, the hardening law exponent D_s, and the maximum volumetric plastic strain W, once at a time. The variations are outlined in Table 5-6. The initial values of these parameters are shown in Table 3-1. Maximum impact force and maximum transmitted force obtained from finite element analysis refer to the peak value of the impact forces and transmitted impact forces on the force time history diagram. The transmitted impact force is the total force that is transferred through the soil to the top of the slab.

As seen from the results of the sensitivity analysis, the soil bulk modulus K and the failure envelope coefficient α_s have the highest influence on the penetration depth. The plastic behavior of the cap model is governed by the value of α_s ,which depends on the angle of internal friction of soil and it refers to the slope of the shear failure line in the cap hardening model. The lower value of α_s implies that the soil reaches the shear failure at a lower value of deviatoric stress. The elastic behavior of the model is governed by the response functions K and G (which is defined here depending on K). The elastic bulk modulus K is defined as a function of the first invariant of the stress (or mean stresses) and plastic strains. The elastic shear modulus G is a function of second invariant of the deviatoric stress as well as elastic strains. The changes in the values of K and G influence the mean stresses, deviatoric stresses, and plastic strains. Therefore, the material properties of the soil should be well evaluated for

proper application of the cap hardening model. The results are not very sensitive to small changes in D_s, R, and W, respectively.

Table 5-6: Sensitivity analysis for the soil material model during impact B5 (E = 118 kJ)

	Max. penetration depth		Max. impact force		Max. transmitted force	
	[mm]	Δ [%]	[kN]	Δ [%]	[kN]	Δ [%]
Reference value	82	--	1940	--	2530	--
K (+10%)	81	-1	2020	4	2610	3
K (-10%)	86	5	1880	-3	2430	-4
α_s (+10%)	81	-1	1960	1	2530	0
α_s (-10%)	92	14	1950	0.5	2540	0.3
R (+10%)	84	2	1940	0	2500	-1
R (-10%)	81	-1	1960	1	2600	3
D_s (+10%)	84	2	1930	-0.5	2500	-1
D_s (-10%)	81	-1	1980	2	2590	2
W (+10%)	84	2	1930	-0.5	2480	-2
W (-10%)	80	-2	1980	2	2620	4

5.5 Mesh size for soil

The mesh size for soil was selected based on the mesh sizes adapted for concrete and was set to be 50 mm. This is due to the fact that the interfaces are defined to calculate the contact forces between soil and concrete. The contact forces for each segment are calculated using the penetration of the nodes of the other contacting segment. For a detailed investigation of soil behavior, however, it is recommended to carry out a mesh size sensitivity analysis for soil.

5.6 Soil response to impact

The influence of boulder shape, boulder weight, and soil depth on the behavior of a layer of soil subjected to a falling-weight impact is investigated using finite element analyses. A flat boulder and a spherical one are considered for this study. The finite element models are shown in Figure 5-4. Only a quarter is modeled due to symmetry. Spherical boulders with masses of 1, 2, and 4 tonnes and four different thicknesses of soil layer are used for this investigation. The length of cube in the horizontal direction and the diameter of sphere (described as boulder size) are both 1 m.

a)   b)
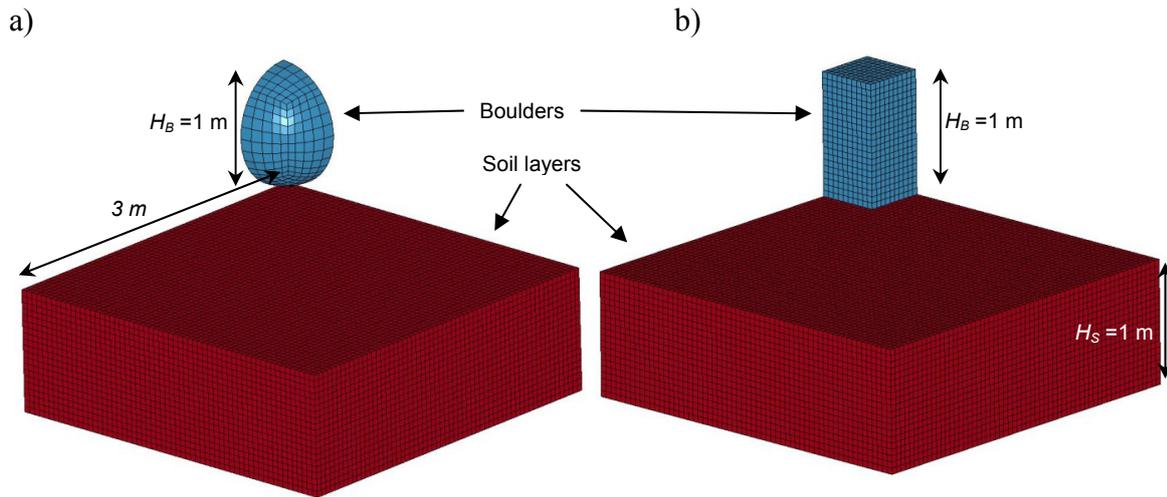
Figure 5-4: Finite element models for impact on a soil layer a) spherical and b) cubic boulder

The variations of penetration depth with respect to impact velocities are shown in Figure 5-5 a for three different masses of boulder having the same geometry. The boulders are spherical, with a diameter of 1 m impacting a 1 m thick layer of soil. $H_B/H_S = 1$, where H_B is the size of the boulder and H_S is the thickness of the soil. The assumption of the different masses having the same geometry may not be realistic but allows the effect of variation of mass and velocity to be explored, while other parameters are kept constant. It can be seen that the maximum penetration depth increases almost linearly with increase in the impact velocity for the impacts that lead to a maximum penetration of 30% of the depth of soil cushion. The ratio of the difference of the penetration for a given velocity (Δ_1/Δ_2 ratio in Figure 5-5 a) remains the same for different velocities and is about 1.4 for this diagram. The maximum displacement varied by a factor of two when the weight of the boulder was increased from 1 tonne to 4 tonnes.

Figure 5-5 b shows the variations of penetration depth with respect to impact velocities for four different thicknesses of soil. For these impacts, a spherical 2 tonne boulder with a diameter of 1 m is used. The penetration depth changes as the ratio of boulder size to soil depth changes. This change is smaller for a ratio of higher than one, since the influence of boundary condition on development of the mechanism in soil is minimized. However, both the thickness as well the lateral extension of the soil layer is limited in reality to the dimension of the gallery.

The nodal displacement vectors for impact of the 2 tonne boulder subjected to a velocity of 4 m/s on soil layers with thicknesses of 0.5 and 1.5 m when the maximum penetration of boulder occurred, as illustrated in Figure 5-5 c demonstrates the difference of the soil response. Heaving of the material around the impact area is higher for the thinner layer of soil, since the boundary conditions limit the penetration of the boulder. The maximum penetration for the boulder increased about 20% for 1.5 m thick soil.

a)

b)

c)
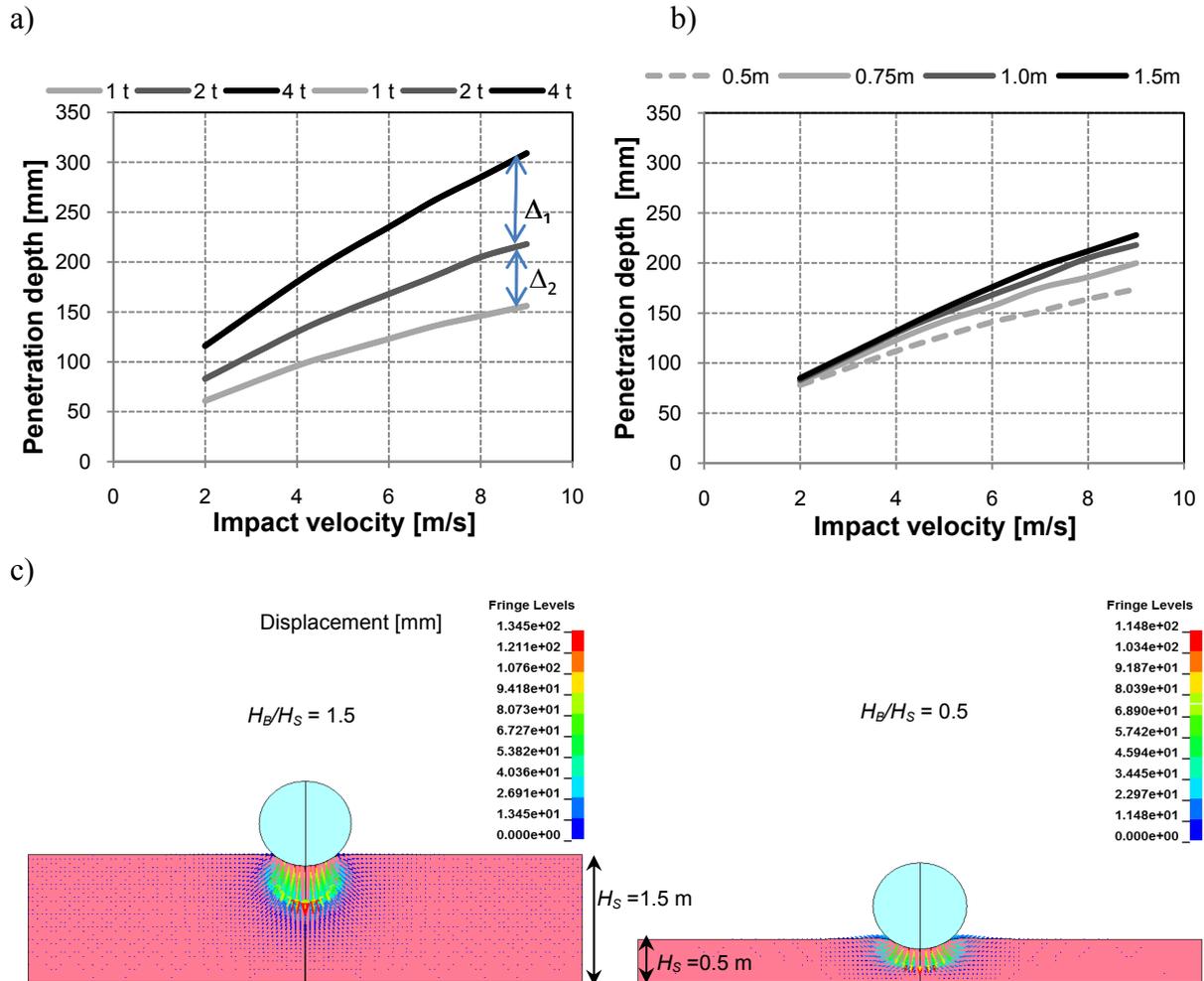
Figure 5-5: Penetration depth of a 1 m diameter boulder into the soil for a) different masses for cushion thickness of 1 m ($H_B/H_S = 1$), b) different soil thicknesses $0.5 < H_B/H_S < 1.5$ for a 2 tonne boulder, and c) displacement vectors for $H_B/H_S = 0.5$ and $H_B/H_S = 1.5$

The influence of the impact velocity on the soil stiffness is also investigated. Figure 5-6 a shows the impact force (contact forces between the boulder and the soil cushion) vs. penetration depth of the boulder for a 4 tonne boulder impacting a 1 m thick layer of soil with different impact velocities. It is seen that the stiffness of the soil increases with increases in the impact velocity, but this increase is rather small for the range of this simulation (up to $E = 162$ kJ). The maximum penetration for this calculation was about 30% of the total thickness of soil.

The impact force defined as the contact forces between the boulder and the soil cushion, vs. penetration depth diagram for different thicknesses of soil subjected to impact of a 2 tonne boulder with a velocity of 4 m/s is plotted in Figure 5-6 b. The slope of force-displacement diagram changes with the increase in the thickness of soil layer, since the displacements are increased due to the change in boundary conditions.

a)

b)
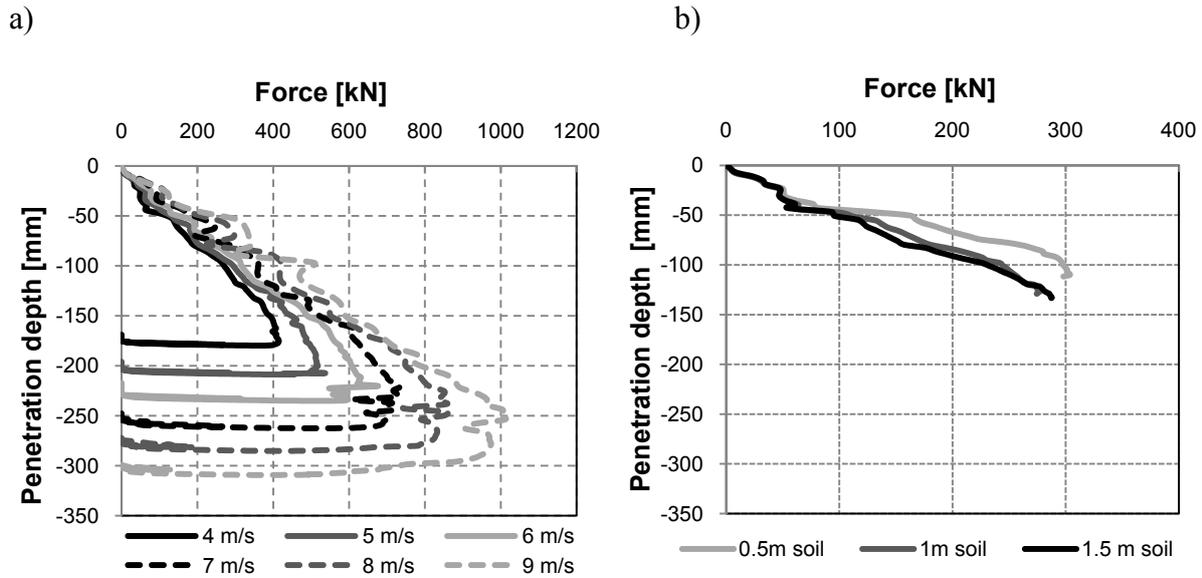
Figure 5-6: Influence of a) impact velocity for $H_B/H_S = 1$ (4 tonne boulder - 1 m thick layer), and b) soil layer thickness for $0.5 < H_B/H_S < 1.5$ (2 tonne boulder - 4 m/s velocity)

The displacement vectors for soil subjected to impact from different shapes of boulder are shown in Figure 5-7 a. Both boulders have a weight of 2 tonnes and are subjected to an impact velocity of 4 m/s. The maximum penetration depth is more than three times higher for the spherical boulder, but the deflections are more localized.

a)

b)
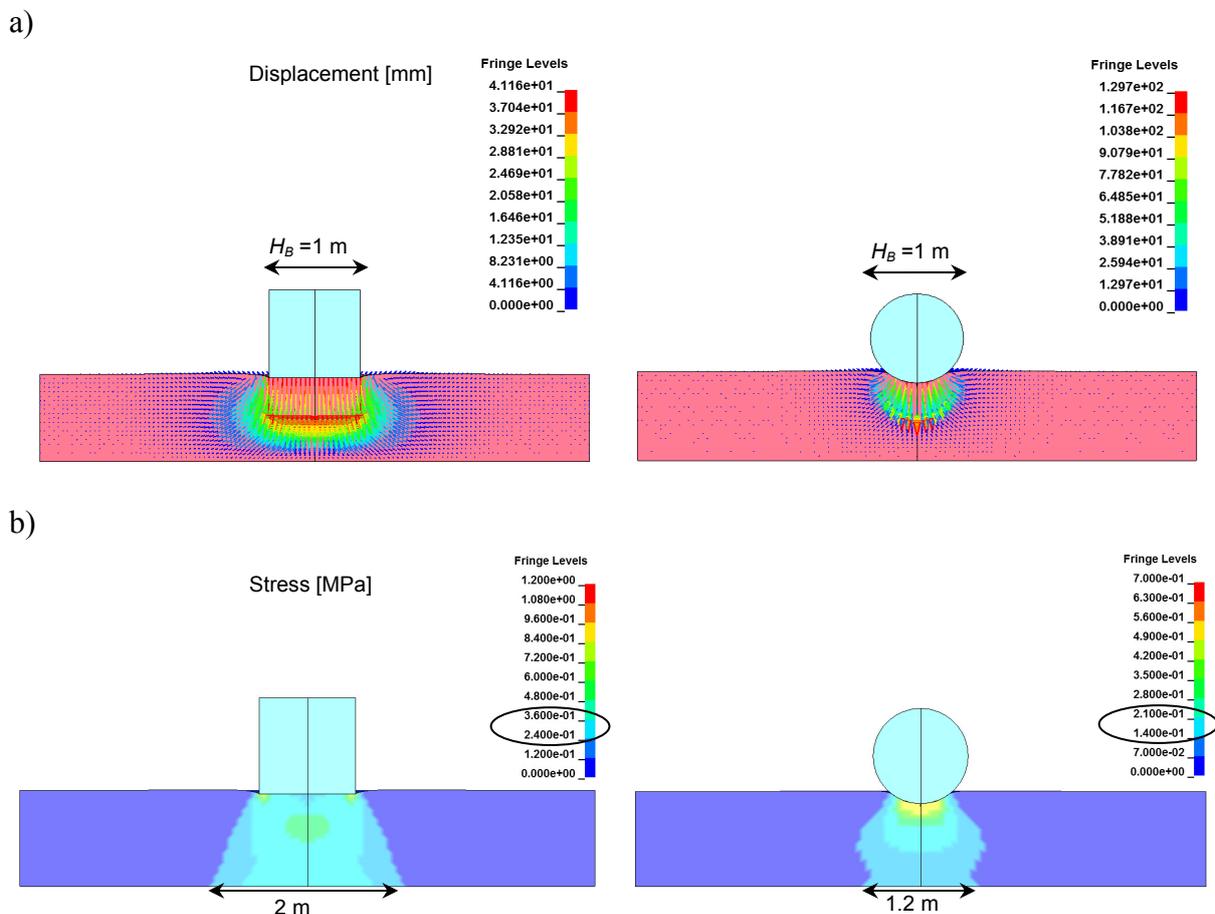
Figure 5-7: Impact of blunt and spherical boulder ($H_B/H_S = 1$) onto the soil: a) displacement vectors, and b) distribution of mean stresses

Figure 5-7 b shows the distribution of the mean stresses in the soil. The stresses on the bottom of the soil layer are distributed over a larger area for the blunt boulder compared to the spherical one. The stresses are also higher at the base of the soil layer when it is subjected to the impact of the blunt boulder, since the impact forces are higher due to lower penetration depth. There is a high compression stress directly below the blunt boulder, which combined with the shear at the edges of the boulder lead to a limited penetration of boulder and thus to higher impact forces.

Figure 5-8 shows the distribution of the mean stresses for a 2 tonne boulder impacting different thicknesses of soil with a velocity of 4 m/s. The ratios of boulder size to thickness of soil are 0.5 and 1.0, respectively. The figure represents the stress state when the impact forces are maximum. For a smaller thickness of cushion, there is a higher concentration of stresses over a smaller area. The stresses are lower and are distributed over a larger area at the bottom of the thicker soil layer.

It is seen from the analysis that the area over which the maximum stresses were concentrated was almost equal to the contact area of the boulder for smaller thicknesses of cushion. The total area over which the stresses were transmitted was equal to the size of the boulder (dotted line in Figure 5-8 a).

Figure 5-8: Distribution of mean stresses [MPa] for 0.5 and 1.0 m thicknesses of soil

It is seen that when the cushion layer has a smaller thickness than the boulder diameter, concentrated punching forces acting on the slab should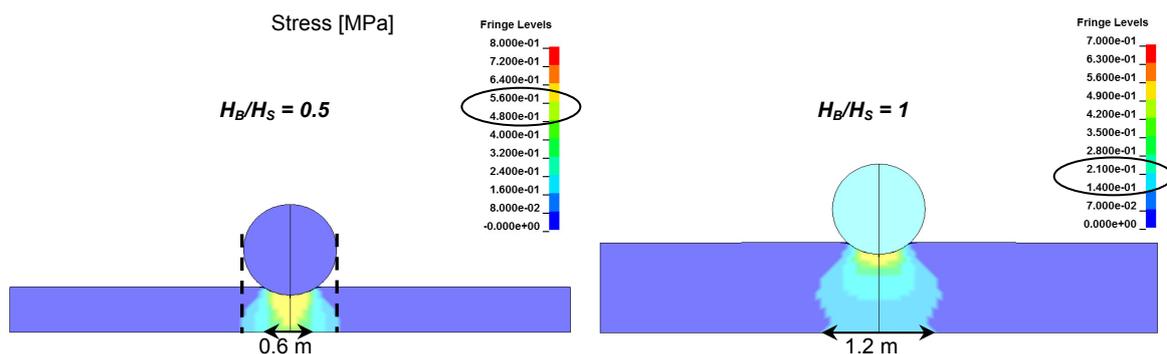 be assumed in a small distribution area. This area can be equal to or smaller than the contact area of the boulder itself. Moreover, the stresses are lower and more distributed for the thicker soil layer, which means the impact forces transmitted through the soil to the slab are lower. The stresses were three times less for the thicker layer of the soil shown in Figure 5-8, compared to the thinner one, and were distributed over an area with twice the diameter.

The impact B1 ($E = 39$ kJ) is modeled using 800 mm and 1200 mm thick layers of soil. The nodal displacement vectors of soil are shown in Figure 5-9 for both models. The size of the boulder and the impact velocity are 700 mm and 9.9 m/s, respectively. A difference between the responses of the cushion layers subjected to the same impact energy can be observed.

The maximum penetration depth directly below the impacting boulder is higher for the case with a thicker cushion layer. The distribution of the load to the slab for the thinner layer of soil is larger (see Figure 6-11) since less energy can be absorbed due to the lower penetration

of the boulder and fewer soil elements incorporated in a shear dissipation mechanism. In the case of the B1 impact, as shown in Figure 4-10, since the thickness of the soil is the least, the least penetration of the boulder is observed. Heaving of the material around the impact area is almost the same for soil thicknesses of 800 and 1200 mm. On the other hand, heaving is the highest for 400 mm soil cushion subjected to the same impact energy (Figure 4-10), due to the boundary conditions which limit the displacements, and the development of a bearing capacity mechanism.

The maximum total energy of the impacting boulder is 38.8 kJ, and for 400, 800, and 1200 mm soil layers the energies of soil are 30.8, 33.6, and 34.4 kJ, respectively. This implies that the energy in 1200 mm soil layer was 12% higher compared to the 400 mm thick soil layer. The maximum energy in the slab covered by a 400 mm thick cushion was about 3 kJ, which is three times higher than the one covered by a 1200 mm thick cushion (1 kJ). The rest of the energy is absorbed by the supporting system of the slab.

a)

b)
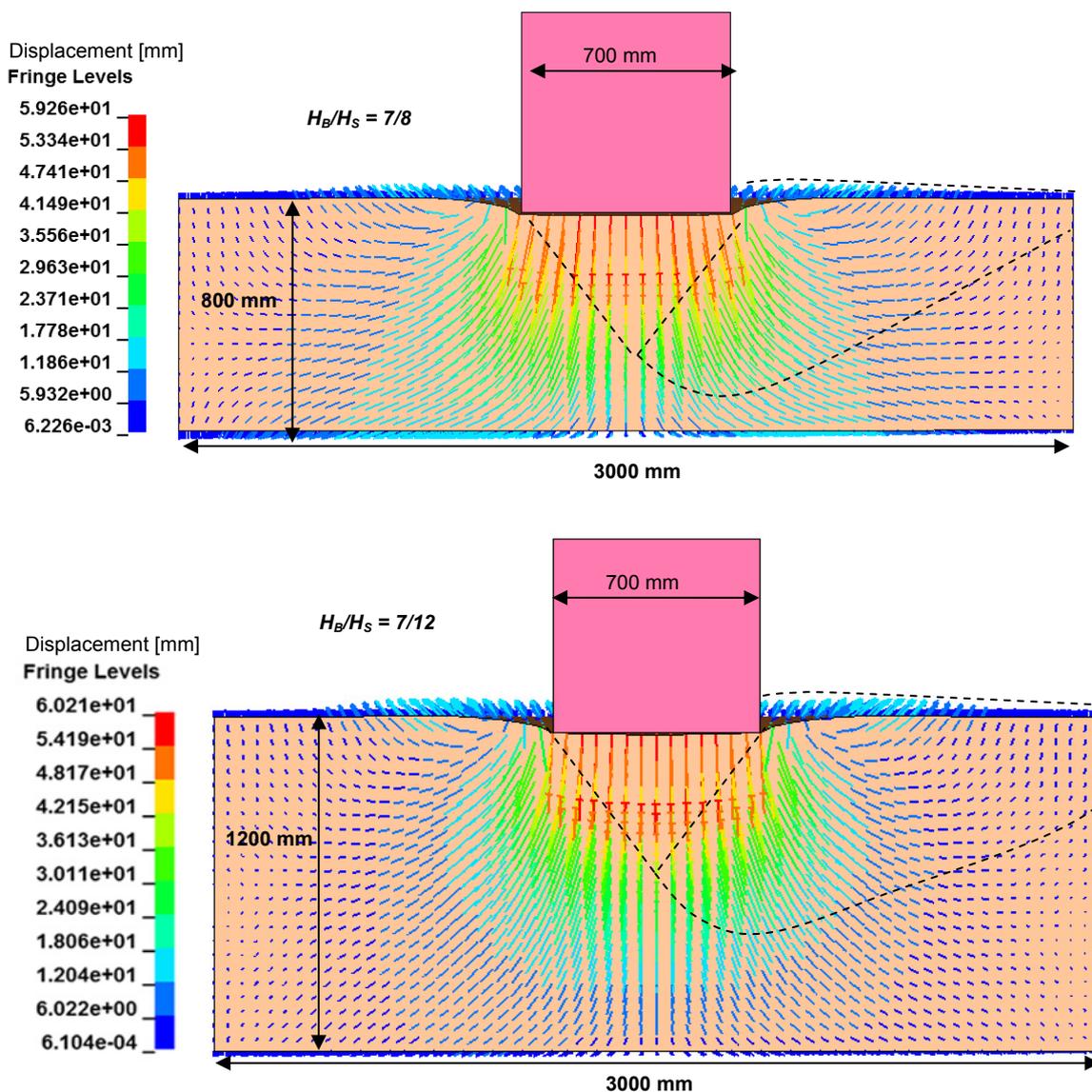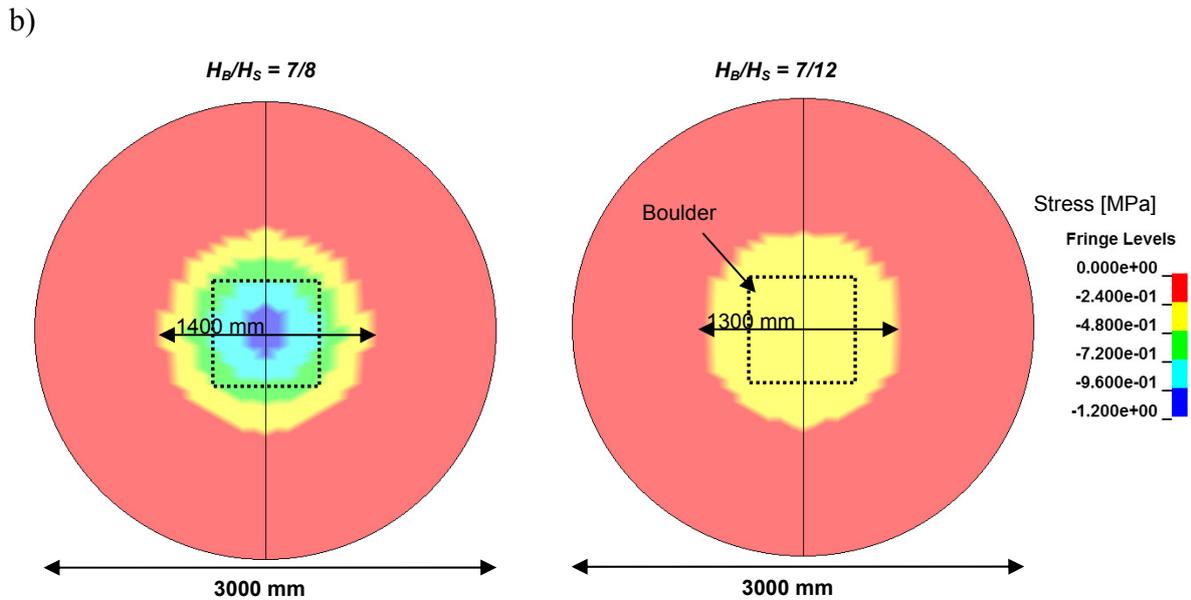
Figure 5-9: Response of different thicknesses of soil for impact energy E = 39 kJ: a) Displacement vectors and idealization of the bearing capacity mechanism (scale 1:25), and b) Distribution of vertical stresses (scale: 1:50)

The distribution of the vertical stresses on the bottom of the soil layer for 800 mm and 1200 mm thick layers of soil as shown in Figure 5-9 b represent the stresses that are transferred to the gallery roof. The total distribution area has almost an equal diameter for both cases, which is twice the size of the impacting boulder. There is a high concentration of stresses at the middle below the impact zone for the 800 mm thick layer of soil and the stresses reduce in radial direction. The 1200 mm thick layer of soil transferred the stresses constantly over the section and the transferred stresses are lower than for the thinner layer of soil cushion.

5.7 Shear reinforcement

Punching behavior due to impact E1 ($E = 118$ kJ) with a stirrup spacing of 150 mm (Figure 5-10) is compared to similar impacts on slabs having 200 and 250 mm stirrup spacings.

Reinforcement:
Top: 10 mm @ 300 mm spacing
Bottom: 22 mm @ 150 mm spacing
Stirrup: 10 @ 150 mm spacing
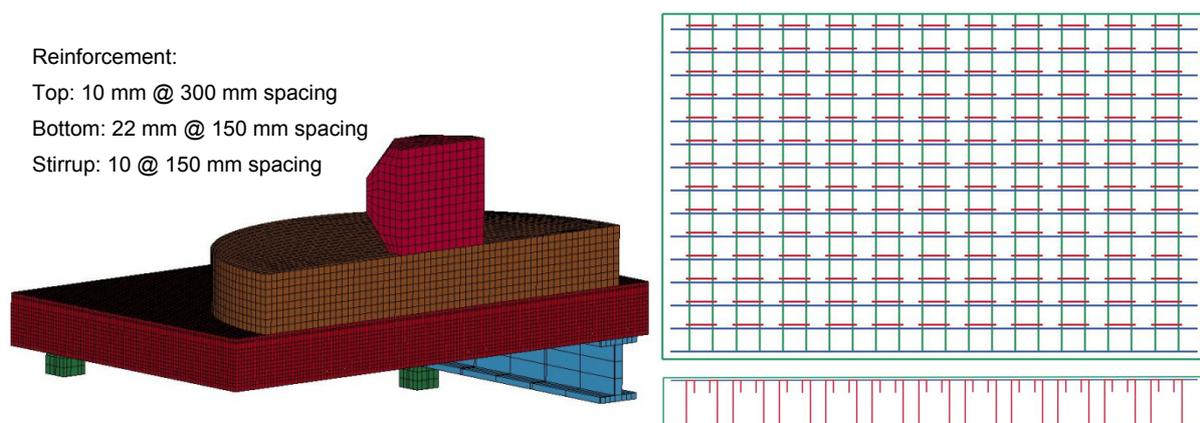
Figure 5-10: Finite element model of impact E1 and the reinforcement layout in the slab

The values of the elastic recovery (*ER*) are compared at the punching location (where the punching cracks occurred) for three slabs with different stirrup spacings. Table 5-7 shows this

comparison. The elastic recovery of the slab in punching is reduced with increase of the stirrup spacings. Finite element analysis confirms that the punching capacity of the slab is lowered by increasing the spacing of the stirrups. The *ER* of the slab without shear reinforcement subjected to the same impact (B5) was 45%, which is increased by 30% when stirrups with a spacing of 150 mm are used. The presence of stirrups helps in reducing the residual deflections when they are not yielded and so the gap between residual and maximum deflection, and thus *ER* becomes larger. The stirrups remained elastic under this impact for all three cases.

Table 5-7: Percentage elastic recovery for different spacing of stirrups (E=118 kJ)

Spacing of stirrups [mm]	150	200	250
Elastic recovery (*ER*) [%]	75	70	65

5.8 Boulder shape

The impact on a slab without a cushion layer is investigated comparing two different shapes of impacting boulder: a blunt (as used in experiments) and a spherical boulder. A direct impact on a slab, similar to series B of the experiments (Schellenberg 2008) is considered here. The support conditions are kept similar as well. The finite element models for the two cases are shown in Figure 5-11. Both boulders have a similar size of 700 mm, which is the diameter of the sphere and the length of the blunt boulder, respectively. The masses of the boulder and the falling height are 800 kg and 7.5 m, respectively (*E* = 59kJ).
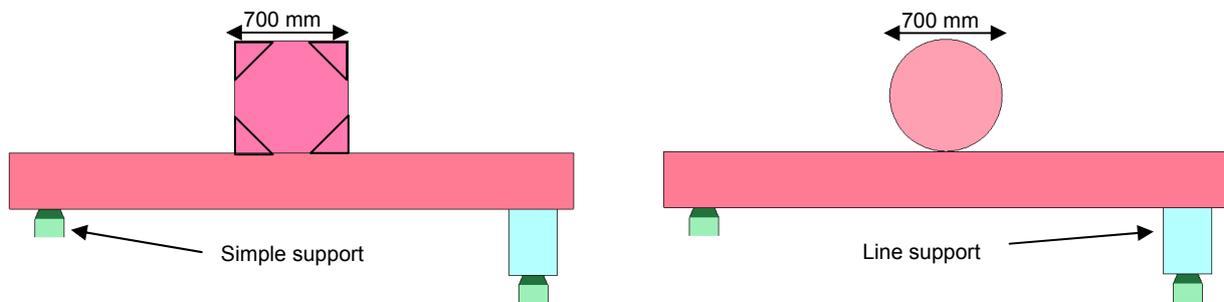
Figure 5-11: Finite element models to study the influence of the boulder shape for E = 59 kJ

The influence of boulder shapes on the punching behavior of slabs is studied by comparing deflection contours for both cases (Figure 5-12). It is observed that the punching behavior is dominant for the slab subjected to impact by a blunt boulder (Figure 5-12 a). Maximum deflection occurs directly under the impact zone. The deflection at the center of the slab is approximately three times higher compared to the slab subjected to the impact from a spherical boulder.
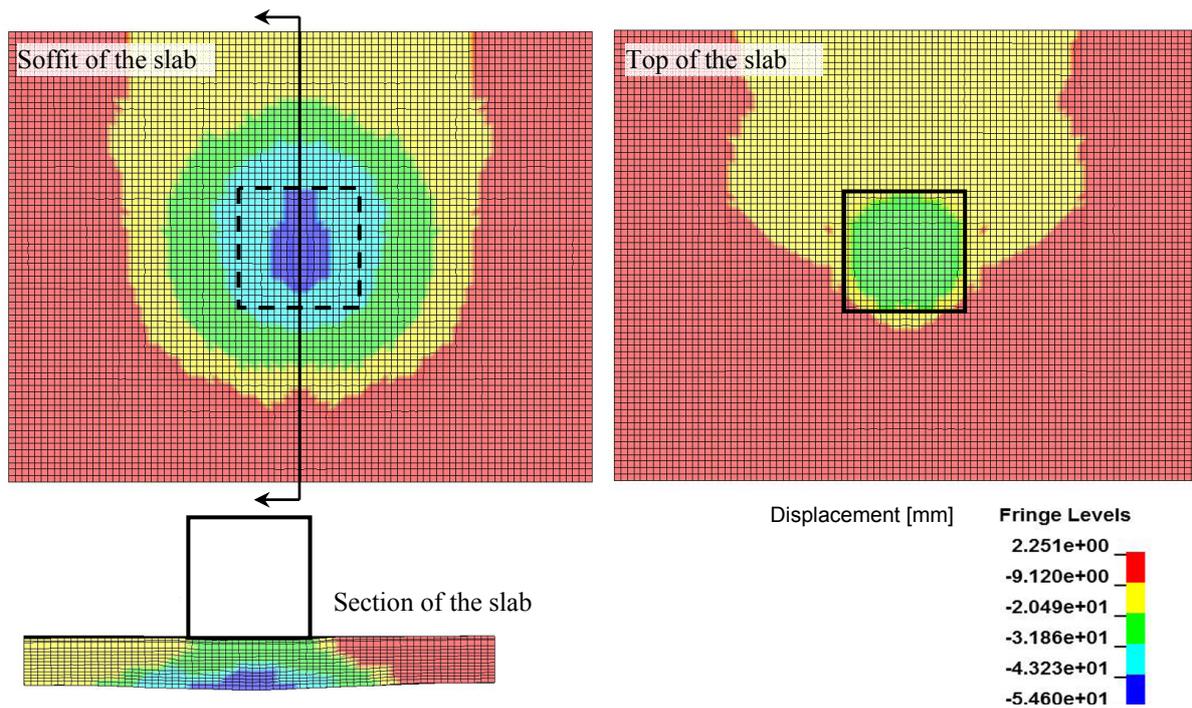
a) Blunt boulder

b) Spherical boulder
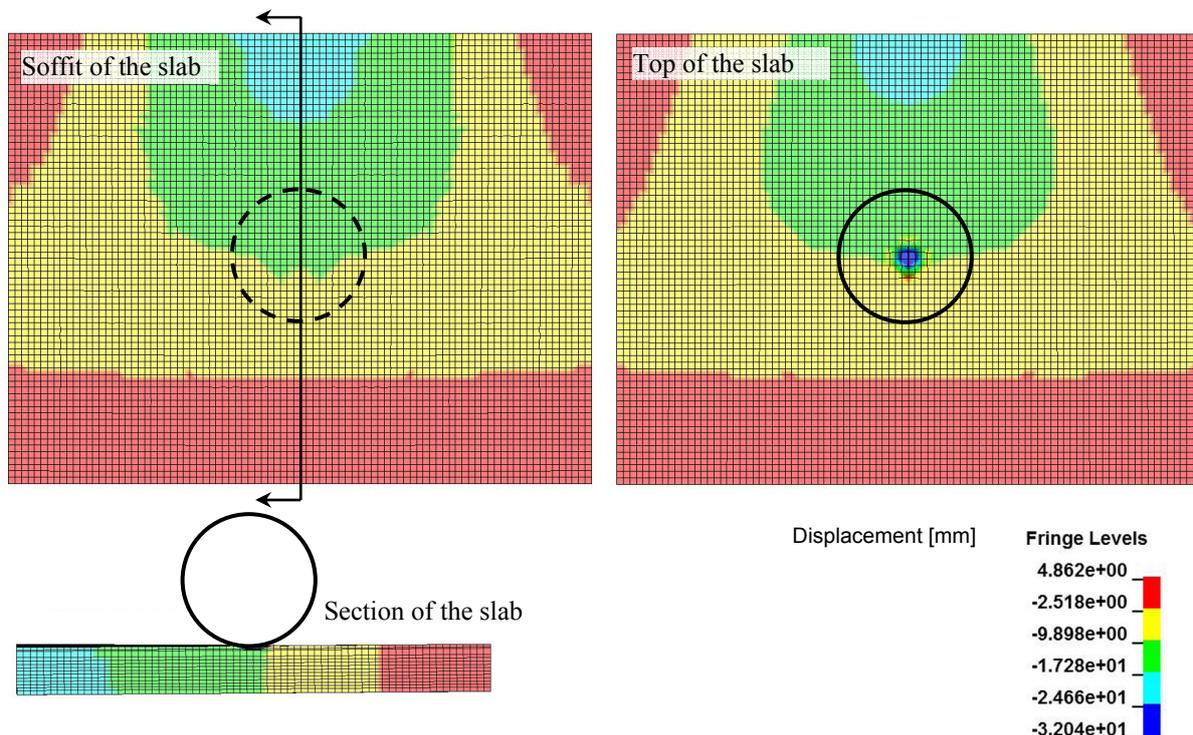
Figure 5-12: Comparison of slab deflections [mm] for a) blunt and b) spherical boulder

Bending behavior is observed for the slab subjected to the impact of a spherical boulder as the maximum deflection occurred at the free end of the slab between the two simple supports (Figure 5-12 b). In this case, high deflections are observed directly at the impacted surface of the slab, which may be due to the local damage and crushing of concrete. This comparison is made based on a relatively small impact energy of 59 kJ. The local damage for the slab subjected to impact of the spherical boulder may be very severe when the boulder delivers a

higher impact energy and this slab may exhibit a brittle mode of failure rather than developing a deformation response in bending, as seen for this case.

Figure 5-13 shows the crack patterns of slabs (contours of zero stresses) subjected to the impact of different shapes of boulder, as obtained from finite element analyses. This confirms the deduced behavior of the slabs, since punching and bending cracks are formed for both slabs. Two cracked zones are observed in the cross section for the slab subjected to the impact of the blunt boulder (Figure 5-13 a). These may form due to the high concentration of stresses exactly under the impact zone. A second cone is formed, which represents the punching of the slab under the impact of boulder. Cracks representing a bending pattern are formed at the soffit for the slab subjected to the impact of the spherical boulder.

a) Blunt boulder   b) Spherical boulder
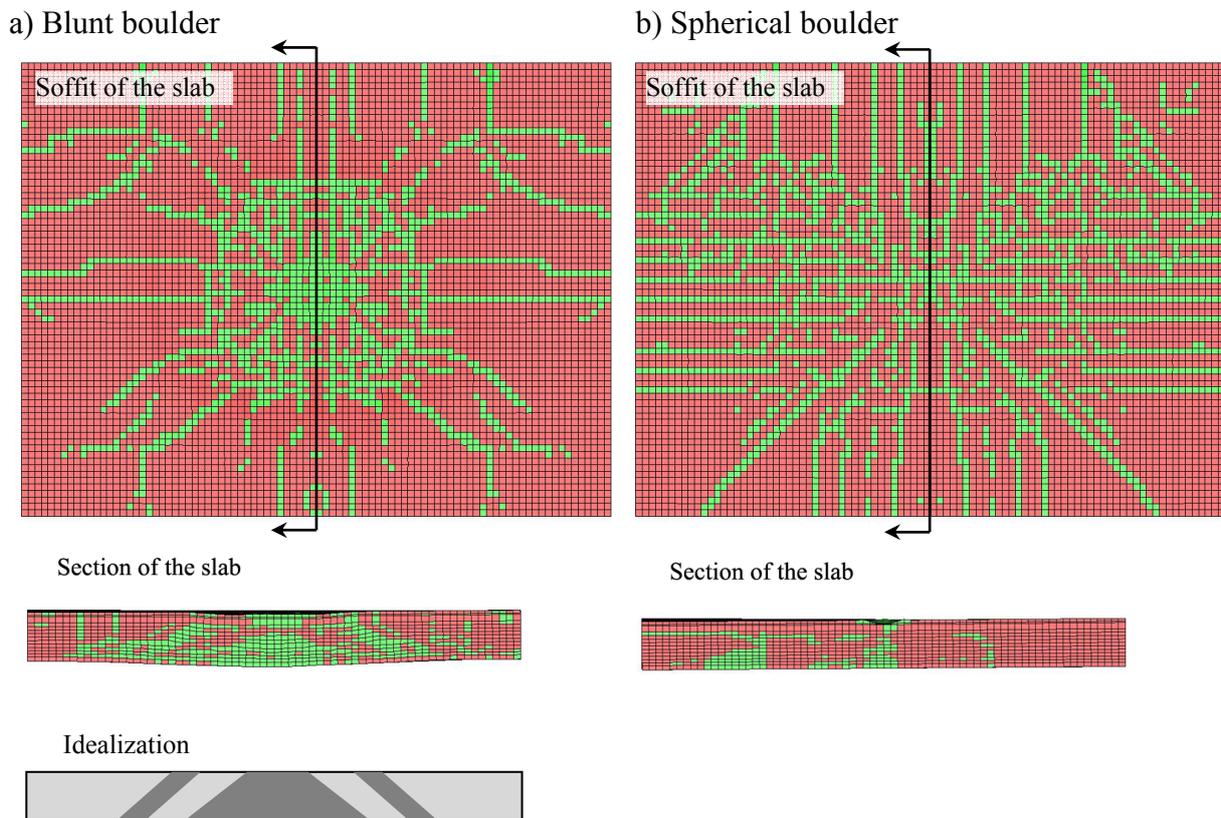
Figures 5-13: Comparison of cracks for the soffit of the slabs subjected to impact of a) a blunt and b) a spherical boulder (E = 59 kJ)

5.9 Consecutive impacts

Consecutive impacts with impact energies of 39 kJ and 118 kJ, respectively, are modeled using finite element analyses. Boulders of 800 kg are assumed to fall five times from a height of 5 m, on slab B of the experimental series. The same slab is also analyzed, when subjected to five impacts with heights of fall of 15 m.

Figure 5-14 a shows the comparison between the maximum deflection that occurred during each impact, for five consecutive impacts with energies of 39 kJ and 118 kJ, respectively. It can be seen that irrespective of previous impact histories of the slab, the maximum deflection remains almost the same for all impacts.

a)

b)
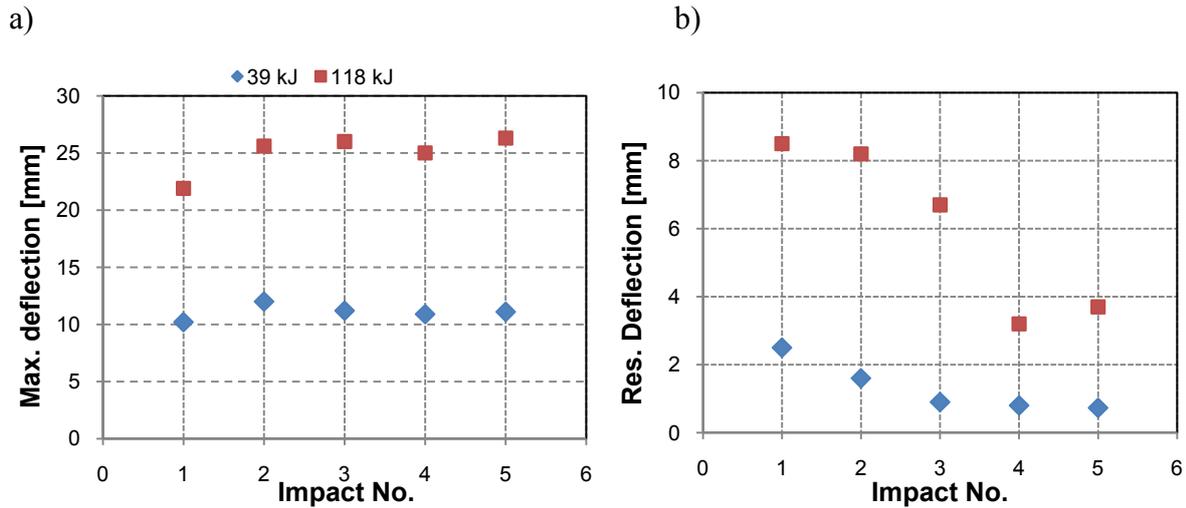
Figure 5-14: Consecutive impacts: a) Maximum deflection for consecutive impacts with similar energies, and b) residual deflection for consecutive impacts with energies of 39 kJ

The comparison between the residual deflections due to each impact is shown in Figure 5-14 b. The residual deflection in the slab is large during the first two impacts. This is due to the fact that before the first impact the slab has not cracked yet. Once the slab has cracked, the additional residual deflection in the slab subjected to a similar impact becomes lower. The additional residual deflection for the last two impacts remained similar. The slab subjected to the impact, can be considered as failed, when the elastic recovery of the slab due to *n* number of impacts, which is defined based on the ratio of the cumulative residual deflection to the cumulative maximum deflection is less a certain threshold.

6 Recommendations for analytical models

Calibration of input parameters of an analytical model using a Three Degrees of Freedom System (3DFS) is presented here. In addition an analytical model using a Two Degrees of Freedom System (2DFS) is proposed.

6.1 Three degrees of freedom system

The application of a System of Multiple Degrees of Freedom (SMDF), as proposed by Schellenberg (2008), is discussed here. The model consists of three masses corresponding to three nonlinear springs (Figure 6-1) and is referred to as the Three Degrees of Freedom System (3DFS) in order to differentiate between the models with two and three degrees of freedom, as used in this study. The model is similar to the model proposed by Schlüter (1987) and Eibl et al. (1988) for the analysis of aircraft collisions with reactor containments. The influence of the input parameters is summarized in this section, and it aims at improving the assumptions made for the proposed analytical model. Therefore, the assignment of masses and spring properties discussed incorporates these improvements.

a)   b)
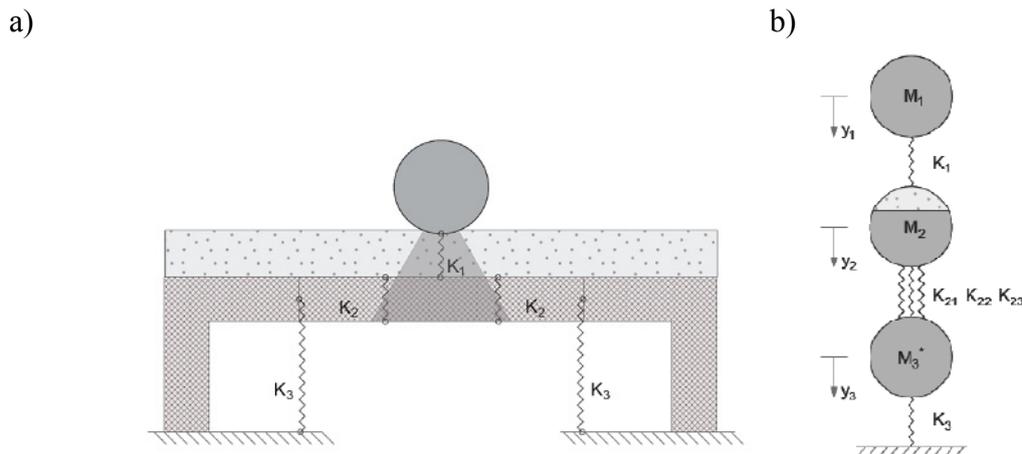
Figure 6-1: System of multiple degrees of freedom (SMDF) a) the section of a gallery and b) the model definition (Schellenberg 2008)

Based on the dynamic equilibrium, the equation of motion can be formulated as:

$$K_g y + M_g \ddot{y} + C_g \dot{y} = F(t) \tag{6-1}$$

where, K_g, M_g, and C_g are the stiffness, mass, and damping matrices of the gallery. y is the displacement matrix and $F(t)$ represents the externally applied force.

6.1.1 The first degree of freedom

The first degree of freedom demonstrates the behavior of soil subjected to impact. The boulder is subjected to an initial velocity and the impact forces are calculated based on deceleration of the boulder and the stiffness of the soil.

6.1.1.1 Mass

The first mass M_1 is the mass of the impacting block, which is provided by the design requirements.

6.1.1.2 Spring

The behavior of the soil as proposed in the initial model (Schellenberg 2008) was assumed by a hardening curve based on an initial stiffness value with an assumed impact area of the boulder. The behavior of the soil subjected to impact is influenced by various parameters such as the thickness of soil layer, size and weight of the boulder, modulus of soil, and the angle of internal friction.

The soil spring is modified and improved here in order to account for the change in stiffness of soil for different thicknesses of soil cushion as well as to account for the shear behavior of the soil. The depth of failure for the shear zone H_f refers to the minimum depth required that the soil layer develops a general shear failure behavior based on Terzaghi's formulation for ultimate bearing capacity of the soil (Terzaghi & Peck 1948), and it can be calculated as:

$$H_f = 2R_0 \tan(45 + \frac{\varphi'}{2}) \tag{6-2}$$

where R_0 is the radius of an equivalent spherical boulder and φ' is the angle of internal friction of soil, respectively. The depth of the shear failure is 1.7 times the size of the boulder for a friction angle of 30°. The ratio of the soil thickness (after penetration) to the boulder size, therefore, is important in predicting the soil behavior.

The load distribution of the soil on the slab for different thicknesses of soil cushion, as shown in Figure 6-2, is assumed for the analytical model, where $\emptyset_{sl}$, e, and y_{max} are the diameter of loading area on the slab, the thickness of soil layer, and the maximum penetration depth of the boulder, respectively. The influence of the slab deflection on the load distribution is neglected here, since the impact forces transmitted through the soil on a rigid base are higher than the forces transmitted to a flexible slab. The assumed distribution is compared to the displacement vectors in soil for three different cases (see Figure 4-10 and Figure 5-9). These cases can be listed as:

Soil embedment 1: e-$y_{max} > 3.4R_0$

Soil embedment 2: $R_0 < e$-$y_{max} < 3.4R_0$

Soil embedment 3: e-$y_{max} < R_0$

The maximum penetration depth at the end of a given impact y_{max} is an initial value set for the expected penetration depth of the boulder. This can be calculated using a single degree of freedom system for impact of a boulder onto the soil with a soil modulus according to Equation 6-5, or using any empirical formula for calculating the penetration depth. A single degree of freedom system is used in this study in order to quantify an initial value for the expected penetration depth. The soil embedment case is therefore chosen based on this initial assumption and the actual penetration depth is later calculated for the chosen behavior.
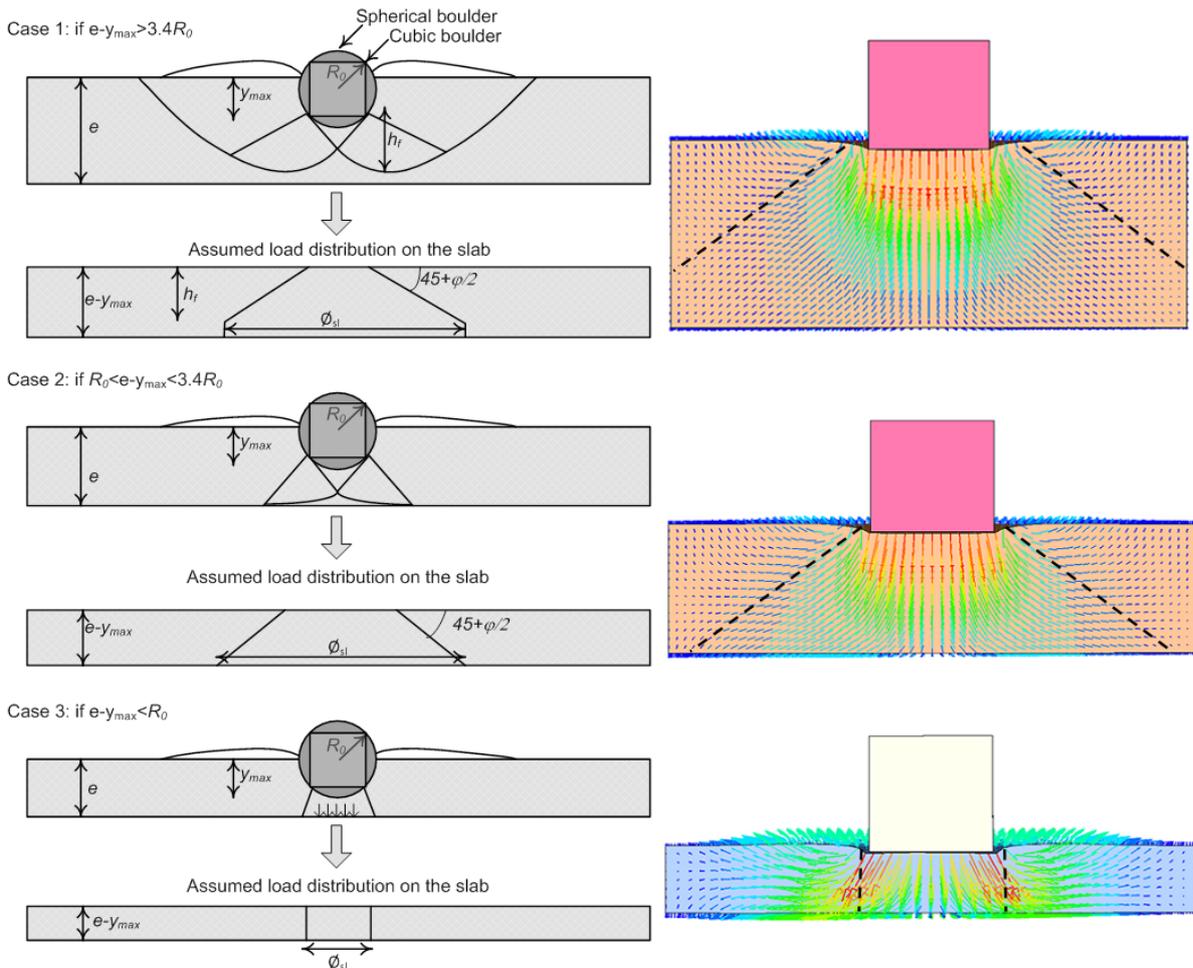
Figure 6-2: Assumed load distribution cone for soil cushion

Even though the soil cushion can decrease the impact stresses on the gallery, the thickness of the soil layer is usually limited since it also increases the dead load on the slab. In many cases, development of a full shear slip surface cannot be expected if the gallery is hit by a large boulder.
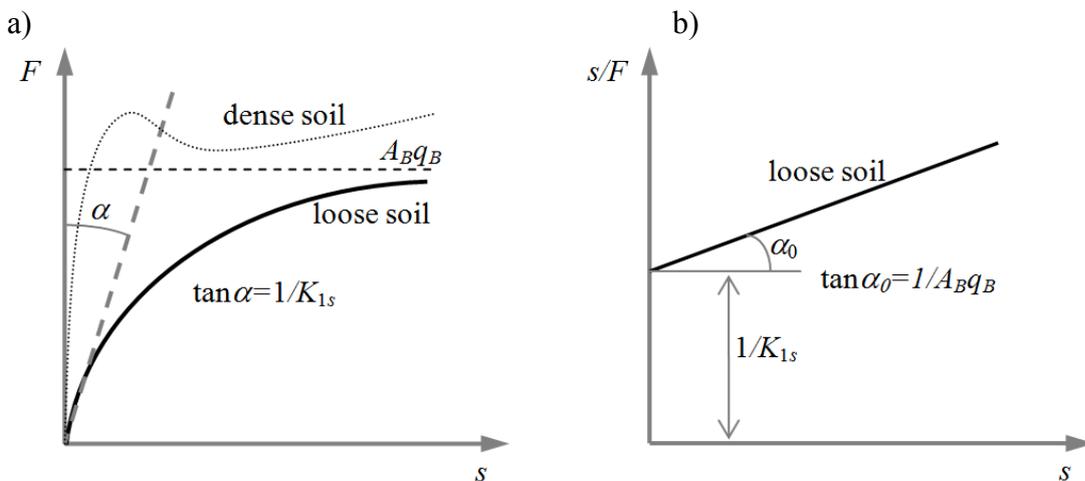
Figure 6-3 Force settlement diagram for a) shear failure of the soil and b) its idealization for loose soil developed based on Pietsch (1982)

The shear behavior (soil embedment 1) is considered by applying an idealized curve (Figure 6-3 b) similar to the one proposed by Pietsch (1982), which is outlined in Studer et al. (2007). The idealization is shown in Figure 6-3 b, where F and s are the force and settlement of a loose soil, respectively. q_B, K_{1s}, and A_B represent the bearing capacity of soil, the frequency dependent stiffness of soil (when the thickness of the soil is not limited), and the contact area of the boulder, respectively.

s/F can be calculated as:

$$\frac{s}{F} = \frac{y_1 - y_2}{F_1} = \frac{1}{K_{1s}} + \frac{y_1 - y_2}{A_B q_B} \tag{6-3}$$

Therefore, the spring force can be calculated as:

$$F_1 = \frac{y_1 - y_2}{\dfrac{1}{K_{1s}} + \dfrac{y_1 - y_2}{A_B q_B}} \tag{6-4}$$

The application of Equation 6-3 is limited since the penetration cannot exceed the thickness of the cushion layer. The soil modulus K_{1s} [N/mm] can be evaluated using the formulation proposed by Lysmer (1965) and by Wolf (1997). The stiffness of the spring for the case impact of a spherical boulder is calculated at each time step as a function of penetration depth of the boulder according to the following formula:

$$K_{1s} = \frac{4Gr}{1 - v} \tag{6-5}$$

$$r = \sqrt{(y_1 - y_2)(2R_0 - (y_1 - y_2))} \tag{6-6}$$

where G, and r are the soil shear modulus [MPa], and the loading radius [mm], respectively. This formulation does not take the velocity of the impact and the shape of the impacting body into consideration. It must be noted that the behavior can be different for soils in different states, for example for the dense soil as shown in Figure 6-3 a. The idealized curve cannot be used for such individual cases and they should be treated separately.

The Terzaghi formula (Terzaghi & Peck 1948) can be used to calculate the bearing capacity of the material. Incorporating the dynamic impedance of the material the bearing capacity can be calculated based, on Chikatamarla (2006), as follows:

$$q_B = rs_\gamma \gamma_s N_\gamma + s_q \gamma_s (y_1 - y_2) N_q + s_c c' N_c + v_0 \sqrt{E_g \rho_s} \tag{6-7}$$

Where:

- γ_s, ρ_s Unit weight [N/m^3] and the density [kg/m^3] of the soil
- s_γ, s_q, s_c Shape factors
- r Radius of the contact area of the boulder [m]
- N_γ, N_q, N_c Constants depending on the friction angle
- c' Cohesion in the soil [N/m^2]

- v_0 Initial impact velocity [m/s]
- E_g Young's modulus of soil [N/m²]

a)

b)

c)
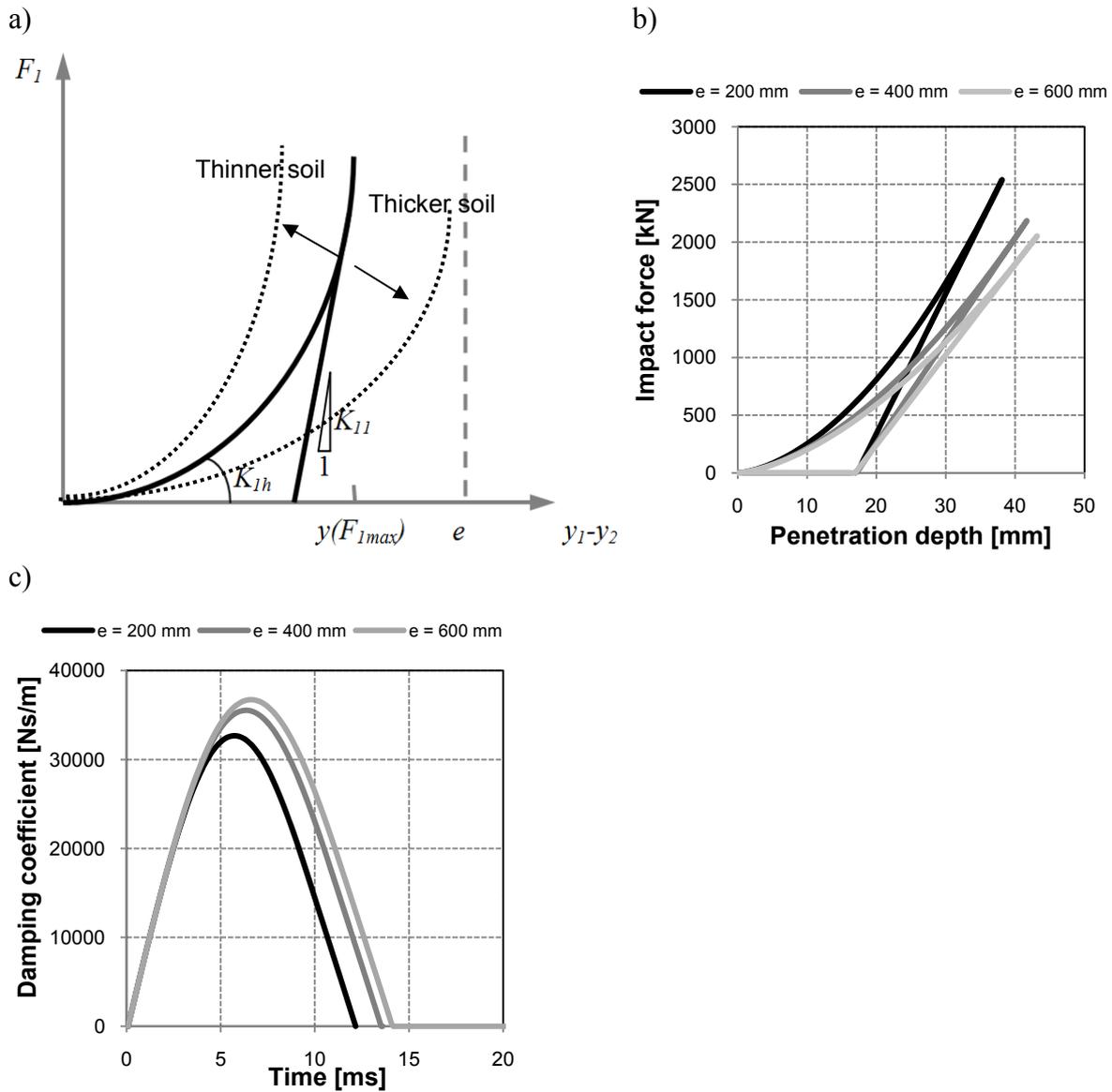
Figure 6-4: Soil spring: a) spring properties for hardening of soil cushion, b) stiffness of different thicknesses of soil, and c) damping for different thicknesses of soil (E = 39 kJ)

The assumed hardening behavior of the soil cushion as shown in Figure 6-4 a (for soil embedment 2 and soil embedment 3) is approximated by a hyperbola with an initial stiffness of K_{1h} and a linear unloading path with stiffness K_{11} that refers to the maximum stiffness reached during loading. The maximum possible penetration is assumed to be equal to the thickness of the cushion layer. For pre-compacted and pre-consolidated soil layers, a full depth penetration of a boulder is not likely to be reached due to the lateral pressure of the surrounding soil. The slopes of the curve, as well as the maximum force tend to change with the thickness of the soil layer as shown in the figure. The model for hardening is modified to account for different responses of soil when the thickness of the cushion later changes, and no initial stiffness is needed to be defined compare to the initial model proposed.

For the hardening behavior, the stiffness for a limited thickness of soil can be calculated as follows for a spherical boulder, which is based on the stiffness of rigid embedded cylindrical foundations (Gazetas 1983):

$$K_{1h} = \frac{4Gr}{1-v}(1+1.28\frac{r}{e})(1+\frac{y_1-y_2}{2r})[1+(0.85-0.28\frac{(y_1-y_2)}{r})(\frac{\frac{(y_1-y_2)}{e}}{1-\frac{(y_1-y_2)}{e}})] \tag{6-8}$$

r is calculated using Equation 6-6. The equation is valid for y_1-y_2 < 2r, and y_1-$y_2 \leq 0.5e$. The formula under-predicts the actual increase in the stiffness for foundations with deeper embedment according to Gazetas (1983).

An example of impacts on soil using an 800 kg boulder with radius of 350 mm, falling from a height of 5 m is illustrated in Figure 6-4 b to show the applicability of the model. Three different thicknesses of soil are used. The stiffness of the soil reduces with increase in the soil thickness as expected. However, this variation of the stiffness with respect to the thickness of soil is only considered for hardening part of the curve. The unloading stiffness of K_{11} is simply assumed here based on the maximum stiffness of the material reached during loading and does not take the variation of the soil thicknesses into consideration. This implies that the maximum values of the penetration depth, as shown in this figure, depend on the thickness of the soil layer but the final penetration depths do not.

6.1.1.3 *Damping*

The damping coefficient of soil, C_s [Ns/m] can be defined as (Wolf 1997):

$$C_s = \rho_s c_v A_B \tag{6-9}$$

where ρ_s is the density of the soil [kg/m^3], c_v is the wave velocity [m/s], and A_B is the loading area [m^2], respectively. Therefore, the above equation can be formulated as a function of penetration depth as:

$$C_s = \pi\rho_s c_v r^2 = \pi\rho_s c_v (y_1-y_2)(2R_0-(y_1-y_2)) \tag{6-10}$$

So the damping force increases with increasing penetration depth of the boulder at each time step. The damping coefficient for different thicknesses of soil according to the example used for stiffness of soil in the previous section is shown in Figure 6-4 c. The coefficient increases with increase of the thickness of soil, since the penetrations are higher.

6.1.2 The second degree of freedom

The second degree of freedom corresponds to the punching behavior of the slab. The forces obtained from this spring provide the sectional forces due to punching. The critical section for punching must be preselected by the engineer and the contributing structural mass, as well as the spring forces, are calculated accordingly.

6.1.2.1 Mass

M_2 corresponds to the mass of the assumed punching cone under the loading location. The mass of the soil compacted between the boulder and the slab is included in M_2. As mentioned in Section 6.1.1.2, the distribution of the forces transmitted through the soil to the slab depends on the thickness of soil layer. Therefore, two different cases are assumed here, which correspond to different thickness of soil layer and diameter of boulder, as shown in Figure 6-5.

a)   b)
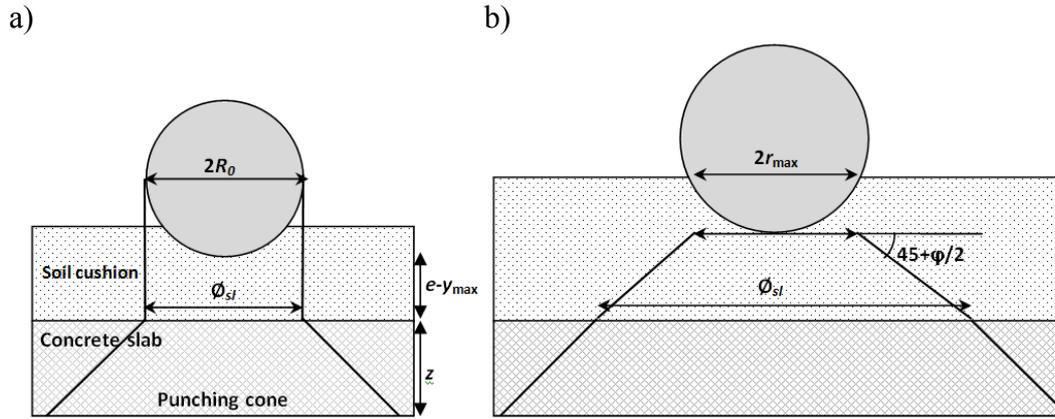
Figure 6-5: Geometry of punching cone for a) $R_0 \geq e\text{-}y_{max}$, and b) $R_0 < e\text{-}y_{max}$

For $R_0 \geq e\text{-}y_{max}$:

$$\text{\O}_{sl} = 2R_0 \tag{6-11}$$

and for $R_0 < e\text{-}y_{max}$:

$$\text{\O}_{sl} = 2r_{max} + 2[(e - y_{max})\tan(45 - \frac{\varphi'}{2})] \tag{6-12}$$

Therefore, M_2 can be expressed as:

For $R_0 \geq e\text{-}y_{max}$:

$$M_2 = \frac{\pi}{12}\left[\gamma_c z(3\text{\O}_{sl}^2 + 6\text{\O}_{sl}z + 4z^2) + 12\gamma_s(e - y_{max})R_0^2\right] \tag{6-13}$$

and for $R_0 < e\text{-}y_{max}$:

$$M_2 = \frac{\pi}{12}\left[\gamma_c z(3\text{\O}_{sl}^2 + 6\text{\O}_{sl}z + 4z^2) + \gamma_s(e - y_{max})(4r_{max}^2 + 2r_{max}\text{\O}_{sl} + \text{\O}_{sl}^2)\right] \tag{6-14}$$

6.1.2.2 Spring

Spring K_2 describes the shear stiffness for the assumed punching shear failure of the concrete slab. With increasing relative displacements of the punching cone compared to the surrounding part of the slab, the behavior is controlled by three contributors: K_{21}: the contribution of the concrete, K_{22}: the contribution of shear reinforcement if existing, and K_{23}: the membrane effect of the bending reinforcement. K_{2h} is the hardening of shear reinforcement, a perfect yielding can be assumed for simplification. The assumed behavior is shown in Figure 6-6 a. The membrane effect represents the post-ultimate behavior of the

reinforced concrete structure and is of importance while evaluating the capacity of the existing structure. It can be neglected while designing new galleries for simplification. Therefore the behavior can be assumed as shown in Figure 6-6 b. The details of the calculation of the spring properties are provided in Schellenberg (2008) and Schlüter (1987).

a)

b)
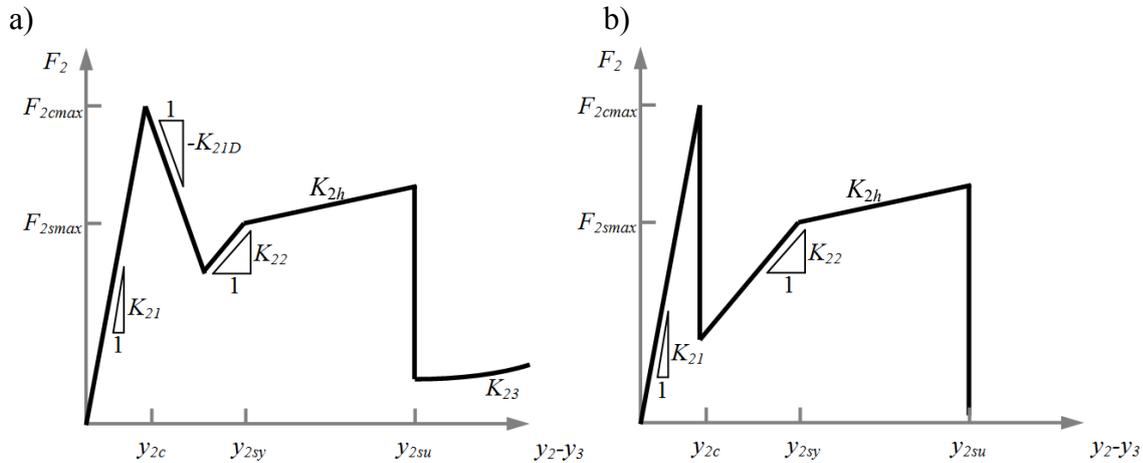
Figure 6-6: Spring properties for K_2: a) according to Schellenberg (2008), and b) simplified

6.1.2.3 Damping

A damping ratio of $\xi = 5\%$ is used for the local behavior of the concrete slab (Schellenberg, 2008). For medium stress intensity (fully cracked) reinforced concrete structures, a damping ratio of $\xi = 1\text{-}4\%$ is suggested (Bachmann et al. 1995). The ratio is between 0.5 and 0.8% for high stress intensity structures. The damping effects of the structure are not of great importance, since usually the first peak is the most relevant one for the analysis of slabs subjected to rockfalls. Therefore, the damping properties of the structure have not been a focus of this study and the proposed values have been used.

6.1.3 The third degree of freedom

The third degree of freedom represents the global response of the slab. The spring forces are calculated based on the contributing modal mass of the structure and the bending stiffness of the slab. The global response also influences the forces in the second degree of freedom.

6.1.3.1 Mass

$M_3{}^*$ is the modal mass of the surrounding structure. The modal mass depends on the boundary conditions of the slab. Therefore, the bending behavior of the slab is scrutinized here for different support conditions.
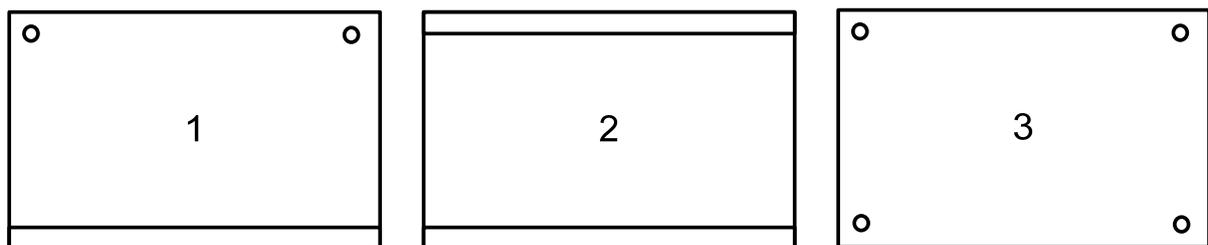
Figure 6-7: Different support conditions for slabs with one line and two simple supports, 2 line supports, and four simple supports

A slab with a line support and two single supports, a slab with two line supports, and a slab with four point supports, refer to case 1, 2, and 3, respectively (Figure 6-7). Case 1 is used as a benchmark to compare with the other cases, as it resembles the experiments carried out. All three slabs have dimensions of 4.5 x 3.5 x 0.35 m and are covered by a 0.4 m thick layer of soil.

Reaction force time histories for different support conditions are shown in Figure 6-8. As expected, the slab with two line supports (case 2) behaves stiffer than the other two, leading to a higher value of maximum reaction forces.
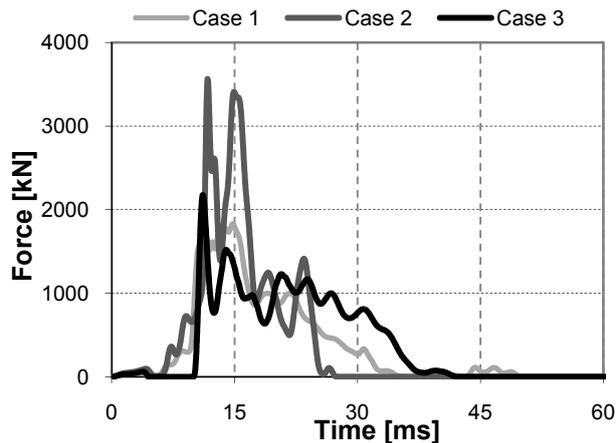
Figure 6-8: Reaction force time histories of impact on slabs with different support conditions

The mid-span deflections for the three cases are shown in Table 6-1. The deflection is lowest for the stiffest slab with two line supports. The value is highest for the slab having four point supports, which behaves with the most flexibility.

Table 6-1: Mid-span deflections of impact on slabs with different support conditions

	Case 1	Case 2	Case 3
Max mid-span deflection [mm]	8.5	7.0	12

The crack patterns are compared in Figure 6-9. For case 3 with four single supports there were no cracks formed directly over the supports. This may be due to the low impact energy ($E = 39$ kJ) the slab is subjected to. The *ER* of the slab at mid-span under this impact was 60%, which implies that the slab is far from failure.

Case 1   Case 2   Case 3
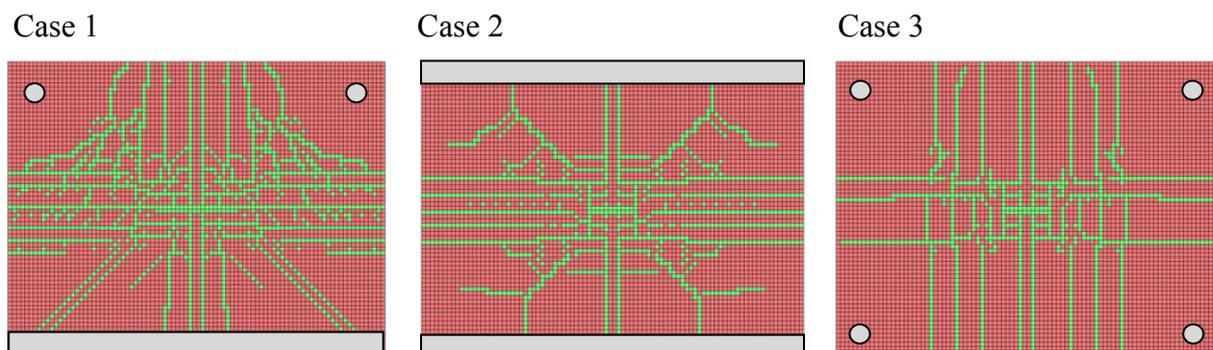
Figure 6-9: Crack patterns of impact on slabs with different support conditions

Table 6-2: Modal mass factor α for loading in center for elastic response using finite element analysis with $v = 0.2$, as well as for plastic response

Boundary condition	Yield lines	Mass factor α [-] Elastic [based on FEM] Plastic [Biggs 1964]				
		Ratio of spans L_z/L_x				
		1.4	1.2	1.0	0.8	0.6
4 restrained		0.10 0.23	0.11 0.20	0.12 0.17	0.11 0.20	0.10 0.23
2 lines 2 restrained		0.12 0.23	0.13 0.20	0.14 0.17	0.15 0.20	0.15 0.23
4 lines		0.18 0.23	0.19 0.20	0.20 0.17	0.19 0.20	0.18 0.23
2 restrained		0.12 0.33	0.14 0.33	0.18 0.33	0.23 0.33	0.26 0.33
1 line 1 restrained		0.19 0.33	0.21 0.33	0.28 0.33	0.33 0.33	0.37 0.33
2 lines		0.30 0.33	0.33 0.33	0.40 0.33	0.44 0.33	0.47 0.33
1 lines 2 points		0.36	0.37	0.43	0.43	0.48
4 points		0.45	0.46	0.47	0.46	0.45
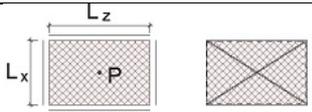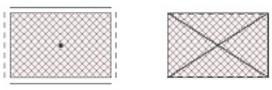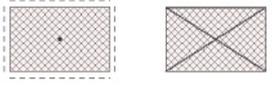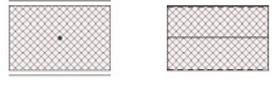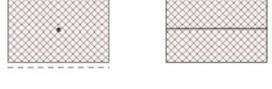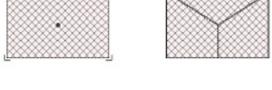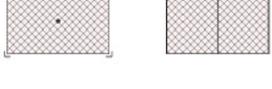
The modal mass of the structure can be calculated as:

$$M_3^* = \alpha M_3 \tag{6-15}$$

where α is the modal mass factor, and can be computed by evaluating (Biggs 1964):

$$\alpha = \frac{\iint_A m_g \phi^2(x,y)\,dx\,dy}{M_3} \tag{6-16}$$

where m_g is the mass per unit area, and $\phi(x,y)$ is the normalized deformed shape of the slab. The initial values of modal mass factors proposed by Schellenberg (2008) are updated here for different support condition and for a Poisson ratio similar to that of concrete. For a slab with a Poisson ratio of 0.2, the elastic modal mass of slabs having different support conditions is investigated using static and elastic finite element analyses (Table 6-2). Finite element analysis software SAP 2000 (2006) is used for these analyses. SAP 2000 is a commercial finite element analysis software produced by Computers and Structure, Inc., USA. The modal mass factor for plastic behavior as mentioned by Biggs (1964) is also listed in the table.

6.1.3.2 Spring

The third spring K_3 describes the global stiffness of the concrete slab taking into account an elastic-plastic behavior of the structure. Initially a bilinear model was adapted, which is replaced here by a curve with three different stiffnesses to account for pre- and post-cracking as well as the post yielding of reinforced concrete slabs (Figure 6-10). The stiffness for the elastic part of the curve up to cracking can be evaluated using the following formulation (Stiglat et al. 1993):

$$K_{30} = \frac{k_w E_c z^3}{12 L_z^2} \qquad (6\text{-}17)$$

This can be modified for the second part of the curve up to yielding to count for effective moment of inertia of the section as follows:

$$K_{31} = \frac{k_w E_c I_e}{L_x L_z^2} \qquad (6\text{-}18)$$

where k_w, I_e, and $L_{x,z}$ are the stiffness factors, effective moment of inertia of the slab, and the slab span in x and z directions, respectively. The third part of the curve can be calculated by choosing a ductility factor for post-yielding behavior of the structure.
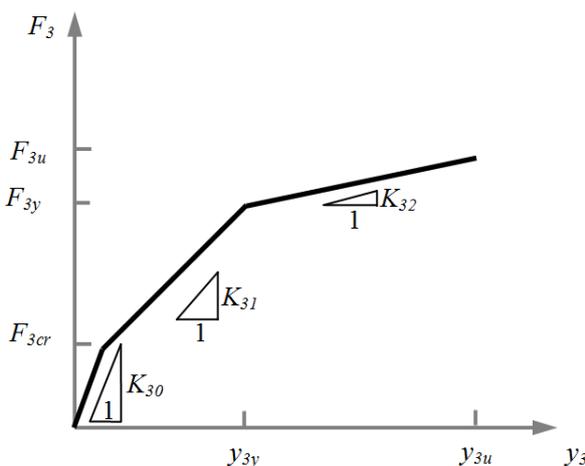
Figure 6-10: Spring properties of K3 for the global bending

The value of k_w can be calculated for different boundary conditions for elastic slabs for a single load at the slab center as follows:

$$k_w = \frac{12(F/\Delta)L_z^{\,2}}{z^3 E_c}$$

(6-19)

where F, Δ, and z are the static point load, the maximum deflection under the point load, and the thickness of the slab, respectively.

The stiffness factor k_w is calculated using the above equation for slabs with a Poisson ratio of 0.2, and for different supports conditions. Elastic finite element analyses are applied using SAP2000 software. These values are listed in Table 6-3, and can be used in equations 6-17 and 6-18 for calculating the stiffness of the slab.

Table 6-3: Stiffness factor k_w for loading in center from elastic finite element analysis with v = 0.2

Boundary condition	Yield lines		Stiffness factor k_w [-]				
			Ratio of spans L_z/L_x				
			1.4	1.2	1.0	0.8	0.6
4 restrained			150	157	184	157	150
2 lines 2 restrained			142	143	147	104	89
4 lines			70	75	89	75	70
2 restrained			141	140	135	81	61
1 line 1 restrained			98	96	89	50	37
2 lines			54	51	45	24	17
1 lines 2 points			26	30	34	21	16
4 points			15	19	26	19	15
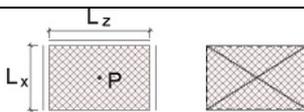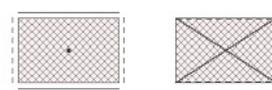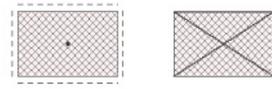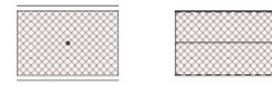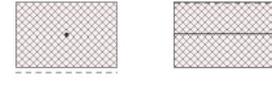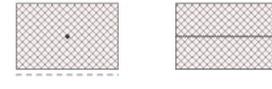
6.1.3.3 Damping

A damping ratio of $\xi = 20\%$ was used for the global behavior of the concrete slab by Schellenberg (2008). When the expected response of a structure may include plastic deformations a ratio between 5 to 20% can be assumed (Sircovich-Saar 2006).

6.2 Two degrees of freedom system

An analytical model is proposed here using a Two Degrees of Freedom System (2DFS), which replaces the soil spring with a triangular pulse load. This is a simplification of the previously described model and thus is similar to the model proposed by Eibl et al. (1988). The model incorporates an externally applied pulse load on the gallery, which represents the impact forces transmitted through the soil cushion onto the roof slab of a gallery.

6.2.1 Pulse load

The impact of a boulder onto the soil produces impact forces, which differ from the transmitted impact force through the soil to the slab. Based on the finite element analysis results, the maximum values of the transmitted impact force (defined as transmitted force) for the experiments on slab A and B were on average 1.2 times higher than the maximum values of the impact force. For these experiments, the thickness of the soil is smaller than the boulder size. As discussed in Section 5.6, the forces transmitted through the soil are higher for a thinner layer of soil. To investigate such an influence, impact B1 was modeled using an 800 mm thick layer of soil. Figure 6-11 shows the plot of impact forces and transmitted forces for impact B1 on 400 mm and 800 mm thick soil layers. It can be seen that when the thickness of soil is almost half of the boulder size (700 mm), the maximum transmitted forces are about 1.3 times the impact forces. On the other hand, for the thickness of soil almost equal to the boulder size, the transmitted forces are 0.7 times the impact forces. When a 800 mm thick layer of soil is used, the duration over which the force is transferred to the slab is almost 3 times longer compared to the slab covered with a 400 mm thick layer of soil.

a)   b)
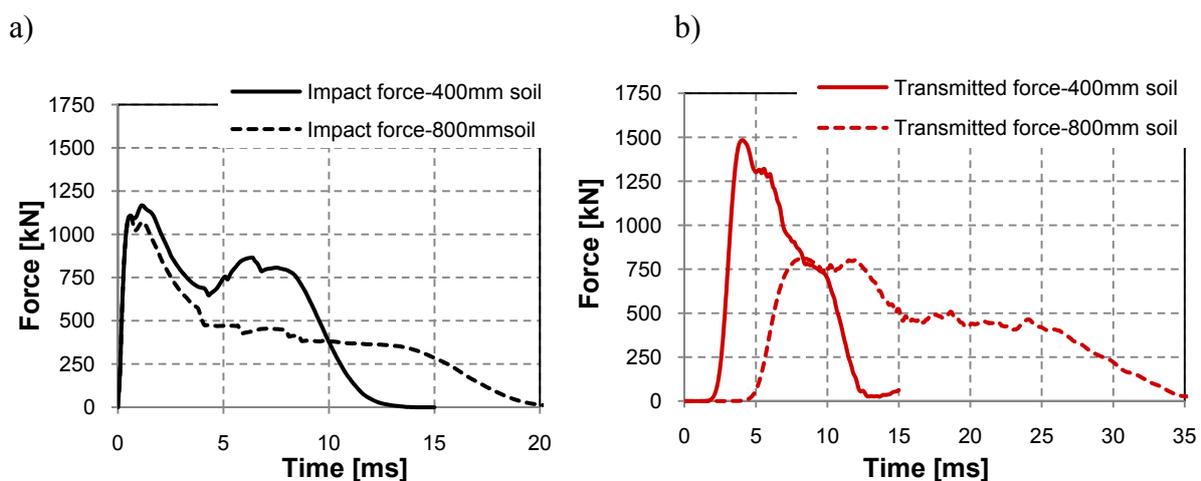
Figure 6-11: a) impact forces and b) transmitted impact forces obtained from finite element analysis for impact B1

In order to incorporate the effect of transmitted forces on the structure, as well as the effect of the boulder shape on the stiffness of soil into the analytical model, an alternate simplified

method, using a two degree of freedom system, is proposed here. External forces are applied on the slab, which resemble the transmitted impact forces. This would require the establishment of a rational method to define such a load on the structure. The analytical method can be used to solve the equation of momentum for two degrees of freedom once the external force is defined, which in this case represents the punching and global behavior of the slab, respectively. The model using a simplified triangular load pulse is shown in Figure 6-12. The abbreviations for bending and punching behavior are kept similar in order to keep it consistent with the 3DFS model.
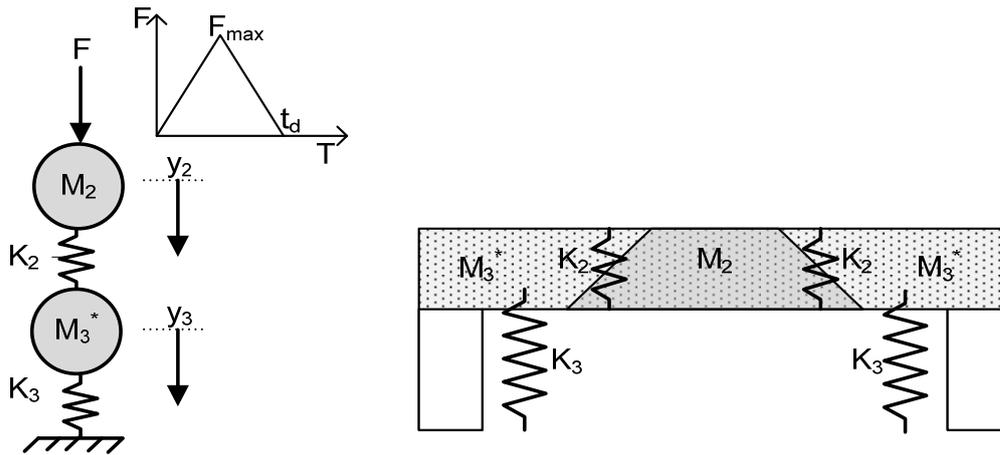
Figure 6-12: System of two degrees of freedom: model definition and load pulse

Figure 6-13 shows the transmitted impact load history obtained from finite element analysis for impact B1. The integral of the force with respect to the time for the first peak of impact load history is defined as impulse. The mean force is defined by dividing the impulse by the time duration of impact. The simplified triangular load pulse diagram is defined as having a maximum impact force, and a maximum time duration impact equal to that of the transmitted impact force history.
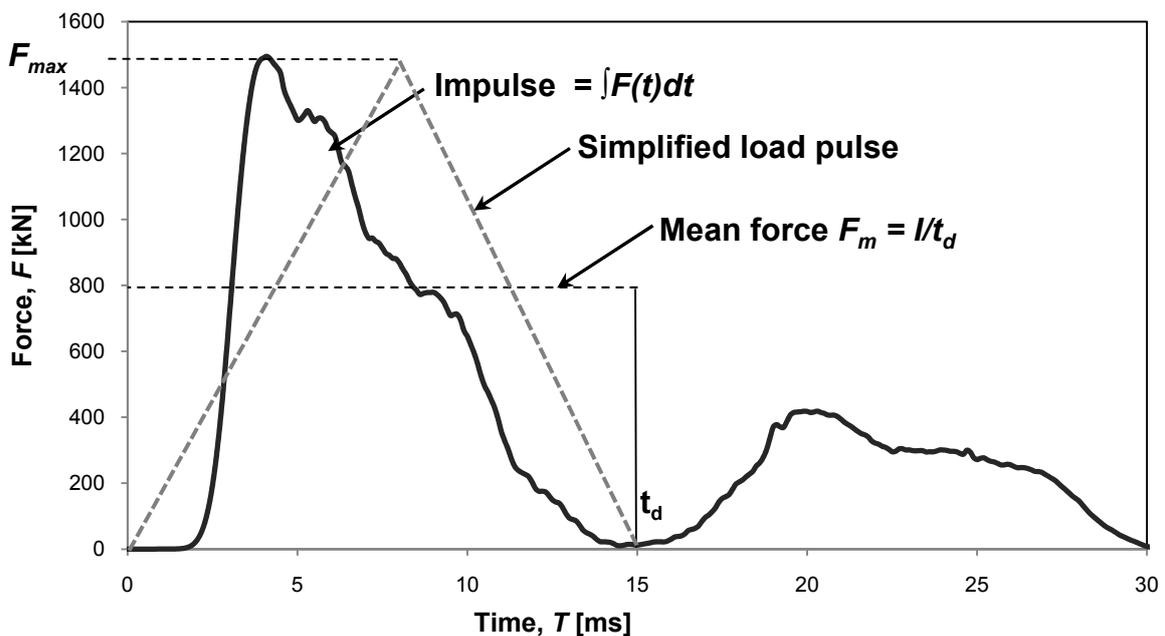
Figure 6-13 Transmitted impact load history on the slab (impact B1), and a simplified load pulse

In order to quantify the triangular pulse load rationally, an application of the work energy theorem is used here and the results obtained are compared to the transmitted force obtained from finite element analysis. According to the work energy principle, the mechanical force is equal to the change in kinetic energy, E.

$$W_E = E = \frac{1}{2} m v_0^2 \qquad \qquad (6\text{-}20)$$

Assuming an ideal plastic behavior of soil under impact, the kinetic energy of the falling body is equal to the dissipated energy. Since the work done equals the average impact force times the distance traveled by the boulder, assuming slab deflections do not influence the impact force the following equation can be formulated:

$$F_E = \frac{E}{D} \qquad \qquad (6\text{-}21)$$

where v_0, and D are the velocity of the impact, and the maximum penetration of the boulder for the given impact energy, respectively. D can be calculated using empirical formulae when the thickness of cushion layer is larger than the penetration depth. Since the penetration of the boulder was measured for each impact during experiments, F_E values can be calculated for two experimental series (slab A and B). A comparison between the average forces calculated using the work energy concept F_E and the mean transmitted impact force F_m obtained from finite element analysis (Figure 6-14 a) shows that both are almost equal.
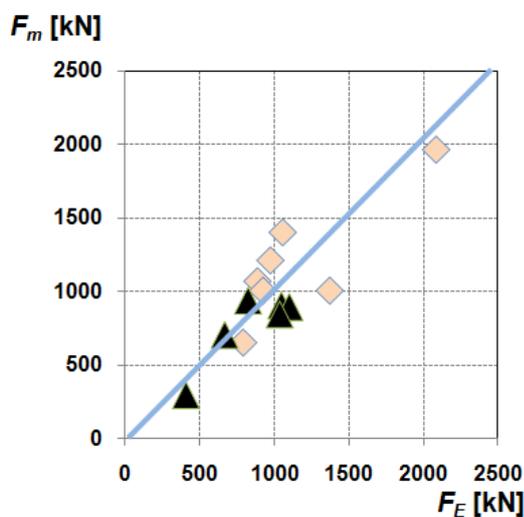
a)   b)
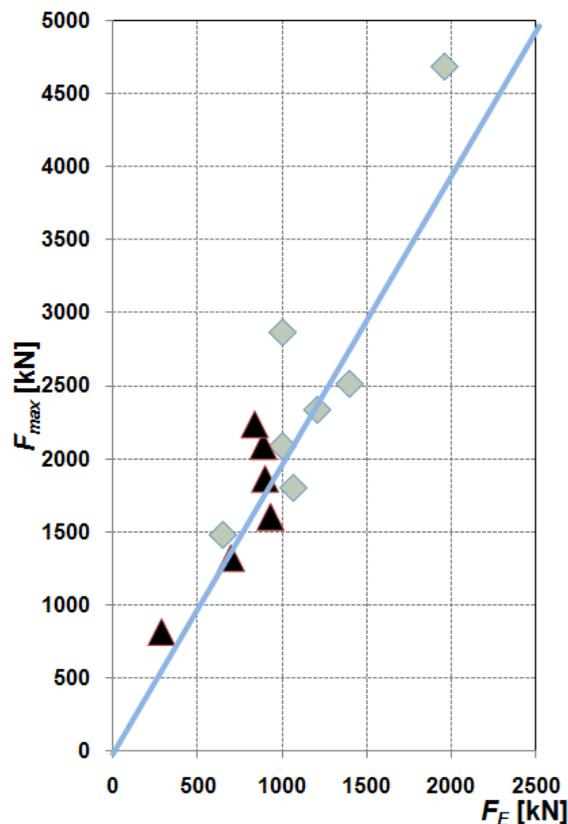
Figure 6-14: Comparison of average impact forces from the work energy principle with a) mean transmitted impact forces, and b) maximum transmitted impact forces obtained from finite elements

Comparison of the maximum transmitted impact force obtained from finite element analysis with average impact forces, on the other hand shows that they vary linearly by a factor of two.

$$F_{max} \cong 2F_E = \frac{mv_0{}^2}{D}$$
(6-22)

Therefore, it is possible to estimate the maximum transmitted impact force when the maximum penetration depth is known. The transmitted forces are larger than the impact forces for these experiments, since the thickness of soil was smaller than the boulder depth. Forces calculated using this equation are larger than the cases with thicker soil layers and are therefore on the safe side. The values of maximum transmitted impact force obtained from finite element analysis $F_{max,}$ and twice the average impact forces $2F_E$ for experimental series B are compared to the maximum impact forces calculated based on the Swiss guideline in Figure 6-15.
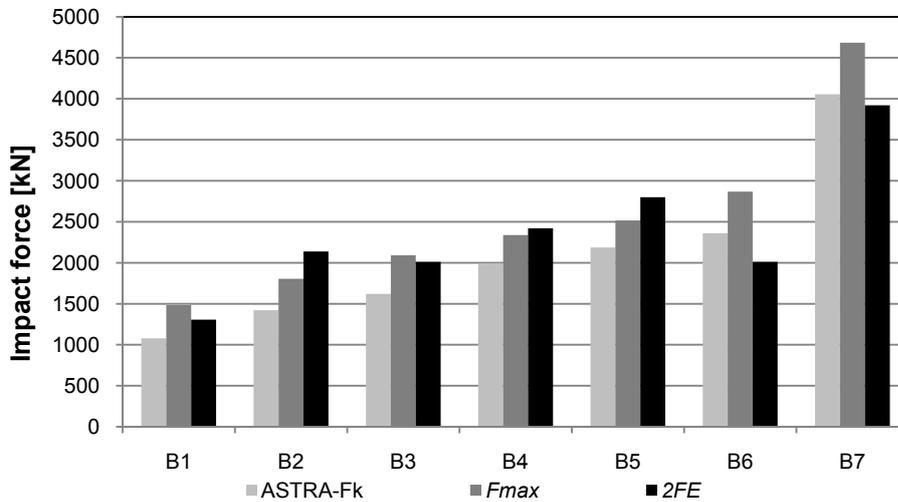
Figure 6-15: Comparison of maximum impact forces for experimental series B

There are various formulae proposed for calculation of the penetration depth of the boulder into the soil. A few of these formulae are discussed herein according to their applicability for three different assumed responses, as shown in Figure 6-2.

A method to calculate the penetration depth is the application of the dimensionless formulae for the penetration depth of concrete (Li and Chen, 2003) to the impact of boulders onto gravel, as proposed by Pichler et al. (2005). The formula is based on formulation of a slip surface as explained in Section 2.1.4. However, the depth of the slip line using this formula is formulated for concrete and is different from that of the soil expressed by Equation 6-2. Therefore it can be applied for shear behavior (soil embedment 1). These formulae are:

$$\frac{D}{2R_0} = \sqrt{\frac{1 + k\pi/4N}{(1 + I/N)} \frac{4k}{\pi} I} \qquad \text{for} \quad \frac{D}{2R_0} \le k$$

$$\frac{D}{2R_0} = \frac{2}{\pi} N \ln\left[\frac{1 + I/N}{1 + k\pi/4N}\right] + k \qquad \text{for} \quad \frac{D}{2R_0} > k$$
(6-23)

and

$$N = \frac{m}{\rho_s (2R_0)^3 BN^*}$$
(6-24)

where ρ_s is the mass density of soil, B is a dimensionless compressibility of soil ($B = 1.2$ for gravel), N^* is the nose shape function, k is the dimensionless length of surface crater, and I is a dimensionless impact function, respectively. The nose shape function is in the range of $0 < N^* \leq 1$, with, $N^* = 1$ for flat, and $N^* = 0.5$ for hemispherical nose, respectively. I and k can be defined as:

$$I = \frac{m v_0^2}{R_i (2R_0)^3}$$
(6-25)

and

$$k = 0.707 + \frac{H_i}{2R_0}$$
(6-26)

where R is the indentation resistance of the target material, $2R_0$ is the diameter of the impacting body, and H_i is the height of the impactor nose, respectively. The value of R_i used in this formula, however, needs quantification based on experiments. Pichler et al. (2005) carried out some impact experiments on gravely soil and proposed a median value of $9.22 \cdot 10^6$ Pa. Back calculating from the experimental series of slab A and B, the average value of R is $6.33 \cdot 10^7$ Pa. The formula proposed by Pichler can be used to calculate the penetration depth. However, a typical value of indentation resistance R_i should be validated by further experiments on soil. This formula can underpredict the soil behavior based on the selection of the value of indentation resistance. In addition, it does not include the effect of draining and pore water pressure of the soil layer.

Another formula for calculating the maximum impact force is provided by the Swiss guideline according to Equation 2-1. The penetration depth for the maximum impact force, therefore, can be calculated according to Equation 6-21. The range of the experiments, on the bases of which the formula is developed, corresponds to soil embedment 2 (see Section 6.1.1.2).

One of the well known formulations for penetration of projectiles into the soil has been summarized by Young (1967). There is an update to the equation published in 1997 (Young 1997). According to this equation, the penetration depth of a projectile into a uniform layer of concrete or soil (excluding frozen soil) is given by:

for $v_0 < 200$ fps (61 m/s)

$$D = 0.3 \cdot S \cdot N \cdot (\frac{W_b}{A})^{0.7} \ln(1 + 2v_0^2 10^{-5})$$

for $v_0 \geq 200$ fps (61 m/s)

$$D_{[in]} = 0.00178 \cdot S \cdot N \cdot (\frac{W_b}{A})^{0.7} \ln(v_0 - 100)$$
(6-27)

$$D_{[mm]} = 25.4 * D_{[in]}$$
(6-28)

where, S, N, W_b, and A are the penetrability of the target (dimensionless), nose performance coefficient (dimensionless), weight of the impacting body (lbs), and cross-sectional area (in^2), respectively.

If the weight of boulder is low, both equations have to be multiplied by a factor K_s; for soil:

$$K_s = 0.2(W_b)^{0.4} \qquad\qquad \text{when } W_b < 60 \text{ lbs (27 kg)} \qquad\qquad (6\text{-}29)$$

For tangent ogive nose shapes, the nose performance coefficient can be obtained from:

$$N = 0.18\frac{H_i}{R_0} + 0.56 \qquad\qquad\qquad\qquad (6\text{-}30)$$

and for conical shapes:

$$N = 0.25\frac{H_i}{R_0} + 0.56 \qquad\qquad\qquad\qquad (6\text{-}31)$$

where, H_i is the length of the penetrator nose.

S ranges between 4 and 6 for gravel deposits and sands without cementation and from 8 to 10 for soil fill material, depending on compaction. The equation was developed based on more than 160 full-scale earth penetration tests with different shapes of projectile and with impact velocities ranging between 33 to 325 m/s. When a projectile impacts the earth surface and moves through the soil, it punches through the soil layer. Therefore, this formula is used for soil embedment 3 (see Section 6.1.1.2).

The results of the penetration depths obtained from the formula of Pichler et al. (2005) assuming the average R for experimental series A (impact energies up to 118 kJ) and B (impact energies up to 196 kJ) are plotted against experimental data in Figure 6-16. In addition, the penetration depths obtained from the formula of Young (1997) and the Swiss guideline (ASTRA 2008) are shown. Compared to the diagonal line denoting parity, it is seen that since the experiments were in the range of the case soil embedment 2, the values obtained from the formula of the Swiss guideline provides the best match. Values of N and S using Young's formula are assumed to be 1 and 10, respectively. N using Pichler's formula is set to 1.4. Young's formula is not used for the 2DFS, since it provides a large scatter from experimental data.

According to Bucher (1997), the impact time can be estimated using the following formula:

$$t_d = \frac{2D}{v_0} \pm 30\% \qquad\qquad\qquad\qquad (6\text{-}32)$$

This model can incorporate other load pulse diagrams easily. For example, a synthetic input impact force time history is also proposed by Calvetti & di Prisco (2009). The definition of the proposed curve depends on reference impact force and reference impact energy.
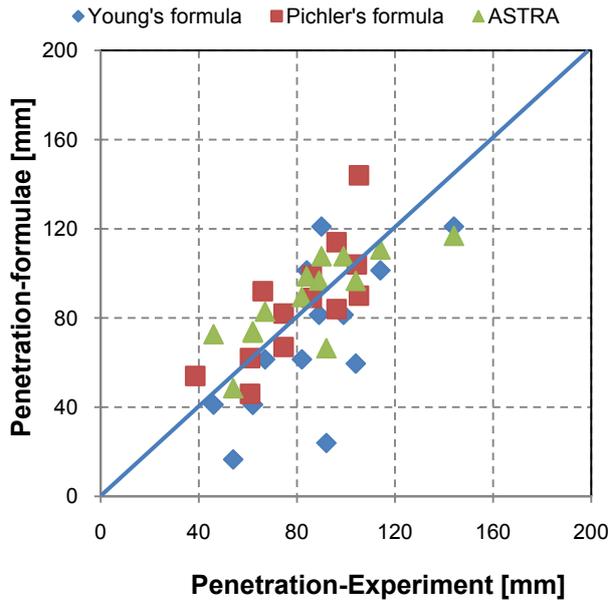
Figure 6-16: Penetration depths obtained from different formulae for experimental series A and B

6.2.2 The first degree of freedom

Once F_{max} and t_d are evaluated, the triangular pulse load can be defined. The structure is then analyzed for this load using two masses and two springs. The first spring is similar to the second spring defined when using a three degrees of freedom system, as outlined in Section 6.1.2. M_2 is the mass of the punching cone of concrete. Since the soil mass is not included in the punching cone for this model, the mass M_2 can be expressed as:

$$M_2 = \frac{\pi}{12}[\gamma_c z(3\emptyset_{sl}^2 + 6\emptyset_{sl}z + 4z^2)] \tag{6-33}$$

where $\emptyset_{sl}$ is calculated according to equations 6-11 to 6-12.

Spring K_2 represents the shear stiffness for the assumed punching shear failure of the concrete slab, which is calculated according to Section 6.1.2.2.

6.2.3 The second degree of freedom

The second degree of freedom can be defined similar to the third degree of freedom using a three degrees of freedom system, which is outlined in Section 6.1.3.

M_3^* is the modal mass of the structure which can be calculated according to Section 6.1.3.1.

Spring K_3 describes the global stiffness of the concrete slab, which can be defined according to Section 6.1.3.2.

6.3 Comparison of results and discussions

The analytical models using the three degrees of freedom system and the two degrees of freedom system are validated against the experimental results, in order to verify the simplifications made for the selection of the physical parameters. The experimental series B (Section 4.1.1) is used for this validation. The parameters for both models (2DFS and 3DFS) are chosen according to sections 6.1 and 6.2, and are outlined in Table 6-4. The input parameters listed in the table are used for calculating spring forces using the MATLAB codes (Appendix C).

Table 6-4: Input parameters used for analytical models and their definition

Parameter	Unit	Definition
Input parameters for 2DFS		
B	[-]	Dimensionless compressibility of soil (Pichler's formula)
H_i	[m]	Height of the impactor nose
R_i	[MPa]	Indentation resistance of the target material
S	[-]	Penetrability of the target (Young's formula)
Input parameters for 3DFS		
c	[N/m^2]	Cohesion in the soil
E	[MPa]	Young's modulus of soil
G	[MPa]	Shear modulus of soil
N_γ, N_q, N_c	[-]	Constants depending on angel of friction
s_γ, s_q, s_c	[-]	Shape factors according to Terzaghi's formula
Common input parameters for both models		
A_{sg}	[%]	Ultimate strain of reinforcement
e	[m]	Thickness of the cushion layer
E_c, E_s	[MPa]	Young's modulus of concrete, and steel reinforcement
f_{cm}	[MPa]	Mean compressive strength of concrete
f_y	[MPa]	Yielding stress of steel reinforcement
g	[m/s^2]	Acceleration due to the gravity
k_w	[-]	Stiffness factor calculated according to Section 6.1.3.2
L_x, L_z	[m]	Length of the slab in x or in z direction

m	[kg]	Mass of the impacting boulder, M_1 in 3DFS
Q_u/M_u	[-]	The ratio of ultimate load to ultimate moment based on yield line theory
R_0	[m]	Equivalent radius of a sphere with similar volume as the impacting body
R_1	[m]	Size of the impacting body (radius or half of the length)
s, s'	[m]	Spacing of tensile, and compressive reinforcement
u, u'	[m]	Concrete cover for bottom and top layer of reinforcement
v_0	[m/s]	Impact velocity of the boulder
z	[m]	Slab thickness
α	[-]	Modal mass factor calculated according to Section 6.1.3.1
γ_c	[kN/m^3]	Unit weight of concrete
v	[-]	Poisson's ratio of the cushion layer
ξ	[-]	Damping ratio of the structure for punching or bending
φ	[°]	Angle of internal friction of the cushion layer
ρ_s	[kg/m^3]	Density of the cushion layer
$\emptyset, \emptyset'$	[m]	Diameter of tensile, and compressive reinforcement
$\emptyset_s, s_s$	[m]	Diameter, and spacing of shear reinforcement

Maximum slab deflections and maximum reaction forces obtained for test series B, using the analytical models, are compared to the experiments in Figure 6-17 a and b. The maximum displacement of the spring representing the global behavior of the slab is compared to the slab deflections. These are maximum values of displacements y_{23} using both models. The slab deflections obtained using 2DFS and 3DFS methods are overestimated compared to the experiments. However, the ones using 2DFS provide a closer agreement. The deflections obtained from analytical models depend on the stiffness defined for the global behavior of the slab. The model considers the stiffness of the full section before cracking and effective stiffness of the cracked section up to yielding. The post yielding stiffness is roughly obtained assuming a ductility factor for the slab, therefore the value for the ultimate deflection is overestimated. This puts the evaluation of the ultimate load on a safe side. The resulting forces in the spring representing the global behavior of the slab are compared to the maximum reaction forces. These are the maximum values of the spring forces F_3 using 2DFS and 3DFS. The maximum reaction forces obtained using 2DFS and 3DFS are in good agreement with the experiments. The reaction forces and deflections are important while considering the global response of the structure; therefore, analytical models perform well in predicting the overall behavior of structure.

A plot of the reaction forces of the slab vs. slab deflection for the first peak of the slab response, for impact B7 is shown in Figure 6-17 c, which corresponds to the force and displacement of the spring representing the global behavior of the slab. The post peak response of the slab is highly influence by its damping, thus only the first peak is considered

here. The maximum and the residual displacement of the slab during impact B7, which led to slab failure, is shown. The elastic recovery (*ER*) of the slab calculated using the criterion (introduced for FE in Section 4.3) amounts to 22 and 19% for the model using 2DFS and 3DFS, respectively. This indicates that a failure criterion using the *ER* concept can also be applied to account for failure using the analytical model. It can be noticed that the upper bound solution overestimating the global behavior stiffness after yielding is on the safe side when establishing the failure criteria based on the ratio of ultimate to yielding load (Schellenberg 2008). On the other hand, this would lead to a lower value of residual deflection and it would not be on the safe side if the failure criterion is based on the residual deflections (*ER* concept). Therefore, a higher margin of safety should be used, while applying the criterion to the analytical model. An *ER* ratio of 25 to 30 can be used to account for failure using the analytical models.

a)

b)

c)
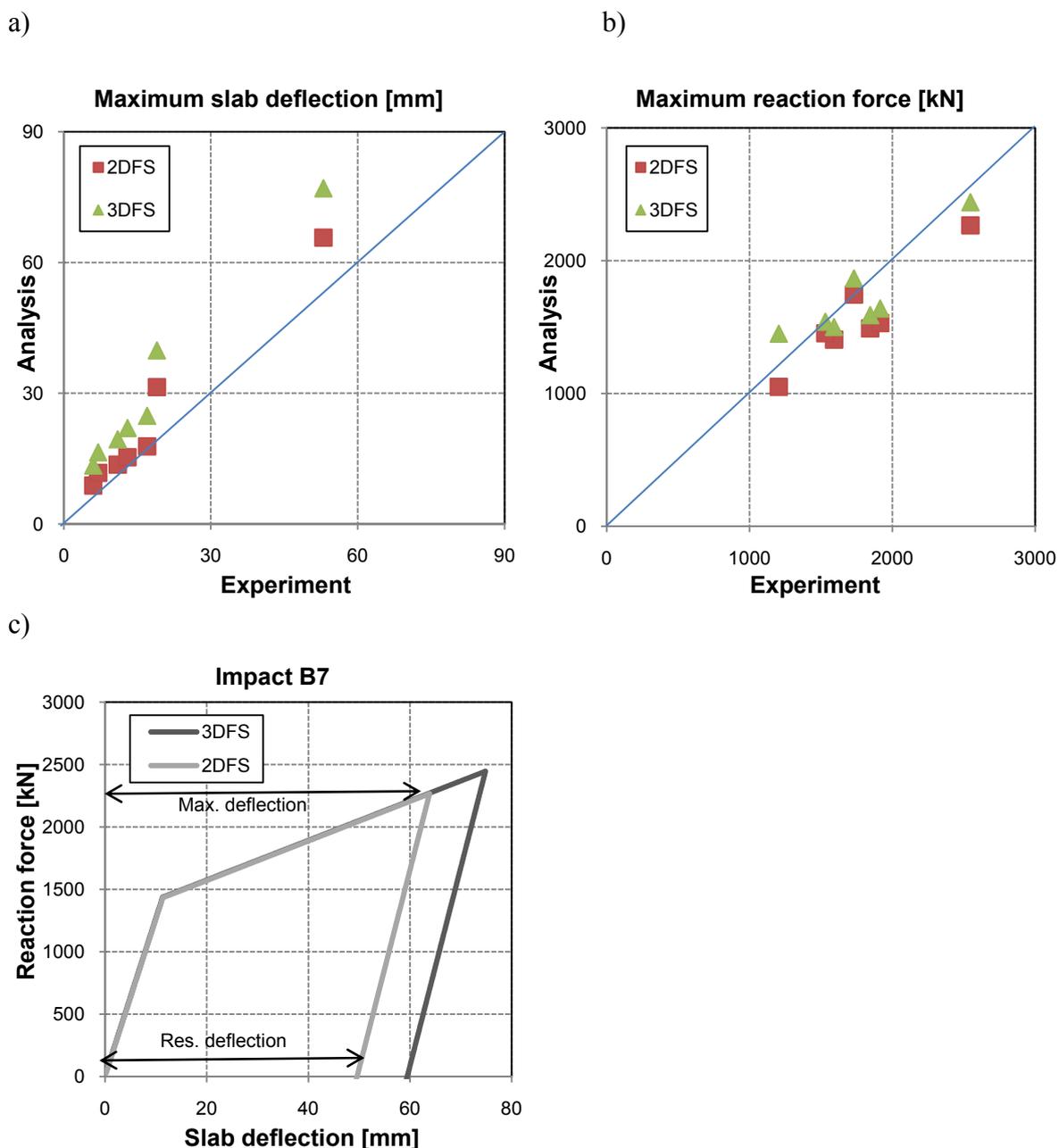
Figure 6-17: Slab response values for the B series obtained using different analytical models a) maximum slab deflections, b) maximum reaction forces, and c) force deflection for impact B7

The maximum penetration depth of the boulder in the soil and the maximum impact forces are compared to the experiments in Figure 6-18 a. The penetration depth for the 2DFS is calculated on the basis of the pulse load definition using different empirical formulae based on the thickness of the soil layer as explained in Section 6.2. The maximum relative displacement of the first spring y_1-y_2 using the 3DFS accounts for a penetration depth calculated based on this model. The penetration depth of the boulder is not well predicted using the analytical model. The empirical formulae used for 2DFS provide a better match. The values calculated based on 3DFS are conservative since the model represents compression hardening behavior for the range of this experimental series (Figure 6-4 a). The finite element results for penetration depth are in good agreement with the experimental ones.

a)

b)

c)
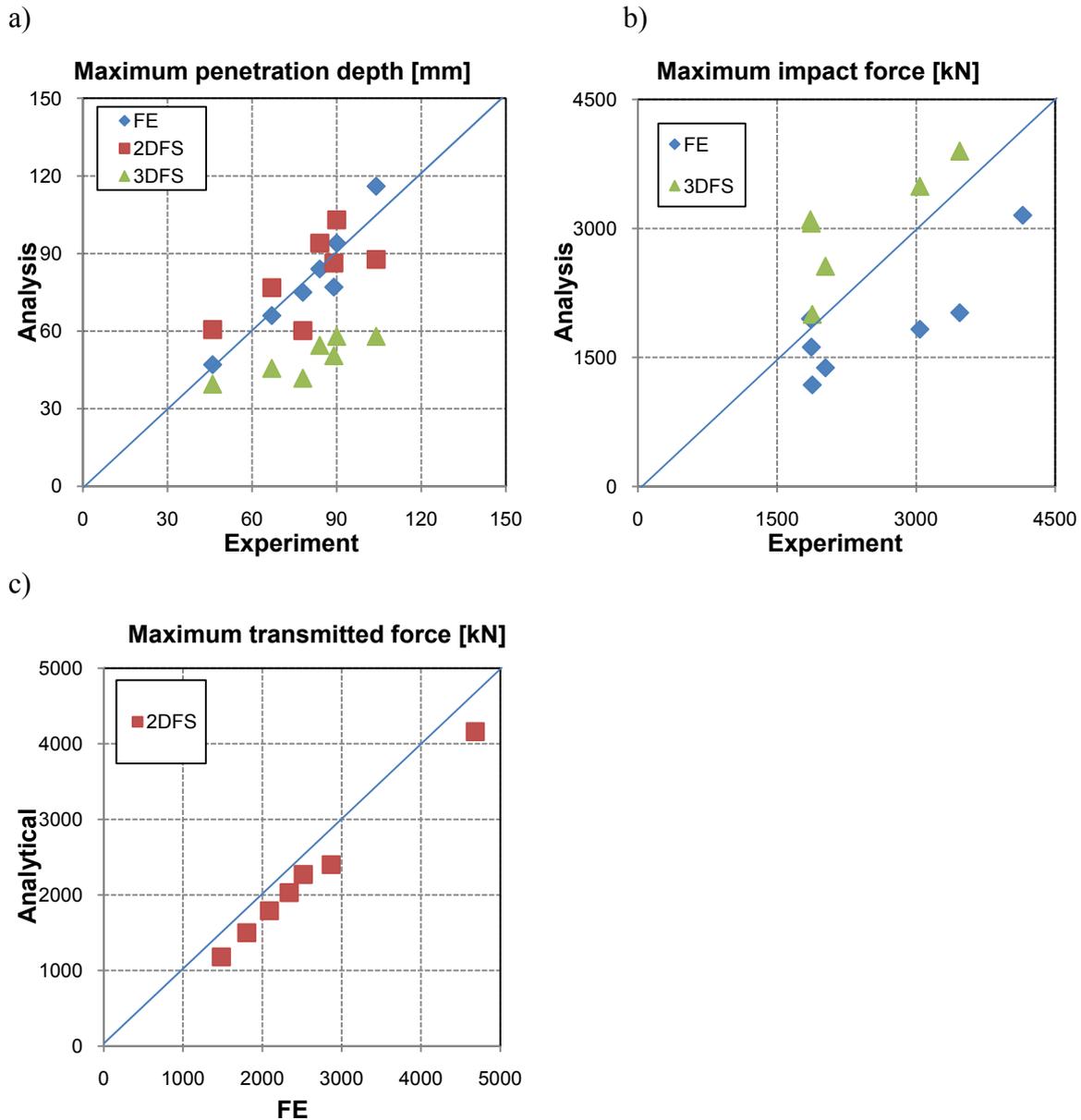
Figure 6-18: Response of soil for B series obtained using different analytical models a) maximum penetration depths, b) maximum impact forces, and c) maximum transmitted impact forces

A comparison between the impact forces obtained using 3DFS and FE with the experiments is shown in Figure 6-18 b. The impact forces calculated using 2DFS can be compared to transmitted impact forces, which are not measured during the experiments and therefore are

not shown on this diagram. The resulting forces in the first spring of the 3DFS are referred to impact forces of the boulder onto the soil and are compared to impact forces calculated based on the acceleration measured in the experiments, which shows the values obtained from 3DFS are more conservative (since they underestimate the penetration depth). The maximum impact forces using finite element analysis are smaller than the experimental data. The forces using finite element analysis are calculated as the interface forces between the impacting boulder and the layer of soil based on the penalty method (see Fiacco & McCormick 1968) by defining master and slave segments. The element size and aspect ratio as well as the stiffness of both master and slave segment influence the results. The contact stiffness is computed for each segment on master and slave side and the smaller value is used. However, the soil response in terms of maximum penetration depth of the boulder into the soil is accurately predicted using finite element analysis (6-18 a). The impact forces obtained using 2DFS on the basis of the empirical formulae are compared to the transmitted impact forces obtained by using finite element analysis in Figure 6-18 c. A good agreement is shown between the two. From the comparison of the above results, it is seen that the overall behavior of a slab can be evaluated by using both analytical models. However, the penetration depth of the boulder and the impact forces are hard to obtain accurately. This implies that a deeper look into the soil behavior is necessary in order to evaluate the capacity of the reinforced concrete galleries.

The failure criterion using the 3DFS model was proposed using relative values for punching and bending failure (Schellenberg 2008). For punching failure, the ratio of maximum punching forces to ultimate punching capacity η_p is used, where $\eta_p = 1$ corresponds to the ultimate limit state. The ratio of maximum reaction forces to the reaction forces at yielding η_b is used for flexure. Ultimate limit state in bending is assumed by $\eta_b = 1.2$. The prediction of yield load using an upper bound solution is on a safe side. The yield load calculated for series B was about 1420 kN. This is based on static yielding of the section and is lower than the actual yielding load of the slab under dynamic load. Considering a factor of 1.2, the slab should fail when the reaction force is 1700 kN. During the experiment, this value was reached under impact B4, therefore this assumption overestimates the forces at failure. The maximum reaction force obtained during impact B7 was 2500 kN. A dynamic increase factor can be added to the factor of 1.2 to reach a closer agreement. The punching failure can be evaluated using the forces in the spring representing the punching cone. Punching failure occurs when the punching force reaches the maximum force concrete can take in tension, once the tensile strength of the concrete is reached the failure is assumed to happen for slabs without shear reinforcement.

The values using the 2DFS do not incorporate Young's formulation since, as explained earlier, it did not provide a good agreement with the experiments. Therefore, for a thin layer of soil (case soil embedment 3, see Section 6.1.1.2) the formula of the Swiss guideline is used for the penetration depth less than half of the soil thickness, and for larger penetration depth, the formulation proposed by Pichler is used.

To verify the physical parameters of the model further, large-scale experiments carried out by Yamaguchi et al. (2010) are validated using the analytical model. The test setup is shown in Figure 2-4 b. Two falling-weight impact tests are carried out on 5 x 4 x 0.4 m slabs (see Section 2.1.2). A 5 tonne boulder is dropped on the center of each slab from heights of 10 and

15 m, respectively. The slabs were covered by a 0.5 m thick layer of soil and were simply supported on two sides. Tensile and compression reinforcement of 19 mm in diameter are placed at a spacing of 125 mm in both directions. The comparison of the maximum response values are shown in Table 6-5.

It is seen from this comparison that the analytical methods overestimate the response values of the structure. The maximum impact forces calculated using 2DFS and 3DFS are on average 2 and 3 times higher than the experimental measurements. It should be noted that the maximum impact force using 2DFS is calculated based on empirical formulae and represents the maximum transmitted impact forces, which may be higher than the impact forces. The slab deflections are 1.6 and 2.3 times higher using 2DFS and 3DFS, respectively. The main challenge here is to choose the appropriate parameters for the soil cushion in order to obtain a reasonable agreement for impact forces. Both methods are, however, on the safe side by overestimating the impact force, but the behavior of soil needs to be further investigated in order to obtain a closer agreement. The soil cushion used during the experiments was rather loose, which also contributes to the mismatch of results. In addition, the 2DFS model predicted accurately the cases with impact energies up to 200 kJ where the Swiss guideline is valid. The results are rather conservative for energies up to 600 kJ since the equation of Swiss design guideline has been extrapolated conservatively. Time durations of the impact forces calculated using analytical models are smaller than in the experiments. However, the time duration of the main triangular peak during the experiments was less than 40 ms. The time durations of the modeled reaction forces are in good agreement with the experiments.

Table 6-5: Comparison of results for large-scale experiment (Yamaguchi et al. 2010)

$H = 10$ m ($E = 490$ kJ)	**Experiment**	**2DFS**	**3DFS**
Max. impact force [kN]	2510	4000	7700
Time duration of impact [ms]	75	35	20
Max. reaction force [kN]	1490	2560	3240
Time duration of reaction [ms]	70	61	57
Max. slab deflection [mm]	64	101	157
$H = 12.5$ m ($E = 613$ kJ)	**Experiment**	**2DFS**	**3DFS**
Max. impact force [kN]	2970	7420	8900
Time duration of impact [ms]	75	21	18
Max. reaction force [kN]	1522	3000	3540
Time duration of reaction [ms]	80	57	58
Max. slab deflection [mm]	86	137	181.5

7 Case study

The rockfall protection gallery Axen-Süd was analyzed by applying a system of multiple degrees of freedom (SMDF) proposed by Schellenberg (2008). The same gallery is used for the current case study in order to compare the numerical results with those derived from the analytical solutions. Moreover, the gallery is analyzed using the three degrees of freedom system (Section 6.1), as well as the two degrees of freedom system (Section 6.2). In addition, a probabilistic analysis of the gallery, as performed by Schubert et al. (2010), is also used for this comparison.

The gallery is composed of a reinforced concrete slab, monolithically connected to a back wall at the rock face, and supported on columns with a spacing of 7.5 m on the valley side (Figure 7-1 a). The slab has a variable thickness of 0.4-0.7 m. The cushion layer has a variable thickness with a maximum of 1 m at the supporting back wall. The impact location is assumed to be at mid-span of the slab, and the thickness of soil at this location is about 0.8 m.

7.1 Finite element model

The behavior of the gallery is studied using finite element analysis. The finite element model of the gallery is shown in 7-1 b. The finite element mesh of the gallery is prepared in collaboration with Muroran Institute of Technology, Japan. Finite element modeling aspects as explained in Chapter 3 are incorporated and the material models for concrete, reinforcement, and soil cushion are adapted accordingly.
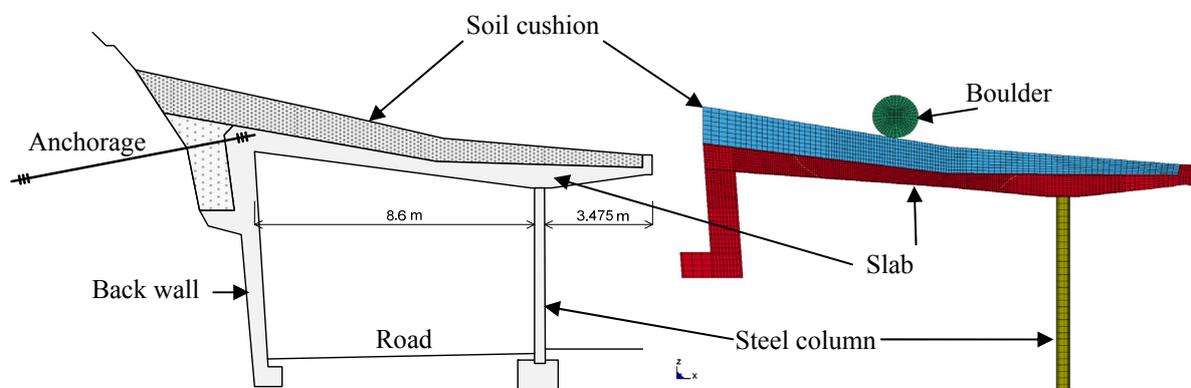
Figure 7-1: Gallery at Axenstrasse a) cross sectional view, and b) finite element mesh

The impact due to single loading is considered, and the effect of consecutive loading and pre-damage on the slab is not incorporated. The columns and the back wall are assumed to have fix support conditions. A concrete compressive strength of 35 MPa, and a tensile strength of 3.5 MPa are used for these models. The yield strength of steel is 500 MPa. A global damping ratio of 2% is assumed for the structure. The impactor is modeled as elastic material with a Young modulus of 30 GPa. A bilinear material model as used for reinforcement (Section 3.3.2) is adapted for the steel columns with a yield strength of 500 MPa. The soil parameters, as listed in Table 3-1, are used for the modeling.

The three-dimensional model and the reinforcement layout of the gallery are shown in Figure 7-2. Impact energies up to 2.7 MJ are modeled using finite element analysis. Boulders with weights ranging from 2500 to 4000 kg are assumed to fall on the slab from heights up to 90 m. All boulders have a diameter of 1.2 m and only the density of the boulders is varied.

a)

b)

Diameters in [mm]
at section A-A
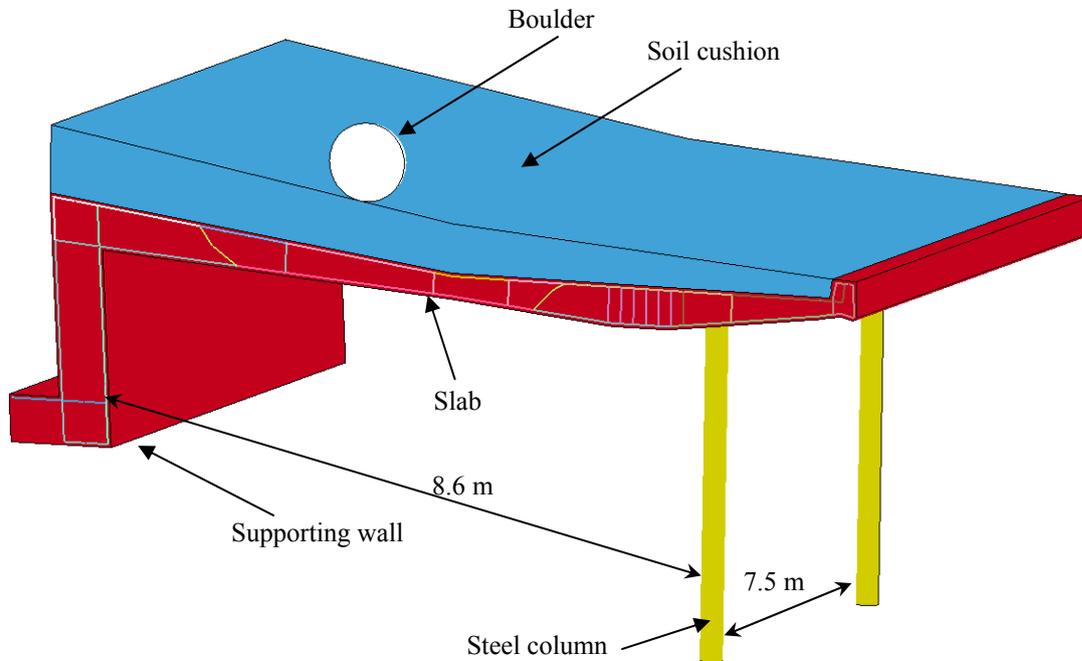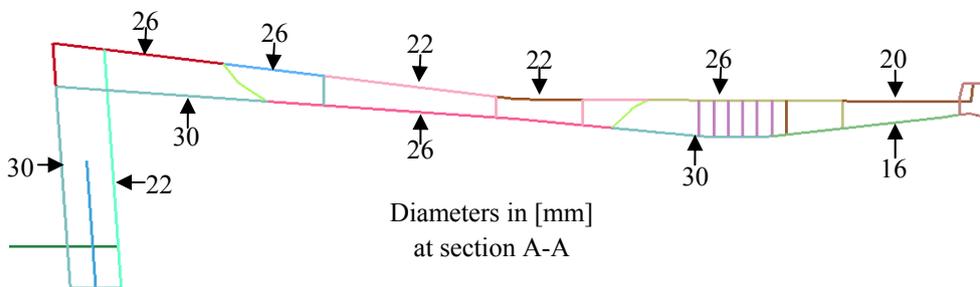
c)
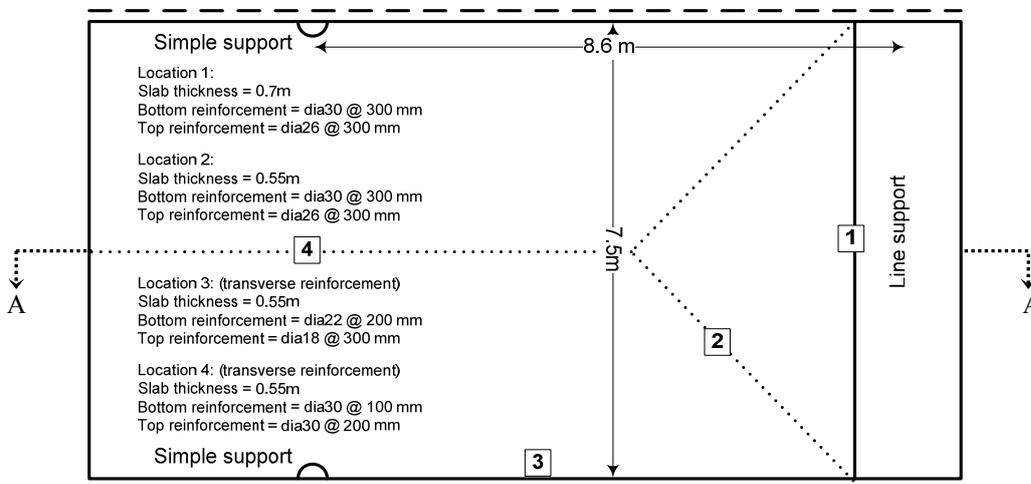
Figure 7-2 Gallery at Axenstrasse a) finite element model b) reinforcement diameters at mid-span section between two columns, and c) overview of reinforcement at various locations (not scaled)

The concept of elastic recovery (*ER*), as mentioned in Chapter 4, is used here to evaluate the capacity and response of the gallery using finite element analysis. The *ER*-values used here are approximate since the slab did not come to a full rest and continued oscillating during the analysis. The slab should be subjected to a critical damping ratio after the impact, using the consecutive impact modeling method proposed in Section 4.1.2.2, for a more accurate evaluation. Since the procedure for a full gallery model requires a large computational time, only the approximate values are used here. A typical curve for the elastic recovery of the section obtained by finite element analysis is shown in Figure 7-3. The rapid change of shape of the curve below the impact zone may refer to a concentration of punching forces at this section.
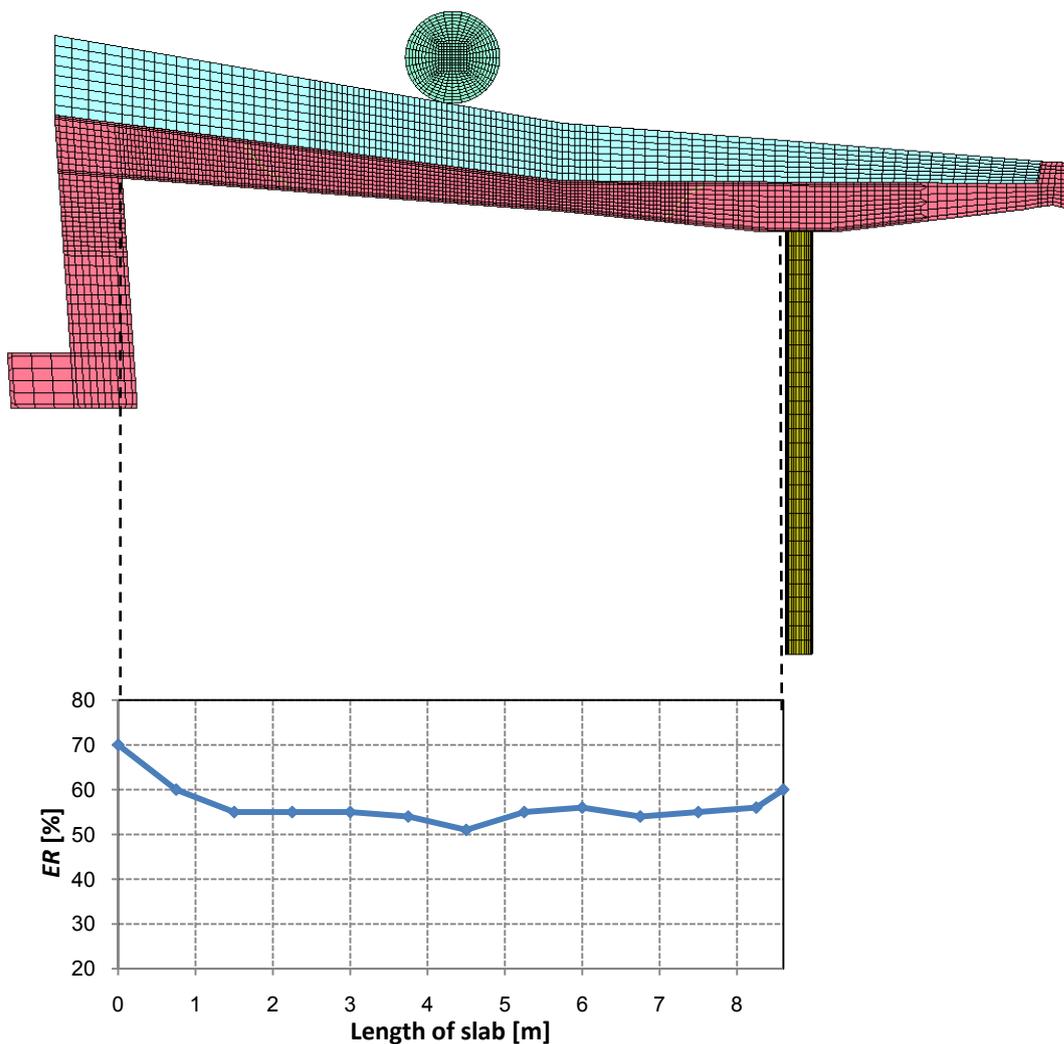
Figure 7-3: Elastic recovery distribution along the section of the gallery for E = 1.76 MJ

7.2 Results and discussions

The results obtained from analyses of the gallery using the analytical models (2DFS and 3DFS), as well as the finite element analysis, are compared in this section.

Figure 7-4 shows the comparison of the load carrying capacity of the slab using SMDF as proposed by Schellenberg (2008) with the improved model (3DFS). The ultimate load

carrying capacity of the slab is evaluated using the analytical models for different sizes of rocks and different falling heights of the boulder. The bending failure for this calculation is reached when the maximum forces in the third spring exceed the maximum ultimate capacity of the slab.

The differences in the bending capacity between the SMDF and the 3DFS are due to several factors, one of which is the selection of input parameters for the modal mass of the slab and the stiffness factor for the global behavior of the slab. The modal mass factors, α used for the old and the improved models are 0.2 and 0.33, respectively. The stiffness ratios, k_w are 33 and 26 using the old and the improved models. It is seen that the choice of the modal mass and stiffness factors has a very high influence in predicting the global response of the gallery. A proper selection of these factors, therefore, is important in order to estimate the bending capacity. By selecting a smaller value for the modal mass, for instance by assuming a plastic behavior, the prediction is on the safe side. The bending stiffness of the gallery, in addition to the mentioned factors, has a high influence on the behavior. The effective stiffness of a cracked section is considered for 3DFS, while elastic stiffness is considered for the SMDF model assuming the whole concrete section is effective before yielding. The yielding of the slab happens at a lower deflection if elastic behavior is assumed, which is adding up to the difference between the two curves. An additional influence is the difference of soil models used and specially the soil damping. A constant soil damping of 7000 Ns/m is assumed in the SMDF model. The soil damping using 3DFS changes depending on the penetration depth and is different. For example, for a 3000 kg boulder falling from a height of 90 m the maximum value of soil damping is 236'000 Ns/m. The accelerations in the other springs are not influenced by this damping in the 3DFS analysis.
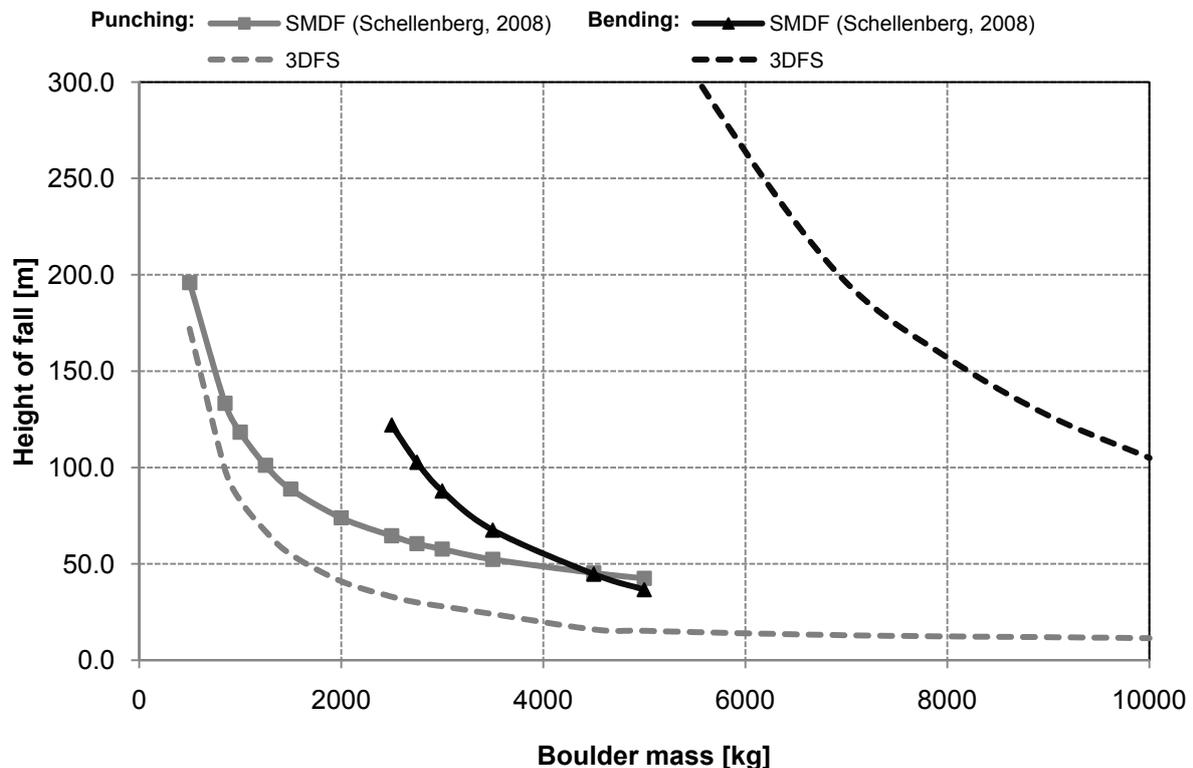
Figure 7-4: Load carrying capacity of the gallery at Axenstrasse using 3DFS

The punching capacity evaluated using the 3DFS model shows more conservative estimates than the SMDF model. The punching failure using the 3DFS is reached when the concrete has reached its tensile strength. The SMDF model considers tension softening for the concrete after this point and therefore the punching failure happens later than in case of the 3DFS.

A further comparison of the load carrying capacity of the gallery is shown in Figure 7-5. A ratio of boulder mass to contact area is used here since the punching capacity of the gallery depends not only on the mass of the boulder but also on the area of the boulder hitting the gallery. In a real situation, a gallery may be hit by an arbitrary boulder where the dimension of each edge would be different. The 2DFS, the 3DFS, and the finite element analysis are used for this comparison. Punching is evaluated to be the governing mode of failure using both 2DFS and 3DFS for this gallery.

It is not possible to distinguish between bending and punching failure mode using finite element analysis for this gallery, since both happen at the same location. Estimates for three different impacts, which led to an *ER* of 40% are shown as single points in this figure. The slab has not reached a failure using finite element analysis based on this criterion for all three points (*ER* = 20% for failure). These points are above the line which represents punching failure using 3DFS and 2DFS. The 3DFS seems to largely overestimate the impact forces and lead to very conservative estimates of the punching capacity of the gallery. The bending capacity of the gallery obtained using the 2DFS and the 3DFS show a smaller difference compared to the punching capacity. This indicates that the soil behavior (the impact load time history) has higher influence on the local behavior of the slab than on its global behavior. The gallery was designed to sustain the impact of a 2500 kg boulder falling from a height of 70 m. According to the 3DFS analysis, the gallery should fail in punching if this boulder is falling from a height of 33 m. The 2DFS shows that the gallery can fail in punching subjected to the impact of a 2500 kg boulder falling from a height of 80 m. The finite element results for the gallery subjected to its design load show that the gallery can sustain this impact without failure. The *ER* ratio of the slab at the zone below the impact is determined to be 44% using finite element analysis, which has not reached the failure criterion of 20% for the slab without shear reinforcement. The *ER* threshold value for failure for this gallery must be set to be larger than 20%. The gallery has some bent bars, which help to restore the residual deflections, even though it does not have shear reinforcement. A value of *ER* = 30% can be assumed for this case.
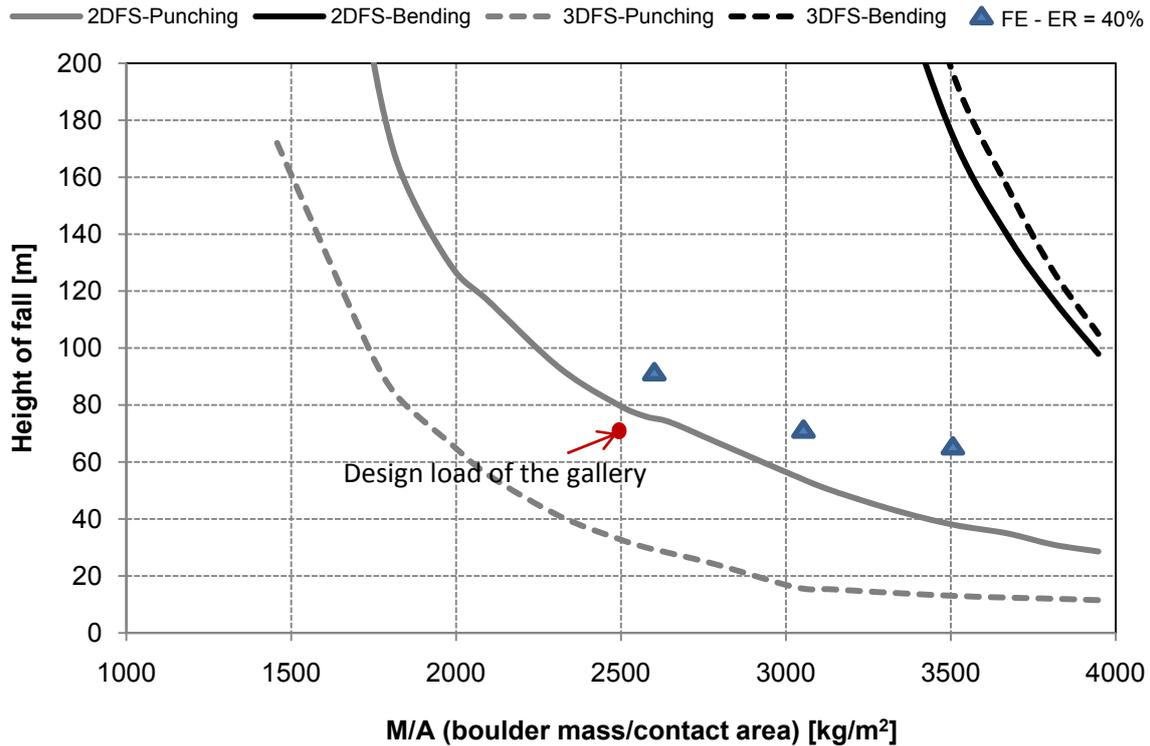
Figure 7-5: Load carrying capacity of the Gallery at Axenstrasse using 2DFS and 3DFS

A further comparison is made for evaluating the capacity of the gallery using finite element methods as well as the 2DFS, and the 3DFS. A boulder of 3000 kg with a radius of 600 mm is dropped from a height of 90 m on the center of the gallery. This is one of the FE points shown on Figure 7-5, where the gallery did not failed based on finite element results (ER = 40%). The maximum penetration of the boulder during impact obtained from finite element analysis is compared to the results obtained from 2DFS and 3DFS in Table 7-1. The soil model using 3DFS behaves very stiffly and the penetration depth obtained using this formula is about 3 times lower than those obtained from finite element analysis. The value is obtained using 3DFS assuming a shear modulus of 50 MPa for soil. The penetration depth will increase to 192 mm if the modulus is reduced to 30 MPa, since the soil stiffness is reduced.

Table 7-1: Comparison of penetration depth of the boulder for Axen-Süd (E = 2.7 MJ)

H = 90 m *M* = 3000 kg	**FE**	**2DFS**	**3DFS**
Max. penetration [mm]	554	414	162

The comparison of the response of the gallery using the finite element analysis, and analytical models is demonstrated in Figure 7-6. The impact force time history obtained from the 3DFS (Figure 7-6 a) shows a peak that is four times higher than the value obtained from finite element analysis, whereas the duration of the impact is four times shorter. The transmitted impact force time history obtained from 2DFS is demonstrated in comparison with the curve obtained from finite element analysis (Figure 7-6 b). The peak value and shape of the curve obtained from 2DFS follows the first peak of the FE curve closely, but the loading occurs

faster. The second peak of the FE curve is due to the contribution of the self weight of the soil, since some part of the soil cushion is detached from the slab initially and reimpacts the slab later. The time duration of the transmitted impact using the 2DFS is shorter compared to the FE curve.

The comparison of the slab deflection, using all three models as demonstrated in Figure 7-6 c, shows that the peak value and the time duration of the maximum deflections are similar to each other. The 2DFS provides a closer match to the finite element results for the peak value of slab deflections. The analysis must run for a longer time duration using analytical models until the slab comes to a full rest.

a)

b)

c)
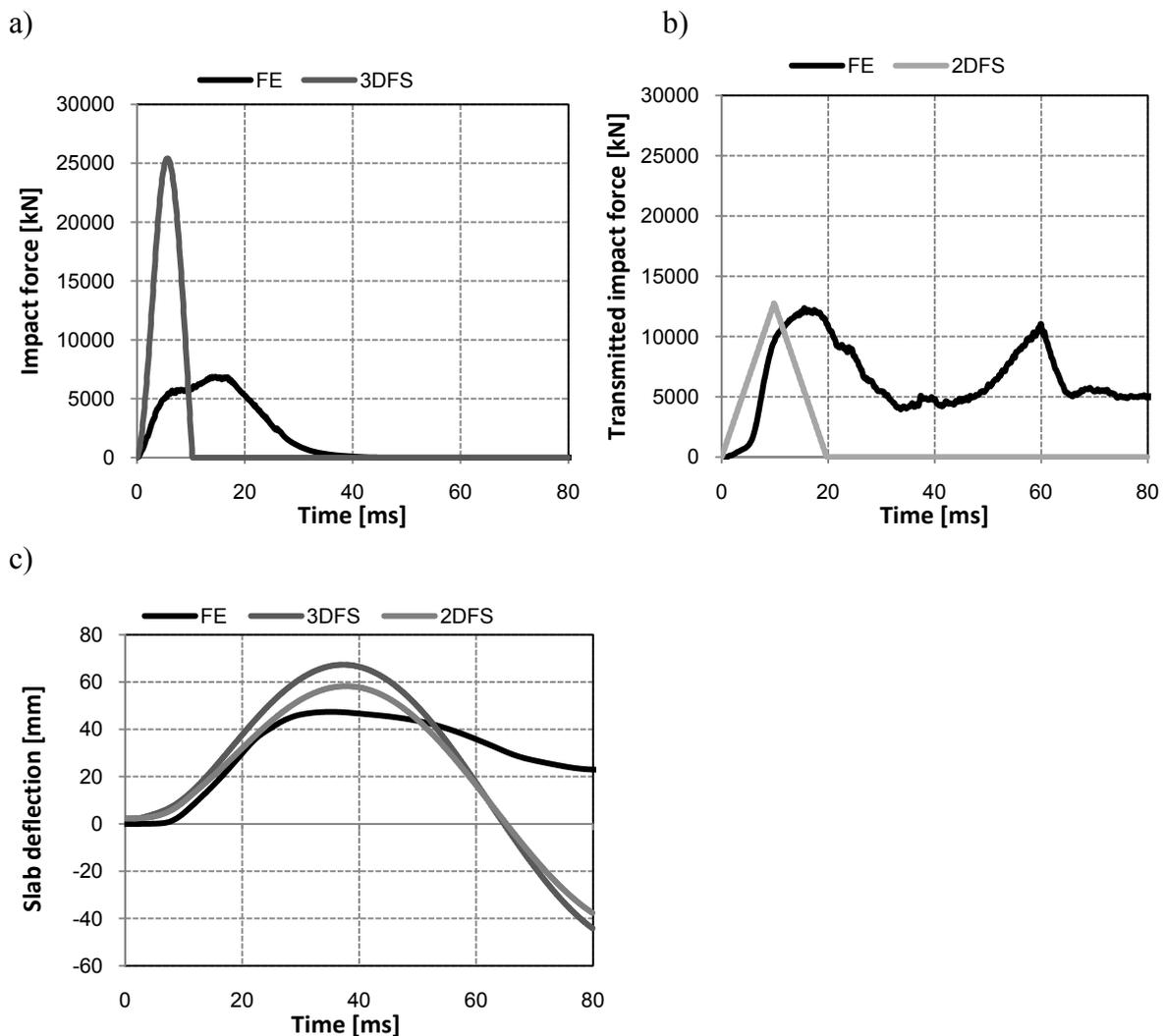
Figure 7-6: Comparison of the response of the Gallery at Axenstrasse using numerical and analytical models

The crack patterns of the gallery obtained from finite element plots of zero stresses (fringe levels between -0.001 to 0.001), for the impact of a 3000 kg boulder falling from a height of 90 m, are shown in Figure 7-7. Formation of punching cracks can be observed below the impact zones, which are extended diagonally towards the line support and the columns. Shear cracks that are formed in diagonal direction can be seen next to the columns. In addition, bending cracks are formed, which are extended horizontally towards the edge supported between the line support and the columns. The shear forces above the columns should be

109

treated separately while designing the gallery using analytical methods, since they model the overall bending behavior of the gallery. The spring forces F_3 obtained from the 2DFS and the 3DFS models can be used for the shear evaluation at the column, by assuming the amount of global reaction force taken by the column.
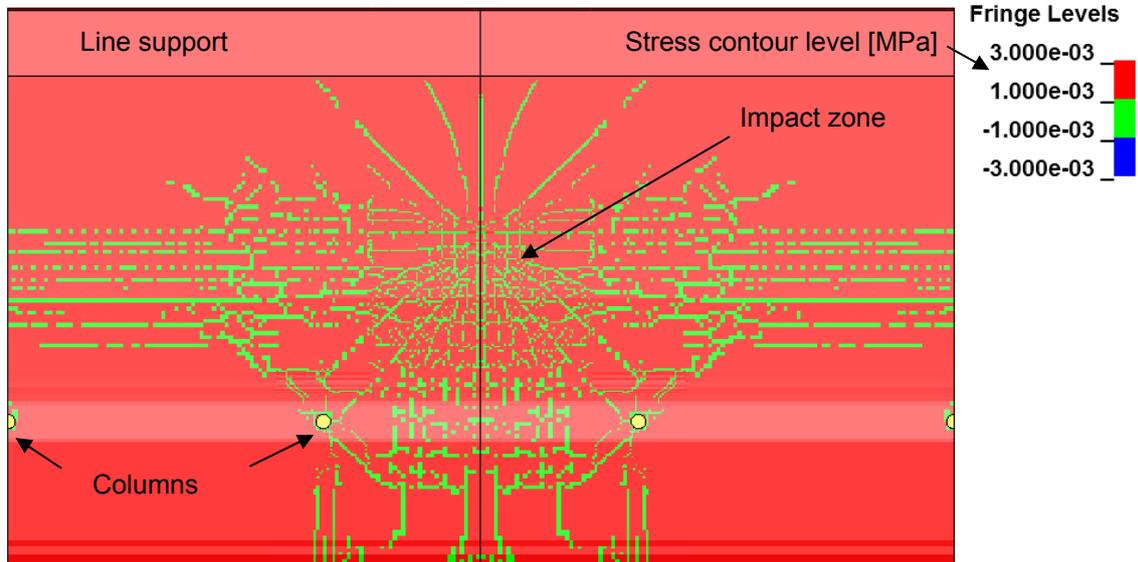
Figure 7-7: Crack patterns of the gallery at Axenstrasse for E = 2.7 MJ

The bending capacity of the gallery is illustrated in terms of the elastic recovery obtained from 2DFS in Figure 7-8 for two different boulder masses. The initial *ER* value of 60% here refers to the cracking of concrete; after cracking the value decreases slightly until the yielding is reached. After this, the *ER* reduces at a large rate until the failure is reached. The punching failure as shown in the figure happened at much lower impact energy (2.2 or 2.5 MJ), before the bending capacity is reached. The punching limit has been reached between the cracking and the yielding of the slab in bending. The slab subjected to impact of a smaller boulder had a lower punching capacity.
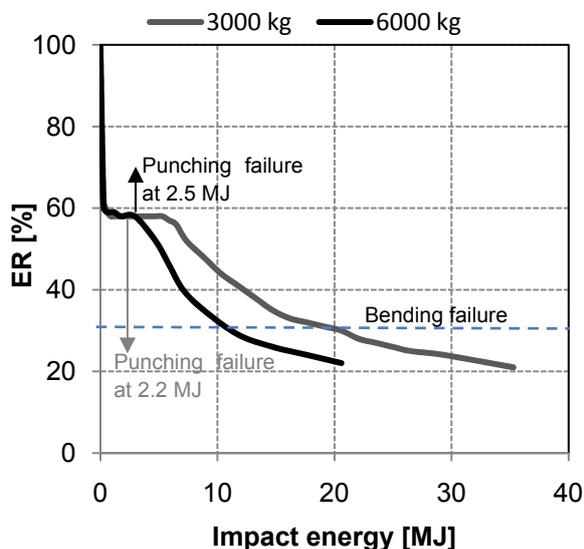
Figure 7-8: Bending capacity of the gallery using 2DFS

A study of probability of failure of the gallery was carried out by Schubert et al. (2010). The SMDF model was used to define the failure for a probabilistic model in order to obtain vulnerability curves. The vulnerability curve for the gallery, assuming an average slab thickness of 0.55 m and a 0.55 m thick cushion layer using the material properties based on the Swiss design code SIA 262 (2003), is shown in Figure 7-9. A C30/37 concrete and B500B/A reinforcement characterized as per the Swiss design code is chosen for the calculation. The evaluation of punching failure for different masses of boulder and impact velocities for this case obtained using the 2DFS model is shown by black squares on the diagram. The probability of the failure for these evaluations is between 0.5 and 1.0 for all the points. These points should fall into the zone with 100% failure probability, if calculated using the SMDF model, which implies that once the uncertainties were incorporated in to the predication, the failure could be roughly predicted, even if different prediction model or different assumptions are used for determining the capacity of the gallery. Such vulnerability curves can also be generated using probabilistic analysis based on the 2DFS and the 3DFS. Probabilistic analysis enables us to incorporate different uncertainties, which for example design related or material related.
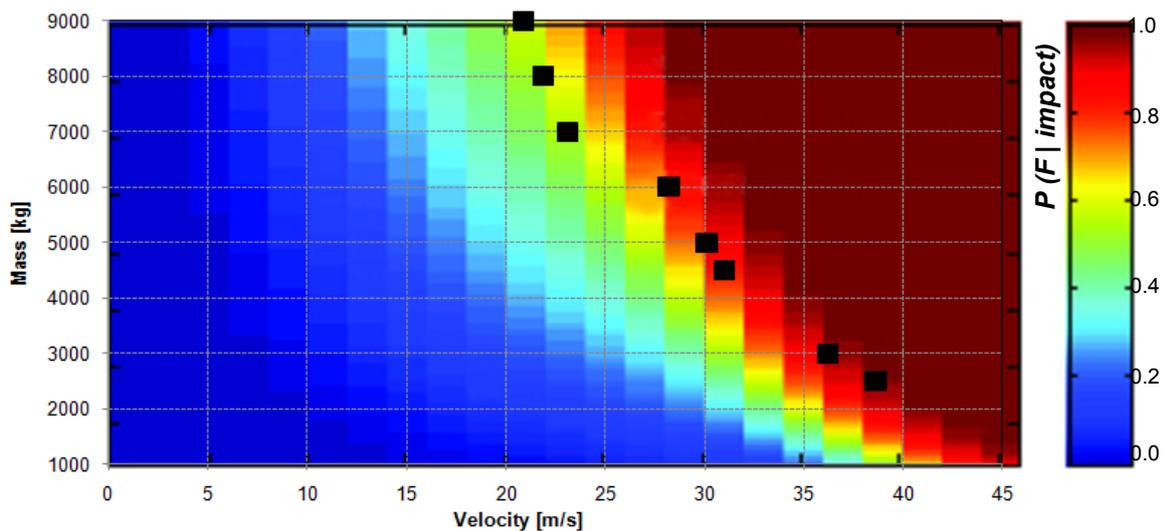
Figure 7-9: A two-dimensional vulnerability curve of the gallery with 0.55 m thick layer of soil (Schubert et al. 2010)

8 Conclusions and prospects

8.1 Overview

This dissertation deals with the numerical simulation of rockfall impacts on reinforced concrete slabs, most of which were covered by a soil cushion. A numerical analysis method using finite element analysis is proposed and the applicability of the method is verified in comparison with existing experimental data up to an impact energy of 300 kJ. A failure criterion is established in order to account for failure using elastic-plastic finite element analysis. In addition, a numerical analysis procedure is developed to model consecutive impacts on reinforced concrete slabs. The finite element analyses are applied to extend the physical tests performed numerically, by using the failure criterion suggested. The influences of the boulder shape, reinforcement behavior, and consecutive impact loading on the response of slabs are investigated. Finite element analyses are used to calibrate the input parameters and to acquire suitable assumptions for an existing analytical model using a system with three degrees of freedom. In addition, an analytical model using two degrees of freedom is proposed. The validity applicability of the analytical models is discussed by comparison to experiments and using a case study.

The main findings of this study, based on the numerical and the analytical methods, and further research opportunities and an outlook are discussed in the following sections. A new performance-based design procedure, called elastic recovery-based design, is proposed to define the performance of galleries on the basis of the knowledge gained and the findings presented in this research.

8.2 Conclusions

It can be concluded, based on the results obtained that finite element methods perform well in predicting the impact capacity of rockfall protection galleries subjected to single and consecutive impact loadings. Suitable modeling of soil cushion was performed by applying a cap-hardening model, which takes the shear and hardening behavior of the soil into consideration. The model represented the behavior of the soil under impact loading well.

The analysis method used here has limitations regarding the post-yielding behavior of concrete, since it does not consider the failure. Therefore, it was important to establish the definition of a failure criterion to limit the design of the concrete slab, rather than only considering the resulting sectional stresses. A residual/maximum displacement-based failure criterion was proposed in this dissertation, which can be used to account for failure using both finite element analysis as well as analytical models.

It is suggested that an elastic recovery threshold of less than 20% using finite element analysis and less than 30% using the analytical models may be used to account for the failure of slabs without shear reinforcement.

The physical models available were able to simulate the impact on the slab covered by a gravel layer only up to energies of 600 kJ. The finite element analyses based on the mentioned failure criterion could extrapolate the simulations numerically for higher input energy levels of up to 2700 kJ for the case study of a real scale gallery.

A new numerical analysis procedure was established, which enables modeling of the slabs subjected to consecutive impact loading. This has facilitated the understanding of the slab response after previous rockfall impacts, by incorporating their loading history. It is seen that if the slab is subjected to consecutive impacts with the same energy, the maximum deflection the slab sustains during every impact remains the same.

Analytical models using two and three degrees of freedom systems can be applied to evaluate the response of the galleries. The effect of the soil thickness on the distribution of the stresses in the soil cushion was studied using numerical analyses, and different distribution of the load on the slab was assumed for analytical model based on this comparison. It was found that the three degrees of freedom system overestimates the impact forces in the spring representing the soil, which puts the evaluation of the response on the safe side.

The new model using a system of two degrees of freedom has been defined by applying external forces to the slab, which resemble the transmitted impact forces between the cushion layer and the slab. This can be calculated by assuming that the slab behaves like a rigid boundary and the behavior of the slab is then analyzed independently of the behavior of the cushion layer. The results obtained from this model show a closer agreement to the experimental data compared with the model using a three degrees of freedom system, but it is still on the safe side by overestimating the forces acting on the gallery.

The analytical models are developed on the basis of physically justified behavior (punching and bending) of the galleries and offer an efficient way to carry out a performance based design of these structures.

8.3 Proposed elastic recovery-based design (ERBD) procedure

A performance-based design procedure is proposed for the design of rockfall protection galleries, incorporating the knowledge gained in this dissertation. A short overview of the background of the performance-based concept that is used for seismic design is presented, before discussing the procedure established for the design of the rockfall impact problem.

Performance-based design procedures were initially introduced for seismic design of buildings by Gulkan & Sozen (1974), and Shibata & Sozen (1976). The structural performance was considered on the basis of displacements in terms of the level of the damage to the structure and a displacement-based seismic criterion was proposed by Priestley (1993). Therefore, the seismic design of buildings shifted towards a displacement-based design. Performance-based design of frame structures based on residual displacements, which measure the residual drifts of single degree of freedom (SDOF) systems as well as multiple degrees of freedom (MDOF) systems are proposed by Christopoulos et al. (2002) and Pampanin et al. (2003).

It is important to select an appropriate performance level for each structure when carrying out performance-based design of structures. Traditionally, the performance level for seismic design is chosen based on a residual deflection of the building. On the other hand, a criterion using a performance level based on residual/maximum displacement ratios was proposed to compute the residual displacement for a number of SDOF systems, which are then extended to the response of MDOF systems through a series of nonlinear analyses (Christopoulos & Pampanin 2004).

A performance-based design procedure is established in this study, which can be applied to the design of rockfall protection galleries using a residual/maximum design ratio. The design criterion based on elastic recovery of the slab, as suggested in Chapter 4, is used for this purpose. The criterion considers not only the residual deflections of rockfall protection galleries under impact, but also the maximum deflection of the slab under the impact loading. The procedure proposed in this study is called elastic recovery-based design, since the elastic recovery is used as the criterion to define the performance of galleries. 2DFS, 3DFS, or finite element methods as outlined in earlier chapters, can be applied for modeling the structure using the ERBD design procedure. Finite element methods can be used when higher accuracy is desired. The 2DFS or 3DFS can be chosen depending on the duration of impact and the natural period of the structure. When the duration of impact is lower than the natural period of the structure, the structure does not yet deform when the impact forces are acting on the soil and an uncoupled solution using 2DFS can be used. Otherwise, 3DFS should be used in analyzing the response of the gallery.

The procedure flow chart for design of rockfall protection galleries is shown in Figure 8-1. The resulting procedure can be summarized as follows:

1. A design criterion is set based on the target performance level, depending on the acceptable probability of failure for a given rockfall event;

2. The geometry and the material properties are defined and the gallery is modeled using numerical methods (2DFS, 3DFS, or finite element analyses);

3. Analysis is performed to calculate the elastic recovery for the given design criterion. If the target performance level is met, the resulting forces are determined and the performance of the structural elements is checked against the design requirements.

The elastic recovery of a typical reinforced concrete slab is shown in step 3 of the procedure (Figure 8-1), where *ER*, *MD*, and *RD*, are the elastic recovery, maximum deflection, and residual deflection of the slab, respectively. It must be noted that punching must be treated separately to bending for analysis using 2DFS and 3DFS.

Step 1: Design Criterion

Hazard	Vulnerability	Probability

No damage   Inelastic behavior   Severe damage

- Impacting mass
- Impacting velocity

ER [%]

100

Collapse

Acceptable probability of failure
or
Acceptable consequences

Assigned for return period
e.g. 30 or 100 years

Impact load [kN]
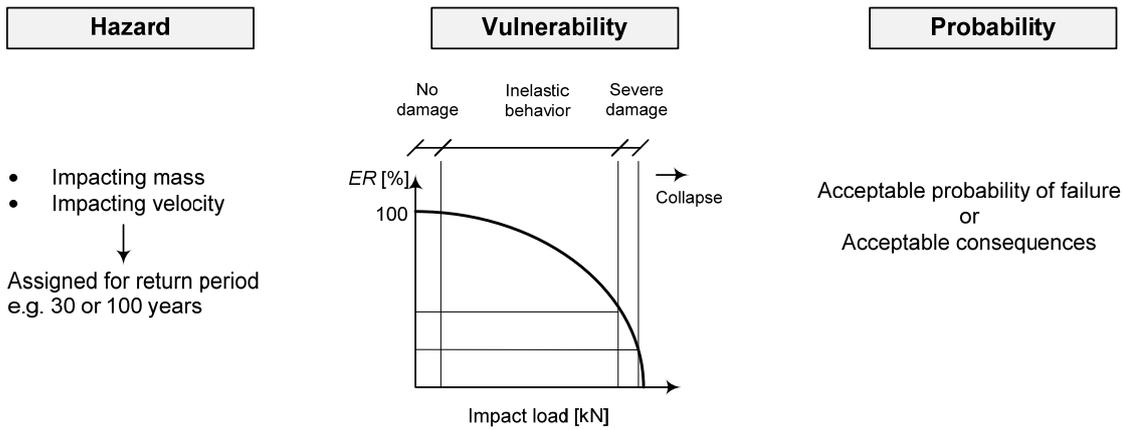
Set ER for target performance level

Step 2: Modeling

- **Define the geometry**
- **Select material and properties**
- **Structural modeling (2DFS, 3DFS, or FE)**

F

F_{max}

t_d

T

F

M_1 y_1

K_1

M_2 y_2

K_2

Step 3: Analysis

- **Calculate the residual deflections and maximum deflections for given design criterion**

F_2

$ER = 1 - (RD/MD)$

F_u
F_y

F_{crack}

y_{crack} y_y y_u y_2

RD

MD

No	Is ER for target performance level met?

Yes

- **Determine the resulting forces**
- **Check performance of structural elements**

ER [%]

100

Target performance

Impact load [kN]

Design members

Figure 8-1: ERBD procedure for a rockfall protection gallery using numerical modeling

8.4 Outlook

The study on the dynamic capacity of the protection galleries can be projected further by a follow-up research, which has been started in 2011 by Christina Röthlin. This study can combine the expertise gained by the experimental, analytical, numerical, and probabilistic modeling and apply them to a round-robin prediction of a full-scale experiment. A full-scale falling-weight test will be performed on a real gallery either making sure that the concrete roof of the gallery remains elastic and does not crack, or for large energies until the collapse of the roof, if the galley is no longer used. A full-scale experiment can validate the assumptions made for the numerical and the analytical models.

The knowledge gained from different rockfall research projects carried out in Switzerland and abroad should be applied for development of a simple design procedure for engineers in practice and to improve the existing guideline. The elastic recovery-based or any other appropriate failure criterion can be used in order to develop a static equivalent design procedure, which corresponds to the dynamic response of a gallery leading to the same probability of failure. Therefore, the modeling uncertainties have to be considered by variation of all parameters involved.

The focus of this study was on reinforced concrete galleries. The analytical models proposed, can be applied to other cases, such as prestressed or composite galleries, by evaluating their global stiffness and by adequately defining the spring representing the global behavior of the gallery. The influence of prestressing on the punching capacity of slabs subjected to the impact loading should be incorporated in terms of the membrane action.

There is a possibility that the columns at both ends of a gallery sustain direct impacts of falling rocks and their capacity should be investigated for such cases and the robustness of the rest of the gallery should be considered. The impact at mid-span was evaluated in this study. When the impact location is close to the supports, the global stiffness is high and the punching forces are critical. The local effects need to be considered for such cases.

The behavior of the cushion material has a major influence on the behavior of the gallery, especially on the punching behavior. The punching behavior of the slab is highly influenced by the shape, size and form of the impacting boulder. An accurate calculation of the penetration depth of the boulder and the impact forces is important in order to determine the punching forces acting on the gallery. The maximum penetration of the boulder and the maximum impact forces according to the Swiss guideline provide a good estimate compared to the experimental data (up to 300 kJ) and a reasonable estimate compared to numerical data (up to 2.7 MJ). The formula can be modified for different shapes of boulders and for higher impact energies leading to penetration of more than half of the thickness of the soil cushion, and by incorporating crushing and dilatancy of soil. Full-scale falling-weight experiments using different thicknesses of the soil cushion and different boulder shapes can facilitate understanding of different influences on the penetration depth and the transmitted impact force as well as acquiring proper assumptions for soil modeling. A closer collaboration between geotechnical and structural engineers, thus is required in order to improve prediction of the overall behavior of the gallery and the soil structure interaction, e.g. to quantify the forces transmitted to the slab and the area over which these forces are distributed.

Notion

Capital letters

A_B	Contact area of the boulder
A_d	Equivalent static force for design of galleries
B	Dimensionless compressibility of soil
C	Ductility coefficient for the response of the gallery
C_g	damping matrices of the gallery
C_s	Damping coefficient of soil
D	Penetration depth of the boulder into the soil
D_s	Hardening law exponent for soil
E	Impact energy
$E_{c,imp}$	Dynamic Young's modulus of concrete
$E_{c,s,g}$	Young's modulus of elasticity for concrete, steel, and gravel
ER	Elastic recovery
F_0	Plastic strength of structure
$F_{1,2,3}$	Forces in springs $K_{1,2,3}$ of the analytical model
F_{3y}	Yielding load
F_E	Average impact force calculated based on the work-energy principle
F_k	Maximum value of impulse action of the boulder on the gallery
$F_{\max}$	Maximum transmitted impact force
$F(t)$	Matrix of applied force of a gallery
F_u	Ultimate load acting on the structure
F_y	First yielding load acting on the structure
G	Shear modulus
H	Falling height of the impacting body
H_B	Size of the boulder
H_i	Height of the impactor nose
H_f	Depth of failure for the shear zone of soil
H_s	Thickness of the soil cushion
H_y	Hardening modulus of steel reinforcement
I	Dimensionless impact function
I_e	effective moment of inertia of the slab
J_1, J_2	Stress invariants
K	Bulk modulus
$K_{1,2,3}$	Stiffness of spring for cushion, shear and bending properties
K_{11}	Unloading stiffness of the soil
K_{1h}	Hardening stiffness of the soil
K_{2h}	Hardening of shear reinforcement
K_{1s}	Frequency dependent stiffness of soil (when the thickness of the soil is not limited)
K_g	Stiffness matrix of a gallery
$L(k)$	Intersection of the ellipse curve with the failure envelope
$L_{x,z}$	Slab span in x and z directions
$M_{1,2,3}$	Mass of the impacting body, punching cone, and rest of the slab
M_3^*	Modal mass of the rest of the slab
MD	Maximum deflection of slab

$M_{E,k}$	Soil modulus of the cover layer
M_g	Mass matrix of a gallery
M_s	Effective mass of the gallery for motion
N	Nose performance coefficient
N_γ, N_q, N_c	Constants depending on the friction angle
N^*	Nose shape function
R	Cap surface axis ratio for soil
R_0	Radius or size of the boulder
R_i	Indentation resistance of the target material
RD	Residual deflection of slab
S	Penetrability of the target
S_s	Degree of saturation of soil
W	Maximum volumetric plastic strain of soil
W_b	Weight of the impacting body
W_E	Work done according to work-energy principle
$X(k)$	Intersection of the ellipse curve with the J_1 axis

Small letters

$a_{1,2,3}$	Accelerations of masses $M_{1,2,3}$
c	Cohesion
c_v	The wave velocity
e	Thickness of cushion layer
f	Yield criterion
$f_{c,imp,k}$	Compressive strength of concrete modified for strain rate effects
$f_{ct,imp,k}$	Tensile strength of concrete modified for strain rate effects
f_{cm},	Mean compressive strength of concrete
f_{ctm}	Mean tensile strength of concrete
f_s	Yield strength of steel
g	Acceleration due to gravity
k	Dimensionless length of surface crater
k_M	Material constant
k_w	Stiffness factor for bending
m	Mass of the impacting block
m_g	Mass per unit area of the gallery
m_k	Characteristic block mass
n_s	Porosity of soil
p	Mean stress
q	Deviatoric stress
q_B	Bearing capacity of the soil
R_0	Radius of an equivalent sphere
r	The loading radius (radius of contact area of the boulder)
s	Settlement of the soil
s_γ, s_q, s_c	The shape factors for soil bearing capacity
t_d	Time duration of the transmitted impact force
v_0	Initial impact velocity
v_k	Characteristic impact velocity
y	Displacement matrix of a gallery
y_0	Deformation capacity of the structure
$y_{1,2,3}$	Displacement of masses $M_{1,2,3}$

y_{max}	Expected penetration depth of the boulder
z	Thickness of the slab

Greek letters

α	Factor for modal mass
α_b	Energy transfer rate to the gallery
α_s	Failure envelope coefficient of soil
α_M	Material constant
δ_y	Static vertical deflection of the gallery at first yielding
δ_u	Static ultimate vertical deflection of the gallery
γ_c	Unit weight of the concrete
γ_s	Unit weight of the soil
$\dot{\varepsilon}_c$	Dynamic strain rate of concrete
$\dot{\varepsilon}_{c0}$	Static strain rate for concrete in compression
$\dot{\varepsilon}_{ct0}$	Static strain rate for concrete in tension
ε_{kk}^p	Volumetric plastic strain
ν	Poisson's ratio
σ_1	Axial stress
σ_3	Lateral stress
$\xi_{2,3}$	Damping coefficients for punching and bending behavior
φ	Internal friction angle of concrete
φ'	Internal friction angle of the cushion layer
φ_k	Characteristic value of internal friction angle of the cushion layer
ρ_s	Density of the soil

Special symbols

$\emptyset_{sl}$	Diameter of the loading area on the slab

Acknowledgement

References

Abdel-Rohman, M., Sawan, J. (1985). *Impact Effect on R.C. Slabs: Analytical Approach*, ASCE Journal of Structural Engineering, Volume 111, pp. 1590-1601.

ASCE Task Committee on Finite Element Analysis of Reinforced Concrete Structures. (1982), *State-of-the-Art Report on Finite Element Analysis of Reinforced Concrete*, ASCE Special Publications.

ASTRA, SBB (1998). *Einwirkungen auf Steinschlagschutzgalerien*, Richtlinie, Bundesamt für Strassen, Baudirektion SBB, Eidgenössische Drucksachen- und Materialzentrale, Bern.

ASTRA (2003). *"Steinschlag": Naturgefahr für die Nationalstrassen*; Schlussbericht der ASTRA-Expertengruppe.

ASTRA (2008). *Einwirkungen infolge Steinschlags auf Schutzgalerien*, Richtlinie, Bundesamt für Strassen, Baudirektion SBB, Eidgenössische Drucksachen- und Materialzentrale, Bern.

Atkinson, J. H. (1993). *An Introduction to the Mechanics of Soils and Foundations: through critical state soil mechanics*, McGraw-Hill Book Company Europe, England.

Bachmann, H., Ammann, W.J., Deischl, F., et al. (1995). *Vibration problems in structures: Practical guidelines*, Birkhäuser, Basel; Boston; Berlin.

Belytschko, T., Lu, Y. Y., Gu, L. (1994). *Element-free Galerkin methods*, International Journal of Numerical Methods in Engineering, Volume 37, pp. 229-256.

Belytschko, T., Organ, D., Krongauz, Y. (1995). *A coupled finite element-element-free Galerkin method*, Computational Mechanics, Volume 17, Number 3, May 1995, pp. 186-195.

Berthet-Rambaud, P., Timsah, Y., Daudeville, L., Mazars, J. (2003). *Finite Element Modelling of Concrete Protection Structures Submitted to Rock Impacts*, Proceedings of 16th ASCE Engineering Mechanics Conference, 16-18 July, University of Washington, Seattle.

Berthet-Rambaud, P., Rerrotin, P., Timsah, Y., Mommessin, M., Mougin, J.-P., Mazars, J., Daudeville, L. (2004). *Impact of a reinforced concrete roof slab by falling rocks: experiments and modeling*, Rivista Italiana di Geotecnica, Volume 2, pp 45-53.

Biggs J. M. (1964). *Introduction to structural dynamics*, McGraw-Hill, New York.

Bolton, M.D. (1986). *The strength and dilatancy of sands*, Geotechnique 36, Number 1, pp. 65-78.

Bowles, J. E. (1996). *Foundation Analysis and Design*, 5th edition, McGraw-Hill Book Company.

Breugnot, A., Gotteland, P., Villard, P., Garcin, P. (2010). *Modelling of block impacts with a combined discrete-continuum approach*, Proceedings of Third Euro Mediterranean Symposium on Advances in Geomaterials and Structures, AGS'10, Djerba, Tunisia, May 10-12, pp. 289-295.

Broadhouse, B. J., Neilson, A. J. (1987). *Modeling reinforced concrete in DYNA3D*, Safety and Engineering Division, United Kingdom Atomic Energy Authority, Winfrith, AEEW-M 2465.

Bucher, K. (1997). *Dynamische Berechnung von Steinschlageinwirkungen*, Proceedings, Schweizerische Gesellschaft für Boden und Felsmechanik, Montreux.

Calvetti, F., di Prisco, C. (2009). *An Uncoupled Approach for the Design of Rockfall Protection* Tunnels, Structural Engineering International, SEI Volume 19, Number 3, pp. 342-347.

CEB Bulletin N° 187 (1988). C*oncrete Structures under Impact and Impulsive Loading*, synthesis report.

Chen, W. F. (1982). *Plasticity in Reinforced Concrete*, McGraw-Hill Book Company, New York.

Chen, W. F., Baladi, G. Y. (1985). *Soil Plasticity: Theory and Implementation*, Elsevier, New York.

Chen, Z., Brannon, R. (2002). *An Evaluation of the Material Point Method*, Sandia Nat. Lab., Albuquerque, NM, Report Number SAND2002-0482.

Chikatamarla, R. (2006). *Optimisation of cushion materials for rockfall protection galleries*, Dissertation, Diss. Number 16315, ETH Zurich, Switzerland.

Christopoulos, C., Filiatrault, A., Folz, B. (2002). *Seismic Response of Self-Centering Hysteretic SDOF Systems*, Earthquake Engineering and Structural Dynamics, Volume 31, pp. 1131-1150.

Christopoulos, C., Pampanin, S. (2004). *Towards Performance-based Seismic Design of MDOF Structures with Explicit Consideration of Residual Deformations*, ISET Journal of Earthquake Technology, Paper Number 440, Volume 41, Number 1, pp. 53-73.

Craig, R. F. (1997). *Soil Mechanics*, Sixth edition, E & FN Spon, London, UK.

Cundall, P. A, Stack, O. D. L. (1979). *A discrete numerical model for granular assemblies*, Géotechnique, 29 (1), pp. 47-65.

Daudeville L., Donzé F. V., Mazars J. (2005). Impacts on Concrete Structures: From the Local Analysis to the Structural behavior, Proceedings of VIII International Conference on Computational Plasticity, COMPLAS VIII, 5-7 September, Barcelona, Spain.

Delhomme, F., Mommessin, M., Mougin, J. P., Perrotin, P. (2007). *Simulation of a block impacting a reinforced concrete slab with a finite element model and a mass-spring system*, Engineering Structures, Volume 29, pp. 2844–2852.

DiMaggio, F., L., Sandler, I. S. (1971). *Material models for granular soils*, J. Engrg. Mech. Div., 97(3), pp. 935-950.

Drucker, D. C., Prager W. (1952). *Soil mechanics and plastic analysis for limit design*, Quarterly of Applied Mathematics, Volume 10, Number 2, pp. 157-165.

Eibl, J., Keintzel, E., Charlier, H. (1988). *Dynamische Probleme im Stahlbetonbau, Teil II, Stahlbetonteile und -bauwerke unter dynamischer Beanspruchung*, Heft 392, Berlin, Deutscher Ausschuss für Stahlbetonbau, 1988.

Eurocode 1. (2006), Actions on structures - Part 1-7: *General actions-Accidental actions*, EN-1991-1-7, Annex C, European Committee for Standardization.

Fiacco, A.V., McCormick, G.P., *Nonlinear Programming: Sequential Unconstrained Minimization Techniques*, John Wiley & Sons, New York, 1968.

FIB (2010). *Model code 2010*, published by International Federation for Structural Concrete (FIB).

Fujikake, K. (2007). *Response analysis of RC beams subjected to impact loads*, Proc., 1st Int. Workshop on Performance, Protection, and Strengthening of Structures under Extreme Loading _CD-ROM_, Univ. of British Columbia, Vancouver.

Gazetas, G. (1983). *Analysis of machine foundation vibrations: state of the art*, Soil Dynamics and Earthquake Engineering, Volume 2, Number 1, pp. 2-42.

Gerber, W., Volkwein, A. (2010). *Impact loads of falling rocks on granular material*, Proceedings of Third Euro Mediterranean Symposium on Advances in Geomaterials and Structures, AGS'10, Djerba, Tunisia, May 10-12, pp. 337-342.

Ghadimi Khasraghy, S. (2005). *Nonlinear finite element analysis of reinforced concrete deep beams*, Masters of Engineering Thesis Number ST-05-13, Asian Institute of Technology, Thailand.

Ghadimi Khasraghy, S. (2008). *Finite element modeling of reinforced concrete slabs subjected to rockfall*, Proceedings of 7th International PhD Symposium in Civil Engineering, Stuttgart, Germany, September 11-13, pp. 61-62.

Ghadimi Khasraghy, S., Kishi, N., Vogel, T. (2009a). *Numerical Simulation of Consecutive Impacts on Reinforced Concrete Slabs*, Sustainable Infrastructure, 33rd IABSE Symposium, 9-11 September, Bangkok, Thailand, pp. 218-219.

Ghadimi Khasraghy, S., Schellenberg, K., Vogel, T. (2009b). *Prediction of shear failure of rockfall protection galleries*, Proceedings of PROTECT2009, Structures under Extreme Loading, Hayama, Japan, August 19-21, pp 43.

Guldenfels, R. (1995). *Die Alterung von Bahnschotter aus Bodenmechanischer Sicht*, Dissertation, Diss. Number 11209, ETH Zurich, Switzerland.

Gulkan P, Sozen M. (1974), *Inelastic response of reinforced concrete structures to earthquake motions*, ACI Journal; Number 71, pp.604-610.

Hegen, D. (1996). *Element-free Galerkin methods in combination with finite element approaches*, Computer Methods in Applied Mechanics and Engineering, Volume 135, Issue 1-2, 15 August 1996, pp.143-166.

Hentz S., Daudeville L., Donzé F. (2003). *Modeling of Reinforced Concrete Structures Subjected to Impacts by the Discrete Element Method*, Proceedings of 16th ASCE Engineering Mechanics Conference, 16-18 July, University of Washington, Seattle.

Hokkaido Development Bureau, Ministry of Land, Infrastructure and Transportation (2001). *Guideline for the design of structures to resist rockfall impacts* (in Japanese).

Hughes, T. J. R., Liu, W. K. (1981a). *Nonlinear Finite Element Analysis of Shells: Part I. Three-Dimensional Shells*, Meths. Appl. Mech. Engrg. 26 (1981), pp. 331–362.

Hughes, T. J. R., Liu, W. K. (1981b). *Nonlinear Finite Element Analysis of Shells: Part II. Two-Dimensional Shells*, Comput. Meths. Appl. Mech. Engrg. 27 (1981), pp. 167–181.

Hungr, O., Evans, S., and Hazzard, J. (1999). *Magnitude and frequency of rock falls and rock slides along the main transportation corridors of southwestern British Columbia*. Canadian Geotechnical Journal, 36, pp. 224–238.

Jacquemoud, J. (1999). *Swiss guideline for the design of protection galleries: background, safety concept and case histories*, Joint Japan-Swiss Scientific Seminar on Impact by Rock Falls and Design of Protection Structures, Kanazawa, Japan.

Japan Road Association (1983). *Manual for anti-impact structures against falling rocks* (in Japanese).

Japan Road Association (2000). *Manual for anti-impact structures against falling rocks* (in Japanese).

King, M. W, Miyamoto, A., Masui, H. (1990). *Failure criteria and nonlinear dynamic analysis of reinforced concrete slabs under impulsive loads*, Proceedings of JCI annual convention 1990, Volume 12, Issue 2, pp. 859-864.

Kishi, N., Mikami, H., Matsuoka, K.G., Ando T. (2002a). *Impact behavior of shear-failure-type RC beams without shear rebar,* International Journal of Impact Engineering, Volume 27, pp. 955-968.

Kishi, N., Kon-No, H., Ikeda, K., Matsuoka, K.G. (2002b). *Prototype impact tests on ultimate impact resistance of PC rock-sheds*, International Journal of Impact Engineering, Volume 27, pp. 969-985.

128

Kishi, N., Ohno, T., Konno, H., Bhatti, A.Q. (2006). *Dynamic response analysis for a large-scale RC girder under a falling-weight impact loading*, Advances in Engineering Structures, Mechanics & Construction, Volume 140. pp. 99-109.

Kishi, N., Mikami, H., Okada, S., Yoshida, H., Schellenberg, K. (2008). *Effects of sand cushion on impact resistant behavior of RC slabs under falling-weight impact test.* Proceedings of annual meeting of Hokkaido section of JSCE, 2008 (in Japanese).

Kishi, N., Okada, S., Kon-No, H. (2009). *Numerical Impact Response Analysis of Rockfall Protection Galleries*, Structural Engineering International, SEI Volume 19, Number 3, pp. 313-320.

Kishi, N. Bhatti, A. Q. (2010). *An equivalent fracture energy concept for nonlinear dynamic response analysis of prototype RC girders subjected to falling-weight impact loading,* International Journal Impact Engineering, Volume 37, Issue 1, pp. 103-113.

Kishi, N., Ghadimi Khasraghy, S., Kon-No, H. (2010). *Numerical analysis method for prototype reinforced concrete girders under consecutive impact loading*, Proceedings of Third Euro Mediterranean Symposium on Advances in Geomaterials and Structures, AGS'10, Djerba, Tunisia, May 10-12, pp. 367-372.

Kon-No, H., Yamaguchi S., Nishi, H., Kishi, N., Kurihashi, Y. (2010). *Falling-weight impact test for 2/5 scale model of rockfall protection gallery with/without sand cushion*. Proceedings of Third Euro Mediterranean Symposium on Advances in Geomaterials and Structures, AGS'10, Djerba, Tunisia, May 10-12, pp. 355-360.

Krauthammer, T. (2008). *Modern Protective Structures*, CRC Press, Taylor & Francis Group, LLC, NW.

Labiouse, V., Descoeudres, F., Montani, S. (1996). *Experimental Study of Rock Sheds Impacted by Rock Blocks*, Structural Engineering International, SEI Volume 6, Number 3, pp. 171-176.

Lancaster, P., Salkauskas, K. (1981). *Surfaces generated by moving least squares methods*. Mathematics of Computation 87, 141–158.

Lau, C. K. (1988). *Scale Effects in Tests on Footings*, PhD dissertation, Cambridge University, pp. 44-51.

Li, Q. M., Chen, X. W. (2003). *Dimensionless formulae for penetration depth of concrete target impacted by a non-deformable projectile*, International Journal of Impact Engineering, Volume 28, pp. 93-116.

LS-DYNA (2006). *Theory Manual,* Livermore Software Technology Corporation, Complied by J. O. Hallquist.

LS-DYNA (2007). *Keyword User's Manual*, Version 971, Livermore Software Technology Corporation.

Lysmer, J. (1965). *Vertical motion of rigid footing*, PhD dissertation, University of Michigan.

May, I. M., Chen. Y., Owen D. R. J., Feng, Y. T., Bere A. T. (2005). *Experimental testing and finite element simulation of the behavior of reinforced concrete beams under impact loading*, Proceedings of VIII International Conference on Computational Plasticity, COMPLAS VIII, 5-7 September, Barcelona, Spain.

McDowell, G. R., Bolton, M. D., Robertson, D. (1996). *The Fractal Crushing of Granular Materials*, J. Mech. Phys. Solids, Volume 44, Number 12, pp. 2079-2102.

Miyamoto A., King M. W., Fuji M. (1991). *Analysis of Failure Modes for Reinforced Concrete Slabs under Impulsive Loads*, ACI Structural Journal, Volume 88, Issue 5, September-October 1991, pp. 538-545.

Miyamoto A., King M. W., Fuji M. (1994). *Integrated Analytical Procedure for Concrete Slabs under Impact Loads*, J. Struct. Engrg., Volume 120, Issue 6, pp. 1685-1702.

Montani, S., Descoedres, F., (1996). *Etude expérimentale de la chute de blocs impactant une dale en béton armé recouverte par des matériaux amortissants*, EVED, Bundesamt für Strassen, Forschungsbericht Nr. 524, VSS, Zürich, 93 pp. & annexe

Montani, S. (1998). *Sollicitation dynamique de la couverture des galleries de protection lors de chutes de blocs*, Dissertation, Nr. 1899, École Polytechnique Fédérale de Lausanne, 190 pp.

Mougin, J.-P., Perrotina, P., Mommessina, M., Tonnelob, J., Agbossou, A. (2005). *Rock fall impact on reinforced concrete slab: an experimental approach*, International Journal of Impact Engineering, Volume 31, Issue 2, February 2005, pp. 169-183.

Nakata, Y., Masuya, H., Kajikawa, Y., Okada, T. (1997). *The Analysis of Impact Behavior of Rock-Shed by Combination of Distinct Element Method and Finite Element Method*, Proceedings of 2nd Asia-Pacific Conference on Shock and Impact Loads on Structures, 25-27 November, Melbourne, Australia.

Nater, P. (2005). *Belastungs- und Verformungsverhalten von geschichteten Bodensystemen unter starren Kreisfundationen*, Diss. ETH Number 16319, Institute for Getotechnical Engineering, ETH Zurich, Switzerland.

Ngo, D., Scordelis, A. C. (1967), *Finite Element Analysis of RC Beams*, ACI Journal, Volume 64, Number 3, pp. 152-163.

Nilson, A. H. (1968), *Nonlinear Analysis of reinforced concrete by the Finite Element Method*, ACI Journal, Volume 65, Number 9, pp. 757-766.

Nilson, A. H. (1972), *Internal Measurement of Bond Slip*, ACI Journal, Volume 69, Number 7, pp. 439-441.

Pampanin, S., Christopoulos, C., Priestley, M.J.N. (2003). *Performance-Based Seismic Response of Frame Structures Including Residual Deformations - Part II: Multi-Degree-of-Freedom Systems*, Journal of Earthquake Engineering, Volume 7, Number 1, pp. 119-147.

Pichler, B., Hellmich, C., Mang, H. A. (2005), *Impact of rocks onto gravel - design and evaluation of experiments*, International Journal of Impact Engineering, Volume 31, pp. 559-578.

Pichler, B., Hellmich, C., Mang, H. A., Eberhardsteiner, J. (2006), *Loading of a Gravel-Buried Steel Pipe Subjected to Rockfall*, ASCE Journal of Geotechnical and Geoenvironmental Engineering, Volume 132, Number 11, November 2006, pp. 1465-1473.

Pietsch, Ch. (1982), *Setzungsberechnung von Lastplatten und Flächengründungen unter Verwendung eines Tragkraftabhängigen Verformungmodulus*, Mitteilungen der Forschungsanstalt für Schifffahrt, Wasser- und Grundbau, Berlin. Schriftenreihe Wasser- und Grundbau, Heft 44, Berlin.

Polak, M. A. (1998*). Modeling Punching Shear of Reinforced Concrete Slabs Using Layered Finite Elements*, ACI structural Journal, Volume 95, Number 1, November-December 1998, pp. 71-80.

Priestley, M. J. N. (1993). *Myths and fallacies in earthquake engineering-conflicts between design and reality*, Bulletin of the New Zealand Society of Earthquake Engineering, Volume 26, Number 3, pp. 329-341.

Rabczuk, T., Eibl, J. (2006). *Modelling dynamic failure of concrete with meshfree methods*, International Journal of Impact Engineering, Volume 32, pp. 1878-1897.

Roesset, J. M., Kausel, E., Cuellar, V., Monte, J. L., Valerio, J. (1994). *Impact of Weight Falling onto the Gravel*, ASCE Journal of Geotechnical Engineering, Volume 120, Number 8, August 1994, pp. 1394-1412.

Saatci, S., Vecchio, F. J. (2009). *Nonlinear Finite Element Modeling of Reinforced Concrete Structures under Impact Loads*, ACI Structural Journal, Volume 106, Number 5, pp. 717-725.

Saito, H. (1995), *Loading Capacities and Failure Modes of Various Reinforced-Concrete Slabs Subjected to High Speed Loading*, Nuclear Engineering and Design, Volume 156, pp. 227-286.

Sangi, A. J., May, I. M. (2009). *High-Mass, Low-Velocity Impacts on Reinforced Concrete Slabs*, 7th European LS-DYNA Conference, 14-15 May, Salzburg, Austria.

SAP 2000 (2006). *Linear and Nonlinear Static and Dynamic Analysis and Design of Three-Dimensional Structures*, Basic Analysis Reference Manual, Computers and Structure, Inc., Berkeley, California, USA.

Sato, H., Mabuchi, T., Ishikawa, N., Enrin, H., Wakabayashi, O. (1999). *Study on impact resistance of rock-shed section model*, Joint Japan-Swiss Scientific Seminar on Impact Load

by Rock Falls and Design of Protection Structures, 4-7 October 1999, Kanazawa, Japan. pp. 59-64.

Schellenberg, K., Volkwein, A., Roth, A., Vogel, T. (2007). *Large-scale impact tests on rock fall galleries*, 7th International Conference on Shock & Impact Loads on Structures, 17 – 19 October, Beijing, pp. 497-504.

Schellenberg, K., Vogel, T. (2007). *Tests and analytical model of rockfall impacts on galleries*, Proceedings of Protect2007, Structures under Extreme Loading, Aug. 20-22, Whistler, p. 27 and CD-ROM file SWO04_Schellenberg.pdf, pp. 1-10.

Schellenberg, K. (2008). *On the design of rockfall protection galleries*, Diss. ETH Number 17924, Institute of Structural Engineering, ETH Zurich, Switzerland.

Schellenberg K., Ghadimi Khasraghy S., Vogel T. (2008). *Impact behavior of reinforced concrete slabs subjected to rockfall loading*, Structures Under Shock and Impact X: Proceeding of Tenth International Conference on Structures Under Shock and Impact (SUSI 2008), 14-16 May, Algarve, Portugal, pp. 25-34, ED N. Jones et al, WIT Press Publications, Southampton, UK.

Schlüter, F. H. (1987). *Dicke Stahlbetonplatten unter stossartiger Belastung – Flugzeugabsturz*, Dissertation, Schriftenreihe des Instituts für Massivbau und Baustofftechnologie, Heft 2.Karlsruhe.

Schmidt-Hurtienne, B. (2001). *Ein dreiaxiales Schädigungsmodell für Beton unter Einschluss des Dehnrateneffektes bei Hochgeschwindigkeitsbelastung*, Massivbau Baustofftechnologie Karlsruhe, Heft 42, 259 pp.

Schubert, M., Jacquemound, J., Straub, D. (2010). *RiskNow - Falling Rocks: Excel© basiertes Werkzeug zur Risikoermittlung bei Stein schlaggalerien*, ASTRA Projekt AGB2008/003, Bericht Nr. 639.

Schwer, L. E. (2001). *Laboratory Tests for Characterizing Geomaterials*, article for FEA information. http://schwer.net/

Schwer, L. E., Murray, Y. D. (2002). *Continuous Surface Cap Model for Geomaterial Modeling: A New LS-DYNA Material Type*, 7th International LS-DYNA Users Conference, 19-21 May, Michigan, pp. 16-35 to 16-50.

Shibata, A., Sozen, M. (1976). *Substitute structure method for seismic design in reinforced concrete*, Jour. Str. Div. ASCE, 102, 6.

SIA 262. (2003). *Concrete Structures*, Swiss Society of Engineers and Architects.

Sircovich-Saar, O. (2006). *Dynamics in the Practice of Structural Design*, WIT Press, UK.

Sonoda, K. (1999). *Ultimate Limit State of Rockshed and Design Method*, Proceedings of Joint Japan-Swiss Scientific Seminar on Impact Load by Rock Falls and Design of Protection Structures, 4-7 October, Kanazawa, Japan, pp. 129-136.

Stiglat, K., Wippel, H. (1993). *Platten*, 3. Aufl., Berlin, München, Ernst & Sohn Verlag, 267 pp.

Studer, J. A., Laue, J. Koller, M. G. (2007). *Bodendynamik*, 3. Auflage, Springer Verlag, Berlin.

Sulsky, R., Chen, Z., Schreyer (1993). *A Particle Method for History-Dependent Materials* , Sandia Nat. Lab., Albuquerque, NM, Report Number SAND93-7044.

Süper, W. (1982). *Rechnerische Untersuchung stossartig beanspruchter Stahlbetonplatten*, Dissertation, Universität Dortmund, 193 pp.

Terzaghi, K., Peck, R. B. (1948). *Soil Mechanics in Engineering Practice*, John Wiley and Sons, New York.

Teysseire, P. (2007). *Geotechnische Eigenschaften von Moränen*, Dissertation, Diss. Number 16322, ETH Zurich, Switzerland.

Thabet, A., Haldane, D. (2000). *Three-Dimensional Simulation of Nonlinear Response of Reinforced Concrete Members Subjected to Impact Loading*, ACI STRUCTURAL JOURNAL, Volume 97, Issue 5, Sep-Oct 2000, pp. 689-702.

Uchida T., Tsubota H, Yamada T. (1985). *Experimental investigations of Reinforced Concrete slabs subjected to impact loading*, Transactions of the 8th International Conference on Structural Mechanics in Reactor Technology J5/1, pp. 173-178.

Vecchio, F. J. (2000). *Disturbed Stress Field Model for Reinforced Concrete: Formulation*, Journal of Structural Engineering, Volume 126, Number 9, 2000, pp. 1070-1077.

Vesic, A. S. (1963). *Bearing capacity of deep foundations in sand*, Highway research record, 39 National Academy of Science, pp. 112-153.

Viggiani, G., Atkinson, J. H. (1995). *Stiffness of fine-grained soils at very small strains*, Geotechnique 45, Number 2, pp. 249-255

Vogel, T., Labiouse, V., Masuya, H. (2009). *Rockfall protection as an integral task*, Structural Engineering International, SEI Volume 19, Number 3, pp. 304-312.

von Mises, R. (1913). *Mechanik der festen Körper im plastisch deformablen Zustand*, Göttin. Nachr. Math. Phys., Volume 1, pp. 582–592.

VSS (1997). *SN 670 008a: Identifikation der Lockergesteine*, Eingetragene Norm der Schweizerischen Normenvereinigung, Vereinigung Schweizerischer Strassenfachleute VSS, Zürich, Switzerland.

Wolf, J.P. (1985). *Dynamic soil-structure interaction*, Englewood Cliffs, N.J., Prentice-Hall, ISBN 0-13-221565-9.

Yamaguchi, S., Kishi, N., Kon-No, H., Nishi, H. (2010). *Falling-weight impact test of large-scale two-side simply supported RC slab with varying cushion layer*, Proceeding of the Japan Institute, Volume 32, pp. 751-756 (in Japansese).

Yamamoto, M., Masuya, H., Onda, S. Horie, Y., Kumagai, T. (2001). *A study on the impact test method and characteristics of behavior of reinforced concrete beam by a weight drop*, Journal of Structural Engineering. *A,* Volume 47 A, pp 1683-1694 (in Japanese).

Young, C. W. (1997). *Penetration Equations*, Sandia Nat. Lab., Albuquerque, NM, Report Number SAND97-2426.

Zineddin M, Krauthammer T. (2007). *Dynamic response and behavior of reinforced concrete slabs under impact loading*, International Journal of Impact Engineering, Volume 34, pp. 1517-1534.

Appendices

A: Calibration of parameters of the cap model

Calibration of parameters shown in Table 3-1, which are used for defining the cap hardening model in finite element analyses are explained here.

The shear modulus G of soil is related to the density, the current stress level, and the velocity of shear waves (see Viggiani & Atkinson 1995). The bulk modulus K of soil is a function of its shear modulus and is also stress dependent. The cap hardening model, however, does not incorporate the variation of shear and bulk modulus of soil and is defined by selecting a constant value. The bulk modulus of soil as shown in Table 3-1 is selected based on the slope of loading-unloading curve of oedometric test result (Figure A-1). The shear modulus of soil is then calculated as a function of bulk modulus and the Poisson's ratio.

The failure envelope coefficient α_s is the slope which defines the failure envelope and can be calculated as a function of the angle of internal friction according to the Equation 5-2. This relates to the slope of the critical state line according to critical state soil mechanics (e.g. Atkinson 1993).

The maximum volumetric plastic strain of soil W is assumed to be a material constant, which is related to the porosity n_s and the degree of saturation S_s of soil and follows the relation (Chen & Baladi 1985):

$$W = n_s (1 - S_s) \qquad\qquad\qquad (A\text{-}1)$$

The degree of saturation of the soil was zero for the experiments (Schellenberg 2008) and the porosity of the soil is 0.2 (with a specific gravity of 2.7).
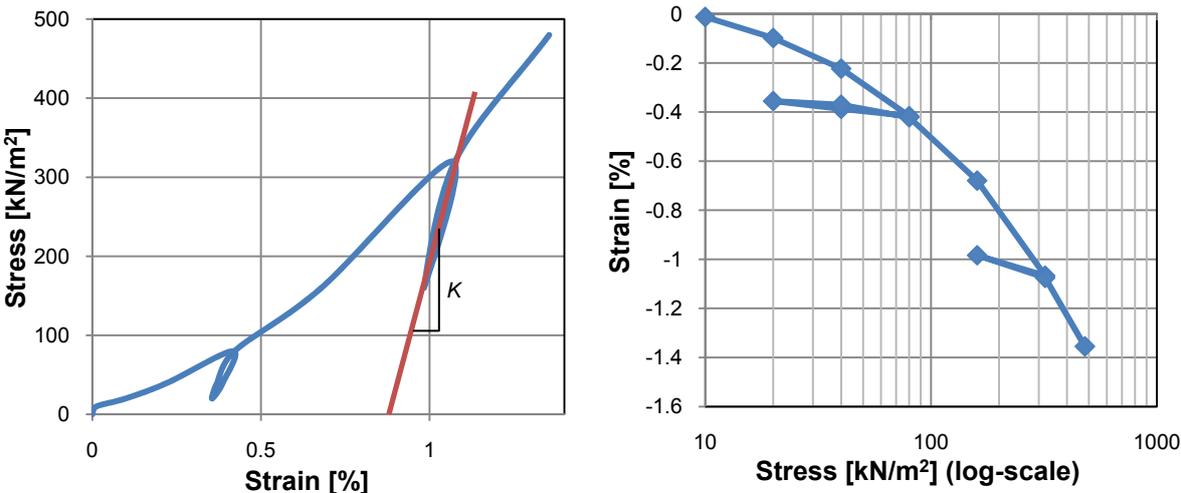
Figure A-1: Oedometric test a) selection of bulk modulus, and b) stress-strain diagram in log-scale

The cap surface axis ratio R and the hardening law exponent D_s can be calibrated using curve fitting to the experimental data. The yield surface for the selected cap model is shown in Figure 3-1, where k is defined as (Chen & Baladi 1985):

$$k = \varepsilon_{kk}^p \tag{A-2}$$

In which, ε_{kk}^p is the volumetric plastic strain. That means the $L(k)$ is the value of J_1 at which the plastic strain is obtained and defines the intersection of the ellipse curve with the failure envelope. The intersection of the ellipse curve with the J_1 axis is defined by $X(k)$ as follows:

$$X(k) = \underbrace{L(k) + R[\alpha L(k)]}_{(1)} = \underbrace{-\frac{1}{D_s}\ln(1 - \frac{\varepsilon_{kk}^p}{W})}_{(2)} \tag{A-3}$$

The volumetric plastic strain is given as:

$$\varepsilon_{kk}^p = W\{1 - \exp[-D_s X(k)]\} \tag{A-4}$$

The value of D_s and R can be chosen by trial and error comparing the plastic strains obtained from the experimental data and those obtained using Equation A-4, as well as to obtain an equal value for both sides (1) and (2) of the equation for the given data set according to Equation A-3. The oedometric test represent the stress state in the soil where the lateral strains are zero, therefore, the curves are plotted for the respective situation (Figure A-2). The triaxial compression test data can be used in addition for data fitting. However, the cap data are only fitted here for oedometric test results and the stress trajectories for other stress states are extrapolated based on calibrated parameters and the Poisson's ratio.
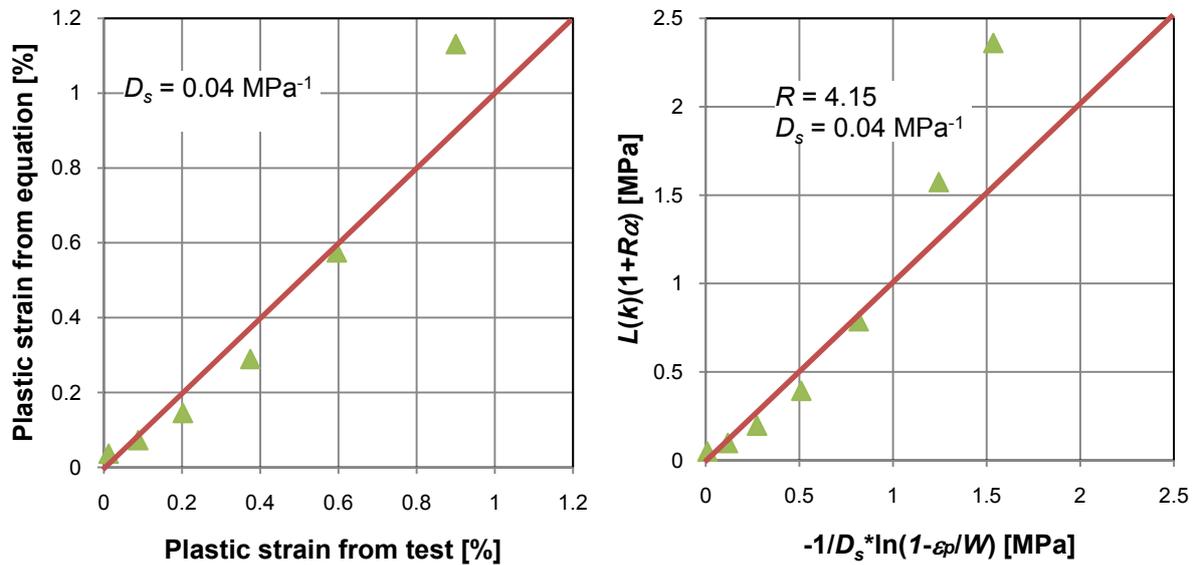
Figure A-2: Selection of cap surface parameters

The uniaxial stress trajectory intersects the cap surface but not the shear failure surface. The stress trajectory is related to the Poisson's ratio ν using the Hooke's law for linear part of uniaxial stress (Schwer 2001):

$$\sigma_3 = \sigma_1 \frac{\nu}{1-\nu} \tag{A-5}$$

Therefore, the mean and deviatoric stresses can be computed as:

$$p = \frac{\sigma_1}{3}\frac{1+v}{1-v} \qquad \text{and} \qquad q = \sigma_1 \frac{1-2v}{1-v} \qquad \text{(A-6)}$$

$$p = \frac{\sigma_1}{3}\frac{1+v}{1-v} \qquad \text{and} \qquad q = \sigma_1 \frac{1-2v}{1-v}$$

B: Input parameters for finite element model in LS-DYNA

Typical input parameters of LS-DYNA for material model as well as sectional properties are shown in here. A few different blocks are chosen as example of input blocks.

B1: General options

B2: Material models

B3: Sections

B1: General options

List of the parameters used:

dt   = Death time when contact surface is deactivated (default=1.0E+20)
endtim = Termination time
fsf   = Coulomb friction scale factor (default=1.0)
msid   = Master segment set ID
nsid   = Node set ID
sfm   = Scale factor on default master penalty stiffness
sfmt   = Scale factor for master surface thickness
sfs   = Scale factor on default slave penalty stiffness
sfst   = Scale factor for slave surface thickness
ssid   = Slave segment set ID
vsf   = Viscous friction scale factor (default=1.0)
vz   = Initial velocity in z-direction

List of the default or unused parameters (zero values)

boxid   = All nodes in the box which belong to node set ID are initialized
bt   = Birth time when contact surface becomes active
dc   = Exponential decay coefficient of friction
dtimin = Reduction (or scale) factor for initial time step size to determine minimum time step
endcys = Termination cycle
endenf = Percent change in energy ratio for termination of calculation
endmas = Percent change in the total mass for termination of calculation
fd   = Dynamic coefficient of friction
fs   = Static coefficient of friction
irigrid = Option to overwrite predefined rigid body velocities
mboxid = Includes in contact definition only for master segments within a defined box
mpr   = Includes the master side in the interface force files
mst   = Optional thickness for master surface
mstyp   = Master segment type
nsidex = Node set ID doe excepted nodes from imposed velocity
penchk = Small penetration in contact search option
sboxid = Includes in contact definition only for slave segments within a defined box
spr   = Includes the slave side in the interface force files
sst   = Optional thickness for slave surface (overrides true thickness)
sstyp   = Slave segment set or node set type
vc   = Coefficient for viscous friction
vdc   = Viscous damping coefficient in percent of critical
vx   = Initial velocity in x-direction
vxr   = Initial rotational velocity about the x-axis
vy   = Initial velocity in y-direction
vyr   = Initial rotational velocity about the y-axis
vzr   = Initial rotational velocity about the z-axis

Termination

*CONTROL_TERMINATION
$---$
$ CONTROL BLOCK
$---$

$# endtim	endcyc	dtmin	endeng	endmas
0.300000	0	0.000	0.000	0.000

Contact

*CONTACT_AUTOMATIC_SURFACE_TO_SURFACE_ID
$---$
$ CONTACT BLOCK
$---$

$# cid	title
1	Boulder to Sand

$# ssid	msid	sstyp	mstyp	sboxid	mboxid	spr	mpr
1	2	0	0	0	0	0	0

$# fs	fd	dc	vc	vdc	penchk	bt	dt
0.000	0.000	0.000	0.000	0.000	0	0.000	1.0000E+20

$# sfs	sfm	sst	mst	sfst	sfmt	fsf	vsf
1.000000	1.000000	0.000	0.000	1.000000	1.000000	1.000000	1.000000

Initial velocity

INITIAL_VELOCITY

$# nsid	nsidex	boxid	irigid
2	0	0	0

$# vx	vy	vz	vxr	vyr	vzr
0.000	0.000	-9900.0000	.000	0.000	0.000

B2: Material models

List of the parameters used:

a0   = Yield function constant for plastic yield function
beta   = Factor for considering hardening
bulk   = Bulk modulus
d   = Hardening law exponent
e   = Young modulus of elasticity
esp   = Strain
etan   = Hardening modulus
g   = Shear modulus
mid   = Material ID
P   = Stress corresponding to the strain value
pc   = Pressure cutoff for tensile fracture
pr   = Poisson's ratio
r   = Cap surface axis ratio
ro   = Density
sigy   = Yield stress
theta = Failure envelope coefficient
w   = Maximum plastic strain

List of the default or unused parameters (zero values)

a1   = Yield function constant
a2   = Yield function constant
alpha = Failure envelope parameter
beta   = Failure envelope exponent
c   = Kinematic hardening coefficient
da   = Axial damping factor (for Belytschko-Schwer beam, only)
db   = Bending damping factor(for Belytschko-Schwer beam, only)
fs   = Failure strain for eroding elements
gmma = Failure envelope exponential coefficient
n   = Kinematic hardening parameter
ref   = Use reference geometry to initialize the pressure
src   = Strain rate parameter, C, for Cowper Symonds strain rate model
srp   = Strain rate parameter, P, for Cowper Symonds strain rate model
toff   = Tension Cut Off, TOFF < 0 (positive in compression)
vcr   = Volumetric crushing option (=0.0: on)
vec   = Vectorization flag
vp   = Formulation for rate effects
x0   = Hardening law exponent

Boulder
```
*MAT_ELASTIC_TITLE
Boulder
$#   mid            ro            e             pr          da      db      not used
       6      2.4300E-9     30000.000      0.200000      0.000   0.000      0
```

Steel beams / load cells

*MAT_ELASTIC_TITLE
Steel Girder

$#	mid	ro	e	pr	da	db	not used
	2	7.8500E-9	2.0600E+5	0.300000	0.000	0.000	0

Steel reinforcement

*MAT_PLASTIC_KINEMATIC_TITLE
Rebars

$#	mid	ro	e	pr	sigy	etan	beta
	7	7.8500E-9	2.0600E+5	0.300000	550.00000 2	060.000	1.000000

$#	src	srp	fs	vp
	0.000	0.000	0.000	0.000

Soil cushion

*MAT_GEOLOGIC_CAP_MODEL_TITLE
Soil Layer

$#	mid	ro	bulk	g	alpha	theta	gamma	beta
	5	2.1750E-9	192.00000	88.599998	0.000	0.356000	0.000	0.000

$#	r	d	w	x0	c	n
	4.150000	0.040000	0.200000	0.000	0.000	0.000

$#	plot	ftype	vec	toff
	2.000000	1.000000	0.000	0.000

Concrete

*MAT_SOIL_AND_FOAM_FAILURE_TITLE
Concrete

$#	mid	ro	g	bulk	a0	a1	a2	pc
	1	2.3500E-9	19900	23333.000	408.32999	0.000	0.000	-3.500000

$#	vcr	ref
	0.0	0.000
	1.0	

$#	eps1	eps2	eps3	eps4	eps5	eps6	eps7	eps8
	0.000	0.0015	1.000000	0.000	0.000	0.000	0.000	0.000

$#	eps9	eps10
	0.000	0.000

$#	p1	p2	p3	p4	p5	p6	p7	p8
	0.000	35.000000	35.000000	0.000	0.000	0.000	0.000	0.000

$#	p9	p10
	0.000	0.000

B3: Sections

List of the parameters used:

cst   = Cross section type
elform = Element formulation equation
nip   = Number of through shell thickness integration points
propt   = Printout option
secid   = Section ID
setyp   = 2D solid element type (1=Lagrangian)
shrf   = Shear factor
t   = Shell thickness at different nodal points
ts   = Beam thickness

List of the default or unused parameters (zero values)

aet   = Ambient element type
edgeset = Edge node set required for shell type seatbelts.
icomp   = Flag for orthotropic/anisotropic layered composite material model
idof   = Applies to shell element types 25 and 26
marea   = Non-structural mass per unit area
nloc   = Location of reference surface (default is at mid surface)
nsloc   = Location of reference surface normal to s axis (default is at center)
nsm   = Nonstructural mass per unit length
ntloc   = Location of reference surface normal to t axis (default is at center)
qr/irid = User defined rule for integration of beam
scoor   = Location of triad for tracking the rotation of the discrete beam element
tt   = Beam thickness (inner diameter for hollow section)

Boulder
```
*SECTION_SOLID_TITLE
Boulder

$#   secid   elform        aet
      6       1             0
```
Steel beams
```
*SECTION_SOLID_TITLE
Boulder

$#   secid   elform        aet
      6       1             0
```
Steel reinforcement
```
*SECTION_BEAM_TITLE
Rebar 1

$#   secid   elform        shrf        qr/irid      cst    scoor     nsm
      7       1            0.830000       0           1    0.000     0.000

$#   ts1      ts2          tt1      tt2     nsloc    ntloc
  10.000000 10.000000     0.000    0.000    0.000    0.000
```

Soil cushion

*SECTION_SOLID_TITLE
Soil Cushion

$# secid   elform   aet
     5   1   0

Concrete

*SECTION_SOLID_TITLE
Concrete

$# secid   elform   aet
     1   1   0

UNP steel section

*SECTION_SHELL_TITLE
UNP

$# secid elform   shrf   nip   propt qr/irid   icomp   setyp
     11   2   0.833000   2   1   0   0   1

$#   t1   t2   t3   t4   nloc   marea   idof   edgset
 20.000000 20.000000 20.000000 20.000000   0.000   0.000   0.000   0

C: MATLAB files

The MATLAB files used for the calculation of Bessel filter, as well as the 2DFS and 3DFS models are listed here.

C1: Bessel filter

C2: Two degrees of freedom system

C3: Three degrees of freedom system

C1: Bessel low-pass filter

```
%%%%%%%%%%%%%%%%%%%%%%%%%%%%%%%%%%%%%%%%%%%%%%%%%%%%%%%%%%%%%%%
%                    Bessel low-pass filter
%                    Coded by Sara Ghadimi Khasraghy
%%%%%%%%%%%%%%%%%%%%%%%%%%%%%%%%%%%%%%%%%%%%%%%%%%%%%%%%%%%%%%%
close all;
n = 6;
w0 = (130)*pi*2; %The frequency with constant group delay
                 %(it isn't cut-off frequency);

%Calculating the filter
[b,a]= besself(n,w0);

%Defining the sampling frequency.
fs = 1/0.1*1000;

[num,den] = bilinear(b,a,fs);

%Filtering the signal Y.
y = filter(num,den,Y);
plot(X,y);
hold on
plot(X,Y,'r')

d=[X,y];
xlswrite('Bessel.xls', d, 'Load History', 'A1');
```

C2: Two degrees of freedom system

```matlab
%%%%%%%%%%%%%%%%%%%%%%%%%%%%%%%%%%%%%%%%%%%%%%%%%%%%%%%%%%%%%%%%%%%%
%                      2DFS with triangular pulse load
%                      Coded by Sara Ghadimi Khasraghy
%%%%%%%%%%%%%%%%%%%%%%%%%%%%%%%%%%%%%%%%%%%%%%%%%%%%%%%%%%%%%%%%%%%%
%%%%%%%%%%%%%%%%%%%%%%%%%%%%  Input block %%%%%%%%%%%%%%%%%%%%%%%%%%%%%%
clear all
clc;
%%%%%%%%%%%%%%%%%%%%%%%%% Impacting Boulder%%%%%%%%%%%%%%%%%%%%%%%%%%%%%%%
NN = 0.68; % Nose shape coefficient Young
W = 4000; % kg weight of the boulder
A = 1120000; % mm2 area of the boulder
R0 = 732; % mm equivalent sphere radius of the impacting body
R1 = 600; % mm size of the boulder
%%%%%%%%%%%%%%%%%%%%%%%%%%%% Loading %%%%%%%%%%%%%%%%%%%%%%%%%%%%%%%%%%
v0 = 9900; % mm/s velocity of impact
DT = 0.00008; % s time step size
TS = 1000; % Number of timesteps
g = 9810; % mm/s2 acceleration due to gravity
%%%%%%%%%%%%%%%%%%%%%%%%%%%% Slab %%%%%%%%%%%%%%%%%%%%%%%%%%%%%%%%%%%%%%
Lx = 3500; % mm
Lz = 4500; % mm
z = 350; % mm
kw = 30; % [-]
alpha = 0.37; % [-]
PMfactor = 4; % Ratio of ultimate load to ultimate unit moment
u1 = 20; % mm concrete cover for tensile reinforcement
u2 = 15; % mm concrete cover for compression reinforcement
dia1 = 22; % mm tensile reinforcement diameter
dia2 = 10; % mm compression reinforcement diameter
s1 = 155; % mm tensile reinforcement spacing
s2 = 300; % mm compression reinforcement spacing
dias = 0; % mm shear stirrups diameter; dias = 0 if there are no stirrups
ss = 150; % mm shear stirrups spacing; ss = 0 if there are no stirrups
c2 = 0.05; % damping ratio for local behavior
c3 = 0.05; % damping ratio for global behavior
b = 1000; % mm, slab stip
Duct= 0.1; % [-] ratio of stiffness after yielding
Hard=1; % %, hardening of steel
Pi=3.141592;
%%%%%%%%%%%%%%%%%%%%%%%%%%%% Soil %%%%%%%%%%%%%%%%%%%%%%%%%%%%%%%%%%%%%%
HN = 0.4; %m height of the impactor nose.
B=1.2; % a dimensionless compressibility of soil
R=63.3; %MPa indentation resistance of the target material
e = 400; % mm thickness of soil layer
phi = 33; % angel of internal friction
stype = 0; % 0 for dense soil and 1 for loose soil
Den = 1700; %kg/m3 density of soil
ysoil=20; %kN/m3
ME=60000;%kN/m2
S = 8; % penetrability of the target
%%%%%%%%%%%%%%%%%%%%%%%%%%%% Material properties %%%%%%%%%%%%%%%%%%%%%%%%%%%%%%
Asg = 55; % promil, ultimate strain of the reinforcement
fcm = 35; % MPa, mean compressive strength of concrete
fy = 500; % MPa, yielding strength of steel
Ec = 30000; % MPa, E-modulus of concrete
Es = 210000; % MPa, E-modulus of steel
yc = 25; % kN/m3, density of concrete
Dmax= 16; % mm, maximum diameter of aggregate
%Allocate space all vectors
F0=zeros(TS,1);
```

```
T=zeros(TS,1);
y2=zeros(TS,1);
FC2=zeros(TS,1);
strainrate=zeros(TS,1);
fctmd=zeros(TS,1);
K21=zeros(TS,1);
K22=zeros(TS,1);
K2=zeros(TS,1);
DeltaFK2=zeros(TS,1);
FK21=zeros(TS,1);
DeltaFK21=zeros(TS,1);
FK22=zeros(TS,1);
DeltaFK22=zeros(TS,1);
Deltay3=zeros(TS,1);
y23=zeros(TS,1);
Deltay23=zeros(TS,1);
FK2=zeros(TS,1);
a2=zeros(TS,1);
v2=zeros(TS,1);
y3=zeros(TS,1);
FC3=zeros(TS,1);
K3=zeros(TS,1);
DeltaFK3=zeros(TS,1);
FK3=zeros(TS,1);
a3=zeros(TS,1);
v3=zeros(TS,1);
%%%%%%%%%%%%%%%%%%%%%%%%%%%%%%%%%%%%%%%%%%%%%%%%%%%%%%%%%%%%%%%%
%                         calculation of pulse load
%%%%%%%%%%%%%%%%%%% Pichler's formula %%%%%%%%%%%%%%%%%%%%%%%%%%%%%%%%%
ks=0.707+HN/(2*R1/1000); % dimensionless length of crater surface
I=W*(v0/1000)^2/((R*1000000)*((2*R1/1000)^3)); % dimensionless impact function
N1=1/(1+4*(HN/(2*R1/1000))^2); % nose shape factor 0<N1<1
N=W/(Den*(2*R1/1000)^3*B*N1); % projectile geometry function
D1=2*R1*sqrt(((1+ks*Pi/(4*N))*4*ks*I)/((1+I/N)*Pi));
term=(1+I/N)/(1+ks*Pi/(4*N));
if D1/(2*R1)>ks;
   D1=2*R1*((2/Pi)*N*log(term)+ks);
end
if D1>e
   D1=e;
end
%%%%%%%%%%%%%%%%%%%%%%%%Montani's formula %%%%%%%%%%%%%%%%%%%%%%%%%%%%%%%
FSwiss=1000*2.8*(e/1000)^(-0.5)*(R0/1000)^0.7*(ME)^0.4*tan(phi*Pi/180)*((W/1000)*(v0/1000)^2/2)^0.6;
%N
D2=1000*W*(v0/1000)^2/FSwiss;
%%%%%%%%%%%%%%%%%%%%%%%%%%Young's formula %%%%%%%%%%%%%%%%%%%%%%%%%%%%%%%%
%         Conversion of units
W10=W*2.2046; % lbs
v10=v0*3.28084/1000; % fps
A10=A*1.55e-3; %in2
%         calculation
if v10<200;
   D10=0.3*S*NN*(W10/A10)^0.7*(log(1+2*v10^2*10^-5));
elseif v10>=200;
   D10=0.00178*S*NN*(W10/A10)^0.7*(log(v10-100));
end
%         Conversion of D
D3=D10*304.8;
if W10<60;
   D3=304.8*D10*0.2*(W10)^0.4;
end
%%%%%%%%%%%%%%%%%%%%%%%%%%%%%%%%%%%%%%%%%%%%%%%%%%%%%%%%%%%%%%%%%%%%%%%%
```

```
Fmax=FSwiss;
D=D2;
if e-D1>3.4*R1;
   D=D1;
   Fmax=W*(v0/1000)^2/(D1/1000);
end
if D>e/2;
  D=D1;
  Fmax=W*(v0/1000)^2/(D1/1000);
end
if D>e
   D=e;
end
Td=2*D/v0; % s the impact duration
%%%%%%%%%%%%%%%%%%%%% Sectional calculations %%%%%%%%%%%%%%%%%%%%%%%%%%
%%%%%%%%%%%%%%%%%%%%%%%%%%%%%%% Bending %%%%%%%%%%%%%%%%%%%%%%%%%%%%%%%
fctm=0.3*fcm^(2/3);
d = z-u1-dia1/2; % mm
ds2=u2+dia2/2; % mm
n=Es/Ec; % [-]
As1=1000*(dia1/2)^2*Pi/s1; % mm2/mm
As2=1000*(dia2/2)^2*Pi/s2; % mm2/mm
ro1=As1/(b*d); % [-]
ro2=As2/(b*d); % [-]
%%%% cracking of concrete
ycrack=((b*z*z/2)+((n-1)*As1*d)+((n-1)*ds2*As2))/((b*z)+((n-1)*(As1+As2)));
Icrack=(Lz*(ycrack)^3)/3+n*As1*(d-ycrack)^2+(n-1)*As2*(ycrack-u2)^2;
Ig=Lz*z^3/12;
Mcrack=fctm*Icrack/(z-ycrack)/1000000;
straincrack=fctm/Ec;
y3crack=straincrack*z;
%%%% yielding of reinforcement
%%%% assuming elastic concrete at yielding
k=(((ro1+ro2)^2*n^2)+(2*(ro1+ro2*ds2/d)*n))^0.5-(ro1+ro2)*n; % [-]
cy=k*d; % mm
strains1=fy/Es; % [-]
strainc=strains1*cy/(d-cy); % [-]
fc=strainc*Ec; % MPa
strains2=strainc*(cy-ds2)/cy; % [-]
fs2=strains2*Es; % Mpa
Cc=0.5*fc*b*cy; % N
Cs=As2*fs2; % N
ybar=((ds2*Cs)+(Cc*cy/3))/(Cc+Cs); % mm
jd=d-ybar; % mm
My=As1*fy*jd/1000000; % kNm/m
%%%%%%%%% effective moment of intertia
Ie=Ig*(Mcrack/My)^3+(1-(Mcrack/My)^3)*Icrack;
if Ie>Ig;
   Ie=Ig;
end
%%%% Ultimate state
cu=(As1*fy-As2*fy)/(0.85*b*fcm); % mm
TSu=As1*fy/1000; %kN/m
CSu=As2*fy/1000; %kN/m
jdu=d-0.4*cu; % mm
Mu=TSu*jdu/1000; % kNm/m
Qu=PMfactor*Mu; % kN ultimate force
Qy=PMfactor*My; % kN yielding force
%%%%%%%%%%%%%%%%%%%%%%%%%%%%%%%%%%%%%%%%%%%%%%%%%%%%%%%%%%%%%%%%%%%%%%%%%%
%%%%%%%%%%%%%%%%%%%%%%%%% Intermediate calculations %%%%%%%%%%%%%%%%%%%%%%
%%%%%%%%%%%%%%%%%%%%%%%%%%%%%%%%%%%%%%%%%%%%%%%%%%%%%%%%%%%%%%%%%%%%%%%%%%
rmax=sqrt(D*(2*R0-D));
```

```matlab
if R0>=(e-D);
    phiSL=2*R0;
elseif R0<(e-D);
    phiSL=2*rmax+2*((e-D)*tan((45-phi/2)*Pi/180));
end
if stype>=1;
    phiSL=2*R0;
end
if phiSL<=0;
    phiSL=2*R0;
end
if phiSL>Lz-2*z;
    phiSL=Lz-2*z;
end
K210=Pi*Ec*(z+phiSL); %N/mm
K30=(kw*Ec*z^3)/(12*Lz^2); %N/mm
Fcrack=K30*y3crack;
if R0<(e-D);
M2=Pi/12*(yc*(z/1000)*(3*(phiSL/1000)^2+6*(phiSL/1000)*(z/1000)+4*(z/1000)^2))*100+Pi/12*((e-D)/1000)*ysoil*(4*(rmax/1000)^2+2*(rmax/1000)*(phiSL/1000)+(phiSL/1000)^2)*100; % kg
end
if R0>=(e-D);
    M2=Pi/12*(yc*(z/1000)*(3*(phiSL/1000)^2+6*(phiSL/1000)*(z/1000)+4*(z/1000)^2))*100+Pi*((e-D)/1000)*ysoil*((R0/1000)^2)*100; % kg
end
    M2P=Pi/12*(yc*(z/1000)*(3*(phiSL/1000)^2+6*(phiSL/1000)*(z/1000)+4*(z/1000)^2))*100;
M3=(Lx/1000)*(Lz/1000)*(z/1000)*yc*100; % kg
M3modal=alpha*M3-M2P; % kg
if M3modal<0;
    M3modal=alpha*M3;
end
if dias<=0;
    row=0;
elseif dias>0;
row=(dias/2)^2*Pi/(ss^2);
end
if dias<=0;
    Asw=0;
elseif dias>0;
Asw=row*Pi*(z^2+(z*phiSL));
end
F2y=Asw*fy;
F3y=Qy*1000;
F3u=Qu*1000;
K220=Asw*Es/z;
TT2=2*Pi*sqrt(M2/(K210*1000));
TT3=2*Pi*sqrt(M3modal/(K30*1000));
C2=2*c2*sqrt(M2*K210*1000); % damping coefficient in punching
C3=2*c3*sqrt(M3modal*K30*1000); % damping coefficient in punching
if dias<=0;
y2sy=0;
elseif dias>0;
    y2sy=z*fy/Es;
end
%%%%%%%%%%%%%%%%%%%%%%%%%%% Initial values %%%%%%%%%%%%%%%%%%%%%%%%%%%%%%%%%%%%
v2(1)=0;
v3(1)=0;
a2(1)=0;
a3(1)=0;
FC2(1)=0;
FC3(1)=0;
strainrate(1)=0;
```

```matlab
fctmd(1)=0;
FK21(1)=0;
DeltaFK21(1)=0;
FK22(1)=0;
DeltaFK22(1)=0;
K21(1)=K210;
K22(1)=K220;
FK2(1)=0;
K3(1)=K30;
K2(1)=K210+K220;
y3(1)=(g*M3modal/1000)/K30;
Deltay3(1)=0;
y2(1)=y3(1)+(g*M2/1000)/K210;
FK3(1)=y3(1)*K30;
y23(1)=0;
Deltay23(1)=0;
DeltaFK2(1)=0;
DeltaFK3(2)=0;
T(1)=0;
%%%%%%%%%%%%%%%%%%%%%%%%% Calculations %%%%%%%%%%%%%%%%%%%%%%%%%%%%%%%%%
for i=2:TS
    T(i)=DT+T(i-1);
%%%%%%%%%%%%%%%%%%%%%%%%% Calculate displacements %%%%%%%%%%%%%%%%%%%%%%%%%%%%%
y2(i)=y2(i-1)+(v2(i-1)*DT); %mm
y3(i)=y3(i-1)+(v3(i-1)*DT); %mm
Deltay3(i)=y3(i)-y3(i-1); %mm
y23(i)=y2(i)-y3(i);
Deltay23(i)=y23(i)-y23(i-1); %mm
%%%%%%%%%%%%%%%%%%%%%%%%% Calculate Stiffnesses %%%%%%%%%%%%%%%%%%%%%%%%%%%%%%
strainrate(i)=Deltay23(i)/(z*DT); %[1/s]
%Calculation of fctmd(i)
if strainrate(i)>0
    fctmd(i)=fctm*(1+0.54*((log10(strainrate(i))+5)/5)); %[N/mm2]
end
if strainrate(i)<=0
    fctmd(i)=fctm; %[N/mm2]
end
if y23(i)<=z*fctmd(i)/Ec;
    K21(i)=K210;
elseif y23(i)>z*fctmd(i)/Ec;
    K21(i)=0;
end
%Calculation of K22(i)
if y23(i-1)>y2sy
    K22(i)=Hard*K220/100; %[N/mm]
elseif y23(i-1)<y2sy
    K22(i)=K220;
end
if y23(i-1)>z*Asg/1000;
    K22(i)=0; %[N/mm]
end
K2(i)=K21(i)+K22(i);
%Calculation of K3(i)
    if FK3(i-1)>F3y
        K3(i)=(Duct)*K30; %[N/mm]
    end
if FK3(i-1)<F3y
    K3(i)=(kw*Ec*Ie)/(Lx*Lz^2);
end
if FK3(i-1)<=Fcrack;
    K3(i)=K30;
end
```

```matlab
if y3(i)<y3(i-1);
   K3(i)=K30;
end
%%%%%%%%%%%%%%%%%%%%%%% Calculate Forces %%%%%%%%%%%%%%%%%%%%%%%%%%%%%
if T(i)<Td/2;
   F0(i)=2*(Fmax*T(i))/Td;
elseif T(i)>Td/2;
   F0(i)=2*(Fmax*(-T(i)+Td))/Td;
end
if T(i)>Td;
   F0(i)=0;
end
%Calculation of FK2(i)
DeltaFK21(i)=Deltay23(i)*K21(i); %[N]
FK21(i)=DeltaFK21(i)+FK21(i-1);
FK22(i)=y23(i)*K22(i);
FK2(i)=FK21(i)+FK22(i);
if K2(i)==0;
   FK2(i)=0;
end
%Determine FK3(i)
FK3(i)=Deltay3(i)*K3(i)+FK3(i-1);
%Determine FC(i)
FC2(i)=C2*(v2(i-1)-v3(i-1))/1000; %[N]
FC3(i)=C3*v3(i-1)/1000; %[N]
%%%%%%%%%%%%%%%%%%%%%%%%%%%%% Calculate accelerations and velocities %%%%%%%%%%
a2(i)= ((F0(i)-FK2(i)-FC2(i))*1000/M2)+g; %mm/s2
v2(i)=v2(i-1)+a2(i)*DT; %mm/s
a3(i)= ((FK2(i)+FC2(i)-FK3(i)-FC3(i))*1000/M3modal)+g; %mm/s2
v3(i)=v3(i-1)+a3(i)*DT; %mm/s
end
plot (T,FK2)
hold on
plot (T,FK3,'r')
hold on
plot (T,F0,'g')
```

C3: Three degrees of freedom system

```
%%%%%%%%%%%%%%%%%%%%%%%%%%%%%%%%%%%%%%%%%%%%%%%%%%%%%%%%%%%%%%%%%
%                        Three degree of freedom system
%                        Coded by Sara Ghadimi Khasraghy/ Manuela Kaufmann
%%%%%%%%%%%%%%%%%%%%%%%%%%%%%%%%%%%%%%%%%%%%%%%%%%%%%%%%%%%%%%%%%
%%%%%%%%%%%%%%%%%%%%%%%%%% Input block %%%%%%%%%%%%%%%%%%%%%%%%%%%%%
clear all
clc;
%%%%%%%%%%%%%%%%%%%%%%%%% Impacting Boulder %%%%%%%%%%%%%%%%%%%%%%%%%%%%
W = 4000; % kg mass of the boulder
A = 1120000; % mm2 area of the boulder
%%%%%%%%%%%%%%%%%%%%%%%%%% Loading %%%%%%%%%%%%%%%%%%%%%%%%%%%%%%%%%
v0 = 9900; % mm/s velocity of impact
DT = 0.00008; % s time step size
TS = 1000; % Number of timesteps
g = 9810; % mm/s2 acceleration due to gravity
R0 = 600; % mm radius of the impacting body
%%%%%%%%%%%%%%%%%%%%%%%%%% Soil %%%%%%%%%%%%%%%%%%%%%%%%%%%%%%%%%%%%%
Gs = 50; % N/mm2 Shear modulus of soil
Esoil = 192; % N/mm2 Young modulus of soil
Poisson = 0.3; %Pisson ratio of soil
Den = 0.0000017; % kg/mm3 density of soil
ysoil = 18; % kN/m3, density of soil
e = 400; % mm thickness of soil cushion
phi = 33; % angle of internal friction
stype = 0; % 0 for dense soil and 1 for loose soil
sy = 0.6; % shape factor
sq = 1.6; % shape factor
sc = 1.6 ;% shape factor
Ny = 18.1; % constant depending on friction angle
Nq = 18.4; % constant depending on friction angle
Nc = 30.1; % constant depending on friction angle
coh = 0; % cohesion in the soil [N/m2]
Pi= 3.141593;%
%%%%%%%%%%%%%%%%%%%%%%%%% Slab %%%%%%%%%%%%%%%%%%%%%%%%%%%%%%%%%%%%%%
Lx = 3500; % mm
Lz = 4500; % mm
z = 350; % mm
kw = 30; % [-]
alpha = 0.54; % [-]
PMfactor = 4.0; % Ratio of ultimate load to ultimate unit moment
u1 = 20; % mm concrete cover for tensile reinforcement
u2 = 15; % mm concrete cover for compression reinforcement
dia1 = 22; % mm tensile reinforcement diameter
dia2 = 10; % mm compression reinforcement diameter
s1 = 155; % mm tensile reinforcement spacing
s2 = 300; % mm compression reinforcement spacing
dias = 0; % mm shear stirrups diameter; dias = 0 if there are no stirrups
ss = 100; % mm shear stirrups spacing; ss = 0 if there are no stirrups
c2 = 0.05; % damping ratio for local behavior
c3 = 0.05; % damping ratio for global behavior
b = 1000; % mm, slab stip
Duct= 0.1; % [-] ratio of stiffness after yielding
Hard=1; % %, hardening of steel
%%%%%%%%%%%%%%%%%%%%%%%% Material properties %%%%%%%%%%%%%%%%%%%%%%%%%%%
Asg = 55; % promil, ultimate strain of the reinforcement
fcm = 35; % MPa, mean compressive strength of concrete
fy = 500; % MPa, yielding strength of steel
Ec = 30000; % MPa, E-modulus of concrete
Es = 210000; % MPa, E-modulus of steel
yc = 25; % kN/m3, density of concrete
```

```matlab
Dmax= 16; % mm, maximum diameter of aggregate
%Allocate space all vectors
y0=zeros(TS,1);
y1=zeros(TS,1);
r=zeros(TS,1);
r0=zeros(TS,1);
C1=zeros(TS,1);
C0=zeros(TS,1);
FC1=zeros(TS,1);
FC0=zeros(TS,1);
K1=zeros(TS,1);
K0=zeros(TS,1);
DeltaFK1=zeros(TS,1);
DeltaFK0=zeros(TS,1);
FK1=zeros(TS,1);
FK0=zeros(TS,1);
SF1=zeros(TS,1);
DeltaSF1=zeros(TS,1);
a1=zeros(TS,1);
a0=zeros(TS,1);
v1=zeros(TS,1);
v10=zeros(TS,1);
T=zeros(TS,1);
y12=zeros(TS,1);
y2=zeros(TS,1);
FC2=zeros(TS,1);
QB=zeros(TS,1);
strainrate=zeros(TS,1);
fctmd=zeros(TS,1);
K21=zeros(TS,1);
K22=zeros(TS,1);
K2=zeros(TS,1);
DeltaFK2=zeros(TS,1);
FK21=zeros(TS,1);
DeltaFK21=zeros(TS,1);
FK22=zeros(TS,1);
DeltaFK22=zeros(TS,1);
Deltay3=zeros(TS,1);
y23=zeros(TS,1);
Deltay23=zeros(TS,1);
FK2=zeros(TS,1);
a2=zeros(TS,1);
v2=zeros(TS,1);
y3=zeros(TS,1);
FC3=zeros(TS,1);
K3=zeros(TS,1);
DeltaFK3=zeros(TS,1);
FK3=zeros(TS,1);
a3=zeros(TS,1);
v3=zeros(TS,1);
%%%%%%%%%%%%%%%%%%%%%% Sectional calculations %%%%%%%%%%%%%%%%%%%%%%%%%%%%%
%%%%%%%%%%%%%%%%%%%%%%%%% Bending
fctm=0.3*fcm^(2/3);
d = z-u1-dia1/2; % mm
ds2=u2+dia2/2; % mm
n=Es/Ec; % [-]
As1=1000*(dia1/2)^2*Pi/s1; % mm2/mm
As2=1000*(dia2/2)^2*Pi/s2; % mm2/mm
ro1=As1/(b*d); % [-]
ro2=As2/(b*d); % [-]
%%%% cracking of concrete
ycrack=((b*z*z/2)+((n-1)*As1*d)+((n-1)*ds2*As2))/((b*z)+((n-1)*(As1+As2)));
```

```matlab
Icrack=(Lz*(ycrack)^3)/3+n*As1*(d-ycrack)^2+(n-1)*As2*(ycrack-u2)^2;
Ig=Lz*z^3/12;
Mcrack=fctm*Icrack/(z-ycrack)/1000000;
straincrack=fctm/Ec;
y3crack=straincrack*z;
%%%% yielding of reinforcement
%%%% assuming elastic concrete at yielding
k=(((ro1+ro2)^2*n^2)+(2*(ro1+ro2*ds2/d)*n))^0.5-(ro1+ro2)*n; % [-]
cy=k*d; % mm
strains1=fy/Es; % [-]
strainc=strains1*cy/(d-cy); % [-]
fc=strainc*Ec; % MPa
strains2=strainc*(cy-ds2)/cy; % [-]
fs2=strains2*Es; % Mpa
Cc=0.5*fc*b*cy; % N
Cs=As2*fs2; % N
ybar=((ds2*Cs)+(Cc*cy/3))/(Cc+Cs); % mm
jd=d-ybar; % mm
My=As1*fy*jd/1000000; % kNm/m
Ie=Ig*(Mcrack/My)^3+(1-(Mcrack/My)^3)*Icrack;
if Ie>Ig;
    Ie=Ig;
end
%%%% Ultimate state
cu=(As1*fy-As2*fy)/(0.85*b*fcm); % mm
TSu=As1*fy/1000; %kN/m
CSu=As2*fy/1000; %kN/m
jdu=d-0.4*cu; % mm
Mu=TSu*jdu/1000; % kNm/m
Qu=PMfactor*Mu; % kN ultimate force
Qy=PMfactor*My; % kN yielding force
%%%%%%%%%%%%%%%%%%%%%%%%%%% Initial soil calculations %%%%%%%%%%%%%%%%%%%%%%%%
%                          using single degree of freedom
v10(1)=v0;
a0(1)=0;
r0(1)=0;
K0(1)=0;
C0(1)=0;
FC0(1)=0;
FK0(1)=0;
y0(1)=0;
Deltay0(1)=0;
DeltaFK0(1)=0;
for i=2:TS
T(i)=DT+T(i-1);
y0(i)=y0(i-1)+(v10(i-1)*DT); %mm
if y0(i)< 0;
    y0(i)=0;
end
cv0=sqrt(Esoil/Den/1000); %mm/s
r0(i)=sqrt(y0(i)*(2*R0-y0(i))); %mm
C0(i)=Pi*Den*cv0*((r0(i)^2)); %Ns/mm
FC0(i)=v10(i-1)*C0(i); %N
K0(i)=4*r0(i)*Gs/(1-Poisson); %N/mm
if K0(i)<K0(i-1);
    K0(i)= K0(i-1);
end
DeltaFK0(i)=K0(i)*(y0(i)-y0(i-1)); % N
FK0(i)=FK0(i-1)+DeltaFK0(i); %N
if FK0(i)<0;
    FK0(i)=0;
end
```

```matlab
a0(i)= -(1000*(FC0(i)+FK0(i))/W)+g; %mm/s2
v10(i)=v10(i-1)+a0(i)*DT; %mm
end
%%%%%%%%%%%%%%%%%%%%%%%%%%%%%%%%%%%%%%%%%%%%%%%%%%%%%%%%%%%%%%%%%%%%%%%
%%%%%%%%%%%%%%%%%%%%%%% Intermediate calculations %%%%%%%%%%%%%%%%%%%%%%%
D=max(y0);
rmax=sqrt(D*(2*R0-D));
if R0>=(e-D);
   phiSL=2*R0;
elseif R0<(e-D);
   phiSL=2*rmax+2*((e-D)*tan((45-phi/2)*Pi/180));
end
if stype>=1;
   phiSL=2*R0;
end
if phiSL<=0;
    phiSL=2*R0;
end
if phiSL>Lz-2*z;
   phiSL=lz-2*z;
end
K210=Pi*Ec*(z+phiSL); %N/mm
K30=(kw*Ec*z^3)/(12*Lz^2); %N/mm
Fcrack=K30*y3crack;
if R0<(e-D);
M2=Pi/12*(yc*(z/1000)*(3*(phiSL/1000)^2+6*(phiSL/1000)*(z/1000)+4*(z/1000)^2))*100+Pi/12*((e-
D)/1000)*ysoil*(4*(rmax/1000)^2+2*(rmax/1000)*(phiSL/1000)+(phiSL/1000)^2)*100; % kg
end
if R0>=(e-D);
   M2=Pi/12*(yc*(z/1000)*(3*(phiSL/1000)^2+6*(phiSL/1000)*(z/1000)+4*(z/1000)^2))*100+Pi*((e-
D)/1000)*ysoil*((R0/1000)^2)*100; % kg
end
   M2P=Pi/12*(yc*(z/1000)*(3*(phiSL/1000)^2+6*(phiSL/1000)*(z/1000)+4*(z/1000)^2))*100;
M3=(Lx/1000)*(Lz/1000)*(z/1000)*yc*100; % kg
M3modal=alpha*M3-M2P; % kg
if M3modal<0;
   M3modal=alpha*M3;
end
if dias<=0;
   row=0;
elseif dias>0;
row=(dias/2)^2*Pi/(ss^2);
end
if dias<=0;
   Asw=0;
elseif dias>0;
Asw=row*Pi*(z^2+(z*phiSL));
end
F2y=Asw*fy;
F3y=Qy*1000;
F3u=Qu*1000;
K220=Asw*Es/z;
TT2=2*Pi*sqrt(M2/(K210*1000));
TT3=2*Pi*sqrt(M3modal/(K30*1000));
C2=2*c2*sqrt(M2*K210*1000); % damping coefficient in punching
C3=2*c3*sqrt(M3modal*K30*1000); % damping coefficient in punching
if dias<=0;
y2sy=0;
elseif dias>0;
   y2sy=z*fy/Es;
end
```

```matlab
%%%%%%%%%%%%%%%%%%%%%%%%  Initial values %%%%%%%%%%%%%%%%%%%%%%%%%%%%%%%%%%%%%%
v1(1)=v0;
a1(1)=0;
r(1)=0;
K1(1)=0;
C1(1)=0;
FC1(1)=0;
FK1(1)=0;
y12(1)=0;
Deltay1(1)=0;
DeltaFK1(1)=0;
SF1(1)=1/(4*rmax*Gs/(1-Poisson)); % mm/N
DeltaSF1(1)=0;
T(1)=0;
v2(1)=0;
v3(1)=0;
a2(1)=0;
a3(1)=0;
FC2(1)=0;
FC3(1)=0;
QB(1)=0;
strainrate(1)=0;
fctmd(1)=0;
FK21(1)=0;
DeltaFK21(1)=0;
FK22(1)=0;
DeltaFK22(1)=0;
K21(1)=K210;
K22(1)=K220;
FK2(1)=0;
K3(1)=K30;
K2(1)=K210+K220;
y3(1)=(g*M3modal/1000)/K30;
Deltay3(1)=0;
y2(1)=y3(1)+(g*M2/1000)/K210;
y1(1)=y2(1);
FK3(1)=y3(1)*K30;
y23(1)=0;
Deltay23(1)=0;
DeltaFK2(1)=0;
DeltaFK3(2)=0;
%%%%%%%%%%%%%%%%%%%%%%%% Calculations %%%%%%%%%%%%%%%%%%%%%%%%%%%%%%%%%%%%%%%%%
for i=2:TS
    T(i)=DT+T(i-1);
%%%%%%%%%%%%%%%%%%%%%%%% Calculate displacements %%%%%%%%%%%%%%%%%%%%%%%%%%%%%%%%%
y1(i)=y1(i-1)+(v1(i-1)*DT); %mm
y2(i)=y2(i-1)+(v2(i-1)*DT); %mm
y12(i)=y1(i)-y2(i); %mm
y3(i)=y3(i-1)+(v3(i-1)*DT); %mm
Deltay3(i)=y3(i)-y3(i-1); %mm
y23(i)=y2(i)-y3(i);
Deltay23(i)=y23(i)-y23(i-1); %mm
%%%%%%%%%%%%%%%%%%%%%%%% Calculate Stiffnesses %%%%%%%%%%%%%%%%%%%%%%%%%%%%%%%%%%%%
cv=sqrt(Esoil/Den/1000); %mm/s
r(i)=sqrt(y12(i)*(2*R0-y12(i))); %mm
if (e-D)>=(3.4*R0);
    K1(i)=4*r(i)*Gs/(1-Poisson); %N/mm
    if y1(i)<y1(i-1);
    K1(i)= Esoil*D;
    end
end
if (e-D)<(3.4*R0);
```

```matlab
    K1(i)=(4*r(i)*Gs/(1-Poisson))*(1+1.28*(r(i)/e))*(1+y12(i)/(2*r(i)))*(1+(0.85-
0.28*(y12(i)/r(i)))*((y12(i)/e)/(1-y12(i)/e)));
end
if K1(i)<K1(i-1);
    K1(i)= K1(i-1);
end
strainrate(i)=Deltay23(i)/(z*DT); %[1/s]
%Calculation of fctmd(i)
if strainrate(i)>0
    fctmd(i)=fctm*(1+0.54*((log10(strainrate(i))+5)/5)); %[N/mm2]
end
if strainrate(i)<=0
    fctmd(i)=fctm; %[N/mm2]
end
if y23(i)<=z*fctmd(i)/Ec;
    K21(i)=K210;
elseif y23(i)>z*fctmd(i)/Ec;
    K21(i)=0;
end
%Calculation of K22(i)
if y23(i-1)>y2sy
        K22(i)=Hard*K220/100; %[N/mm]
elseif y23(i-1)<y2sy
    K22(i)=K220;
end
if y23(i-1)>z*Asg/1000;
    K22(i)=0; %[N/mm]
end
K2(i)=K21(i)+K22(i);
%Calculation of K3(i)
    if FK3(i-1)>F3y
        K3(i)=(Duct)*K30; %[N/mm]
    end
if FK3(i-1)<F3y
    K3(i)=(kw*Ec*Ie)/(Lx*Lz^2);
end
 if FK3(i-1)<=Fcrack;
    K3(i)=K30;
end
if y3(i)<y3(i-1);
    K3(i)=K30;
end
%%%%%%%%%%%%%%%%%%% Calculate Forces %%%%%%%%%%%%%%%%%%%%%%%%%%%%%%%%%%%%%
if (e-D)>=(3.4*R0);

QB(i)=((r(i)/1000)*sy*ysoil*1000*Ny+sq*(y12(i)/1000)*ysoil*1000*Nq+sc*coh*Nc+(v0/1000)*sqrt((Esoil*10
00000)*(Den*1000000000)))/1000000; %N/mm2
    DeltaSF1(i)=y12(i)/(Pi*r(i)^2*QB(i));
    SF1(i)=DeltaSF1(i)+1/(4*rmax*Gs/(1-Poisson));
    FK1(i)=y12(i)/SF1(i);
    if FK1(i)>=(QB(i)*Pi*r(i)^2);
        FK1(i)=(QB(i)*Pi*r(i)^2);
    end
    if y1(i)<y1(i-1);
        FK1(i)=K1(i)*(y12(i)-y12(i-1))+FK1(i-1);
    end
    if FK1(i)<0;
        FK1(i)=0;
    end
end
if (e-D)<(3.4*R0);
    DeltaFK1(i)=K1(i)*(y12(i)-y12(i-1)); % N
```

```matlab
    FK1(i)=FK1(i-1)+DeltaFK1(i); %N
end
if FK1(i)<0;
    FK1(i)=0;
end
%Calculation of FK2(i)
DeltaFK21(i)=Deltay23(i)*K21(i); %[N]
FK21(i)=DeltaFK21(i)+FK21(i-1);%[N]
FK22(i)=y23(i)*K22(i);
FK2(i)=FK21(i)+FK22(i);
if K2(i)==0;
    FK2(i)=0;
end
%Determine FK3(i)
FK3(i)=Deltay3(i)*K3(i)+FK3(i-1);
%Determine FC(i)
C1(i)=Pi*Den*cv*((r(i)^2)); %Ns/mm
if C1(i)<0;
    C1(i)=0;
end
FC1(i)=(v1(i-1)-v2(i-1))*C1(i); %N
FC2(i)=C2*(v2(i-1)-v3(i-1))/1000; %[N]
FC3(i)=C3*v3(i-1)/1000; %[N]
%%%%%%%%%%%%%%%%%%%%%%%%%%% Calculate accelerations and velocities %%%%%%%%%%%%%%%%
a1(i)= -(1000*(FC1(i)+FK1(i))/W)+g; %mm/s2
if FK1(i)<=0;
    a1(i)=g;
end
v1(i)=v1(i-1)+a1(i)*DT; %mm
a2(i)= ((FK1(i)-FK2(i)-FC2(i))*1000/M2)+g; %mm/s2
v2(i)=v2(i-1)+a2(i)*DT; %mm/s
a3(i)= ((FK2(i)+FC2(i)-FK3(i)-FC3(i))*1000/(M3modal))+g; %mm/s2
v3(i)=v3(i-1)+a3(i)*DT; %mm/s
end
plot (T,FK1)
hold on
plot (T,FK2,'r')
hold on
plot (T,FK3,'g')
```

D: Input blocks for analytical models

A typical input block used for analytical models for calculations listed in chapters 5 and 6 is provided.

D1: Experiments (Schellenberg 2008)

D2: Experiments (Yamaguchi et al. 2010)

D3: Case study

D1: Experiments (Schellenberg 2008)

2DFS

```
%%%%%%%%%%%%%%%%%%%%%%%%%%%  Input block %%%%%%%%%%%%%%%%%%%%%%%%%%%%%%%%%%%
%%%%%%%%%%%% Impacting Boulder
NN = 0.68; % Nose shape coefficient Young
W = 4000; % kg weight of the boulder
A = 1120000; % mm2 area of the boulder
%%%%%%%%%%%%%%%%%%%%%%%%%%% Loading %%%%%%%%%%%%%%%%%%%%%%%%%%%%%%%%%%
v0 = 9900; % mm/s velocity of impact
DT = 0.00008; % s time step size
TS = 1000; % Number of timesteps
g = 9810; % mm/s2 acceleration due to gravity
R0 = 732; % mm equivalent sphere radius of the impacting body
R1 = 600; % mm size of the boulder
%%%%%%%%%%%%%%%%%%%%%%%%%%%% Slab %%%%%%%%%%%%%%%%%%%%%%%%%%%%%%%%%%%%%%
Lx = 3500; % mm
Lz = 4500; % mm
z = 350; % mm
kw = 30; % [-]
alpha = 0.37; % [-]
PMfactor = 4; % Ratio of ultimate load to ultimate unit moment
u1 = 20; % mm concrete cover for tensile reinforcement
u2 = 15; % mm concrete cover for compression reinforcement
dia1 = 22; % mm tensile reinforcement diameter
dia2 = 10; % mm compression reinforcement diameter
s1 = 155; % mm tensile reinforcement spacing
s2 = 300; % mm compression reinforcement spacing
dias = 0; % mm shear stirrups diameter; dias = 0 if there are no stirrups
ss = 150; % mm shear stirrups spacing; ss = 0 if there are no stirrups
c2 = 0.05; % damping ratio for local behavior
c3 = 0.05; % damping ratio for global behavior
b = 1000; % mm, slab stip
Duct= 0.1; % [-] ratio of stiffness after yielding
Hard=1; % %, hardening of steel
Pi=3.141592;
%%%%%%%%%%%%%%%%%%%%%%%%%%%%%% Soil %%%%%%%%%%%%%%%%%%%%%%%%%%%%%%%%%%%%%
HN = 0.4; %m height of the impactor nose.
B=1.2; % a dimensionless compressibility of soil
R=63.3; %MPa indentation resistance of the target material
e = 400; % mm thickness of soil layer
phi = 33; % angel of internal friction
stype = 0; % 0 for dense soil and 1 for loose soil
Den = 1700; %kg/m3 density of soil
ysoil=20; %kN/m3
ME=60000;%kN/m2
S = 8; % penetrability of the target
%%%%%%%%%%%%%%%%%%%%%%%% Material properties%%%%%%%%%%%%%%%%%%%%%%%%%%%%%%
Asg = 55; % promil, ultimate strain of the reinforcement
fcm = 35; % MPa, mean compressive strength of concrete
fy = 500; % MPa, yielding strength of steel
Ec = 30000; % MPa, E-modulus of concrete
Es = 210000; % MPa, E-modulus of steel
yc = 25; % kN/m3, density of concrete
%%%%%%%%%%%%%%%%%%%%%%%%%%%%%%%%%%%%%%%%%%%%%%%%%%%%%%%%%%%%%%%%%%%%%%%%%%
```

3DFS

```
%%%%%%%%%%%%%%%%%%%%%%  Input block %%%%%%%%%%%%%%%%%%%%%%%%%%%%%%%%%%
%%%%%%%%%%%%%%%%%%%%%%%    Impacting Boulder%%%%%%%%%%%%%%%%%%%%%%%%%%%%%
W = 4000; % kg mass of the boulder
A = 1120000; % mm2 area of the boulder
%%%%%%%%%%%%%%%%%%%%%%%% Loading %%%%%%%%%%%%%%%%%%%%%%%%%%%%%%%%%%%%
v0 = 9900; % mm/s velocity of impact
DT = 0.00008; % s time step size
TS = 1000; % Number of timesteps
g = 9810; % mm/s2 acceleration due to gravity
R0 = 600; % mm radius of the impacting body
%%%%%%%%%%%%%%%%%%%%%%%%%%%% Soil%%%%%%%%%%%%%%%%%%%%%%%%%%%%%%%%%%%%%%
Gs = 50; % N/mm2 Shear modulus of soil
Esoil = 192; % N/mm2 Young modulus of soil
Poisson = 0.3; %Pisson ratio of soil
Den = 0.0000017; % kg/mm3 density of soil
ysoil = 18; % kN/m3, density of soil
e = 400; % mm thickness of soil cushion
phi = 33; % angle of internal friction
stype = 0; % 0 for dense soil and 1 for loose soil
sy = 0.6; % shape factor
sq = 1.6; % shape factor
sc = 1.6 ;% shape factor
Ny = 18.1; % constant depending on friction angle
Nq = 18.4; % constant depending on friction angle
Nc = 30.1; % constant depending on friction angle
coh = 0; % cohesion in the soil [N/m2]
Pi= 3.141593;%
%%%%%%%%%%%%%%%%%%%%%%%%%% Slab %%%%%%%%%%%%%%%%%%%%%%%%%%%%%%%%%%%%%%
Lx = 3500; % mm
Lz = 4500; % mm
z = 350; % mm
kw = 30; % [-]
alpha = 0.54; % [-]
PMfactor = 4.0; % Ratio of ultimate load to ultimate unit moment
u1 = 20; % mm concrete cover for tensile reinforcement
u2 = 15; % mm concrete cover for compression reinforcement
dia1 = 22; % mm tensile reinforcement diameter
dia2 = 10; % mm compression reinforcement diameter
s1 = 155; % mm tensile reinforcement spacing
s2 = 300; % mm compression reinforcement spacing
dias = 0; % mm shear stirrups diameter; dias = 0 if there are no stirrups
ss = 100; % mm shear stirrups spacing; ss = 0 if there are no stirrups
c2 = 0.05; % damping ratio for local behavior
c3 = 0.05; % damping ratio for global behavior
b = 1000; % mm, slab stip
Duct= 0.1; % [-] ratio of stiffness after yielding
Hard=1; % %, hardening of steel
%%%%%%%%%%%%%%%%%%%%%%%%%%%%%%%%%%% Material properties
%%%%%%%%%%%%%%%%%%%%%%%%%%%%%%
Asg = 55; % promil, ultimate strain of the reinforcement
fcm = 35; % MPa, mean compressive strength of concrete
fy = 500; % MPa, yielding strength of steel
Ec = 30000; % MPa, E-modulus of concrete
Es = 210000; % MPa, E-modulus of steel
yc = 25; % kN/m3, density of concrete
%%%%%%%%%%%%%%%%%%%%%%%%%%%%%%%%%%%%%%%%%%%%%%%%%%%%%%%%%%%%%%%%%%%%%%
```

D2: Experiments (Yamaguchi et al. 2010)

2DFS

```
%%%%%%%%%%%%%%%%%%%%%% Input block %%%%%%%%%%%%%%%%%%%%%%%%%%%%%%%%%%%%%%%%%
%%%%%%%%%%%%%%%%%%%%%% Impacting Boulder  %%%%%%%%%%%%%%%%%%%%%%%%%%%%%%%%%%%
NN = 0.623; % Nose shape coefficient Young
W = 5000; % kg weight of the boulder
A = 785000; % mm2 area of the boulder
%%%%%%%%%%%%%%%%%%%%%% Loading %%%%%%%%%%%%%%%%%%%%%%%%%%%%%%%%%%%%%%%%%
v0 = 14000; % mm/s velocity of impact
DT = 0.00008; % s time step size
TS = 1000; % Number of timesteps
g = 9810; % mm/s2 acceleration due to gravity
R0 = 500; % mm equivalent sphere radius of the impacting body
R1 = 500; % mm size of the boulder
%%%%%%%%%%%%%%%%%%%%%% Slab %%%%%%%%%%%%%%%%%%%%%%%%%%%%%%%%%%%%%%%%%
Lx = 5000; % mm
Lz = 4000; % mm
z = 400; % mm
kw = 24; % [-]
alpha = 0.44; % [-]
PMfactor = 5; % Ratio of ultimate load to ultimate unit moment
u1 = 30; % mm concrete cover for tensile reinforcement
u2 = 30; % mm concrete cover for compression reinforcement
dia1 = 19; % mm tensile reinforcement diameter
dia2 = 19; % mm compression reinforcement diameter
s1 = 125; % mm tensile reinforcement spacing
s2 = 125; % mm compression reinforcement spacing
dias = 13; % mm shear stirrups diameter; dias = 0 if there are no stirrups
ss = 450; % mm shear stirrups spacing; ss = 0 if there are no stirrups
c2 = 0.05; % damping ratio for local behavior
c2 = 0.02; % damping ratio for global behavior
b = 1000; % mm, slab stip
Duct= 0.1; % [-] ratio of stiffness after yielding
Hard=1; % %, hardening of steel
Pi=3.141592;
%%%%%%%%%%%%%%%%%%%%%% Soil %%%%%%%%%%%%%%%%%%%%%%%%%%%%%%%%%%%%%%%%%
HN = 0.175; %m height of the impactor nose.
B=1.2; % a dimensionless compressibility of soil
R=63.3; %MPa indentation resistance of the target material
e = 500; % mm thickness of soil layer
phi = 30; % angel of internal friction
stype = 0; % 0 for dense soil and 1 for loose soil
Den = 1700; %kg/m3 density of soil
ysoil=17; %kN/m3
ME=40000;%kN/m2
S = 10; % penetrability of the target
%%%%%%%%%%%%%%%%%%%%%% Material properties %%%%%%%%%%%%%%%%%%%%%%%%%%%%%%
Asg = 55; % promil, ultimate strain of the reinforcement
fcm = 34.2; % MPa, mean compressive strength of concrete
fy = 393; % MPa, yielding strength of steel
Ec = 30000; % MPa, E-modulus of concrete
Es = 210000; % MPa, E-modulus of steel
yc = 25; % kN/m3, density of concrete
%%%%%%%%%%%%%%%%%%%%%%%%%%%%%%%%%%%%%%%%%%%%%%%%%%%%%%%%%%%%%%%%%%%%%%%%%%
```

3DFS

```
%%%%%%%%%%%%%%%%%%%%%% Input block %%%%%%%%%%%%%%%%%%%%%%%%%%%%%%%%%%%%%%
%%%%%%%%%%%%%%%%%%%%%% Impacting Boulder %%%%%%%%%%%%%%%%%%%%%%%%%%%%%%%%%
W = 5000; % kg mass of the boulder
A = 785000; % mm2 area of the boulder
%%%%%%%%%%%%%%%%%%%%%% Loading %%%%%%%%%%%%%%%%%%%%%%%%%%%%%%%%%%%%%%%%%%
v0 = 14000; % mm/s velocity of impact
DT = 0.00008; % s time step size
TS = 1000; % Number of timesteps
g = 9810; % mm/s2 acceleration due to gravity
R0 = 500; % mm radius of the impacting body
%%%%%%%%%%%%%%%%%%%%%%%%%% Soil %%%%%%%%%%%%%%%%%%%%%%%%%%%%%%%%%%%%%%%%%
Gs = 30; % N/mm2 Shear modulus of soil
Esoil = 50; % N/mm2 Young modulus of soil
Poisson = 0.3; %Pisson ratio of soil
Den = 0.0000017; % kg/mm3 density of soil
ysoil = 18; % kN/m3, density of soil
e = 500; % mm thickness of soil cushion
phi = 30; % angle of internal friction
stype = 0; % 0 for dense soil and 1 for loose soil
sy = 0.6; % shape factor
sq = 1.6; % shape factor
sc = 1.6 ;% shape factor
Ny = 18.1; % constant depending on friction angle
Nq = 18.4; % constant depending on friction angle
Nc = 30.1; % constant depending on friction angle
coh = 0; % cohesion in the soil [N/m2]
Pi= 3.141593;%
%%%%%%%%%%%%%%%%%%%%%%%% Slab %%%%%%%%%%%%%%%%%%%%%%%%%%%%%%%%%%%%%%%%%%%
Lx = 5000; % mm
Lz = 4000; % mm
z = 400; % mm
kw = 24; % [-]
alpha = 0.44; % [-]
PMfactor = 5.0; % Ratio of ultimate load to ultimate unit moment
u1 = 30; % mm concrete cover for tensile reinforcement
u2 = 30; % mm concrete cover for compression reinforcement
dia1 = 19; % mm tensile reinforcement diameter
dia2 = 19; % mm compression reinforcement diameter
s1 = 125; % mm tensile reinforcement spacing
s2 = 125; % mm compression reinforcement spacing
dias = 13; % mm shear stirrups diameter; dias = 0 if there are no stirrups
ss = 450; % mm shear stirrups spacing; ss = 0 if there are no stirrups
c2 = 0.05; % damping ratio for local behavior
c3 = 0.02; % damping ratio for global behavior
b = 1000; % mm, slab stip
Duct= 0.1; % [-] ratio of stiffness after yielding
Hard=1; % %, hardening of steel
%%%%%%%%%%%%%%%%%%%%%%%% Material properties %%%%%%%%%%%%%%%%%%%%%%%%%%%%
Asg = 55; % promil, ultimate strain of the reinforcement
fcm = 34.2; % MPa, mean compressive strength of concrete
fy = 393; % MPa, yielding strength of steel
Ec = 30000; % MPa, E-modulus of concrete
Es = 210000; % MPa, E-modulus of steel
yc = 25; % kN/m3, density of concrete
%%%%%%%%%%%%%%%%%%%%%%%%%%%%%%%%%%%%%%%%%%%%%%%%%%%%%%%%%%%%%%%%%%%%%%%%%
```

D3: Case study

2DFS

```
%%%%%%%%%%%%%%%%%%%%% Input block %%%%%%%%%%%%%%%%%%%%%%%%%%%%%%%%%%%%
%%%%%%%%%%%%%%%%%%%%%% Impacting Boulder %%%%%%%%%%%%%%%%%%%%%%%%%%%%%%%%%
NN = 0.74; % Nose shape coefficient Young
W = 6000; % kg weight of the boulder
A = 1592000; % mm2 area of the boulder
%%%%%%%%%%%%%%%%%%%%%% Loading %%%%%%%%%%%%%%%%%%%%%%%%%%%%%%%%%%%%%%%
v0 = 82800; % mm/s velocity of impact
DT = 0.00008; % s time step size
TS = 1000; % Number of timesteps
g = 9810; % mm/s2 acceleration due to gravity
R0 = 712; % mm equivalent sphere radius of the impacting body
R1 = 712; % mm size of the boulder
%%%%%%%%%%%%%%%%%%%%%%%%%%% Slab %%%%%%%%%%%%%%%%%%%%%%%%%%%%%%%%%%%%%%
Lx = 8600; % mm
Lz = 7500; % mm
z = 550; % mm
kw = 26; % [-]
alpha = 0.33; % [-]
PMfactor = 8.6; % Ratio of ultimate load to ultimate unit moment
u1 = 30; % mm concrete cover for tensile reinforcement
u2 = 30; % mm concrete cover for compression reinforcement
dia1 = 30; % mm tensile reinforcement diameter
dia2 = 22; % mm compression reinforcement diameter
s1 = 150; % mm tensile reinforcement spacing
s2 = 300; % mm compression reinforcement spacing
dias = 0; % mm shear stirrups diameter; dias = 0 if there are no stirrups
ss = 150; % mm shear stirrups spacing; ss = 0 if there are no stirrups
c2 = 0.05; % damping ratio for local behavior
c3 = 0.05; % damping ratio for global behavior
b = 1000; % mm, slab stip
Duct= 0.1; % [-] ratio of stiffness after yielding
Hard=1; % %, hardening of steel
Pi=3.141592;
%%%%%%%%%%%%%%%%%%%%%%%%%%%%%%% Soil %%%%%%%%%%%%%%%%%%%%%%%%%%%%%%%%%%
HN = R1/1000; %m height of the impactor nose.
B=1.2; % a dimensionless compressibility of soil
R=63.3; %MPa indentation resistance of the target material
e = 800; % mm thickness of soil layer
phi = 33; % angel of internal friction
stype = 0; % 0 for dense soil and 1 for loose soil
Den = 2000; %kg/m3 density of soil
ysoil=20; %kN/m3
ME=50000;%kN/m2
S = 8; % penetrability of the target
%%%%%%%%%%%%%%%%%%%%%%%%%%% Material properties %%%%%%%%%%%%%%%%%%%%%%%%%%
Asg = 55; % promil, ultimate strain of the reinforcement
fcm = 35; % MPa, mean compressive strength of concrete
fy = 500; % MPa, yielding strength of steel
Ec = 30000; % MPa, E-modulus of concrete
Es = 210000; % MPa, E-modulus of steel
yc = 25; % kN/m3, density of concrete
%%%%%%%%%%%%%%%%%%%%%%%%%%%%%%%%%%%%%%%%%%%%%%%%%%%%%%%%%%%%%%%%%%%%%%%
```

3DFS

```
%%%%%%%%%%%%%%%%%%%%% Input block %%%%%%%%%%%%%%%%%%%%%%%%%%%%%%%%%%%%%%%%
%%%%%%%%%%%%%%%%%%%%% Impacting Boulder %%%%%%%%%%%%%%%%%%%%%%%%%%%%%%%%%%%
W = 3000; % kg mass of the boulder
A = 1130000; % mm2 area of the boulder
%%%%%%%%%%%%%%%%%%%%%% Loading %%%%%%%%%%%%%%%%%%%%%%%%%%%%%%%%%%%%%%%%%%%%
v0 = 42000; % mm/s velocity of impact
DT = 0.00008; % s time step size
TS = 1000; % Number of timesteps
g = 9810; % mm/s2 acceleration due to gravity
R0 = 600; % mm radius of the impacting body
%%%%%%%%%%%%%%%%%%%%%%%%%%% Soil %%%%%%%%%%%%%%%%%%%%%%%%%%%%%%%%%%%%%%%%%%
Gs = 50; % N/mm2 Shear modulus of soil
Esoil = 100; % N/mm2 Young modulus of soil
Poisson = 0.3; %Pisson ratio of soil
Den = 0.0000020; % kg/mm3 density of soil
ysoil = 20; % kN/m3, density of soil
e = 800; % mm thickness of soil cushion
phi = 33; % angle of internal friction
stype = 0; % 0 for dense soil and 1 for loose soil
sy = 0.6; % shape factor
sq = 1.6; % shape factor
sc = 1.6 ;% shape factor
Ny = 18.1; % constant depending on friction angle
Nq = 18.4; % constant depending on friction angle
Nc = 30.1; % constant depending on friction angle
coh = 0; % cohesion in the soil [N/m2]
Pi= 3.141593;%
%%%%%%%%%%%%%%%%%%%%%%%%%% Slab %%%%%%%%%%%%%%%%%%%%%%%%%%%%%%%%%%%%%%%%%%%
Lx = 8600; % mm
Lz = 7500; % mm
z = 550; % mm
kw = 26; % [-]
alpha = 0.33; % [-]
PMfactor = 8.6; % Ratio of ultimate load to ultimate unit moment
u1 = 30; % mm concrete cover for tensile reinforcement
u2 = 30; % mm concrete cover for compression reinforcement
dia1 = 30; % mm tensile reinforcement diameter
dia2 = 22; % mm compression reinforcement diameter
s1 = 150; % mm tensile reinforcement spacing
s2 = 300; % mm compression reinforcement spacing
dias = 0; % mm shear stirrups diameter; dias = 0 if there are no stirrups
ss = 100; % mm shear stirrups spacing; ss = 0 if there are no stirrups
c2 = 0.05; % damping ratio for local behavior
c3 = 0.05; % damping ratio for global behavior
b = 1000; % mm, slab stip
Duct= 0.1; % [-] ratio of stiffness after yielding
Hard=1; % %, global hardening
%%%%%%%%%%%%%%%%%%%%%%%% Material properties %%%%%%%%%%%%%%%%%%%%%%%%%%%%%%
Asg = 55; % promil, ultimate strain of the reinforcement
fcm = 35; % MPa, mean compressive strength of concrete
fy = 500; % MPa, yielding strength of steel
Ec = 30000; % MPa, E-modulus of concrete
Es = 210000; % MPa, E-modulus of steel
yc = 25; % kN/m3, density of concrete
%%%%%%%%%%%%%%%%%%%%%%%%%%%%%%%%%%%%%%%%%%%%%%%%%%%%%%%%%%%%%%%%%%%%%%%%%%%
```

Curriculum vitae

Personal data:

Name:	Sara Ghadimi Khasraghy
Date of birth:	07 April 1978
Nationality:	Iranian

Qualifications:

2006-2011:   Doctoral candidate in Structural Engineering, ETH Zurich, Switzerland.

2003-2005:   M.Eng. in Structural Engineering, Asian Institute of Technology (AIT), Thailand.

Graduated in May 2005 with 3.7 GPA, Master's thesis: Nonlinear Finite Element Analysis of Reinforced Concrete Deep Beams.

1999-2002:   B.Eng. in Civil Engineering, NED University of Engineering & Technology, Karachi, Pakistan (migration/transfer program from Iran).

Graduated in March 2002 with 87.5%, Bachelor's thesis: Design of an Inter-City Bus Terminal for Karachi.

1996-1998:   Bachelor of Civil Engineering student, Mesbah-e-Danesh Private College, Karaj, Iran.

Awards and scholarships:

2003-2005:   Japanese government scholarship for Master of Engineering, Asian Institute of Technology, Thailand.

2002:   Certificate of academic merit for securing first class, second position (ranked 2nd out of 161 students) at the Bachelor of Civil Engineering, NED University of Engineering & Technology, Pakistan.

Work experience:

2006-2011:   Research and Teaching Assistant, Institute of Structural Engineering, ETH Zurich, Switzerland.

2004-2006:   Research Associate and Software Development Engineer, Asian Center for Engineering Computations and Software (ACECOMS), AIT, Thailand.

2002-2003:   Jr. Structural Engineer, Engineering Associates, Karachi, Pakistan.

Other activities:

2009, 2011:   Assisting ETH student teams for concrete canoe competition, 12. & 13. Deutsche Betonkanu-Regatta.

2009-2010:   Board member of AVETH, academic association of scientific staff at ETH Zurich, Switzerland.

2003-2004:   Chair person of Sports & Leisure Committee, Student Union, AIT, Thailand.

1994-2004:   Aerobics, Tae Kwon Do, and Weight Training instructor.

1994-1998:   Tae Kwon Do national champion, member of Iranian national team of Tae Kwon Do, and Black Belt from World Tae Kwon Do Federation.